

AD-A055 465

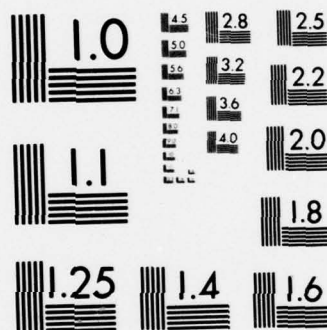
A KALMAN FILTER DESIGN FOR THE SPACE SHUTTLE ORBITER
INERTIAL MEASURING U. (U) AIR FORCE INST OF TECH
WRIGHT-PATTERSON AFB OHIO SCHOOL OF EN. D A VAN LIERE
DEC 77 AFIT/GGC/EE/77-10 F/G 22/2

1/2

UNCLASSIFIED

NL





MICROCOPY RESOLUTION TEST CHART
NATIONAL BUREAU OF STANDARDS-1963-A

AD A055465

AU NO. _____
DC FILE COPY

FOR FURTHER TRAN

①

AIR FORCE INSTITUTE OF TECHNOLOGY



AIR UNIVERSITY
UNITED STATES AIR FORCE

A KALMAN FILTER DESIGN FOR THE SPACE
SHUTTLE ORBITER INERTIAL MEASURING UNIT DURING
DECRBIT/REENTRY USING GLOBAL POSITIONING
SYSTEM SATELLITE INFORMATION

THESIS

AFIT/GGC/EE/77-10

Dennis A. Van Liere
Capt USAF

DDC

PROFORM

JUN 22 1978

RESERVE

E

SCHOOL OF ENGINEERING

DISTRIBUTION STATEMENT A

Approved for public release;
Distribution Unlimited

WRIGHT-PATTERSON AIR FORCE BASE, OHIO

13 08 13 181

1

AD A055465

AD No. DDC FILE COPY

6 A KALMAN FILTER DESIGN FOR THE SPACE SHUTTLE ORBITER INERTIAL MEASURING UNIT DURING DEORBIT/REENTRY USING GLOBAL POSITIONING SYSTEM SATELLITE INFORMATION.

9 Masters THESIS

AFIT/GCC/EE/77-10

10 Dennis A. Van Liere
Capt USAF

11 Dec 77

12 183 p.

16 7p71

17 00

DDC
RECEIVED
JUN 22 1978
E

Approved for public release; distribution unlimited.

A KALMAN FILTER DESIGN FOR THE SPACE SHUTTLE
ORBITER INERTIAL MEASURING UNIT DURING DEORBIT/REENTRY
USING GLOBAL POSITIONING SYSTEM SATELLITE INFORMATION

THESIS

Presented to the Faculty of the School of Engineering
of the Air Force Institute of Technology
Air University
in Partial Fulfillment of the
Requirements for the Degree of
Master of Science

ACCESSION for		
RTS	White Section	<input checked="" type="checkbox"/>
DS	Buff Section	<input type="checkbox"/>
UNANNOUNCED		<input type="checkbox"/>
JUSTIFICATION		
BY		
DISTRIBUTION/AVAILABILITY CODES		
Dist.	AVAIL. and/or	SPECIAL
A		

by

Dennis A. Van Liere, B.S.

Capt

USAF

Graduate Electrical Engineering

December 1977

Preface

The proposed topic for this study was suggested by personnel of the Math Physics Branch of the Mission Planning and Analysis Division of the National Aeronautics and Space Administration at Johnson Space Center. Material support in the form of tables of values, access to previous studies, and magnetic computer trajectory simulation tapes was supplied by the personnel of this branch. Partial sponsorship for this study was provided by the Advanced Navigation Group of the Reference Systems Branch of the Air Force Avionics Laboratory, Wright-Patterson AFB.

I would like to take this opportunity to express thanks to several individuals who made it possible for me to complete as much of this study as I did. First, I have very sincere appreciation for the guidance and learning that I received from Professor Peter S. Maybeck, both advisor and teacher. Mr. Robert T. Savely, director of the Math Physics Branch at NASA also deserves special thanks for taking the time to provide the topic for this study and the information and material mentioned above. In addition, the help and hospitality of those under him, especially Messrs. R. E. Eckelkamp and B. F. Cockrell were invaluable to me, both during my brief visit, and afterwards, during the study itself. I especially want to thank Dr. Harold Jones of The Analytic Sciences Corporation for his ear, his time, and his help during my study. Major Ken Meyers, original sponsor for my study, gave me the initial encouragement to think that the study was, in fact, possible. Mr. Bill Bustard of the Data Automation Section at AFIT also deserves a special thanks for all his help during the more than 800 times input was made to the computer under my problem. It is impossible to mention

all of the others who provided support to my study, but I want all to know I am deeply grateful for all help received.

I want to give special thanks to my wife, Nancy, for her patience during this year and a half for all the inconveniences that she had to put up with. Finally, I want to thank my typist, Rosalie Gibler, for being so easy to work with.

Contents

	<u>Page</u>
Preface.	ii
List of Figures.	vi
List of Tables	vii
Abstract	viii
I. Introduction	1
Purpose	1
Deorbit/Reentry of the Space Shuttle Orbiter.	2
Global Positioning System	3
Assumptions and Limitations	4
Report Organization	5
II. Space Shuttle Coordinate Systems and Transformations	7
Reference Coordinate Frames	7
Earth Centered Inertial Frame	7
East-North-Up Reference Frame	9
Relative Velocity Frame	10
Platform Frame.	10
III. Global Positioning System.	12
Description	12
Using GPS	13
IV. Error Covariance Propagation Equations	15
Covariance Analysis Equations	15
Measurement Underweighting.	19
V. Space Shuttle IMU and GPS Truth Model.	21
Description	21
Error States.	22
System Dynamics Matrix and Process Noise Matrix	23
Truth Model Data Base	34
Notes on Satellite Modeling Values.	36
Truth Model Measurement Matrix and Measurement Noise.	37
VI. Kalman Filter Design	40
Basis for Kalman Filter	40
Filter Description.	41
17-State Filter	43

Contents

	<u>Page</u>
11-State Filter	49
8-State Filter.	53
Baseline Filter	54
VII. Results and Conclusions.	55
Results	55
Optimal Filter.	56
17-State Filter	57
11-State Filter	61
8-State Filter.	63
Conclusion.	65
Bibliography	67
Appendix A: Computer Generated Plots.	69
73-State Optimal Filter	69
17-State Filter, Slow Update Rate	77
17-State Filter, Fast Update Rate	89
11-State Filter, Pre-Blackout	101
11-State Filter, Post-Blackout.	113
8-State Filter, Pre-Blackout.	125
8-State Filter, Post-Blackout	134
Appendix B: Description of Computer Programs Used	143
Software.	143
GCAP.	144
IGI	145
Impulsive Control	147
Appendix C: Filter Parameter Presentation and Comparison.	148
Appendix D: Addendum: Results After Model Error Correction	150
Corrected Specific Force Schedule	150
Filter Modifications.	151
Corrected Filter Performance.	152
Conclusion.	153
Vita	171

List of Figures

<u>Figure</u>		<u>Page</u>
1	Space Shuttle Deorbit/Reentry Trajectory.	2
2	Aries-Mean-of-1950, Earth Centered Inertial Frame . . .	8
3	System Dynamics Matrix.	23
4	Non-zero Blocks Within Partitions <u>A</u> and <u>B</u> of System Dynamics Matrix	24
5	Quartz Crystal Clock Error Model.	30
6	Definition of <u>B</u> Partition Blocks for System Dynamics Matrix.	31
7	Satellite Dynamics Block Definition	33
8	Kalman Filter Dynamics Matrix	45
9-19	Performance Plots, 73-State Optimal Filter.	71-76
20-41	Performance Plots, 17-State Filter, 30.72 Sec Update. .	78-88
42-63	Performance Plots, 17-State Filter, 15.36 Sec Update. .	90-100
64-85	Performance Plots, 11-State Filter, Pre-Blackout. . .	102-112
86-107	Performance Plots, 11-State Filter, Post-Blackout . .	114-124
108-123	Performance Plots, 8-State Filter, Pre-Blackout . . .	126-133
124-139	Performance Plots, 8-State Filter, Post-Blackout. . .	135-142
140	Generalized Functional Block Diagram for Modified GCAP	145
141-156	Performance Plots, 8-State Filter, Pre-Blackout, Corrected	154-161
157-172	Performance Plots, 8-State Filter, Post-Blackout, Corrected	163-170

List of Tables

<u>Table</u>	<u>Page</u>
I Deorbit Truth Model Error States.	22
II Definition of MTU Error States.	31
III Satellite State Definition.	33
IV Truth Model Data Base -- IMU, MTU, and Satellites	35
V Kalman Filter Error States and Initial Conditions	42
VI 17-State Filter Design Parameters	45
VII 11-State Filter Process Noise Spectral Density.	50
VIII Post-Blackout Initial Conditions, 8- and 11-State Filters .	52
IX 17-State Slow and Fast Update Rate Comparison	61
X Pre-Blackout Comparison of 11- and 8-State Filter Performance	63
XI Post-Blackout Comparison of 11- and 8-State Filter Performance	64
XII Comparison of TASC Suggested Filter Process Noise and Measurement Noise Strengths with Final Study Values, 11-State Filter	148
XIII Full Lower Triangle of 6x6 Initial Covariance Matrix, Position and Velocity States, at Deorbit Ignition, Filter.	149
XIV Full Lower Triangle of 6x6 Initial Covariance Matrix, Position and Velocity States, at Deorbit Ignition, Truth Model	149
XV Full Lower Triangle of 6x6 Initial Covariance Matrix, Position and Velocity States, at Exit-Blackout, Filter.	149
XVI Full Lower Triangle of 6x6 Initial Covariance Matrix, Position and Velocity States, at Exit-Blackout, Truth Model	149

Abstract

✓ This report studies three Kalman Filter implementations for the de-orbit/reentry phase of a Space Shuttle Orbiter mission profile. Each design uses measurements from Global Positioning System satellites to update Kalman Filter estimates of selected error states and to bound the Shuttle's INS error growth. Covariance analysis techniques are used to compare the performances of 17-state, 11-state, and 8-state filter designs using a digital computer simulation of a NASA OPT-1 Space Shuttle mission trajectory. A 73-state truth model of the Space Shuttle IMU, the Orbiter GPS receiver Master Tuning Unit, and the GPS satellite constellation is used as a system simulation to examine the performance of the design filters. The results are shown primarily in the form of computer-generated plots of both filter indicated errors and true system errors versus time. It is concluded from the results that an 8-state filter design is able to perform well enough to be a primary candidate for design implementation, and also that further refinements are necessary in the user clock model of the design Kalman Filter. ↗

A KALMAN FILTER DESIGN FOR THE SPACE SHUTTLE
ORBITER INERTIAL MEASURING UNIT DURING DEORBIT/REENTRY
USING GLOBAL POSITIONING SYSTEM SATELLITE INFORMATION

I. Introduction

Purpose

This study is an investigation of minimum Kalman Filter state size required to achieve specified accuracy from the Space Shuttle Orbiter (hereafter referred to as the Orbiter) aided inertial navigation system (INS) during deorbit/reentry operation. The Kalman Filter designs studied utilize range and pseudo range-rate measurements from the Air Force's Global Positioning System (GPS) satellites as an updating aid for bounding the INS's inherent error growth.

NASA's Orbiter uses three KT-70 based Inertial Measuring Units (IMUs) for its navigation and for providing much of its guidance information during deorbit/reentry. NASA proposes to use a Kalman Filter, a recursive data processing algorithm residing in the Orbiter's onboard computer, to limit IMU error growth during the deorbit/reentry portion of the mission. The proposed filter (Ref 10:2.7 and 9:4.4) uses a pseudo drag measurement scheme to compute a drag update measurement for the Kalman Filter during initial deceleration and ionospheric blackout (Ref 9:4.4 and 10:A.1). This involves computation of a pseudo measurement of drag from the IMU accelerometer outputs and comparison of these measurements to expected values of drag generated from current estimates of position and velocity from the IMU and from table look up routines. This was to be the sole updating aid for the IMU until after exit from

ionospheric radio blackout. At this time TACAN and baro altimeter measurements would replace pseudo drag as the updating aids for the Kalman Filter.

This study investigates the use of GPS measurements as updating aids for the filter from deorbit ignition onward to ionospheric blackout, and again after blackout ends rather than TACAN and baro altimeter measurements. Measurements would be unavailable for a brief period during ionospheric blackout, during which time pseudo drag would be used to bound the rate of error growth. After blackout ends GPS measurements would continue until the Orbiter reached 20,000 feet above mean sea level (MSL) when the microwave landing system (MLS) would take over. Except for the period of ionospheric blackout, GPS measurements are the sole updating aids used in the filter designs studied.

Deorbit/Reentry of the Space Shuttle Orbiter

The data for the simulated trajectory in this study is from a NASA-supplied data tape (Ref 16) for NASA's early Orbiter mission OFT-1 trajectory (Ref 8:6). The deorbit operation begins with deorbit ignition, which occurs approximately over New Zealand for this trajectory, and ends with landing at Edwards Air Force Base, California (see Fig 1).

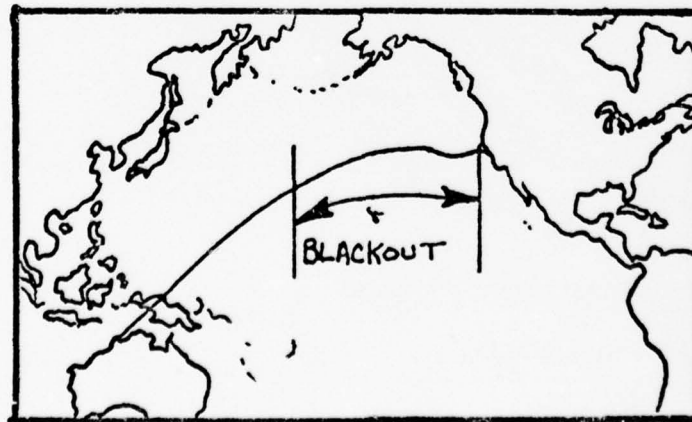


Figure 1. Space Shuttle Deorbit/Reentry Trajectory

Deorbit ignition occurs at an altitude of 727,550 feet. Ionospheric blackout is not well defined for the L band GPS signals, but for this study is assumed to occur at an altitude of approximately 293,000 feet, 22 minutes, 11 seconds after deorbit ignition. It is assumed to end at 177,500 feet, 10 minutes, 45 seconds later, at which time GPS signals are again available for processing. From this point until the MLS takes over there is another 9 minutes, 37 seconds during which GPS measurements are used.

Global Positioning System

The Air Force's Global Positioning System (GPS) will eventually provide worldwide navigation capability to users that are able to receive signals transmitted by navigation satellites currently being tested. Very accurate position and velocity information will be available for those users that can process all the information on the GPS satellite signals and that can select an optimum configuration of four satellites out of those that are visible to them (Ref 1:18-19).

The Space Shuttle will be able to use this information to maintain accurate position and velocity fixes without having to resort to ground-link information. This information can also be used to place a bound on the error growth inherent in the onboard IMU through the use of Kalman Filter error estimation.

This study simulates a 24 satellite constellation that propagates in time as actual satellites would (see Chapter III and Appendix B). The simulation employs a satellite selection criterion to obtain a "best" four-satellite configuration of the satellites that are visible to the Orbiter. Measurements from these four satellites in the

simulation are used to update a simulation of the Kalman Filter estimate of errors being committed by the Orbiter IMU and the filter then applies a correction to the IMU itself based on its updated estimate of these errors.

Assumptions and Limitations

A fundamental assumption of this study is that a radio blackout period of specified length exists during reentry due to ionospheric effects. During this period of blackout, GPS signals are not available for processing. It is assumed that drag update, described earlier, will be used during this blackout period to limit error growth. Due to limitations of time and resources, drag updating was not implemented in the simulations of this study. Because of this, the performance of the design filters were investigated in two phases, from deorbit ignition to blackout, and from exit blackout to 20,000 feet.

An initialized covariance of errors matrix at deorbit ignition was supplied by NASA (Ref 5) for position and velocity errors. Initial conditions on other errors were taken from studies done for NASA by The Analytic Sciences Corporation (TASC) (Ref 10:2.38-2.40 and 11:2.13-2.14) as were some of the initial conditions for the filter. These initial conditions assume an uploaded navigation fix and an IMU alignment by star tracker two hours prior to deorbit, with no GPS measurements taken until time for deorbit. TASC supplied an initialized covariance matrix for the position and velocity errors at exit blackout (Ref 12). The values in the matrix assume GPS measurements until blackout and the use of drag updating during blackout (Ref 11:2.23-2.24).

Even though the Global Positioning System will not be completed until 1984, a completed system of 24 satellites is assumed. This is because the use of test phase GPS configurations has been investigated by TASC already (Ref 11:Chap 2) and the aim of this study was to investigate Kalman Filter design to use GPS signals rather than to investigate the effects of degraded GPS configuration upon filter performance. Also assumed is the use of a high accuracy receiver on the Orbiter which is capable of processing all information available on the GPS signals and designed for the type of highly dynamic platform that the Orbiter will be (Ref 10:1.6).

Finally, it is assumed that linear approximations to the real world can be made so that linear differential equation description can be used to form a model of the IMU error description. This is not very restrictive and should not affect the validity of the study. This will allow the Covariance Analysis to be used as a tool in designing the Kalman Filter. In forming the models that describe the errors, Gaussian descriptions and whiteness of noises used in the models are both assumed so that the errors can then be described as Gaussian, characterized by their means and variances.

Report Organization

This report will present the elements of the study in the following order by chapter. Chapter II will discuss Space Shuttle coordinate systems and transformations. Range and range rate measurements using GPS will be presented in Chapter III. Covariance propagation equations used in the simulation are described in Chapter IV. In Chapter V the "Truth Model" description of the Space Shuttle IMU and GPS is given, and Chapter VI describes the Kalman Filter designs that were investigated

in this study. Chapter VII presents the results of the study and the conclusions drawn from these results. Appendix A is composed of the computer generated plots that present detailed results of the filter-indicated filter performance and the true filter performance. Appendix B presents a general description of the computer program used to perform the covariance analysis and a depiction of those portions of the program unique to this study. Appendix C presents filter design parameters recommended in other studies and compares them to the final design values of this study. Appendix D consists of an addendum presenting results for the 8-state filter design with a corrected schedule of specific force to the truth model clock states. It will present performance plots and a discussion of the results.

II. Space Shuttle Coordinate Systems and Transformations

Reference Coordinate Frames

The coordinate frames of interest in describing the motion of the Orbiter and the measurements of the GPS range and range-rate are described in the following figures and paragraphs. These are the coordinate frames specified by NASA (Ref 4) and described and used by TASC in NASA sponsored studies relating to Space Shuttle deorbit/reentry navigation (Ref 9:A.0-A.5) from which the following definitions come.

Earth Centered Inertial Frame

The coordinate frame most important to this study was the earth centered inertial frame or ECIF, which will be denoted by a superscript i . Of course, this is only an approximation to an inertial reference frame, being attached to the earth, but since it is nonrotating with respect to the "fixed" stars, for short term use it is an adequate approximation. It is in this reference frame that the navigation calculations are performed, the GPS simulation is made, and most of the trajectory data is provided. It can be described verbally as having the Z^i axis positive through the earth's spin axis, the X^i axis through Aries of 1950, and the Y^i axis completing the third axis of the right hand triad (see Figure 2).

Each of the other reference frames are related to the ECIF frame by transformation matrices, described in the next sections. The transformation matrices either transform from a frame, x , ($T_{i/x}$) to the ECIF, or to a frame, x , ($T_{x/i}$) from the ECIF.

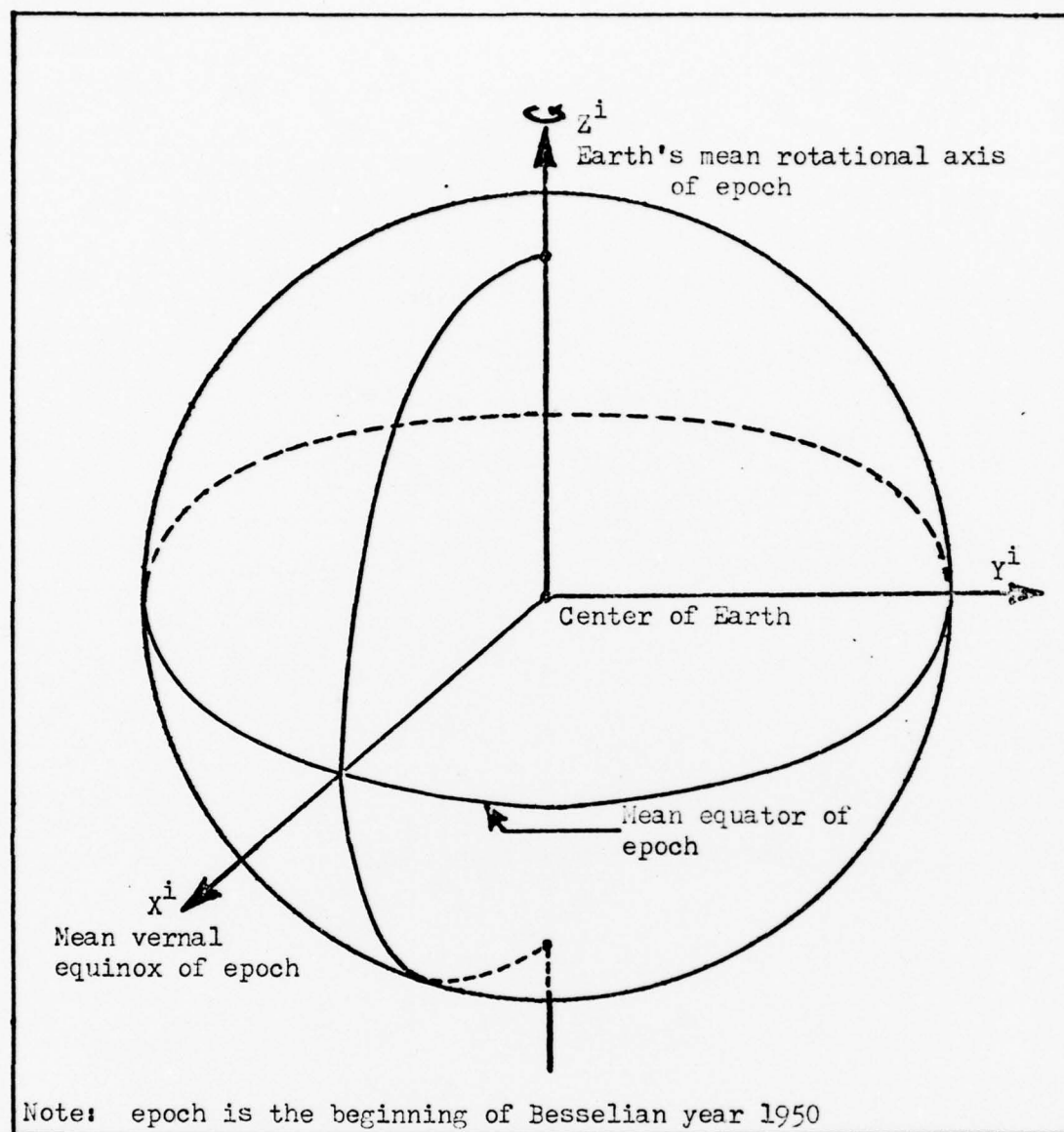


Figure 2. Aries-mean-of-1950, Earth Centered Inertial Frame

East-North-Up Reference Frame

The local level, east-north-up (ENU) frame is used in this study in the algorithm that calculates which four satellites to use out of the set of all visible satellites. This frame is best described by the way in which it is generated. The up unit vector, $\underline{1U}$ is described as being along the Orbiter's position vector, \underline{RU} , from earth center to the vehicle. The east unit vector, $\underline{1E}$ is described as the resultant of the cross product of the polar unit vector, $\underline{1Z}^i$ and the Orbiter position vector, \underline{RV} . The north unit vector is then the cross product of $\underline{1U}$ and $\underline{1E}$. This calculation is described mathematically as follows:

$$\underline{1U} = \frac{\underline{RU}}{|\underline{RU}|} \quad (1)$$

$$\underline{1E} = \frac{\underline{1Z}^i \times \underline{RU}}{|\underline{1Z}^i \times \underline{RU}|} \quad (2)$$

$$\underline{1N} = \underline{1U} \times \underline{1E} \quad (3)$$

The direction cosine matrix to transform from the ECIF to the ENU is then:

$$T_{LL/i} = \begin{bmatrix} \overleftrightarrow{\underline{1E}} \\ \overleftrightarrow{\underline{1N}} \\ \overleftrightarrow{\underline{1U}} \end{bmatrix} \quad (4)$$

Relative Velocity Frame

The frame which is used to relate gravity deflections and anomaly to the calculations is the Relative Velocity Frame (V), related to the Orbiter's earth relative velocity vector. The unit vectors which are used to define the transform from the V frame to the ECIF frame for computation purposes are defined by the use of the unit vector $\underline{1U}$ and the position vector \underline{RU} , defined previously, $\underline{1VR}$, the unit vector along the Orbiter's earth relative velocity vector, and \underline{VU} , the Orbiter's inertially referenced velocity. Mathematically, this transform is described as:

$$\underline{1VR} = \frac{\underline{VU} - \underline{WIE} \times \underline{RU}}{|\underline{VU} - \underline{WIE} \times \underline{RU}|} \quad (5)$$

where \underline{WIE} is the earth's spin vector. Furthermore, letting:

$$\underline{1W} = \underline{1U} \times \underline{1VR} \quad (5a)$$

the transform is defined as:

$$\underline{T}_{i/V} = \begin{bmatrix} \uparrow \underline{1U} \downarrow & \uparrow \underline{1VR} \downarrow & \uparrow \underline{1W} \downarrow \end{bmatrix} \quad (6)$$

Platform Frame

The final frame of interest is the platform coordinate frame, or P frame, in which the accelerometer measurements and gyro bias errors are

defined. The Orbiter uses a space stable IMU platform, which is defined at launch, and thus the transform from the platform frame to the ECIF frame is a simple rotation which remains constant throughout the mission. The transform direction cosine to go from the P frame to the ECIF frame was provided by NASA (Ref 16) and is given by

$$\underline{T}_{i/P} = \begin{bmatrix} 5.5711564 \text{ E-1} & -1.4125705 \text{ E-1} & -8.1833281 \text{ E-1} \\ -1.4473482 \text{ E-1} & -9.8686101 \text{ E-1} & 7.1813144 \text{ E-2} \\ -8.1772488 \text{ E-1} & 7.8433026 \text{ E-2} & -5.7-24052 \text{ E-1} \end{bmatrix} \quad (7)$$

III. Global Positioning System

Description

Currently the Air Force and Navy are jointly developing a system that will use signals from a network of satellites to provide worldwide navigation capability with high accuracy to suitably equipped users. At present the system is entering a test and evaluation period (Phase I) during which a limited number of satellites will be used to prove concepts and evaluate initial designs. When complete (Phase III) the system will consist of three major segments which are to be called the space segment, the user segment, and the control segment. An intermediate period (Phase II) for further refinement of equipment and evaluation may or may not be implemented depending on need and cost. Completion of the system is presently scheduled for 1984 (Ref 3:4.7).

In Phase III the space segment will consist of 24 satellites divided into groups of 8 satellites spread out in each of three evenly spaced, circular, nonsynchronous orbits. The satellites will be in an orbit of period equal to 11 hours 58 minutes so that each satellite will repeat a ground track once every 24 hours. The satellites will use cesium standard clocks to provide a very accurate clock signal with low drift characteristics. Each satellite will transmit coded signals with highly directional characteristics. These signals will allow a user to determine his own relative position, velocity and clock error factors by using the information coded into the signals.

The user segment will consist of an L band antenna, an onboard clock or timing unit, a receiver capable of processing all or part of the signal available from the satellites, and an onboard computer

to process the information. When a user's set is to be employed, it will scan above its local horizon and automatically select four satellites from those visible that will provide the best geometrical configuration to give the best accuracy (see Appendix B). The measurements received from each of the four satellites selected will then provide a basis for the computer solution to three components of position plus the user clock bias factor, and if desired, the solution to three components of velocity plus the user clock frequency error.

The control segment will consist of four monitor stations located in the United States and Guam and an upload station at Vandenberg Air Force Base in California. These stations will monitor the accuracy of each satellite's signals and the actual position of each satellite. Once each day, as a satellite makes its closest approach to Vandenberg, updated clock and ephemeris information will be uploaded to the satellite.

Using GPS

The way in which the satellites provide the information to the user will be by transmitting two distinct signals on separate L band frequencies, giving the time the signal was transmitted plus the satellite position and velocity at that time. By measuring the Doppler shift in the signals the user will be able to compute a range rate to the satellite. By synchronizing its clock to those of the satellites, the time difference from signal transmission to reception can be used to determine range to the satellite. Use of the two separate L band signals will allow the user to determine the variation in velocity computed due to ionospheric effects on the signals.

The fact that the satellite will be uploaded daily is an indication that there is some decay in the accuracy of information to be expected as well as some slight clock drift. The time since uploading will thus be a factor in the accuracy of the information obtained by the user, and so also in the magnitude of the error committed by using this information. Typical magnitudes of RMS range error are approximately five feet just prior to upload and approximately one foot just after upload. Comparable magnitudes in the RMS range rate errors are approximately 0.003 feet per second just prior to upload and 0.0005 feet per second just after upload (Ref 10:2.8).

IV. Error Covariance Propagation Equations

Covariance Analysis Equations

This chapter presents the basic covariance time propagation equations. The equations propagate the filter estimated error covariance and the system actual error covariance. The notation used will also be presented. The derivation of the Kalman Filter is well documented in the literature and the references provide two sources (Ref 13:5.7-5.40 and 14:247-261). The actual implementation within the General Covariance Analysis Program (GCAP) (Ref 6) is presented in Appendix B. The error model equations for the system, or "truth" model, and for the suboptimal Kalman Filter are presented in the next chapters.

The Kalman Filter requires a linear or linearized differential equation description of the system. This is acknowledged to be only an approximation to the real world nonlinear model which would be much more difficult to implement on a digital computer. The system model used is an integrated simulation of all of the significant errors committed by the Space Shuttle IMU and by GPS. These errors include both those errors caused by imperfections in the system sensors, such as gyro drifts and platform misalignments, and also those errors caused by environmental factors such as ionospheric delay effects and gravitational deflections and anomaly. The vector of errors, denoted \underline{dx} , is modeled as the difference between the indicated vector of state variables, denoted by $\hat{\underline{x}}$, and the true vector of state variables, denoted by \underline{x} .

The error state variables are modeled by first order linear differential equations of the form

$$\dot{\underline{x}}(t) = \underline{F}(t)\underline{x}(t) + \underline{G}(t)\underline{w}(t) \quad (8)$$

where

$\underline{x}(t)$ is the vector of error state variables.

$\underline{F}(t)$ is the system dynamics matrix.

$\underline{G}(t)$ is a gain matrix.

$\underline{w}(t)$ is a vector of white noise inputs.

Since the error state variables and white noises are assumed Gaussian, they can be completely described by:

- 1) the mean of the state variable vector:

$$\overline{\underline{x}}(t) = E[\underline{x}(t)] \quad (9)$$

- 2) the covariance of the state variables:

$$\underline{P}(t) = E[(\underline{x}(t) - \overline{\underline{x}}(t))(\underline{x}(t) - \overline{\underline{x}}(t))^T] \quad (10)$$

- 3) the mean of the white noises, which is zero:

$$E[\underline{w}(t)] = \underline{0} \quad (11)$$

and

- 4) the covariance kernel of the white noise inputs:

$$\underline{Q}(t_1)\delta(t_1 - t_2) = E[\underline{w}(t_1)\underline{w}^T(t_2)] \quad (12)$$

where $\delta(t_1 - t_2)$ is the delta function.

Linear measurements are available of certain of the state variables at discrete instants in time and are modeled to be of the form

$$\underline{Z}(t_k) = \underline{H}(t_k)\underline{x}(t_k) + \underline{v}(t_k) \quad (13)$$

generated as a difference between INS and GPS outputs, where

$\underline{Z}(t_k)$ is the vector of difference measurements.

$\underline{H}(t_k)$ is the measurement matrix.

$\underline{v}(t_k)$ is a vector of corruptive white noise.

The discrete time corruptive white noise is, as was the continuous time $\underline{w}(t)$, modeled as Gaussian with zero mean and covariance kernel described as

$$E[\underline{v}(t_1)\underline{v}(t_2)^T] = \begin{matrix} \underline{R}(t_1), & t_1 = t_2 \\ \underline{0} & , t_1 \neq t_2 \end{matrix} \quad (14)$$

It is also assumed that the system white noises and the corruptive measurement noises are uncorrelated for all time,

$$E[\underline{w}(t_1)\underline{v}(t_2)^T] = \underline{0}, \text{ all } t_1, t_2 \quad (15)$$

For notational convenience the reference to the independent variable (t) will be dropped and time dependence will be assumed unless specifically noted otherwise.

The covariance of the errors must satisfy the matrix differential equation

$$\dot{\underline{P}} = \underline{F}\underline{P} + \underline{P}\underline{F}^T + \underline{G}\underline{Q}\underline{G}^T \quad (16)$$

between sample times and it is the solution to this equation that propagates the error covariance forward in time. In the actual implementation \underline{G} is an $n \times n$ identity matrix, and thus, in the above differential equation $\underline{G}\underline{Q}\underline{G}^T$ will be denoted by \underline{Q} only.

The Kalman Filter is used to provide an estimate of the errors being committed by the system. This estimate is corrected at discrete times by a Kalman "gain" weighted residual, $\underline{K}_F(\underline{Z} - \underline{H}\underline{x})$ added to the estimate. At the time of the "update" of the estimate, a correction is also applied to the system, based upon the filter computed gain. In other words, once the errors are estimated and measurements are taken to correct the estimate, the IMU is driven so as to remove the estimated errors from it also.

Thus the propagation of the estimated error covariance forward in time becomes more than just a solution to the differential equation above, but must also include the measurement update equations, which are provided by Kalman Filter theory. Propagation equations for a covariance analysis are presented here.

From an initial condition of

$$\underline{P}_0 = E[(\underline{dx}_0)(\underline{dx}_0)^T] \quad (17)$$

the covariance is propagated forward in time, and also between measurement updates by

$$\dot{\underline{P}} = \underline{F}\underline{P} + \underline{P}\underline{F}^T + \underline{Q} \quad (18)$$

At measurement update times the Kalman gain is calculated as

$$\underline{K}_F = \underline{P}^- \underline{H}^T [\underline{H} \underline{P}^- \underline{H}^T + \underline{R}]^{-1} \quad (19)$$

where the superscript minuses indicate time at the instant of taking a measurement and just prior to an update. The covariance is updated then by

$$\underline{P}^+ = \underline{P}^- - \underline{K}_F \underline{H} \underline{P}^- \quad (20)$$

where the plus indicates as the minus signs above but just after update incorporation. The General Covariance Analysis Program used assumes complete impulsive control over those states which are updated. This will be discussed further in Appendix B.

Measurement Underweighting

While the above equations accurately describe the basic Kalman Filter covariance propagation and update relationships, one change has been made, in accord with the previous studies by The Analytic Sciences Corporation (TASC). That change is the incorporation of measurement underweighting (Ref 10:2.18-2.19). This is a modification of the Kalman gain calculation as

$$\underline{K}_F = \underline{P}^- \underline{H}^T [\underline{u}_m \underline{H} \underline{P}^- \underline{H}^T + \underline{R}]^{-1} \quad (21)$$

where \underline{u}_m is the measurement underweighting factor and is a scalar larger than one. The factor used is equal to 1.2 until the root sum of the position variances (the square root of the sum of the position covariances, $P(1,1)$, $P(2,2)$ and $P(3,3)$), is less than 1,000 feet.

When this occurs, the factor is set to one, effectively turning off measurement underweighting. The underweighting remains off unless the root sum goes above 1,000 feet once again.

Measurement underweighting is used to prevent the filter from making sudden changes in state estimates during initial transient periods when a new sensor is acquired, such as when a satellite set changes. This reduces the possibility of filter divergence and will also reduce filter sensitivity to a single bad measurement (Ref 10:2.18).

V. Space Shuttle IMU and GPS Truth Model

Description

The design Kalman Filter's effect on actual system performance and error growth is the final evaluation of its effectiveness. It is not possible, or even desirable, to perform this check on the actual system during the many iterations on the various Kalman Filter parameters. Because of this, a simulation model of the actual system is used, which is referred to as the truth model. As mentioned in Chapter IV, the truth model consists of all the significant error states in the Space Shuttle IMU and in the GPS measurements.

The truth model used in this study is a modification of the truth models used in earlier studies on this problem (Ref 9:3.2-3.12, 10:4.9-4.19, and 11:2.13-2.14). It is a modification in that the state order is somewhat different, certain GPS states are modeled in a slightly different manner, and the unique portions of the trajectory used plus the ultimate aim of the study, allowed deletion of certain states used in these previous studies. The deleted states are for external aids such as TACAN and baro altimeter, as well as "pseudo drag" update (Ref 9:4.4), which were not used in this study.

First, the error states are presented, followed by a discussion of the truth model system dynamics matrix and the associated process noise covariance kernel. Next, the truth model data base, which includes initial conditions and modeling values for the covariance propagation equations, will be discussed. The chapter will be concluded with a presentation of the measurement matrix for the truth model plus the associated corruptive measurement noise covariance.

Error States

Table I defines the error states and number of error sources for this study's truth model. The 73-state truth model consists of 36 IMU-related states, 3 states for gravity deflections and anomaly, 6 user clock states for the Orbiter Master Timing Unit (MTU), and 28 satellite error states. These last 28 states are actually a quadruple repetition of a 7-state model for each of the four satellites used during each update.

Table I: Deorbit Truth Model Error States

Section	States	Error Source	No. of States	No. of Error Sources
<u>A_a</u>	1-3	Position Errors	3	3
	4-6	Velocity Errors	3	3
<u>B_a</u>	7,8	User Clock Phase, Freq.	2	2
<u>A_a</u>	9-11	Platform Misalignments	3	3
	12-14	Accelerometer Biases	3	3
	15-17	Gyro Bias Drifts	3	3
<u>B_b</u>	18-21	Other MTU Clock States	4	4
<u>A_b</u>	22-24	Accel. Scale Factors	3	3
	25-30	Accel. Misalignments (Assym. and Non-orthog.)	6	6
	31-33	Accel. Non-Linearities	3	3
	34-36	Gravity Deflections and Anomaly	3	3
	37-42	Gyro Mass Unbalances (g-sensitive drifts)	6	5
	43-45	Gyro Anisoclasticity (g ² -sensitive drifts)	3	3
	46-73	Satellite Error States	28	28

The sections referenced in Table I refer to the section of the system dynamics matrix which helps to define the models for the states in that section (see Figure 3).

System Dynamics Matrix and Process Noise Matrix

The system dynamics matrix will be presented in three sections, as shown in Figure 3, and listed in Table I. The sections break the error states into three main groupings. First, sections labeled A_1 , which relate the IMU-related states, including the gravity model errors, will be presented. Next will be a discussion of the Orbiter MTU error model, depicted in sections B_1 , followed by a description of section C, which contains the GPS satellite error models.

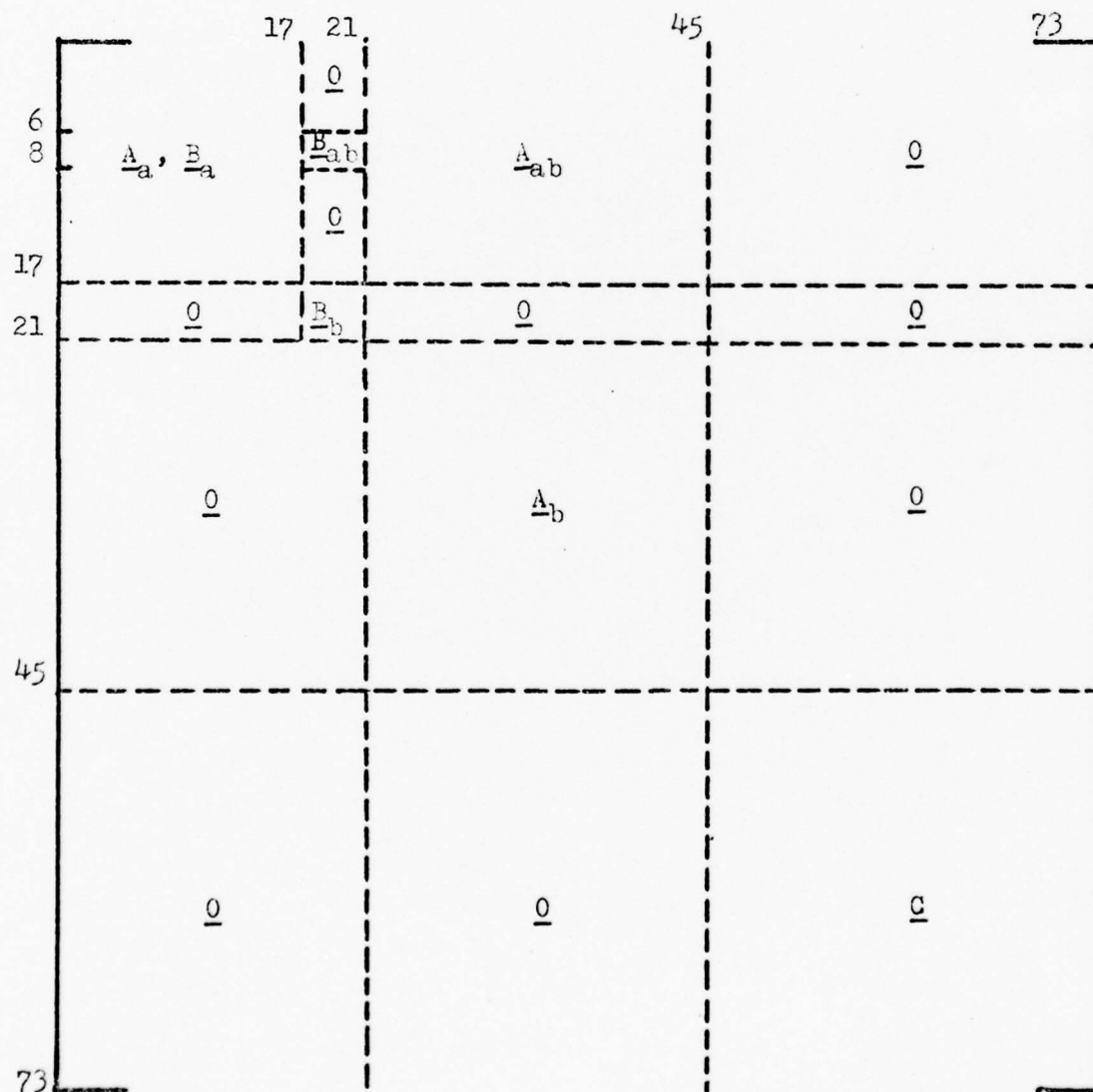


Figure 3. System Dynamics Matrix

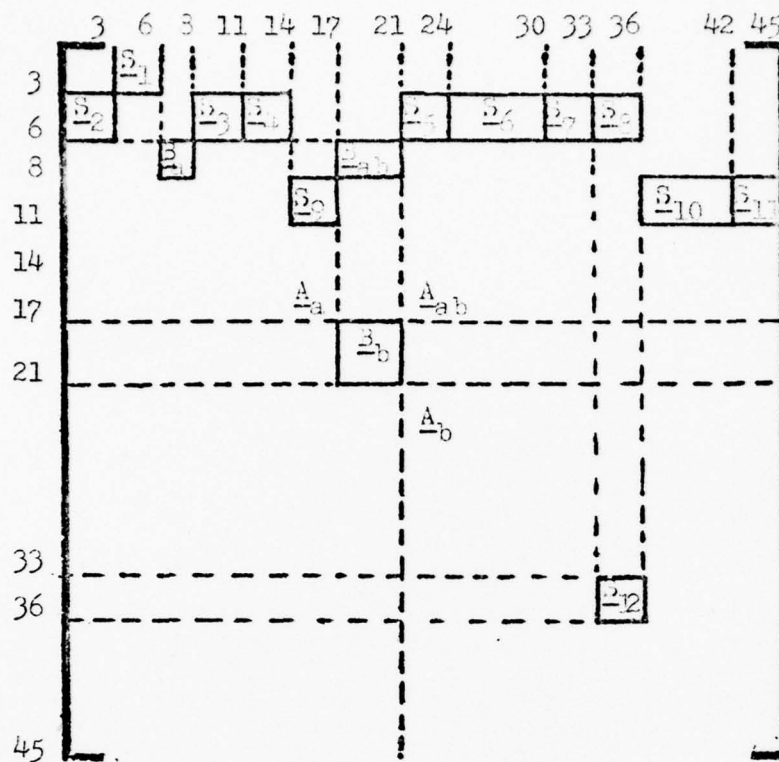


Figure 4. Nonzero Blocks Within Partitions A and B of System Dynamics Matrix

Figure 4 presents an expanded view of the partitions of Figure 3 labeled \underline{A}_a , \underline{A}_{ab} , \underline{A}_b , \underline{B}_a , \underline{B}_{ab} , and \underline{B}_b . The part labeled \underline{A}_{ab} contains the coupling between error states in the \underline{A}_a and \underline{A}_b sections, which are the IMU related states. The \underline{A} portions are easiest described by discussing the nonzero blocks labeled \underline{S}_i , component by component. Each of the blocks will be presented in order and defined by their relational functions.

Notation developed in previous studies (Ref 9:E.1-E.20) will be followed as much as possible. In this regard the following definitions are presented.

$$\begin{bmatrix} f_1 \\ f_2 \\ f_3 \end{bmatrix} = \text{Specific Force vector in P (platform) frame} \quad (22)$$

$T_{i/p}$ is the 3x3 transformation matrix to go from the P frame to the ECIF (i) (see Chapter II). It is used because the platform misalignments, accelerometer errors and gyro drifts are defined in the P frame, while velocity and position errors are defined in the ECIF frame.

Block S_1 relates velocity errors to the position error rates and is defined as

$$\underline{S}_1 = \underline{I}_{3 \times 3} \quad (23)$$

Block S_2 is defined by

$$\underline{S}_2 = - \frac{\mu}{|\underline{RU}|^3} \left[\underline{I} - \frac{3}{|\underline{RU}|^2} \underline{RU} \underline{RU}^T \right] \quad (24)$$

where

μ is the gravitational constant

\underline{I} is a 3x3 identity matrix

\underline{RU} is the 3x1 position vector (in ECIF, see Chapter II)

Block S_3 relates platform misalignment errors to the velocity error rates by

$$\underline{S}_3 = T_{i/p} \underline{F}_p \quad (25)$$

where

$$\underline{F}_p = \begin{bmatrix} 0 & -f_3 & f_2 \\ f_3 & 0 & -f_1 \\ -f_2 & f_1 & 0 \end{bmatrix} \quad (26)$$

Block \underline{S}_4 relates accelerometer bias errors to the velocity error rates by

$$\underline{S}_4 = \underline{I}_{3 \times 3} \quad (27)$$

Block \underline{S}_5 couples accelerometer scale factor errors to the velocity error rates by

$$\underline{S}_5 = \underline{T}_{i/p} \underline{F}_1 \quad (28)$$

where

$$\underline{F}_1 = \begin{bmatrix} f_1 & 0 & 0 \\ 0 & f_2 & 0 \\ 0 & 0 & f_3 \end{bmatrix} \quad (29)$$

Block \underline{S}_6 relates accelerometer misalignments to the velocity error rates by

$$\underline{S}_6 = \underline{T}_{i/p} \underline{F}_2 \quad (30)$$

where

$$\underline{F}_2 = \begin{bmatrix} f_2 & f_3 & 0 & 0 & 0 & 0 \\ 0 & 0 & f_1 & f_3 & 0 & 0 \\ 0 & 0 & 0 & 0 & f_1 & f_2 \end{bmatrix} \quad (31)$$

Block \underline{S}_7 relates accelerometer nonlinearities to the velocity error rates by

$$\underline{S}_7 = \underline{T}_{i/p} \underline{F}_3 \quad (32)$$

where

$$\underline{F}_3 = \begin{bmatrix} f_1^2 & 0 & 0 \\ 0 & f_2^2 & 0 \\ 0 & 0 & f_3^2 \end{bmatrix} \quad (33)$$

Block \underline{S}_8 relates gravity deflections and anomaly to the velocity error rates through the use of $\underline{T}_{i/v}$, developed in Chapter II, by

$$\underline{S}_8 = \underline{T}_{i/v} \quad (34)$$

Blocks \underline{B}_a , \underline{B}_{ab} , and \underline{B}_b will be described in the next section of this chapter.

Block \underline{S}_9 relates the gyro bias errors to the platform misalignment error rates by

$$\underline{S}_9 = \underline{I}_{3 \times 3} \quad (35)$$

Block \underline{S}_{10} couples the gyro mass unbalances to the platform misalignment error rates by

$$\underline{S}_{11} = \underline{F}_4 \quad (36)$$

where

$$\underline{F}_4 = \begin{bmatrix} f_1 & f_2 & 0 & 0 & 0 & 0 \\ 0 & 0 & f_2 & f_3 & 0 & 0 \\ 0 & 0 & 0 & 0 & f_3 & f_2 \end{bmatrix} \quad (37)$$

Block \underline{S}_{11} relates the gyro anisoeelasticities to the platform misalignment rates by

$$\underline{S}_{11} = \underline{F}_5 \quad (38)$$

where

$$\underline{F}_5 = \begin{bmatrix} f_1 f_2 & 0 & 0 \\ 0 & f_2 f_3 & 0 \\ 0 & 0 & f_2 f_3 \end{bmatrix} \quad (39)$$

Block \underline{S}_{12} , located along the diagonal, relates to the modeling of the gravity deflections and anomaly as first order Gauss-Markov processes and is defined as

$$\underline{S}_{12} = \begin{bmatrix} -\frac{V_R}{du} & 0 & 0 \\ 0 & -\frac{V_R}{dv} & 0 \\ 0 & 0 & -\frac{V_R}{dw} \end{bmatrix} \quad (40)$$

where

\underline{V}_R is the Orbiter's earth-relative velocity and

du , dv , and dw are altitude dependent correlation distances expressed in a table lookup routine.

The process noise spectral density of the white noises utilized in the modeling of the gravity error states are defined by the desired steady state values for the errors modeled here. The values are given by

$$Q_j = 2(\sigma_j)^2 \left(\frac{V_R}{d_j} \right) \quad (41)$$

σ_j is the standard deviation of the gravity model error. The effect of the gravity errors decreases with altitude so that at 250,000 feet the standard deviations have been attenuated by three (Ref 9:3.8-3.9, 7:3.21-3.22).

Part B is defined by the Orbiter MTU quartz crystal clock error model, shown in Figure 5, also given in the earlier TASC studies (Ref 10: 2.23-2.25). Figure 6 depicts the definition of the B blocks and Table II defines the states.

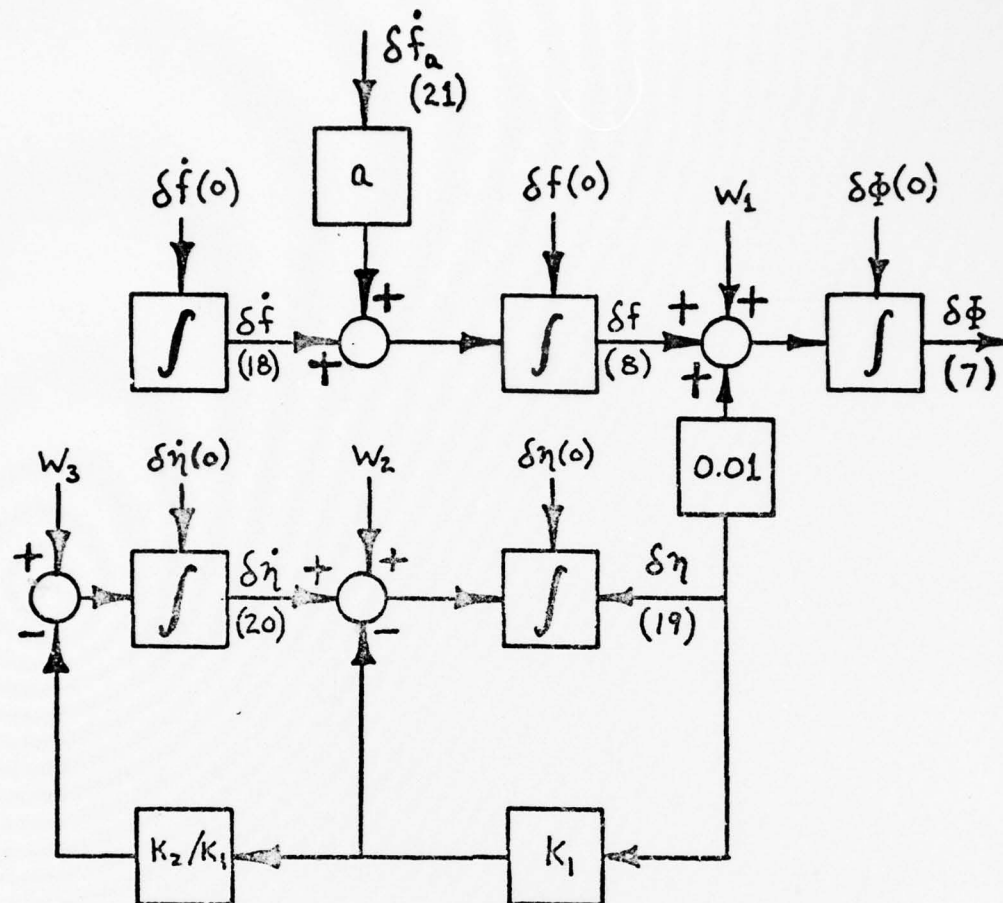


Figure 5. Quartz Crystal Clock Error Model

In Figure 5, the factors labeled K_1 and K_2 are constants which have the values 1.01×10^{-1} and 1×10^{-4} , respectively. The block labeled "a" is the shuttle acceleration along the major thrust axis in g's. In this study "a" was approximated by the acceleration load factor along the x-body axis. It is supplied to the simulation by a table lookup routine as a function of time since deorbit ignition, with values for the table from a previous study (Ref 8:63,82). (See Chapter VII for discussion of error in this model.)

The process noise spectral density employed in the simulation is presented in Equation 42, which shows the linear dependence of w_1 , w_2 , and w_3 upon each other, i.e., their correlation.

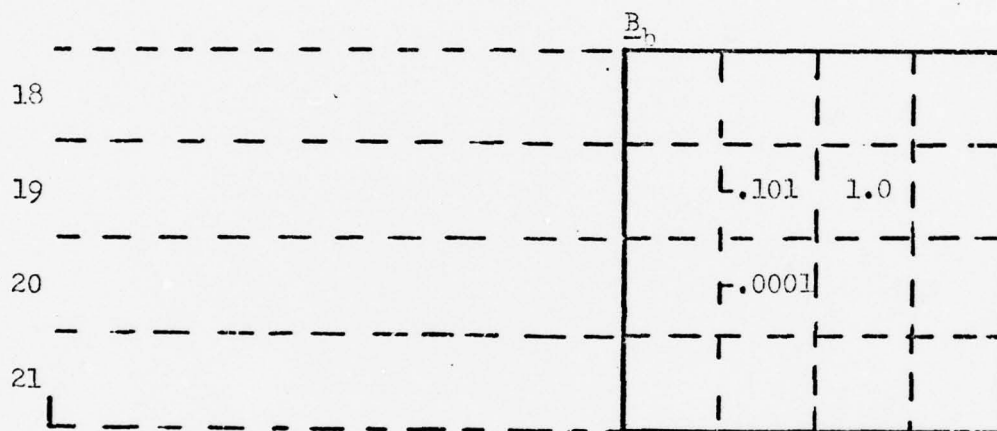
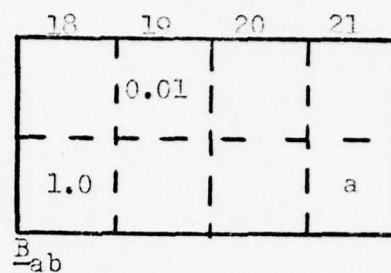
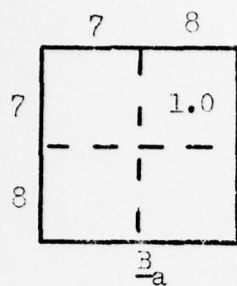


Figure 6. Definition of \underline{B} Partition Blocks for System Dynamics Matrix

Table II: Definition of NTU Error States

State	Symbol	Description	Units
7	ϕ	Phase Error	feet
8	f	Frequency Error	ft/sec
18	\dot{f}	Aging	ft/sec ²
19	η	Flicker Freq. Error	ft/sec
20	$\dot{\eta}$	Random Freq. Rate Error	ft/sec ²
21	\dot{f}_a	Acceleration Sensitivity	ft/sec ² /g
--	w_1	White Process Noises	ft/sec
--	w_2		ft/sec ²
--	w_3		ft/sec ³

$$Q_B = \begin{matrix} & \begin{matrix} 7 & 8 & 18 & 19 & 20 & 21 \end{matrix} \\ \begin{matrix} 7 \\ 8 \\ 18 \\ 19 \\ 20 \\ 21 \end{matrix} & \begin{bmatrix} 4.56 \times 10^{-3} & 0 & 0 & 4.14 \times 10^{-1} & 4.51 \times 10^{-3} & 0 \\ 0 & 0 & 0 & 0 & 0 & 0 \\ 0 & 0 & 0 & 0 & 0 & 0 \\ 4.14 \times 10^{-1} & 0 & 0 & 3.77 \times 10^1 & 4.10 \times 10^{-1} & 0 \\ 4.51 \times 10^{-3} & 0 & 0 & 4.10 \times 10^{-1} & 4.47 \times 10^{-3} & 0 \\ 0 & 0 & 0 & 0 & 0 & 0 \end{bmatrix} \end{matrix} \quad (42)$$

where

Q_{11} is in (ft/sec)²/sec

Q_{44} is in (ft/sec²)²/sec

Q_{55} is in (ft/sec³)²/sec

Part C contains the satellite states with each satellite modeled by using a modification of the MTU clock model plus terms for range bias errors and ionospheric delay effects. This was done because a model for the satellites was not readily available, as some values are still under test and evaluation and some values are still classified. The modifications to the user clock model were made so that the numbers used would be "close" to expected performance values given in the literature (Ref 10:2.7-2.8,3:5.2-5.12).

The modifications led to the use of a five-state satellite clock model. This is the same configuration as for the MTU model, but with the acceleration sensitivity state deleted, with two additional states added to this to account for range bias error and ionospheric delay error. The dynamics model for one satellite is presented in Figure 7 as it appears in the system dynamics matrix. The clock model of Figure 5 minus the acceleration sensitivity state is an accurate depiction of the clock portion of the satellite model. Table III

defines the states and the units of the states. Note that Figure 7 could be any one of the four 7x7 blocks that compose block diagonal C in Figure 3.

0	1.0	0	0.01	0	0	0
0	0	1.0	0	0	0	0
0	0	0	0	0	0	0
0	0	0	-.101	1.0	0	0
0	0	0	-.0001	0	0	0
0	0	0	0	0	0	0
0	0	0	0	0	0	0

Figure 7. Satellite Dynamics Block Definition

Table III: Satellite State Definition

States	Description	Units
46, 53, 60, 67	Clock Phase Error	feet
47, 54, 61, 68	Clock Frequency Error	ft/sec
48, 55, 62, 69	Aging Bias Error	ft/sec ²
49, 56, 63, 70	Flicker Frequency Error	ft/sec
50, 57, 64, 71	Random Frequency Rate Error	ft/sec ²
51, 58, 65, 72	Range Bias Error	feet
52, 59, 66, 73	Ionospheric Delay Error	ft/sec

Reiterating that although the satellite models do not represent a documented model for the proposed cesium-standard GPS satellites, the numbers do give a fairly representative magnitude of errors to be expected by using these satellites. The magnitudes for the modified clock model's initial conditions and white noises are basically scaled

values proportional to the values used in the Orbiter MTU model. The major error contributions are modeled in the range bias error states and the ionospheric delay states. Equation 43 gives the process noise spectral density used in each one of the four satellite models.

$$\underline{Q}_S = \begin{bmatrix} 5. \text{ E-09} & 0 & 0 & 4. \text{ E-07} & 4.5 \text{ E-09} & 0 & 0 \\ 0 & 0 & 0 & 0 & 0 & 0 & 0 \\ 0 & 0 & 0 & 0 & 0 & 0 & 0 \\ 4. \text{ E-07} & 0 & 0 & 4. \text{ E-05} & 4. \text{ E-07} & 0 & 0 \\ 4.5 \text{ E-09} & 0 & 0 & 4. \text{ E-07} & 4.5 \text{ E-09} & 0 & 0 \\ 0 & 0 & 0 & 0 & 0 & 0 & 0 \\ 0 & 0 & 0 & 0 & 0 & 0 & 0 \end{bmatrix} \quad (43)$$

Note that the scaling factor used for the standard deviations from the MTU clock model to the satellite model was 10^{-3} , so that the process noise's spectral density differs by a factor of 10^{-6} . The units are the same as for \underline{Q}_b (see Equation 42).

Truth Model Data Base

The truth model data base includes the initial conditions on the truth model states as initialized covariances, the associated process noise spectral densities where applicable, and the corruptive measurement noise strengths, plus any time constants for time correlated states. The process noise spectral densities have been presented earlier.

The initial conditions have been derived from two basic sources, as mentioned in the introduction. The initial conditions are presented in Table IV.

Table IV: Truth Model Data Base--IMU, MTU and Satellites

State	Description	Initial Standard Deviation
1	Position- X^i *	5,417 feet
2	Position- Y^i *	2,844 feet
3	Position- Z^i *	9,332 feet
4	Velocity- X^i *	9.863 fps
5	Velocity- Y^i *	3.101 fps
6	Velocity- Z^i *	7.115 fps
7	MTU clock phase	100 feet
8	MTU clock freq.	0.01 fps
9-11	Platform misalign.	1.377E-03 rad/axis
12-14	Accel. Biases	1.607E-03 fps ² /axis
15-17	Gyro Bias Drifts	1.697E-06 rad/sec
18	MTU Aging	3.86E-06 fps ²
19	Flicker Freq. Error	20.2 fps
20	Random Freq. Err. Rate	1.37 fps ²
21	Clock Accel. Sensitiv.	0.1 fps ² /g
22-24	Accel. Scale Factors	100 ppm/axis
25-30	Accel. Misaligns.	7.272E-05 rad(@ 6 comp)
31-33	Accel. Non-Linearity	1.089E-07 fps ² /g ²
34	Gravity Anomaly	function of
35	Gravity Deflection	altitude, see
36	Gravity Deflection	text, Eq 41
37-42	Gyro Mass Unbalance	3.770E-09 rad/s/g
43-45	Gyro Anisoelectricity	3.770E-09 rad/s/g ²
46-73	Sat clock phase	0.1 feet
	Sat clock freq.	1.0E-04 fps
	Sat Aging	3.86E-09 fps ²
	Flicker Freq. Error	0.0201 fps
	Random Freq. Rate Err.	1.391E-03 fps ²
	Sat Range Bias	3.5 feet
	Ionospheric delay	0.0024 fps

*Note that position and velocity errors have strong cross correlations in the inertial frame.

Notes on Satellite modeling values

The method used in choosing the values for the clock model portion of the satellite modeling has been discussed earlier. The filter is driven by the difference between actual measurements and estimated (predicted) measurements. The satellite contributed errors reflected in this difference remain to be discussed. The errors are modeled in both the satellite models and in the measurement noise vector, \underline{V} , and thus in its covariance kernel, \underline{R} .

As explained in Chapter III, the time since upload of the satellites by the ground station at Vandenberg is a factor in the accuracy of the measurements taken. This is due to the satellite clock drift and satellite ephemeris error (Ref 10:2.7-2.8). Another main error contribution is the ionospheric delay. The ionospheric delay is reported to be of the same order of magnitude as the satellite clock errors (Ref 3:5-10).

The values used in the truth model assume that the satellites have not been recently uploaded. The trajectory of the Orbiter during the deorbit/reentry portion of the mission simulated occurs over almost one fourth of the earth's circumference to the west of Vandenberg AFB. It is thus reasonable to expect that a large portion of the satellites used would be those that had not yet been uploaded (see Chapter III). This may not be as true during the post-blackout time period, but this factor was not taken into account in the modeling.

With this in mind, the values for the range bias and ionospheric delay states initial conditions were chosen to reflect values of 3.5 feet and 2.4×10^{-3} feet per second, respectively.

Truth Model Measurement Matrix and Measurement Noise

The truth model measurement matrix reflects the three areas of contribution to error in the difference measurement, which are IMU errors, user clock errors, and satellite errors. An advanced design GPS receiver capable of simultaneous measurement processing for four satellites has been assumed. The Kalman Filter incorporates the information as eight measurements; four each of position and four each of velocity, or one of each from each of the four satellites in use. The primary measurement updating interval used in this study was 30.72 seconds between measurement updates. This value was chosen arbitrarily, but to reflect an interval during which great change in dynamics would not be encountered, and one less than the interval in which the satellite constellation was tested for best geometry. The measurement sequence is assumed not to start until just prior to deorbit.

As noted in Chapter IV, the measurements (or more correctly, the difference measurements) are described by

$$\underline{Z} = \underline{H} \underline{\hat{x}} + \underline{v} \quad (44)$$

which is the difference between actual receiver measurements of range and range-rate, and the predicted measurement using INS indicated values. At measurement update times the filter corrects its estimate of errors by adding the Kalman gain weighted residual, $\underline{K}_F(\underline{Z} - \underline{H} \underline{\hat{x}})$, to the estimate.

The measurement equation is composed of a set of four pseudo-range and four pseudo-range-rate equations which are derived in the literature (Ref 2:14-16, 73-84, and 7:4.50-4.53). These pseudo-range equations

include user clock phase errors, satellite clock phase errors, satellite range bias errors, and satellite ephemeris errors. Terms from user clock frequency errors, satellite clock frequency errors, user and satellite random frequency errors and an ionospheric delay term are included in the pseudo-range rate equation. The Orbiter's position and velocity errors are also included in these equations from the IMU position and velocity states. Satellite ephemeris errors and satellite clock errors are actually indistinguishable from each other in reception, and their effects are accounted for together. Each equation also has an associated corruptive white measurement noise term, part of \underline{V} , whose covariance kernel \underline{R} is included in the Kalman Filter equations.

The measurement matrix is of the form

$$\underline{H}_S = \begin{matrix} & \begin{matrix} 6 & 7 & 8 \end{matrix} & & \begin{matrix} 19 \end{matrix} & & \begin{matrix} 45 & 52 & 59 & 66 & 73 \end{matrix} \\ \begin{matrix} 1 \\ 2 \\ 3 \\ 4 \\ 5 \\ 6 \\ 7 \\ 8 \end{matrix} & \begin{bmatrix} \underline{H}_{S1} & 1 & & 0 & & & & & \\ & & 1 & & 0.01 & & \underline{D} & & \\ & & & & & & & & 0 \\ \underline{H}_{S2} & 1 & & 0 & & & & \underline{D} & \\ & & 1 & & 0.01 & & & & \\ \underline{H}_{S3} & 1 & & 0 & & & & & \underline{D} \\ & & & & & & 0 & & \\ \underline{H}_{S4} & 1 & & 0 & & & & & \underline{D} \\ & & 1 & & 0.01 & & & & \end{bmatrix} & \end{matrix} \quad (45)$$

Where the blocks \underline{H}_{Sj} are each described by

$$\underline{H}_{Sj} = \begin{bmatrix} \underline{lr}_{xj} & \underline{lr}_{yj} & \underline{lr}_{zj} & 0 & 0 & 0 \\ 0 & 0 & 0 & \underline{lr}_{xj} & \underline{lr}_{yj} & \underline{lr}_{zj} \end{bmatrix} \quad (46)$$

and $\underline{l}_{i,s}$ is the unit vector component in the i^{th} direction to the j^{th} satellite in the inertial frame (i).

The block labeled \underline{D} and repeated four times in \underline{H}_S is given by

$$\underline{D} = \begin{bmatrix} -1 & 0 & 0 & 0 & 0 & -1 & 0 \\ 0 & -1 & 0 & -0.01 & 0 & 0 & -1 \end{bmatrix} \quad (47)$$

These blocks couple the appropriate satellite errors to either position or velocity states during measurement updates.

The covariance \underline{R} of the corruptive measurement noise is diagonal, with values used, again, from earlier studies (Ref 11:2.14), given by $(12 \text{ ft})^2$ for each of the four range error equations and $(0.05 \text{ ft/sec})^2$ for the four range rate error equations.

VI. Kalman Filter Design

Basis for Kalman Filter

The Kalman Filter is based upon a reduced order model of the system truth model, described in Chapter V. Major error states of interest are modeled in the filter, and the unmodeled errors from the system are taken into account by changes in the way the major errors are modeled. This is often done either by adding white noise to a state model, or by completely changing the state model, such as by changing from a bias model to a first order Gauss-Markov process. The filter is implemented in a reduced order, or suboptimal, model so that it can be used practically for online estimation and correction of the error states of interest.

As explained in Chapter IV, the filter makes corrections to the real world INS, and in the simulation corrections are made to the truth model. Based on these assumed corrections, the Kalman Filter also corrects its own estimate of the error states. The corrections are based upon measurements taken from an aiding source external to the IMU at discrete times, which in this study is the GPS receiver. The source should have good long term information characteristics to offset the INS's poor long term characteristics, while taking full advantage of the INS's good "short term" characteristics.

In the INS, the dominant mode affecting INS characteristics is the 84 minute "Schuler Pendulum" oscillation period. Significant errors may arise when this mode is observed, especially at quarter period intervals. It is thus over a period short in relation to these intervals that the INS exhibits its good short term characteristics. GPS, on the other hand, may present "noisy" measurements over a short term. Taken over a period

long enough for the INS to exhibit error growth however, the characteristics are quite good.

Filter Description

The Kalman Filter error states used in this study are a subset of the truth model states described in Chapter V. Information on filter states used and initial design values is based largely upon earlier studies (Ref 9:4.1-4.9, 10:4.5-4.9, and 11:2.10-2.12), which in turn refer to NASA filter specification.

Based upon the suggested designs of these earlier efforts, an initial design of a 17-state filter was implemented. Tuning was accomplished on this 17-state model. Based upon insight gained from the performance of this design, an 11-state filter and an 8-state filter were also implemented, and the results compared to the performance of the 17-state design. Since this study examined the use of GPS measurements both prior to and after blackout in two phases, the design of the filters was accomplished in the region prior to blackout, and then performance was examined in the region below blackout. Only the 11- and 8-state filters' performances were examined in the post-blackout region because of the 11-state filter's performance being so close to the 17-state filter's performance in the pre-blackout time frame.

The error states utilized in the 17-state design are listed in Table V. The order of the states was arranged with an eye toward removal of the last six states for implementation of the 11-state filter. Likewise, removal of the next three states led to the states used in the 8 state design. This was also the reason that states 7 and 8 were removed from states 18-21 in the truth model portion dealing with the

Table V. Kalman Filter Error States and Initial Conditions

State	Description	Standard Deviation
1	Position- X^i	1,330 feet
2	Position- Y^i	6,339 feet
3	Position- Z^i	20,507 feet
4	Velocity- X^i	20.931 feet/sec
5	Velocity- Y^i	6.525 feet/sec
6	Velocity- Z^i	15.235 feet/sec
7	Clock Phase	1,200 feet
8	Clock Frequency	0.05 feet/sec
9-11	Platform Misalignments	2.753E-03 rad
12-14	Accelerometer Biases	1.70E-03 feet/sec ²
15-17	Gyro Bias Drifts	1.697E-07 rad/sec

MTU. The particular arrangements of which states to drop in going from one design to the next were again based upon the previously mentioned TASC studies for NASA (Ref 9:4.1-4.4, 10:2.37-2.40, and 11:2.10-2.12). The values used in each filter design are discussed in the sections dealing with each individual design. Since the initial conditions did not change from design to design for the variances of the error states, they are presented in Table V for the 8- and 11-state designs also.

The initial conditions for the position and velocity states were originally given in a separate coordinate frame not used in this study (Ref 11:2.11). The transformation of the entire 6x6 initial position-velocity covariance, including cross correlations, was performed by computer using a transformation matrix provided in the references (Ref 9:A.3). The resulting complete 6x6 (lower triangle only) initial covariance for this, as well as the post-blackout phase is presented in Appendix C.

The design parameter values derived from the efforts of this study will be presented next along with an explanation of why they were

chosen. The performances of each of the three filter designs will be presented and compared in Chapter VII. As mentioned earlier, the designs used are based largely upon studies done for NASA by TASC (Ref 9:4.1-4.9 and 11:2.10-2.12). The suggested filter design parameters from these studies are summarized in Appendix C and compared there to the final design parameters from this study.

17-State Filter

The design of the 17-state filter and its "tuning" led naturally to the designs of the 11- and 8-state filters. General comments about the method of design and tuning of the 17-state filter, especially as it relates to the first 8 states, will apply to the discussion of the other two designs as well.

The first 17 states of the system truth model are modeled in the filter. Where the models used for these 17 filter states differ from the truth model, attempts have been made to account for the effects of the unmodeled error states upon these 17 states. This has been done in three general ways.

First, the initial covariance matrix was changed for some states to reflect a greater uncertainty in the knowledge of the state's condition. This is important if the filter design is to be general, as the real world error states may not be as small as the values that have been assumed for the truth model in this study. If the filter begins by underestimating the system errors, the performance may not be such that system errors are bounded and divergence of system errors may occur.

Second, the effects of some unmodeled states have been somewhat added through increases in the strength of process noise on some states.

This can be especially effective if the missing state can be approximated by a bias.

Finally, in two of the groups of states, the accelerometer biases and the platform misalignments, the state models have been changed from zero order models with inputs from other states, to first order Gauss-Markov process models (Ref 9:4.5).

Specifically, the modeling changes for the various states are as follows. The position error model remains the same as the truth model except for the increase in uncertainty reflected by the increase in initial conditions. The velocity state's error model is changed by both an increase in covariance and the addition of process noise. The process noise helps to compensate for the effects of truth model states 22 through 36, missing in the filter. Clock state 8 is modified so that it too has driving corruptive white noise. As mentioned above, the model for the platform misalignment error states is a first order Gauss-Markov process in the filter. It has a very large time constant (not infinite) with driving white noise inputs from the gyro bias drift rate errors. The accelerometer bias error states are modeled as first order Gauss-Markov processes too, with shorter time constants and driving white noise inputs. The models for the gyro bias drift error states are unchanged from the truth model.

These results are shown in Figure 8, the filter dynamics matrix, and Table VI, which gives numerical values for the time constants and defines the values for the process noise covariance matrix, Q_f , assumed diagonal. Note in Figure 8, blocks without entries indicate zero-fill for that block.

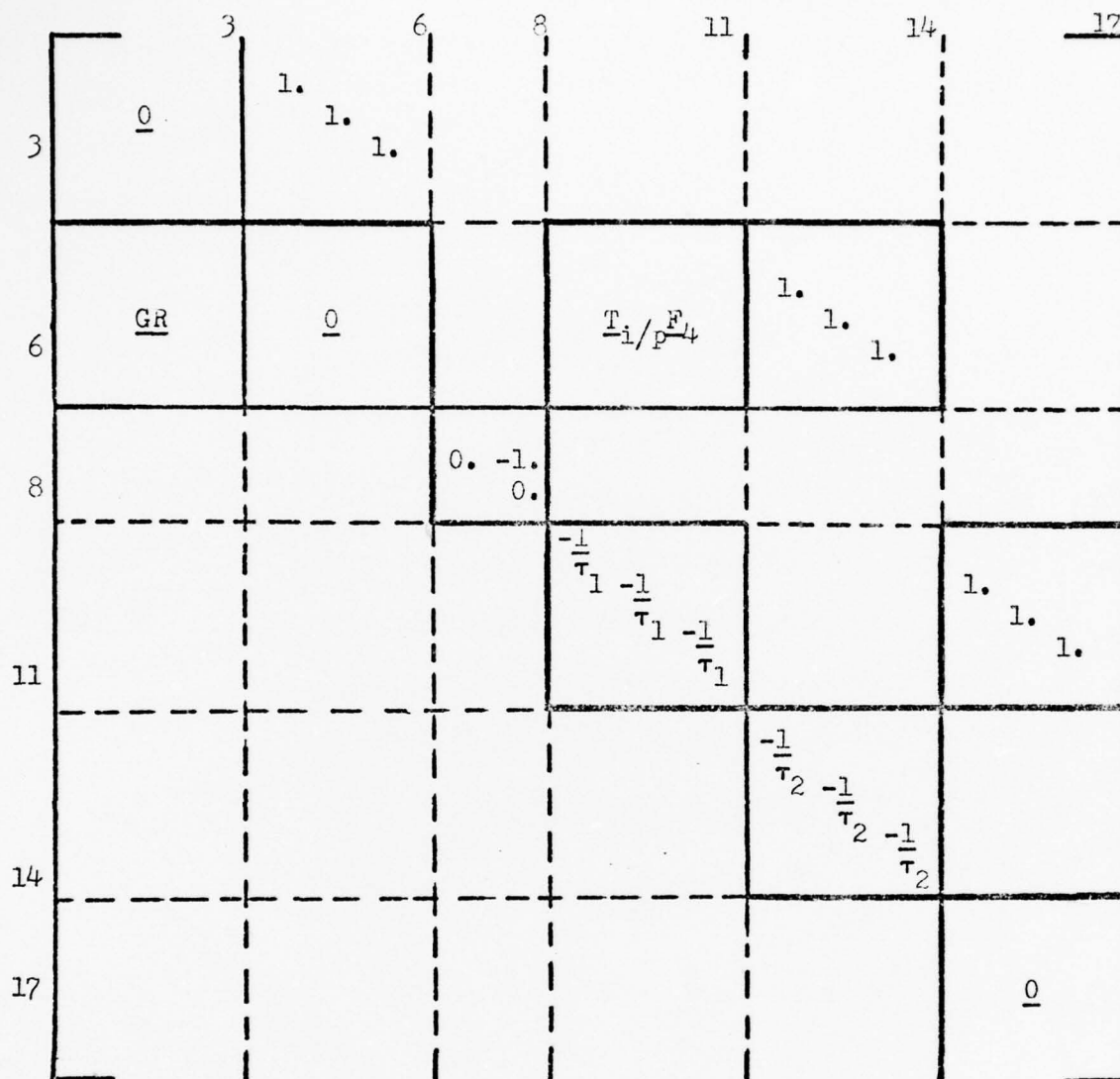


Figure 8. Kalman Filter Dynamics Matrix

Table VI. 17-State Filter Design Parameters

State	Time Constant	Process Noise Spec Density
1-3	--	--
4,5	--	0.1076 (ft/sec) ² /sec
6	--	0.08 (ft/sec) ² /sec
7	Infinity	10.0 (ft) ² /sec
8	Infinity	1. X 10 ⁻³ (ft/sec) ² /sec
9-11	2.4 X 10 ⁵ sec	1.5842 X 10 ⁻¹³ (rad) ² /sec
12-14	60 sec	9.6335 X 10 ⁻⁸ (ft/sec ²) ² /sec
15-17	--	--

Note that state 6 has a different value of noise spectral density than states 4 and 5, the other two velocity states. Since the velocity state computations are performed in the inertial reference frame, the geometry of the Orbiter's reentry profile can give some insight into the reasons for having a difference. Note, in the filter dynamics matrix (Fig 8), and also in the system dynamics matrix (Figs 3 and 4 and Eqs 25-33), that the velocity errors are quite dependent upon the vehicle sensed specific force. For the CFT-1 trajectory, the heading is primarily east-west. Translated to the inertial frame, it can be said that the primary velocity components of the Orbiter's inertial velocity vector will be in the X^i and Y^i direction. This will also be true of the Orbiter acceleration vector's primary components. Thus, larger errors are to be expected on the X^i and Y^i velocity channels. Since smaller errors are expected on the Z^i velocity channel, to estimate those errors better, a smaller Q_F is required for that channel.

Note that this is true only for this trajectory and would certainly not be true for a polar orbit reentry. However, it can be expected that the nature of the Space Shuttle missions will be quite structured, and it should be straightforward to extend this idea to other missions. Whether the extra accuracy from the better estimation of individual channel velocity errors would be worth the effort that would be required, is not within the scope of this study.

The noise spectral density values for states 7 and 8 are quite high compared to suggested values in TASC studies (Ref 11:2.11) (see Appendix C). The values were developed iteratively while "tuning" the filter to estimate more closely the observed errors in corresponding system states. The system states for the clock were affected by the acceleration

sensitivity state, which couples in the component of longitudinal acceleration on the shuttle (see truth model discussion, Chapter V). This component increases gradually prior to blackout, until at blackout, its effect is seen in a high level of error in both states 7 and 8. The high values for the strength of the process noises here are to force the filter to estimate these error levels more correctly over a broad range. This is discussed more fully in Chapter VII in the results section.

The values for the process noise spectral density for states 9-11 were also the result of an iterative process. They are related to the choice of initial condition for the misalignment states in the filter, chosen to be twice the initial misalignment assumed for corresponding states in the truth model. These values, along with the presence in the filter of the gyro bias states allowed the performance of the filter to closely approximate that of the system.

The time constant value, initial conditions and noise spectral density for states 12-14 are suggested values from an earlier TASC study (Ref 9:4.5) in which the modeling of these states was addressed. Including these states, as well as states 15-17, can be seen more as an aid to model the velocity errors and platform misalignments correctly than to estimate the accelerometer biases and gyro bias drifts correctly. This is because the accelerometer biases, along with the platform misalignments, represent a major error contribution to the velocity states. The gyro bias drifts contribute significantly to the platform misalignments and thus, also to the velocity errors (Ref 9:5.7). Thus, by adding the last six states, the modeling of the velocity and platform misalignment states have been made more complete.

The measurement matrix for the filter is identical to the left 8x3 portion of the system measurement matrix. It does not change from filter design to filter design. Equation 48 describes the matrix.

$$\underline{H}_f = \begin{bmatrix} H_{f1} & 1 & 1 \\ H_{f2} & 1 & 1 \\ H_{f3} & 1 & 1 \\ H_{f3} & 1 & 1 \end{bmatrix} \quad (48)$$

Where, as in the truth model measurement matrix, the partitions \underline{H}_{fj} contain vectors to each of the 4 satellites being used, and are described by

$$\underline{H}_{fj} = \begin{bmatrix} \underline{lr}_{xj} & \underline{lr}_{yj} & \underline{lr}_{zj} & 0 & 0 & 0 \\ 0 & 0 & 0 & \underline{lr}_{xj} & \underline{lr}_{yj} & \underline{lr}_{zj} \end{bmatrix} \quad (49)$$

and \underline{lr}_{ij} is the unit vector component in the i^{th} direction to the j^{th} satellite, given in the inertial frame.

The associated corruptive measurement noise matrix does however, change from filter design to filter design. In all designs it is 8x8 and diagonal, and the same values repeat for the corruptive noise on the filter range error measurement strengths for each of the four measure-

ments. The same is true for the range rate measurement errors. The 17-state filter measurement noise strength values are given in the following equations.

$$R_{fri} = 800 \text{ (ft)}^2 \quad (50)$$

$$R_{fvi} = 0.05 \text{ (ft/sec)}^2 \quad (51)$$

11-State Filter

A 17-state filter presents more computational burden to the onboard computer than is allowed by NASA for the Kalman Filter function. Thus, an 11-state design is, at present, the proposed filter to be used with GPS as an external aid (Ref 11:2.10). There is a significant saving in onboard computer workload by using an 11-state filter instead of the 17-state design. This savings is seen in the numbers of storage words, and the number of adds, multiplies, divides, etc., that must be done for each iteration.

The 11-state design parameters were developed largely from insight gained in the tuning process for the 17-state filter. The process noise spectral densities for this design are listed in Table VII. The initial conditions and time constants remained the same as those given for the 17-state filter (see Tables V and VI).

Notice that the process noise spectral density of the velocity error states remain the same as in the 17-state design. There does not seem to be a significant need for any change in this parameter. The design philosophy employed is conservative in estimating the errors on these

Table VII. 11-State Filter Process Noise Spectral Density

State	Value
1-3	0.0
4,5	$0.1076 \text{ (ft/sec)}^2/\text{sec}$
6	$0.08 \text{ (ft/sec)}^2/\text{sec}$
7	$10.0 \text{ (ft)}^2/\text{sec}$
8	See Equation 52
9-11	$1.557 \times 10^{-10} \text{ (rad)}^2/\text{sec}$

channels and also on the clock states. This is due to observed divergence tendencies in the system error states. The level of noise strength is actually higher than is required to compensate for unmodeled (in the filter) error states. Thus, the level of noise spectral density used in both the 11- and 8-state filters for the velocity channels drives the velocity errors in the filter's pre-update estimates to approximately the same level as in the 17-state design (see discussion of results, Chapter VII).

The noise spectral density for state 7 is the same as in the 17-state filter, for the same reasons. It was desired to use the same value as in the 17-state design for state 8 in the 8- and 11-state filter clock models also. However, this value, in conjunction with the measurement noise strengths chosen, resulted in numerical difficulties due to initial transient conditions. This problem was overcome by changing both the process noise spectral density for this state and the measurement noise strengths on both the position and velocity measurements gradually from values which did not cause problems, to values which equaled the values used in the 17-state filter. These changes in values, as functions of time, t , since the initial time, t_0 , are reflected in the following set of equations.

$$Q_{f8} = \begin{Bmatrix} 3.0 \times 10^{-5} \\ 3.0 \times 10^{-4} \\ 1.0 \times 10^{-3} \end{Bmatrix} (\text{ft/sec})^2/\text{sec} \begin{cases} t - t_0 \leq 85 \text{ sec} \\ t - t_0 \leq 130 \text{ sec} \\ t - t_0 > 130 \text{ sec} \end{cases} \quad (52)$$

$$R_{fr} = \begin{Bmatrix} 10,000 \\ 1,000 \\ 800 \end{Bmatrix} (\text{ft})^2 \begin{cases} t - t_0 \leq 85 \text{ sec} \\ t - t_0 \leq 130 \text{ sec} \\ t - t_0 > 130 \text{ sec} \end{cases} \quad (53)$$

$$R_{fv} = \begin{Bmatrix} 2.5 \times 10^{-2} \\ 3.5 \times 10^{-2} \\ 5.0 \times 10^{-2} \end{Bmatrix} (\text{ft/sec})^2 \begin{cases} t - t_0 \leq 85 \text{ sec} \\ t - t_0 \leq 130 \text{ sec} \\ t - t_0 > 130 \text{ sec} \end{cases} \quad (54)$$

The time intervals chosen slowed the convergence of the filter and system error states to a steady state condition sufficiently so that the transient problems were eliminated.

The noise spectral density for the misalignment states needed slight increases due to the removal of the gyro bias error states which directly contribute to the corresponding errors in the system model.

In the post blackout time period, the same basic design is still valid. Because error buildup during the time of radio blackout (and thus, no GPS measurements) is quite severe (Ref 11:2.15), when the GPS measurement sequence is reinitiated there is again the possibility of transient problems. Because of the error buildup, the initial conditions are somewhat changed. The first 8 states have propagated without benefit of the high accuracy of GPS measurements for 10 minutes. Even though drag updating is assumed to be used, its effect is only to slow error growth by 1/3 (Ref 9:5.4-5.5). Finally, the longitudinal component of

acceleration on the Orbiter falls off significantly during the blackout period (Ref 8:63), which sharply reduces its forcing effect on the errors in states 7 and 8 of the truth model.

The initial conditions for the filter position and velocity states in the post blackout time period come from one of the TASC studies (Ref 11:2.15). The entire 6x6 (lower triangle) covariance for these states is given in Appendix C. The square roots of the diagonal elements of the covariances are presented in Table VIII. The process noise spectral densities remain the same on all states except on state 8.

Table VIII. Post Blackout Initial Conditions, 8- and 11-State Filters

State	Initial Standard Deviation
1	10,833 feet
2	5,074 feet
3	10,135 feet
4	31.85 feet/sec
5	18.82 feet/sec
6	29.01 feet/sec
7	1,200 feet
8	2.0 feet/sec
9-11	2.753 x 10 ⁻⁵ radians

The high initial condition on state 8 reflects error buildup prior to blackout as well as during the blackout region. Because the longitudinal acceleration has decreased during blackout however, as the filter begins estimating the error on this state, corrections are applied to the truth model. These corrections can now cause a decrease in the errors because the longitudinal acceleration effects, coupled through the acceleration sensitivity state of the truth model are so reduced. In order to prevent the numerical difficulties during the transient conditions mentioned earlier, and to prevent the filter from reducing

its estimate of the error too rapidly for state 8 (which could result in underestimating the truth model error state), time varying values for the noise spectral density for state 8 and the measurement noise strengths were again applied. These values are summarized in the following set of equations.

$$Q_{f8} = \begin{Bmatrix} 3. \times 10^{-5} \\ 6. \times 10^{-5} \\ 3. \times 10^{-5} \end{Bmatrix} (\text{ft/sec})^2/\text{sec} \begin{cases} t - t_0 \leq 85 \text{ sec} \\ t - t_0 \leq 130 \text{ sec} \\ t - t_0 > 130 \text{ sec} \end{cases} \quad (55)$$

$$R_{fr} = \begin{Bmatrix} 10,000 \\ 1,000 \\ 800 \end{Bmatrix} (\text{ft})^2 \begin{cases} t - t_0 \leq 85 \text{ sec} \\ t - t_0 \leq 130 \text{ sec} \\ t - t_0 > 130 \text{ sec} \end{cases} \quad (56)$$

$$R_{fv} = \begin{Bmatrix} 2.5 \times 10^{-2} \\ 3.5 \times 10^{-2} \\ 9.0 \times 10^{-3} \end{Bmatrix} (\text{ft/sec})^2 \begin{cases} t - t_0 \leq 85 \text{ sec} \\ t - t_0 \leq 130 \text{ sec} \\ t - t_0 > 130 \text{ sec} \end{cases} \quad (57)$$

The measurement noise strengths used allow the filter to heavily weight the GPS measurements and to apply as much of the accuracy available in the measurements as possible.

8-State Filter

The 8-state filter needed no special tuning effort to achieve performance comparable to that of the 11-state design. Limits of time and resources precluded any work other than investigation of the performance of a filter derived using the design parameters of the 11-state filter,

minus the three misalignment states. Thus the discussion of the 11-state design parameters applies for this section as well. This is not altogether unreasonable, since as was stated earlier, the noise spectral density on the velocity states presents a conservative approach. Because of this, the effect of the misalignment states on the velocity channels in the filter is minimized in the 11-state design. This can be seen by comparing the computer plots of the 11- and 8-state designs in Appendix A, for both regions of operation, above and below blackout.

Baseline Filter

A final run was accomplished for comparison purposes with an "optimal" baseline filter. This was performed by operating a filter based upon the truth model within the Covariance Analysis structure. Since this is a filter design which completely models all error states, it will demonstrate the best possible performance by a Kalman Filter design.

This is somewhat misleading because the GCAP software assumes complete impulsive control of the states being estimated by the filter, and this is, of course, impossible. However, insight can be gained into the performance of the actual suboptimal design filters by comparing their performances with that of this baseline filter.

VII. Results and Conclusions

Results

This section presents the observed filter performance, which is an examination of how well the filter was able to control truth model error growth in the states being estimated. The computer-generated plots in Appendix A will be the focus of the discussion, since they allow trends of control or of divergence to be seen at a glance.

As briefly noted in Chapter V, the assumed model of the specific force schedule on the longitudinal axis of the Orbiter for the clock model was modeled incorrectly. Due to a misinterpretation of a graph in creating the table lookup routine for the specific force schedule (Ref 8:63,82), the pre-blackout region had a specific force schedule beginning too early and building to too high a value. The post-blackout region did not have enough specific force. Unfortunately, this error was not discovered until the study was complete. The results of this error are not serious enough to invalidate the basic conclusions of this study, but trends of the achieved performance values are in error. The basic effect has been to make the pre-blackout results much more pessimistic than they should be, and to make the post-blackout results much too optimistic. The performance of the filter is not in question, but the performance in the regions for which the results are presented needs to be examined in the light of the above information.

An attempt is being made to correct this deficiency in the study by providing a more correct schedule of acceleration load to be coupled to the clock frequency and phase error states by the acceleration sensitivity state. The results of this effort will be implemented on the 8-state filter design, and the performance of this design will be examined

under these more correct conditions. When complete, the results will be summarized and attached to this report as an addendum. Meanwhile, the results of this study will be presented as a function of the assumed model. See Appendix D for correction addendum.

The results are presented in four sections, which follows the same arrangement as the plot presentation in Appendix A. The results of the "Baseline" design, or optimal 73-state filter implementation, will be presented first. Next the performance of the 17-state filter design will be examined, including a comparison of its performances under two updating rates. In the third section, the performance of the 11-state filter design will be presented for both the pre- and post-blackout regions of employment. Finally, the 8-state results are discussed and compared to the previous designs for both time periods of operation. Note that the 17-state design was implemented only in the pre-blackout region, because the 11-state filter was able to perform so well in comparison in that same time period.

The plots present a side by side comparison of the filter indicated performance of the system error states being estimated, with the actual system error on those states. For each filter design, the performance of states one through eleven were plotted, except for the 8-state implementation, for which only the first eight states were graphed.

Optimal Filter

As discussed in Appendix B, and Chapter VI, an implementation of all 73-states in a filter mechanization within the software structure used is unrealistic. This is due to the assumption of complete impulsive control at update intervals, over the states being estimated. However, the implementation does give some insight to levels of performance that may

possibly be achieved in other designs.

The most important state in the truth model affecting the accuracy the simulation was able to achieve was the acceleration sensitivity state in the clock model. Its effect is seen largely in the plots of the system clock frequency error, and to a lesser extent in the clock phase error plots.

The effect of complete impulsive control in the optimal filter can clearly be seen here by examining the plots of the clock phase and frequency error (Figures 9 and 10). There is no great corruption of performance as the modeled longitudinal component of acceleration increases. This is because internal states in the clock model are reset at update times. This is really not physically possible. Thus, to the extent that this occurs here and in the satellite model portion of the truth model (which states are obviously impossible to reset), this portion of the simulation is not realistic.

The results here, however, can be used to identify trends and to indicate some absolute limits in accuracy. For example, the plots of velocity error (Figures 14-16), and of misalignment angles (Figures 17-19), very clearly indicate the results to be expected as real world specific force increases toward the end of the pre-blackout period. The inability to estimate the misalignment angles because of lack of sensed specific force after deorbit thrust cuts off is also evident. This knowledge is useful in interpreting the results of the actual filter design implementations in the following sections.

17-State Filter

The 17-state results served to set a level of performance from an initial filter design that was expected to provide the "best" results

of the designs implemented. Two updating periods were implemented; one update every 30.72 seconds (determined by integration step size), and one update every 15.36 seconds.

For each filter design (17-, 11-, and 8-state), the performance of the user clock phase and frequency error states was due to virtually identical model implementations, and thus the discussion in this section is applicable (in the pre-blackout region) to other sections as well.

As stated in the previous section, the most important factor in the accuracy achievable was the performance of the user clock. Specifically, the response of the user clock model to the assumed longitudinal component of acceleration was important in the results achieved on the velocity and position channels. Recall that the acceleration sensitivity state couples this component of acceleration to the clock frequency error state, which in turn drives the clock phase error state. System performance at update times depends on these two states and thus will vary with the level of the longitudinal acceleration component.

Because of the buildup of this acceleration component, it was impossible to choose time invariant filter parameters that would allow the filter to correctly estimate clock frequency over the entire time period. Thus a compromise estimation level was chosen (see Figures 22-23). Note that the filter begins by "overestimating" the true error. This is to say that the filter-indicated error is larger than the actual error being committed. This will be termed a conservative design when done intentionally. As the acceleration model builds up, the filter-indicated error is very close to the system error for a time; and then as the time period approaches blackout, the error grows and the filter is "underestimating" the actual error, or indicating less error than is actually being committed. Even during this period of underestimation the filter

is still applying positive correction to the system error at update periods, and is bounding the error quite well. The peak error observed also corresponds roughly to the highest level of acceleration expected during reentry operations on the longitudinal axis (Ref 8:63).

It is evident that a filter design with time invariant parameters for the clock frequency error model is incapable of estimating clock frequency error well over the entire range of acceleration levels expected. The level chosen here is a practical compromise. This does, however, suggest that benefit could be gained with an acceleration dependency for parameters, notably Q_f and R_f for the velocity states. This will be discussed further in the Conclusions section.

The clock phase error plots (Figures 20, 21) show that, even though a tendency exists for the errors on this state to grow, the filter is able to bound the error growth adequately. The filter's estimation is somewhat conservative to allow for the error growth tendency, and thus overestimates the system error over most of the range.

The effects of the performance of these two states is seen in the filter performance on the position and velocity error states. The position states performance follows very closely that observed on the clock phase error (see Figures 24-29) in shape and in magnitude. Similarly, the velocity state's performance (see Figures 30-35) is strongly influenced by the user clock frequency error state. An example of how the filter copes with this influence can be seen in the plots of filter-indicated and true error for the y^i velocity error (Figures 32 and 33), which is the worst case performance in all designs.

The estimation is initially very conservative. The system error states on the velocity channels is actually corrupted during measure-

ment updates at certain points as the clock frequency error grows. The filter, of course does not have knowledge of this with its simplified model, yet continues to apply a correction to the velocity errors as a "steady-state" is reached at each level. The overall effect is to bound the error. The rapid growth of the error on the velocity states at the end of the period is due to the increase (actual) in specific force as the Orbiter enters the atmosphere. The filter is still able to apply strong corrections at update periods in response to this error growth.

Another effect of the increase in specific force is the ability of the filter to estimate misalignment angles more effectively. The misalignment states (see Figures 36-41) performance is not affected much (if at all) by the clock states. The filter's estimate of errors on these states is very conservative, estimating much more error growth than actually occurs in the system states. As mentioned in the discussion of the baseline (optimal) filter, after deorbit thrust is cut off (@ 4 minutes after deorbit ignition) until specific force mounts as atmospheric drag builds the filter is unable to estimate misalignments to a great degree. This is reflected in the relatively flat area on the true error plots for these states. As specific force grows, however, the filter is able to estimate these errors more effectively and is thus able to apply strong correction to the misalignments.

Implementation of a faster updating rate is shown in the next series of plots (Figures 42-63). By using an update rate which was twice as fast, only minimal benefits in terms of accuracy were achieved, as seen by comparing these plots with the previous set. Table IX compares the values for selected system error states at the next to final update

before blackout. Pre- and post-update values are presented for both the 15.36 second and the 30.72 second update periods. Whether the extra computational load would be worth the gains in accuracy are subjects for further study.

Table IX: 17-State Slow and Fast Update Rate Comparison

State	System (True) Error Std Deviation 17-State Filter, $t = t_0 + 1351$ sec			
	Update = 15.36 sec		Update = 30.72 sec	
	t^-	t^+	t^-	t^+
2, y^i Position Error (feet)	23.7	15.6	44.8	24.3
5, y^i Velocity Error (ft/sec)	0.91	0.88	1.11	1.14
8, Clock Freq Error (ft/sec)	1.20	0.74	1.94	0.97
10, y^p Misalignment (radians)	8.99×10^{-4}	8.11×10^{-4}	1.15×10^{-3}	8.16×10^{-4}

A final, interesting piece of information that can be gleaned from these performance plots is the effect of the particular satellite constellation in use upon accuracy. This effect is most apparent in the plots for state 1, x^i position (Figures 24, 25). Several instances of stronger than usual corrections to system error are immediately apparent, especially at $t = 430$ sec, 670 sec, 920 sec, and 1350 sec. These correspond to times at which the satellite selection algorithm switched to a new set of four satellites, based on GDOP considerations. This shows dramatically that the choice of satellites can have a significant effect upon the accuracy that can be achieved using GPS measurements.

11-State Filter

The 11-state design was derived, to a large degree, from the design parameters of the 17-state filter. Much of its performance is there-

fore very similar to that of the 17-state filter (see Figures 64-85). The major insight gained is that the effects of states 12-17 can be adequately compensated by state noise additions. As a matter of fact, the plots for the pre-blackout region show that better estimations of the misalignment errors was achieved in this design (see Figures 80-85). This resulted in the 11-state design providing slightly better performance on the velocity channels at the end of the region, when the misalignment states were rapidly changing. Other differences are so quantitatively small that they will not be summarized. Because of this fact, of the two designs, only the 11-state design performance was examined in the post-blackout region.

In the post-blackout region (see Figures 86-107) the modeling (incorrect, see chapter opening discussion) of the longitudinal component of acceleration on the Orbiter as significantly decreasing, allowed the filter to apply large corrections to the clock frequency and phase errors (see Figures 80-83). This allowed substantial improvement over the pre-blackout region performance. Actually, this performance is more to be expected during the pre-blackout region with correct modeling of acceleration inputs to the clock. In contrast, the performance of the system observed during the simulation of last half of the pre-blackout region would be the expected performance in the post-blackout region.

The real world levels of specific force, sensed by the IMU allowed significant corrections to be applied to the misalignment states (see Figures 102-107). Their effect on the velocity errors was reduced to a great degree. Several periods at which the Shuttle is making correction turns in its trajectory become apparent in their effect upon

the ability of the filter to apply large corrections to misalignment states. This is due to increases in specific force in all directions during these turns.

The effect of the reduction in the misalignment errors may not be readily apparent until the 11-state results are compared with the 8-states results. This will be discussed in the next section.

8-State Filter

Surprisingly, the performance of the 8-state filter is very close to that of the 11-state filter. Before discussion of the plots is begun, a comparison of results on selected states between the 11-state and 8-state designs will be presented. The numbers quoted will be for the error state values, after the next to the last update is performed for both pre-blackout and post-blackout regions. These are given in Tables X and XI.

Table X: Pre-Blackout Comparison of 11- and 8-State Filter Performance

State	System (True) Error Std Deviation $t = t_0 + 1351 \text{ sec}$			
	11-State Filter		8-State Filter	
	t^-	t^+	t^-	t^+
2, Y^1 Position Error (feet)	42.7	24.3	42.2	25.1
5, Y^1 Velocity Error (ft/sec)	0.96	1.13	0.93	1.13
8, Clock Freq Error (ft/sec)	1.94	0.962	1.94	0.959
10, Y^P Misalignment (radians)	1.24×10^{-3}	1.08×10^{-3}	1.40×10^{-3}	1.40×10^{-3}

THIS PAGE IS BEST QUALITY PRACTICABLE
FROM COPY FURNISHED TO DDC

Table XI: Post-Blackout Comparison of 11- and 8-State Filter Performance

State	System (True) Error Std Deviation $t = t_0 + 553 \text{ sec}$			
	11-State Filter		8-State Filter	
	t^-	t^+	t^-	t^+
2, y^i Position Error (feet)	7.3	6.9	22.1	6.9
5, y^i Velocity Error (ft/sec)	0.091	0.046	1.36	0.047
8, Clock Freq Error (ft/sec)	0.020	0.019	0.020	0.019
10, y^p Misalignment (radians)	1.06×10^{-4}	1.01×10^{-4}	1.38×10^{-3}	1.38×10^{-3}

First of all, notice that the primary differences lie in the magnitude of misalignment angles and in the t^- values, in the post-blackout region. The performances after updates, at t^+ , are virtually identical. Also, the pre-blackout region results indicated very little difference existed between the two design performances. This is because of the real lack of specific force inputs to the IMU and thus to the filter, and thus the previously discussed inability to estimate misalignments, until the end of the period. The short period over which correction to the misalignments does occur in the 11-state filter is not long enough for the effects to be seen in the velocity and position errors. In a sense then, the filter implementations are almost identical for much of this time period.

This is not true in the post-blackout region. A quick comparison of the plots for the 8-state filter performance (see Figures 124-139) for the post-blackout region with those of the 11-state filter (see Figures 86-107) indicate several differences, especially in the velocity states. The plots show, and Table XI confirms, that after updates have taken place, the values for the two filters are very close, except for

the misalignment states. It is this difference in misalignment state error values that is responsible for the large difference at pre-update time periods. The value of estimating the misalignment angles in the post-blackout region can be seen in its effect of reducing the rate of error growth on the velocity states, and thus on the position states also.

On the other hand, the high accuracy of the GPS measurements provides a post-update level of accuracy that gives the 8-state filter the ability to provide an average level of error on the position and velocity states which is quite good. With the corrections to the clock model acceleration input these numbers will worsen somewhat, but will still be acceptable.

Conclusion

There are two main conclusions that this study has provided. These are:

- There is a need to model filter parameters for the clock frequency error state with a sensitivity to longitudinal axis acceleration.
- The 8-state filter design can perform at a level which will adequately bound error growth in the IMU.

These two conclusions will be discussed separately in the next few paragraphs.

Even though the acceleration modeling for the input to the clock sensitivity state is in error regarding the time at which it is applied, the levels modeled will be encountered at other points in the mission profile. Thus, the filter will be called upon to deal with essentially the conditions presented, except at different times in the profile. Because of this, the filter performance on the clock frequency error

state can be seen to be a compromise. If the filter parameters, Q_{f8} (the filter noise spectral density for state number 8), and R_{fv} (the measurement noise strength for the pseudo-range-rate measurements) were made to be dependent on the longitudinal component of specific force, the filter estimate would better be able to reflect the true error conditions. The variation around the estimation level chosen for the design of this study would not have to be great to provide much improvement in the performance observed.

This study has demonstrated that the 8-state filter is able to perform adequately over a wide range of conditions. The effects of not estimating the platform misalignments during the short time period after blackout (and also during blackout) have the effect of slowing convergence for the velocity error states, and through them, the position error states also. The system and filter are not as sensitive to specific force inputs as when the misalignments are estimated. These factors do not affect performance as much with the high accuracy GPS measurements as they might with other, less accurate external aids.

For this reason, the 8-state filter should be given serious consideration as the design choice during deorbit/reentry operations, when GPS is used as an external aid. With the improvements that may be possible with better estimation of clock frequency errors, the 8-state design should provide IMU accuracy well within required limits.

Bibliography

1. Bogen, A. H. Geometric Performance of the Global Positioning System. Aerospace Corporation, AD-783210, 21 June 1974.
2. Butler, R. R., and Rhue, G. T. Kalman Filter Design for an Inertial Navigation System Aided by Non-Synchronous Satellite Constellations. Unpublished thesis. Wright-Patterson Air Force Base, Ohio: Air Force Institute of Technology, March 1974.
3. Cretcher, C. K. Navstar Global Positioning System: System Description, Program Plan, and User Performance. The Aerospace Corporation. Unpublished report, May 1974.
4. Davis, L. D. Coordinate System for the Space Shuttle Program. National Aeronautics and Space Administration, NASA TM X-58153, NASA Johnson Space Center, Houston, Texas, October 1974.
5. Eckelkamp, R. E. Effects of Ground Altitude Update on Onboard Entry Navigation. Informal memorandum. NASA Johnson Space Center, Houston, Texas, 3 January 1977.
6. Hamilton, E. L., et al. The General Covariance Analysis Program (GCAP), An Efficient Implementation of the Covariance Analysis Equations. Air Force Avionics Laboratory, Wright-Patterson Air Force Base, Ohio, June 1974.
7. Heller, W. G. Models for Aided Inertial Navigation System Sensor Errors. The Analytic Sciences Corporation, for Defense Mapping Agency Aerospace Center, St. Louis Air Force Station, Missouri, 8 February 1975.
8. Hiott, J. M. OFT-1 Preliminary Flight Profile for Deorbit Through Landing. JSC Internal Note No. 76-FM-68, NASA Johnson Space Center, Houston, Texas, 7 September 1976.
9. Jones, H. L., and Luders, G. Space Shuttle Entry and Landing Navigation Analysis. The Analytic Sciences Corporation, TR-302-2, 31 July 1974.
10. Jones, H. L., et al. Space Shuttle Navigation Analysis. The Analytic Sciences Corporation, TR-548-2, September 1976.
11. MacDonald, T. J., et al. Quarterly Progress Report for the Period Ending 28 February 1977. The Analytic Sciences Corporation, PR-1001-6, 29 April 1977.
12. Matchett, G. A. Personal communication, The Analytic Sciences Corporation, 2 August 1977.
13. Maybeck, P. S. Stochastic Models, Estimation and Control. Unpublished textbook manuscript, 1975.

14. Meditch, J. S. Stochastic Optimal Linear Estimation and Control. New York: McGraw-Hill Book Company, 1969.
15. Meyers, K. A., and Butler, R. R. Simulation Results for an Integrated GPS/Inertial Aircraft Navigation System. Air Force Avionics Laboratory, Wright-Patterson Air Force Base, Ohio, 1976.
16. OFT-1 Deorbit to Landing: Shuttle Trajectory Data Tape No. V05983. National Aeronautics and Space Administration, NASA Johnson Space Center, Houston, Texas, 19 March 1976.
17. Sinha, P. K. Integrated GPS/Inertial Simulator Computer Program. Intermetrics Corporation, 4 August 1977.

Appendix A

Computer Generated Plots

This appendix will present the computer generated plots of the filter performance. There will be seven sections, or one section for each filter implementation. First will be the baseline or 73-state optimal filter plots. Next will be the 17-state filter with 30.72 second update period, followed by the 17-state filter with a 15.36 second update period. Fourth will be the 11-state filter design plots for the pre-blackout time period, and then the 11-state filter results in the post-blackout region. Sixth will be the 8-state filter performance plots in the pre-blackout region, and finally, the 8-state filter design plots in the post-blackout region.

Note that position and velocity results are referenced to the earth centered inertial frame (i), clock errors are absolute and are not referenced to any frame, and misalignment angles are referenced to the platform (p) frame. For each section, except for the baseline filter plots, each page will present a side by side comparison of filter indicated error, \hat{dx}_i , for a particular state with the true system error, dx_i , for that state. The baseline filter plots, the 17-state filter plots, and the 11-state filter plots will each present results for states one through eleven. The 8-state filter results will be given by plots for states one through eight.

73-State Optimal Filter

The following 11 plots (Figures 9-19) show the performance of a 73-state optimal filter implementation. Only one plot for each of the first 11 states is shown because the filter and system would have the

same performance, given the same initial conditions. This is because the filter would be using a near perfect model of the system.

Fig 9 Optimal 73-State True Error, δx_7

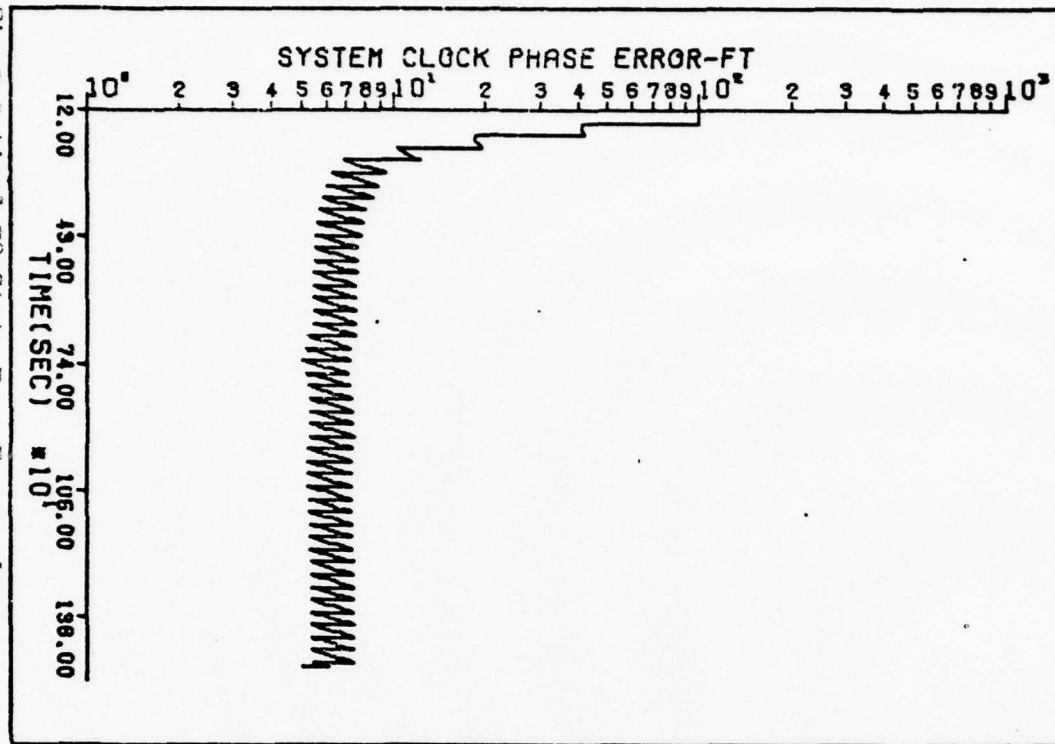


Fig 10 Optimal 73-State True Error, δx_8

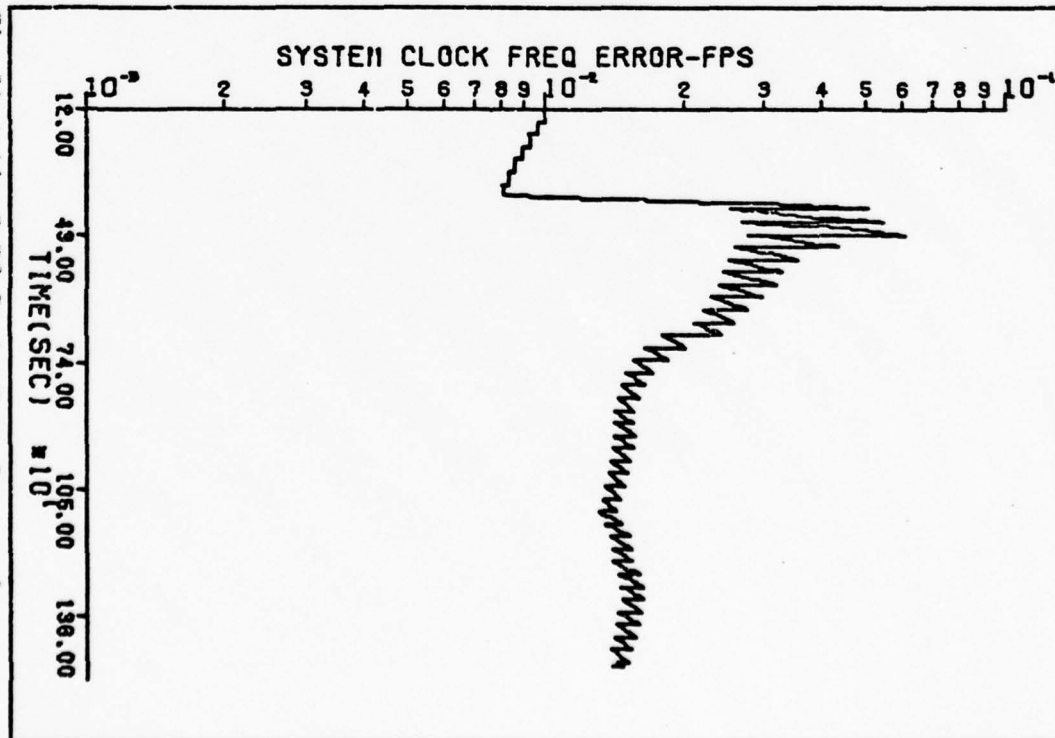


Fig 11 Optimal 73-State True Error, dx_1

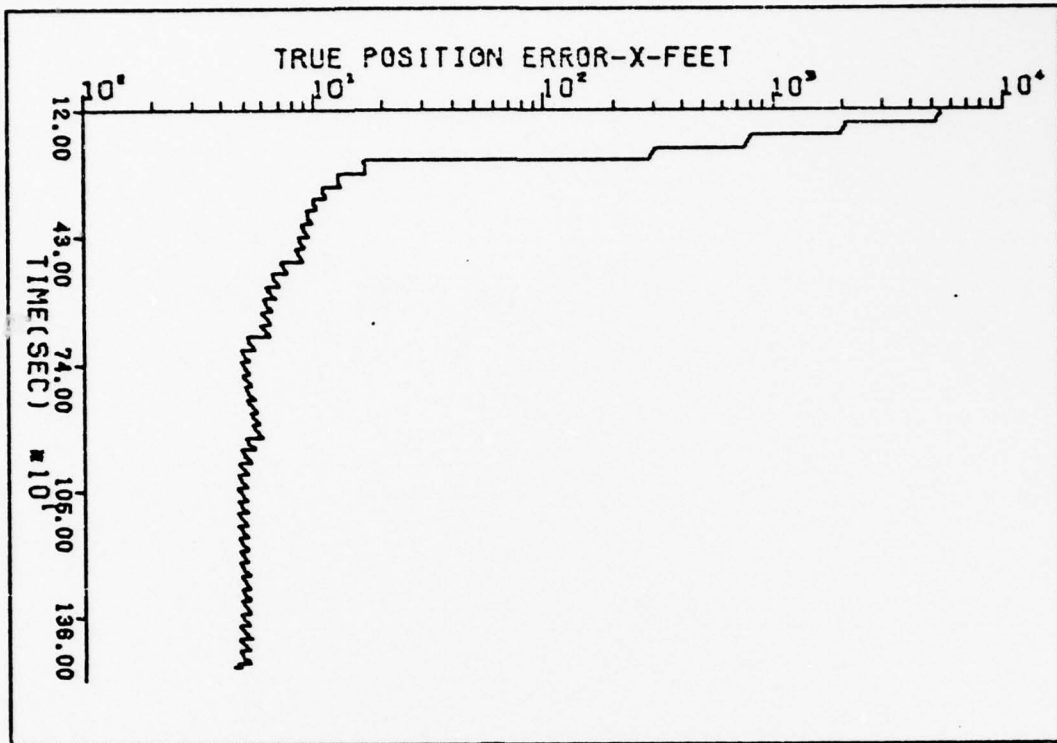
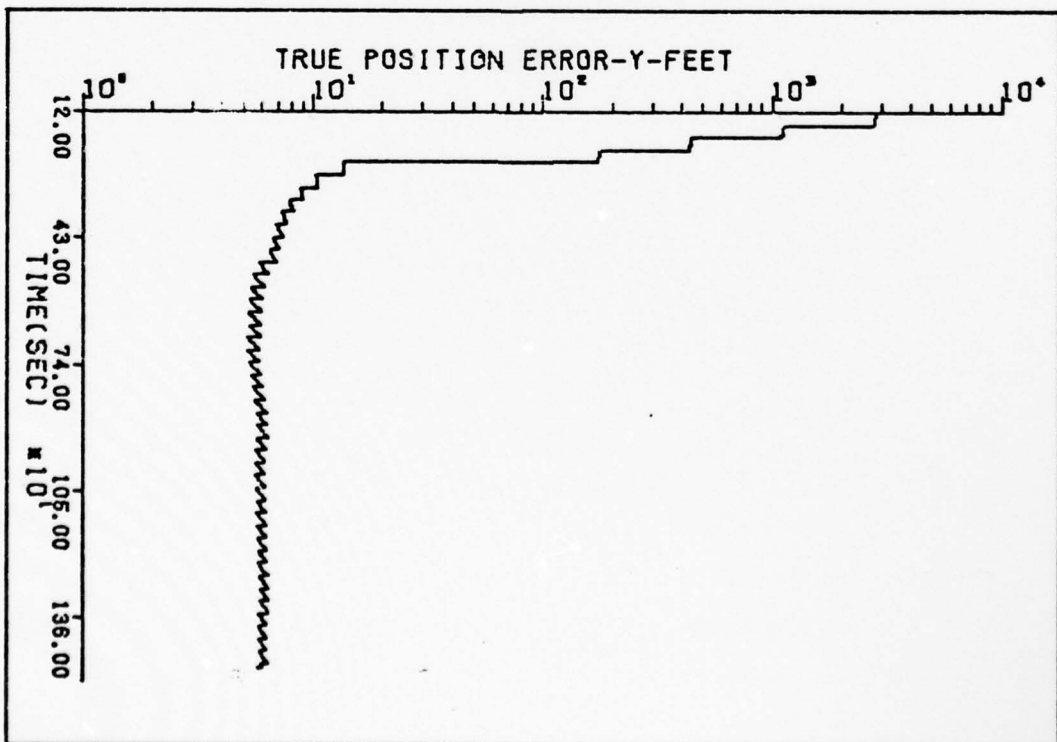


Fig 12 Optimal 73-State True Error, dx_2



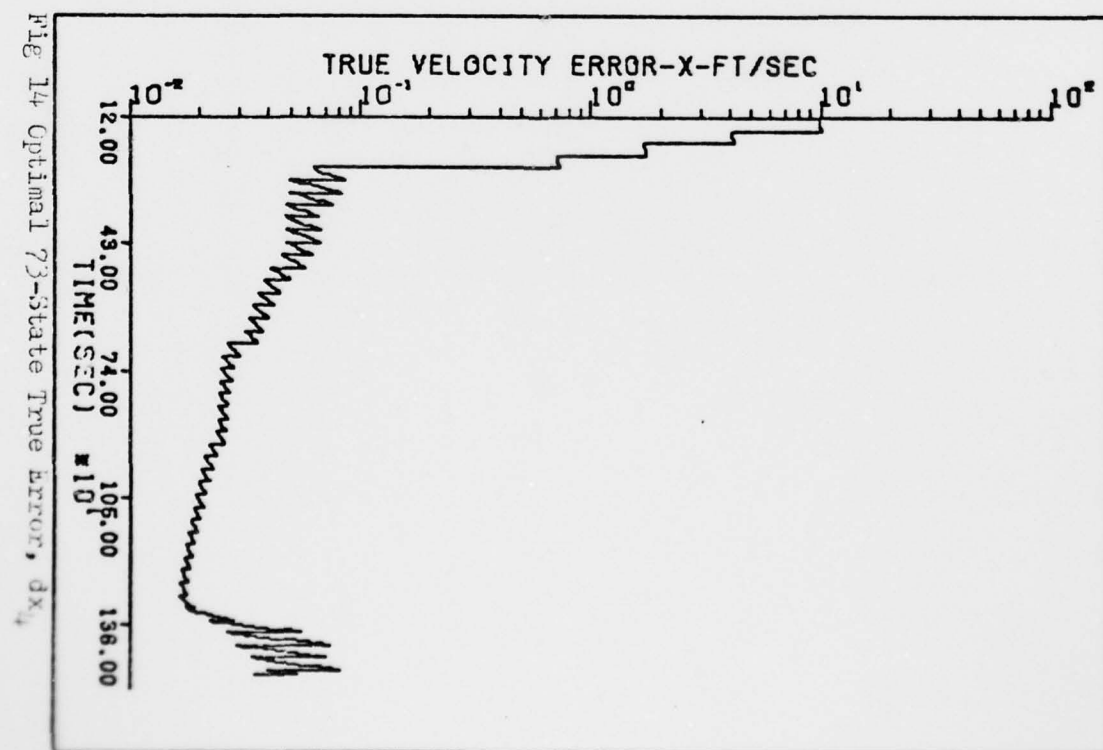
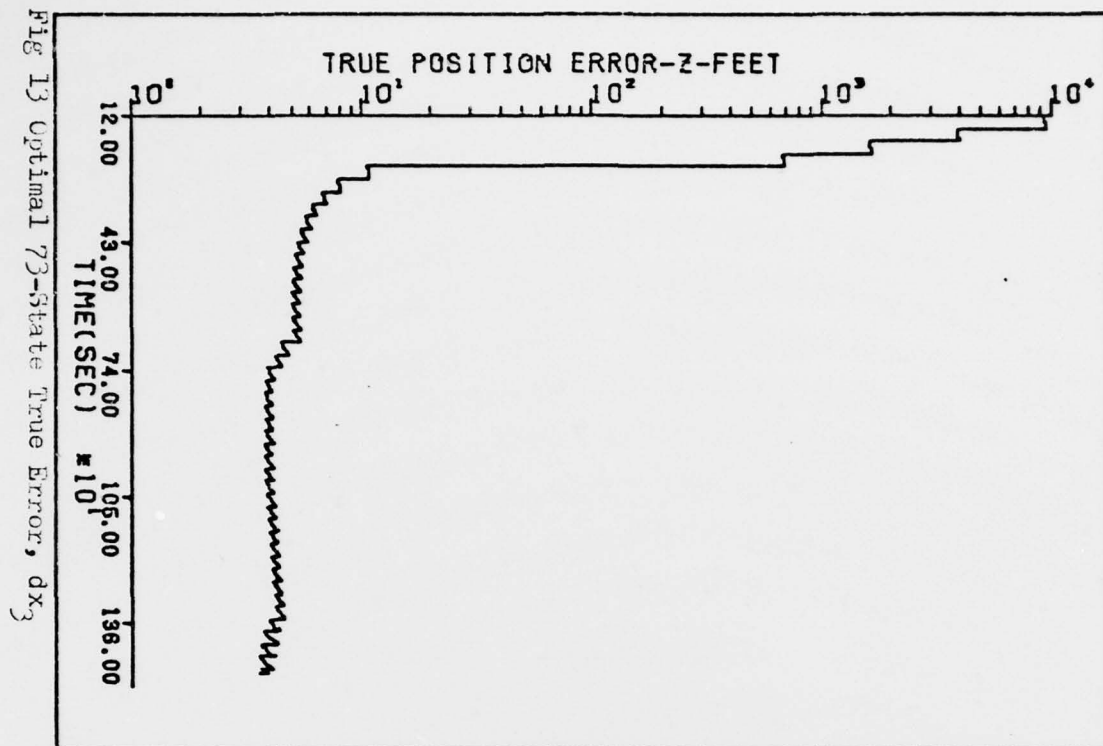


Fig 15 Optimal 73-State True Error, dx_5

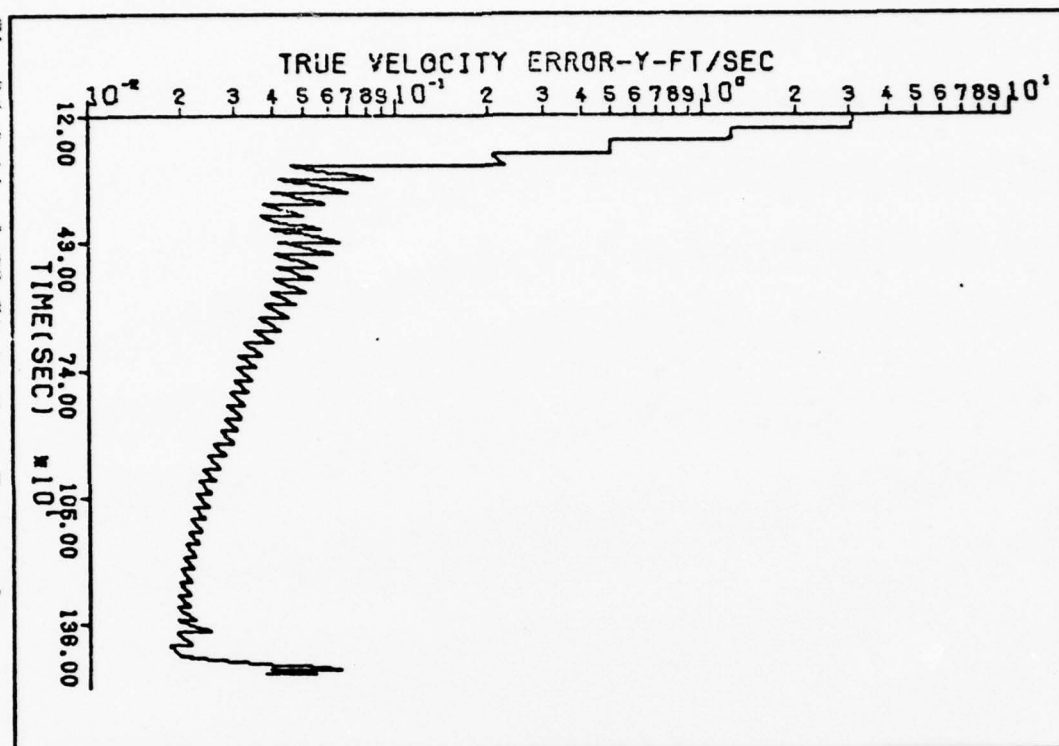
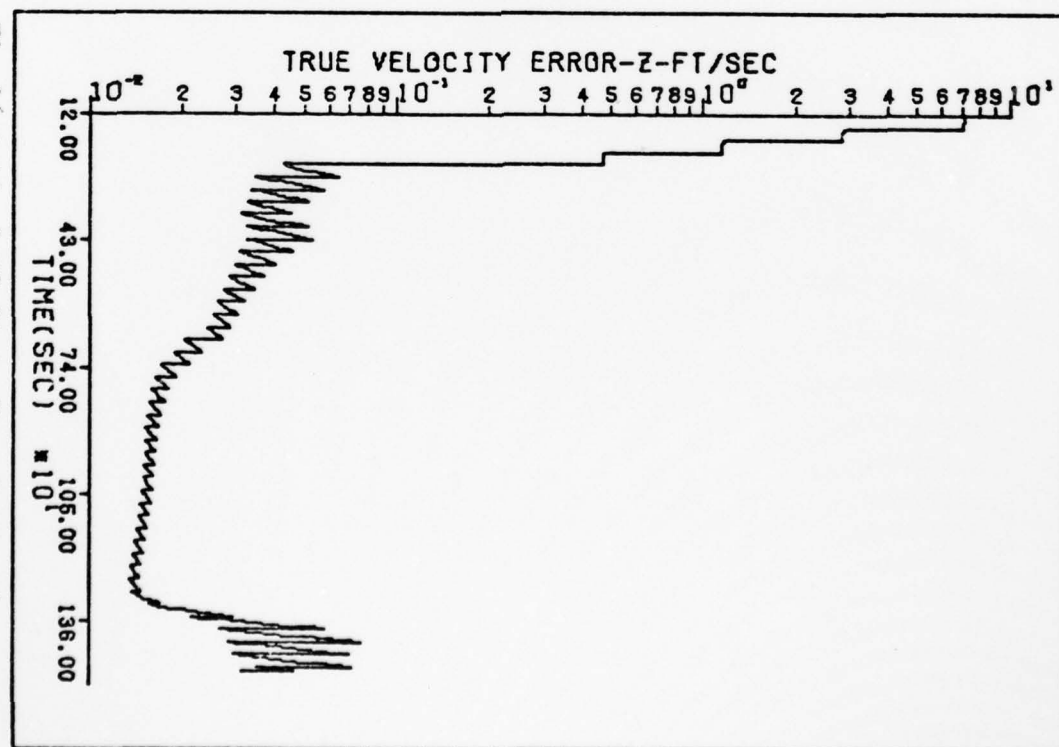


Fig 16 Optimal 73-State True Error, dx_6



182

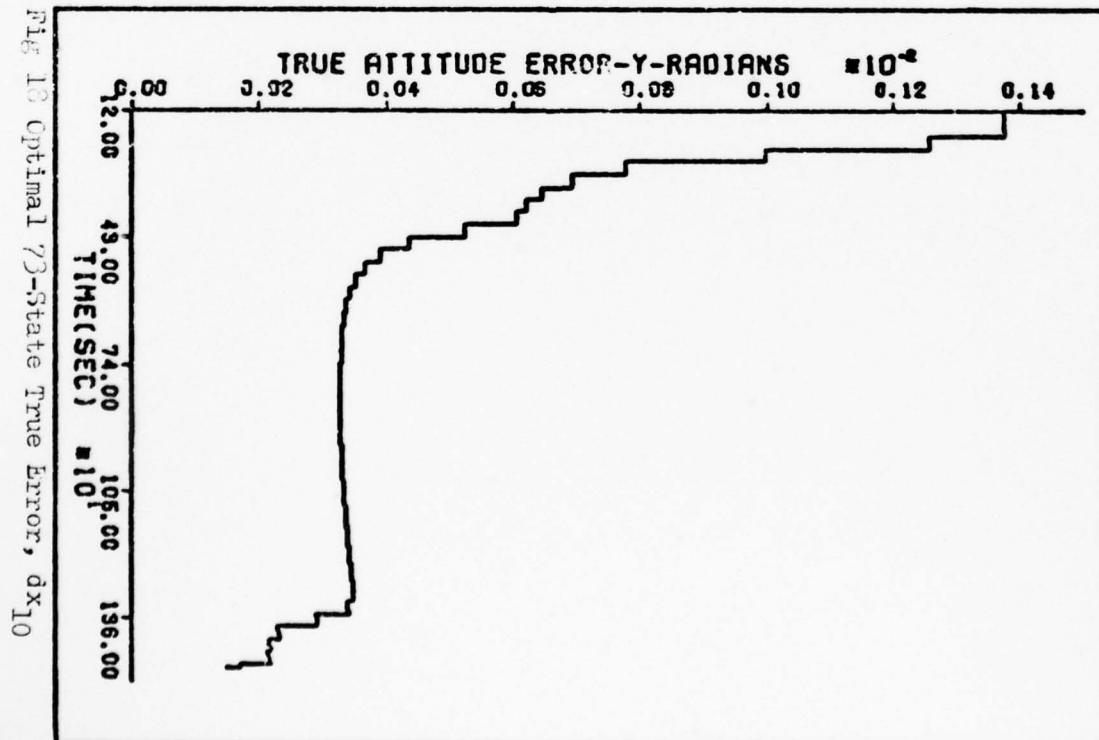
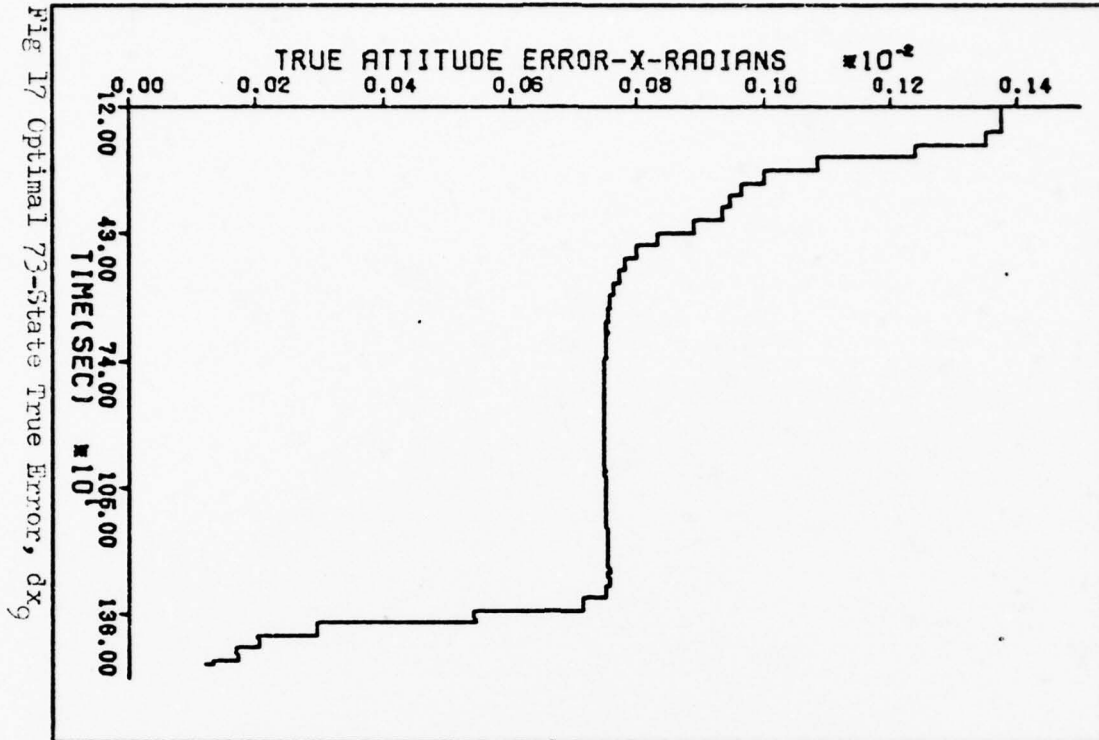
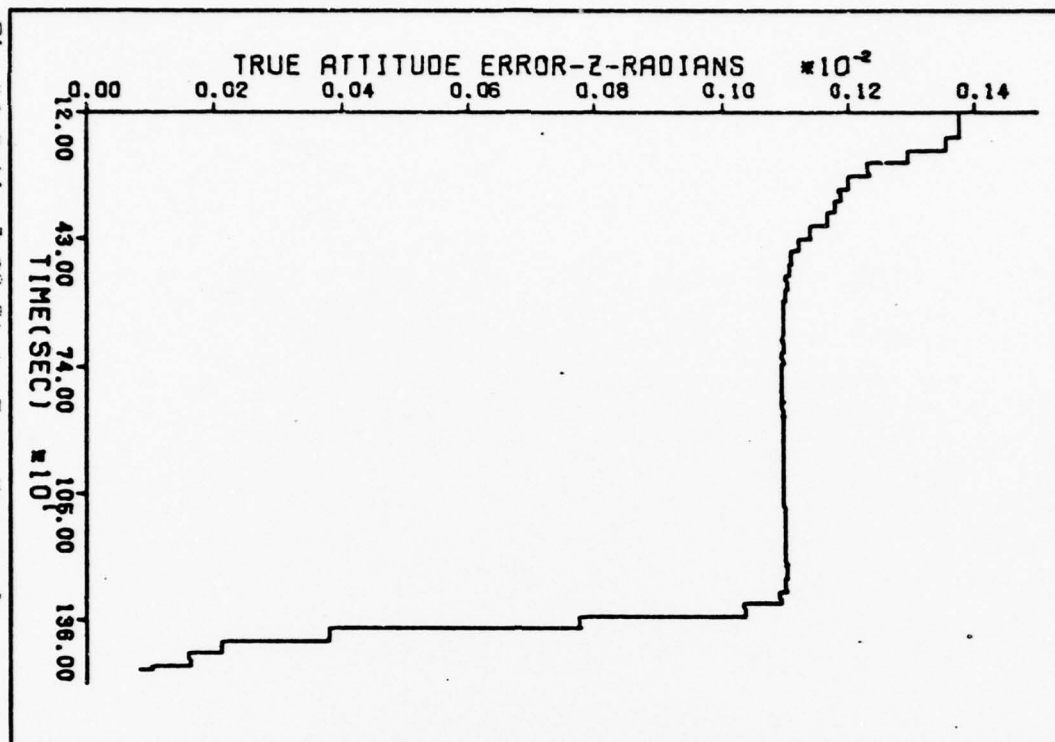


Fig 19 Optimal 73-State Time Error, δx_{11}



17-State Filter, Slow Update Rate

The following section presents the performance plots for the 17-State Filter. These plots are for states one through eleven, and represent a simulation with a 30.72 second measurement update period. The first time point for which data was taken uses 120.55 seconds as reference or $t(0)$. The data ends at assumed blackout, or 1482.71 seconds.

Fig 20 17-St hst Error, 30.72 Sec Updt, dx₇

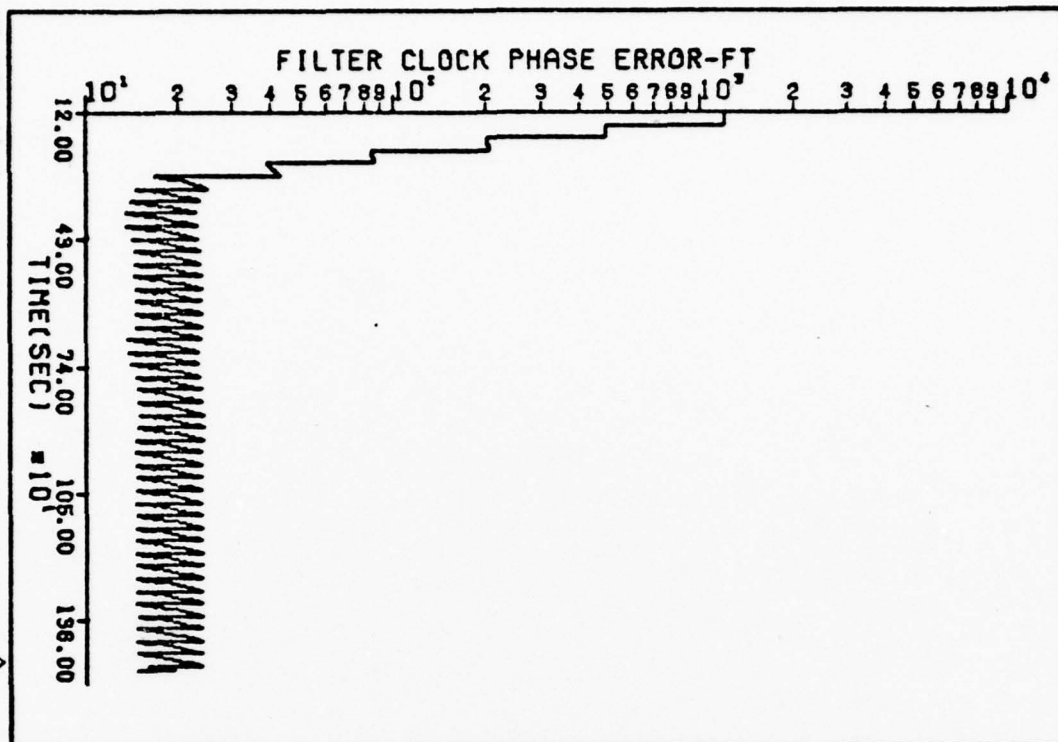
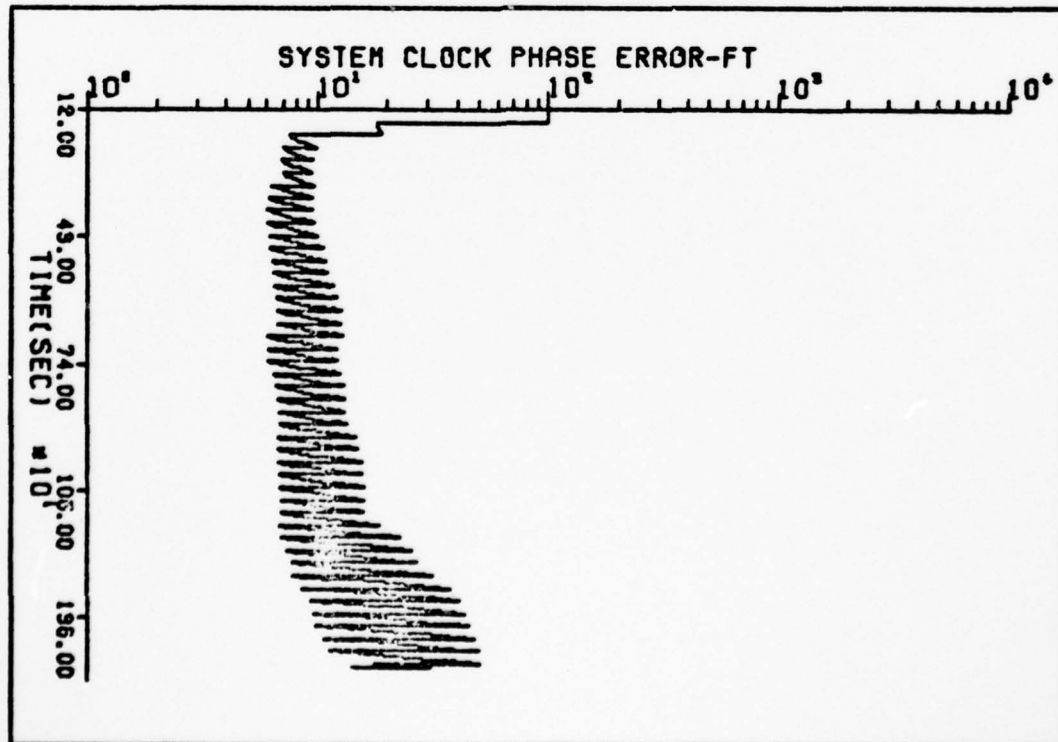


Fig 21 17-St Time Error, 30.72 Sec Updt, dx₇



64

Fig 22 17-St Est Error, 30.72 Sec Updt, dx₈

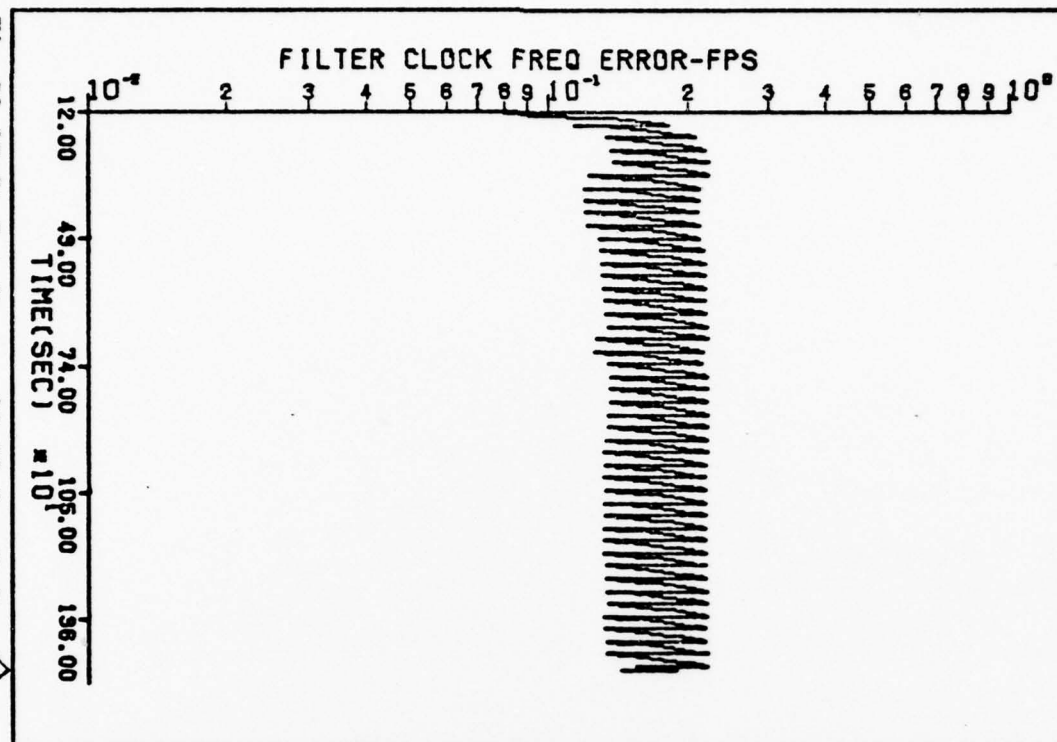
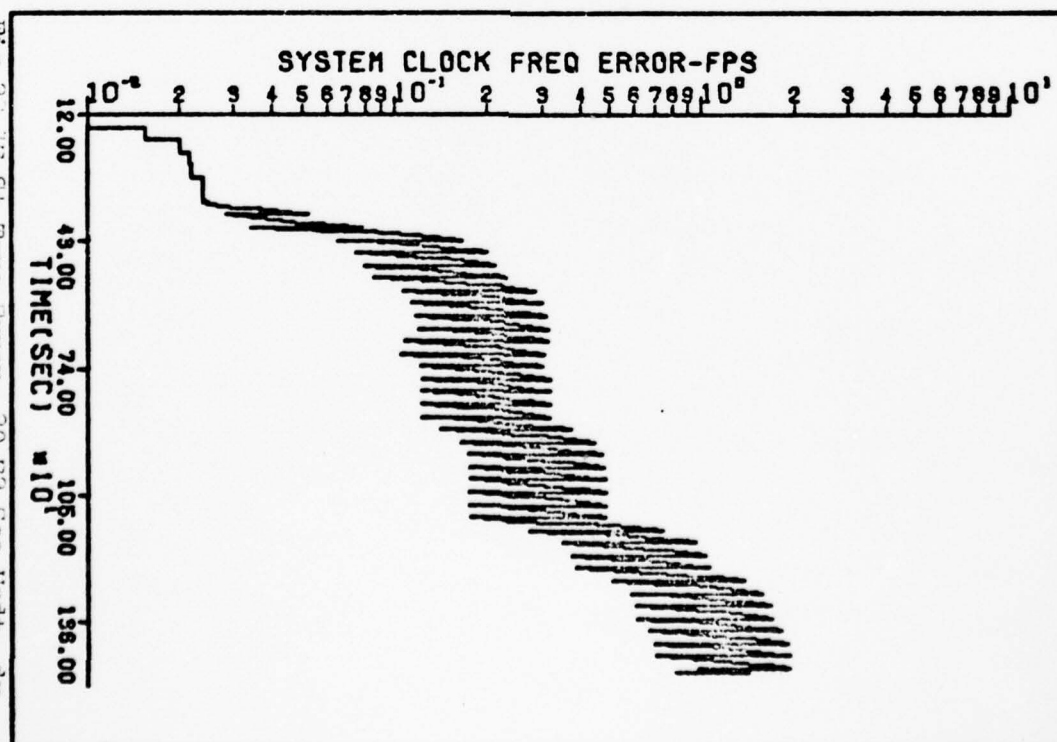


Fig 23 17-St True Error, 30.72 Sec Updt, dx₈



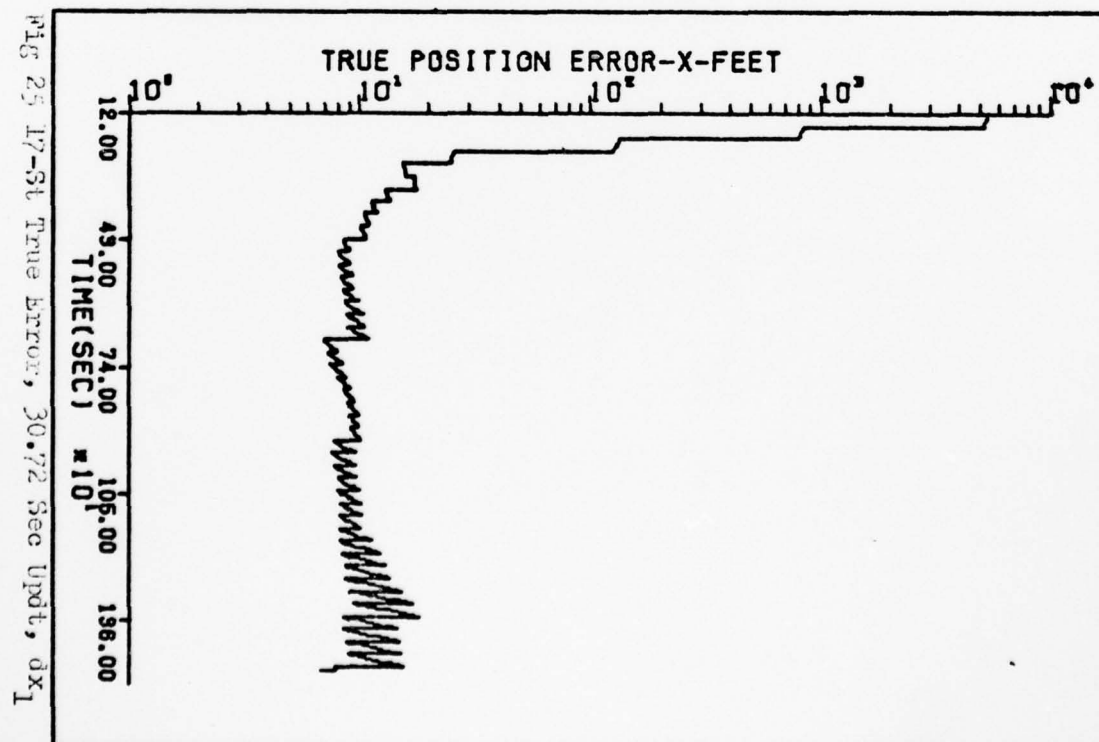
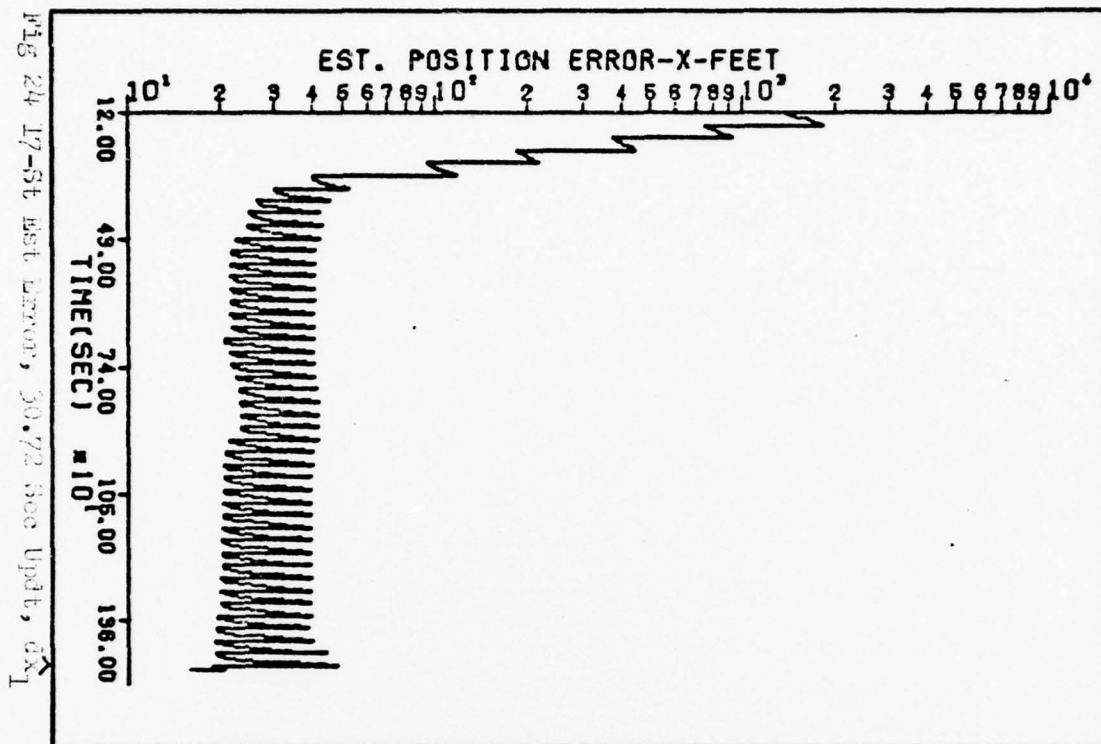


Fig 26 17-St Est Error, 30.72 Sec Updt, δx_2

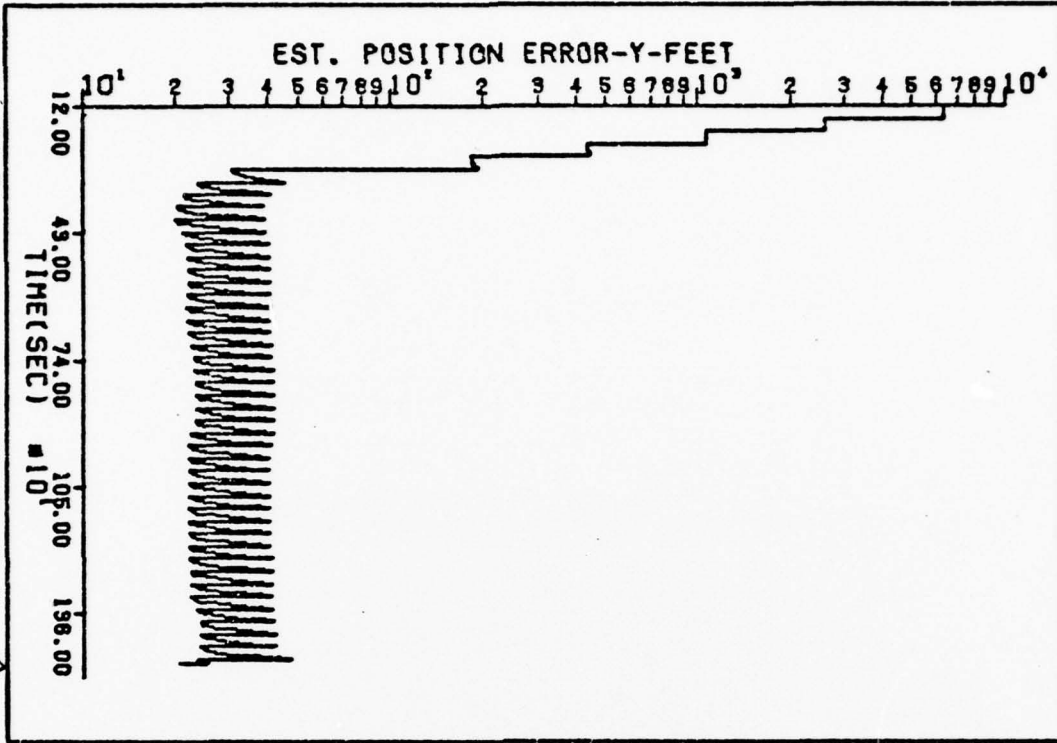


Fig 27 17-St True Error, 30.72 Sec Updt, δx_2

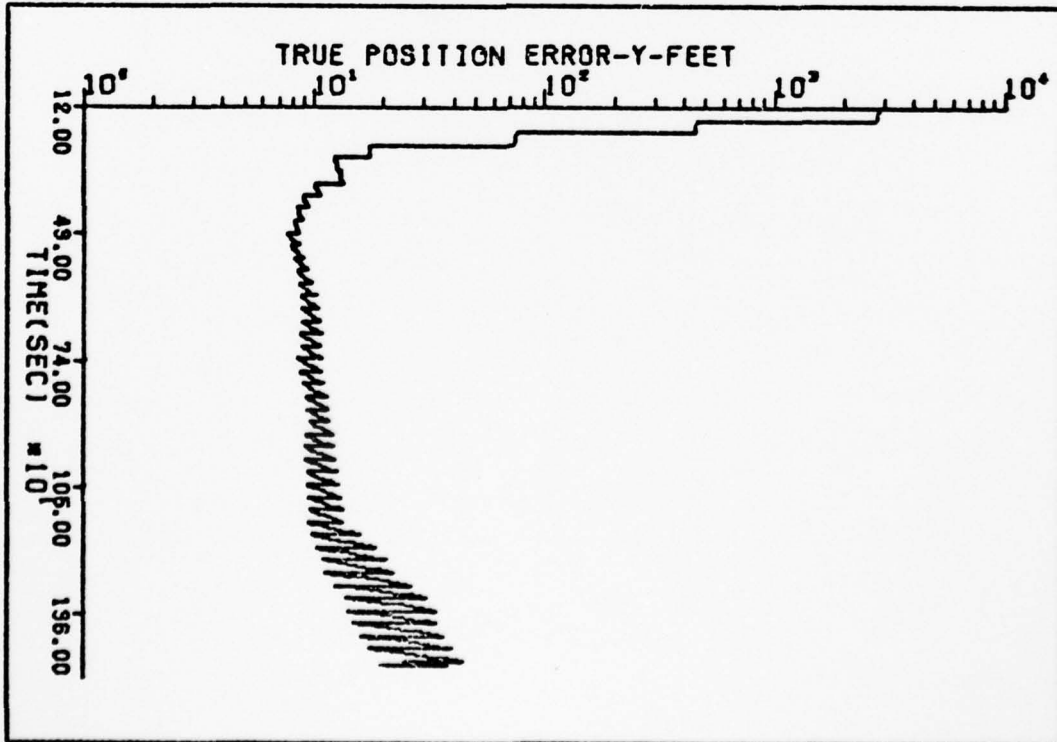


Fig 28 17-5t Est Error, 30.72 Sec Updt, dx_3

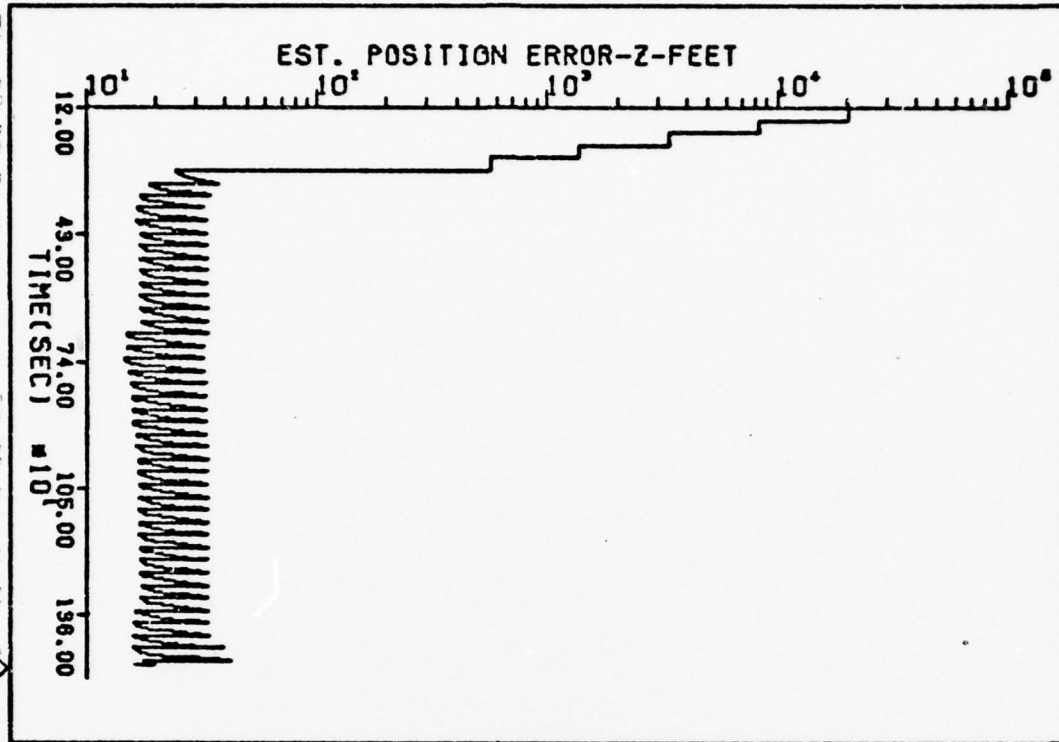


Fig 29 17-5t True Error, 30.72 Sec Updt, dx_3

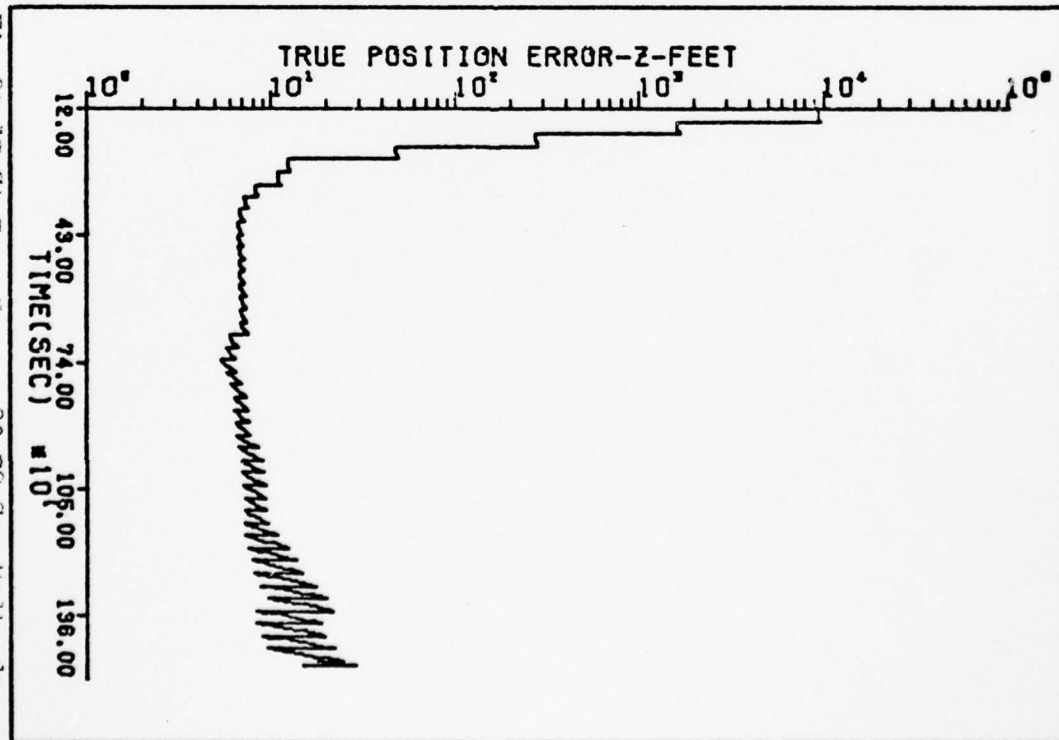


Fig 30 17-St Est Error, 30.72 Sec Updt, dx₄

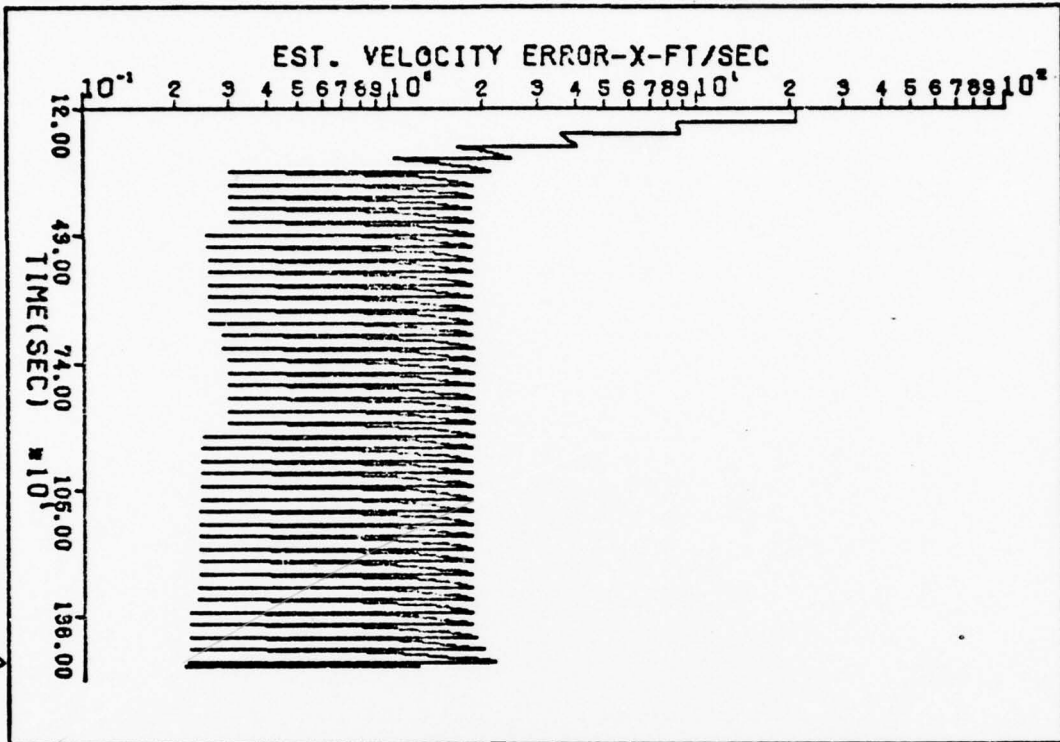
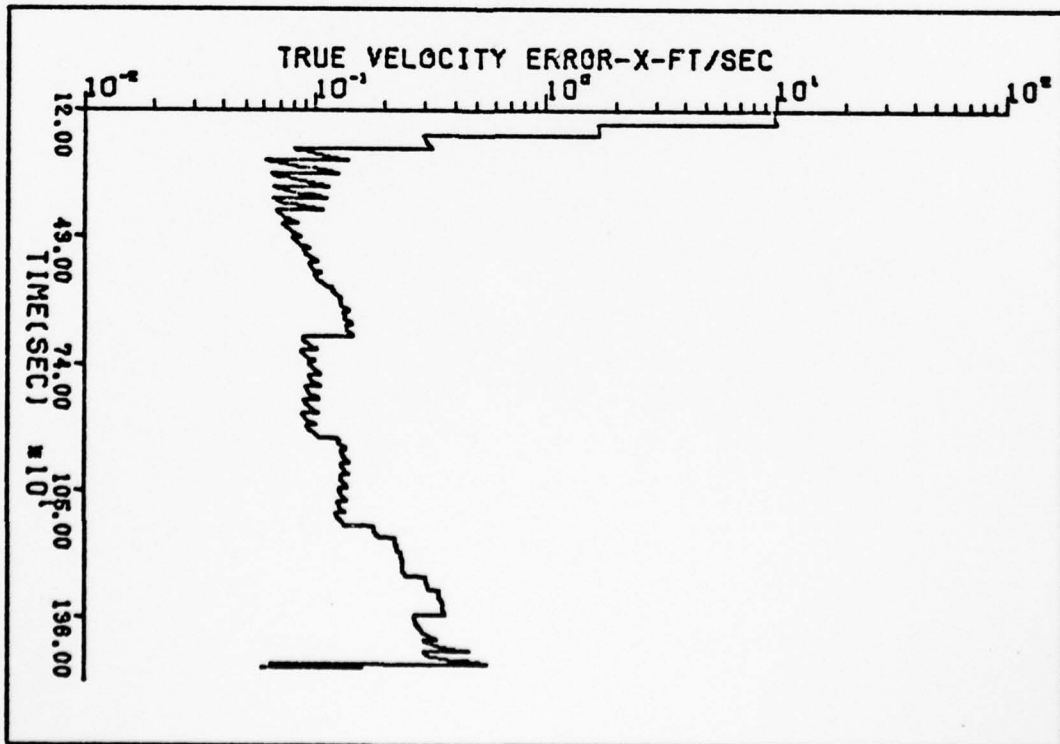


Fig 31 17-St True Error, 30.72 Sec Updt, dx₄



82

Fig 32 17-5t Est Error, 30.72 Sec Updt, dx_5

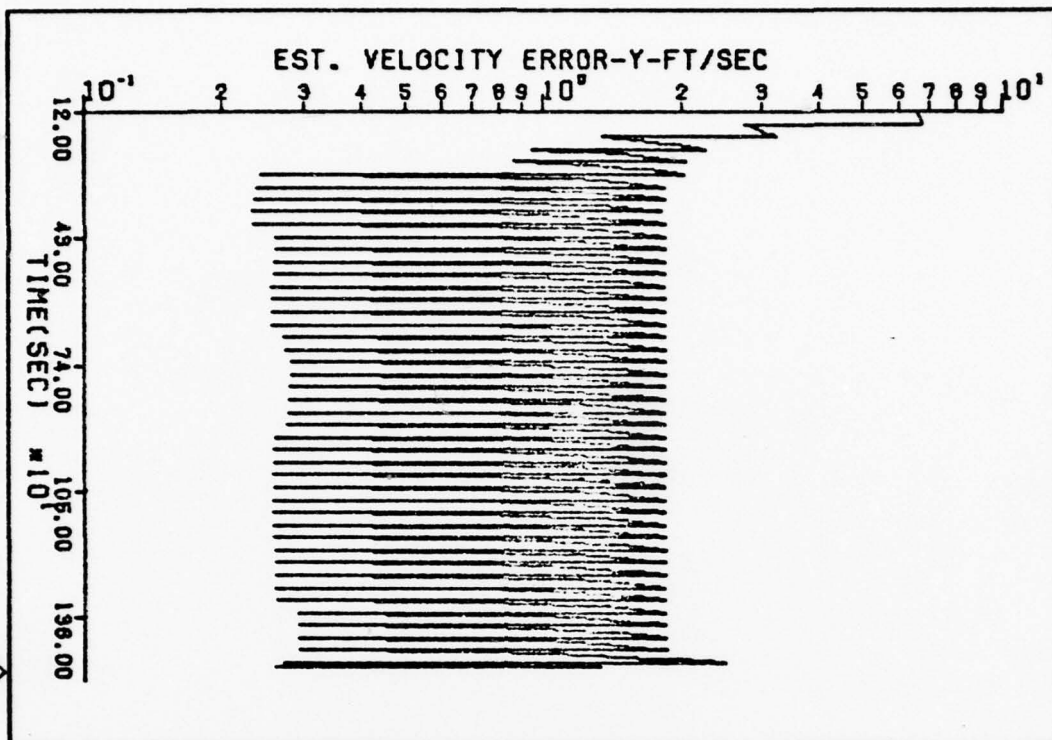
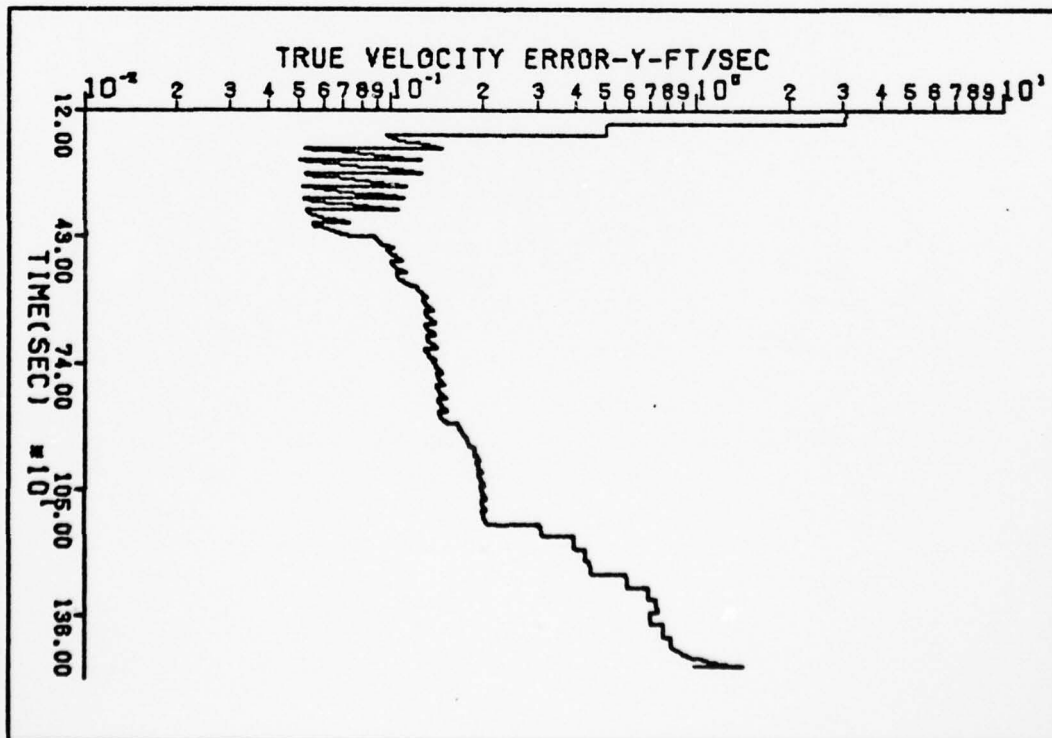


Fig 33 17-5t True Error, 30.72 Sec Updt, dx_5



10

Fig 34 17-5t Est Error, 30.72 Sec Updt, dx6

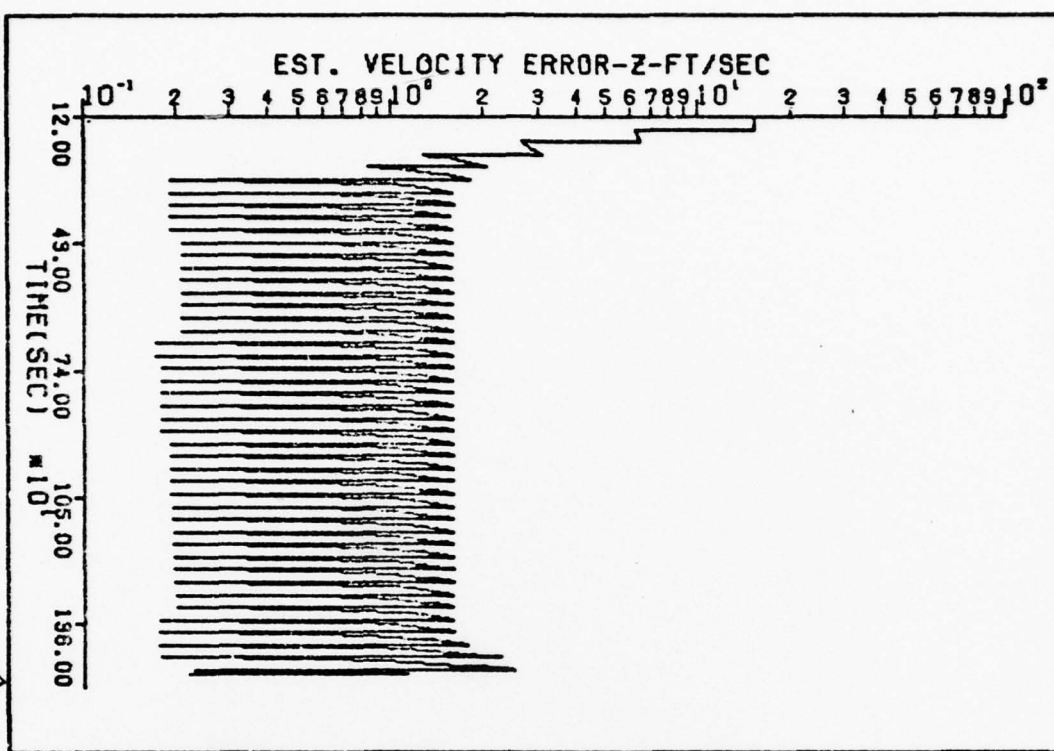
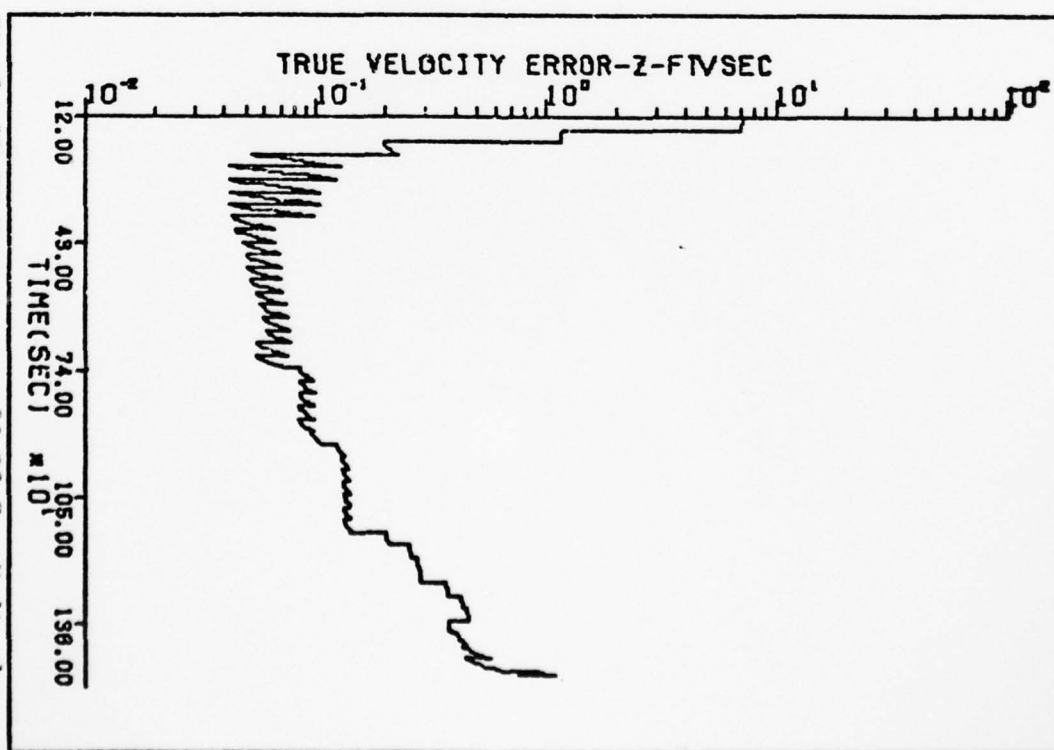


Fig 35 17-5t True Error, 30.72 Sec Updt, dx6



XX

Fig 36 17-St Est Error, 30.72 Sec Updt, δx_g

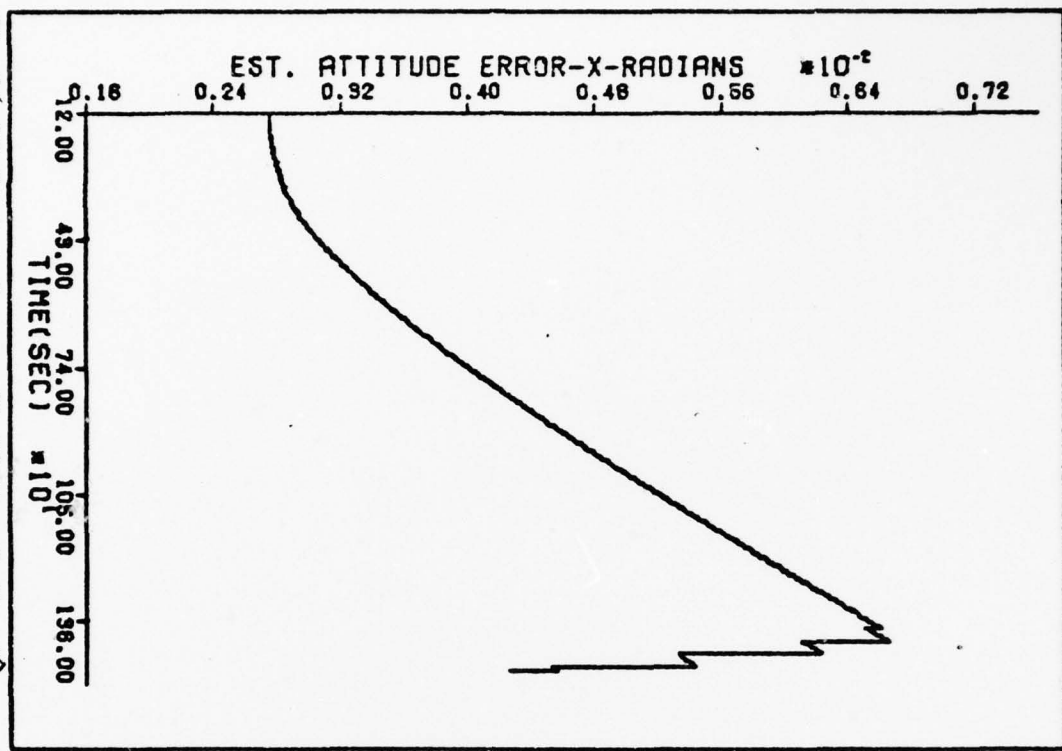
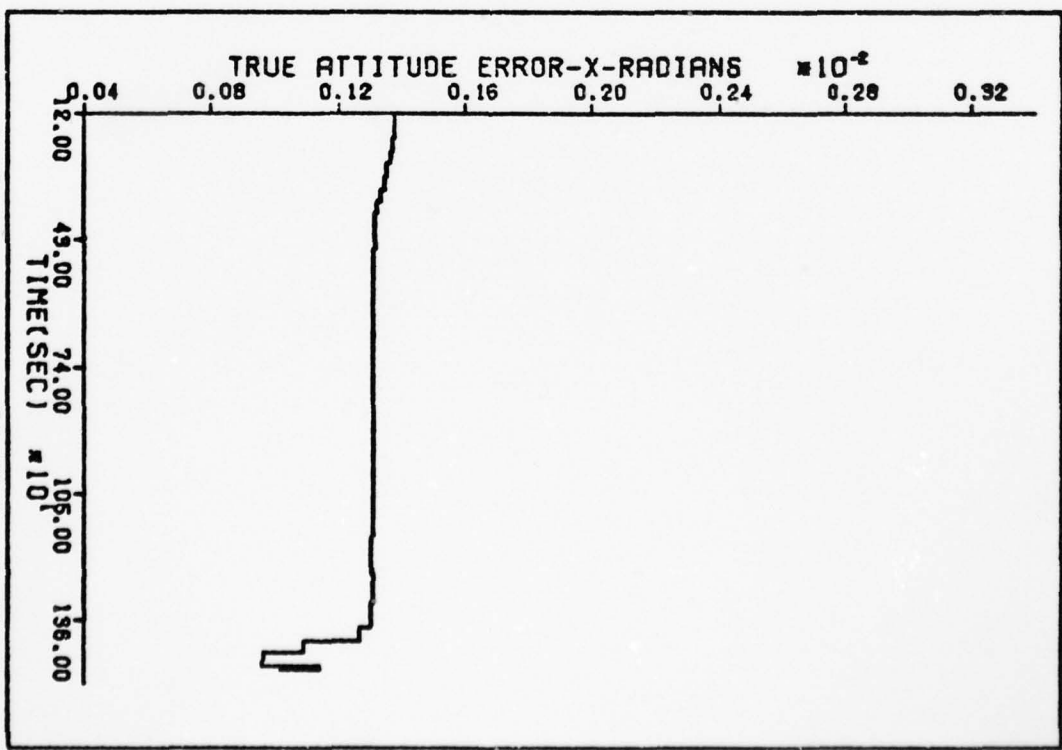


Fig 37 17-St True Error, 30.72 Sec Updt, δx_g



AD-A055 465

A KALMAN FILTER DESIGN FOR THE SPACE SHUTTLE ORBITER
INERTIAL MEASURING U. (U) AIR FORCE INST OF TECH
WRIGHT-PATTERSON AFB OHIO SCHOOL OF EN. D A VAN LIERE
DEC 77 AFIT/GGC/EE/77-10

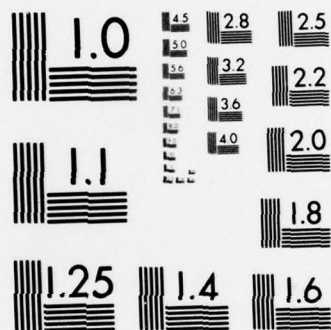
2/2

UNCLASSIFIED

F/G 22/2

NL





MICROCOPY RESOLUTION TEST CHART
NATIONAL BUREAU OF STANDARDS-1963-A

Fig 38 17-St Est Error, 30.72 Sec Updt, δx_{10}

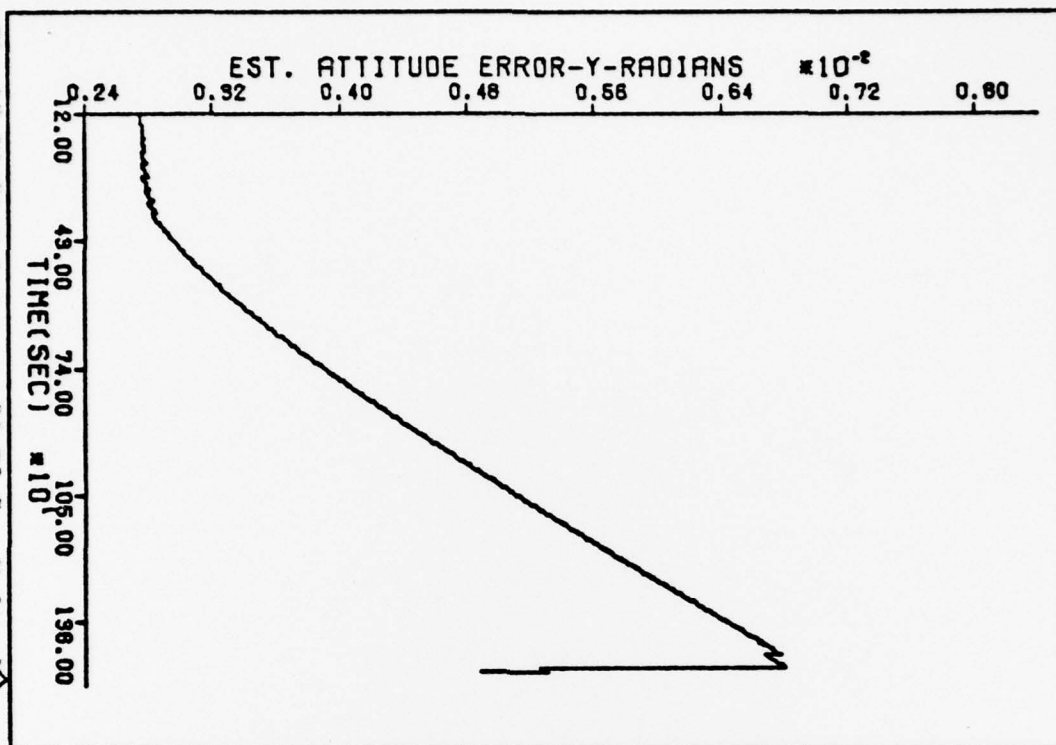
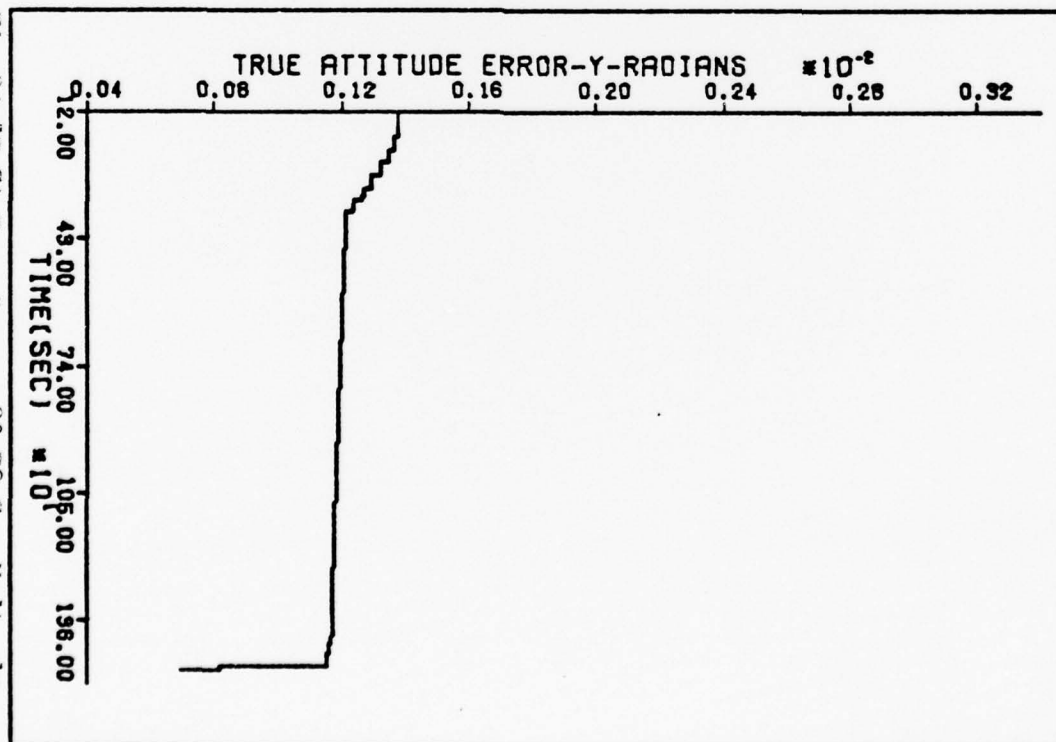
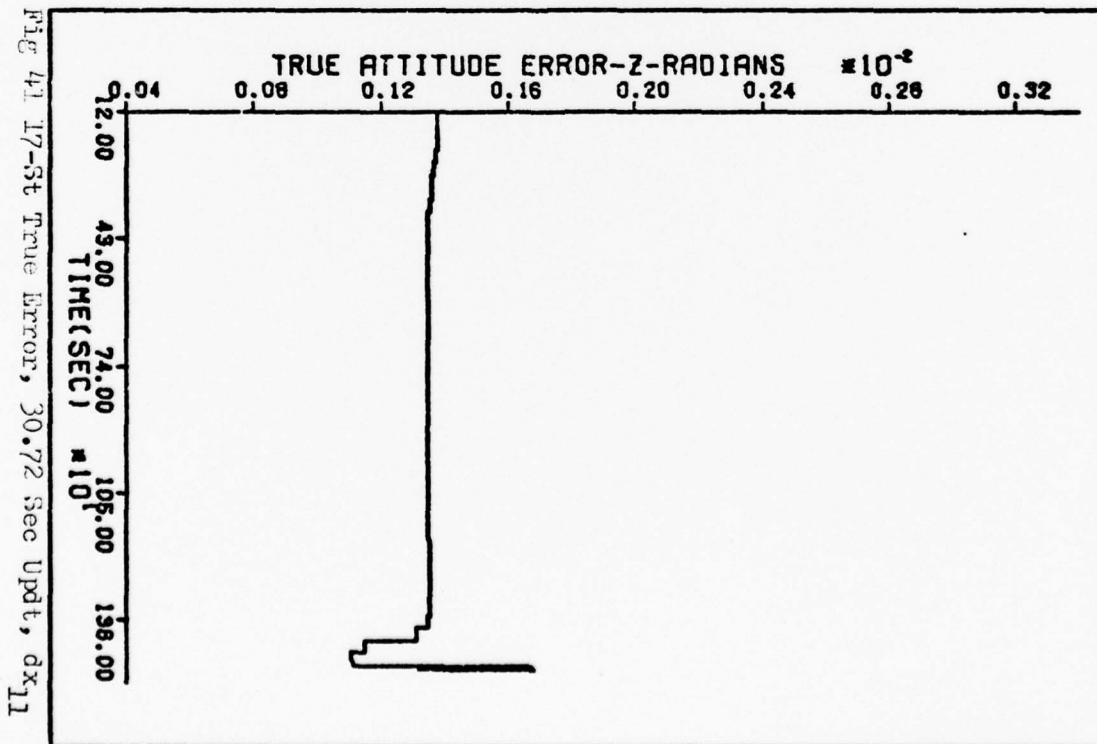
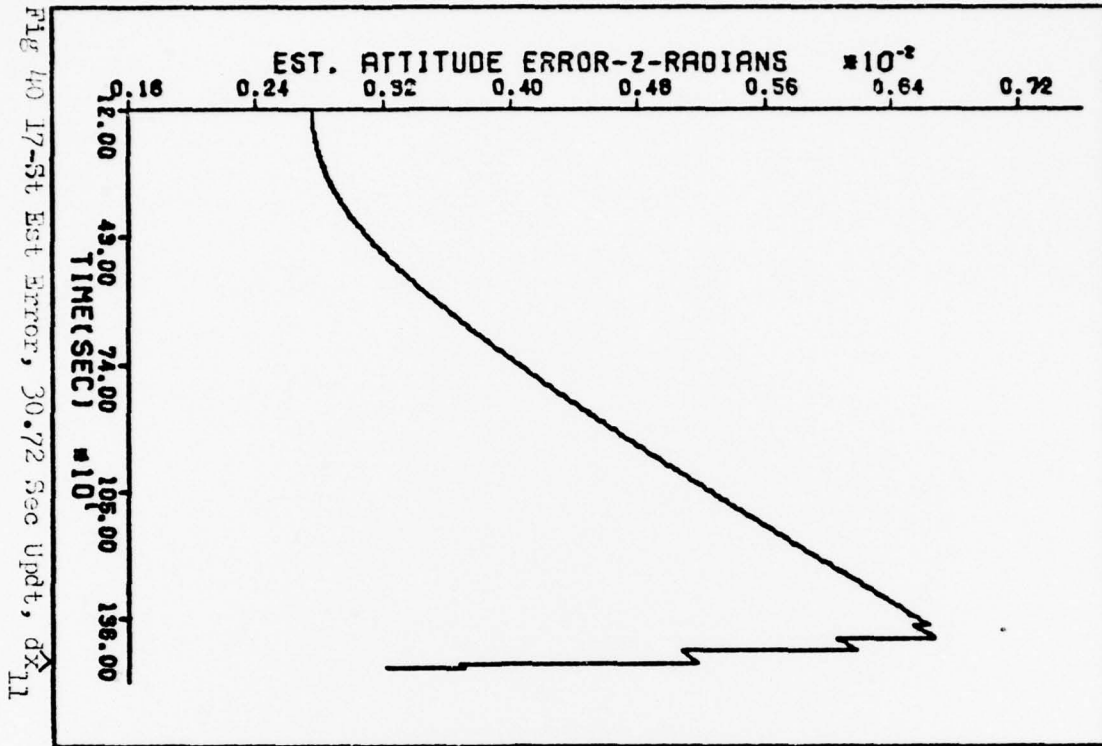


Fig 39 17-St True Error, 30.72 Sec Updt, δx_{10}



88



17-State Filter, Fast Update Rate

This section presents the performance plots for the 17-State Filter with a measurement update period of 15.36 seconds.

XX

Fig 42 17-St Est Error, 15.36 Sec Updt, dx₇

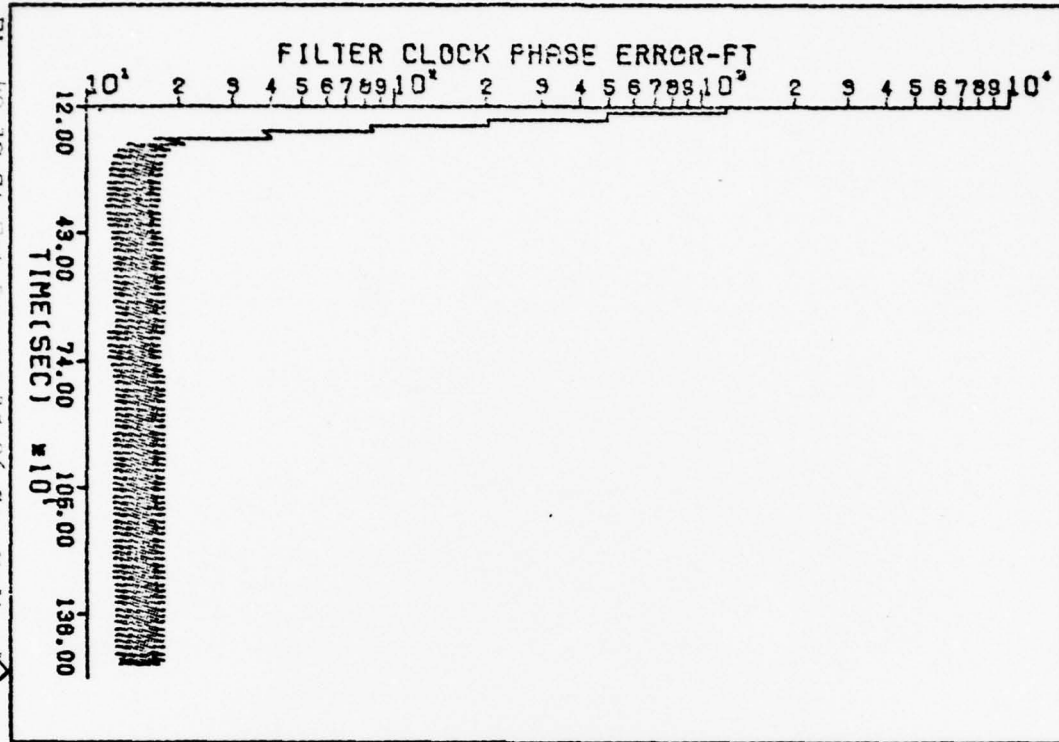
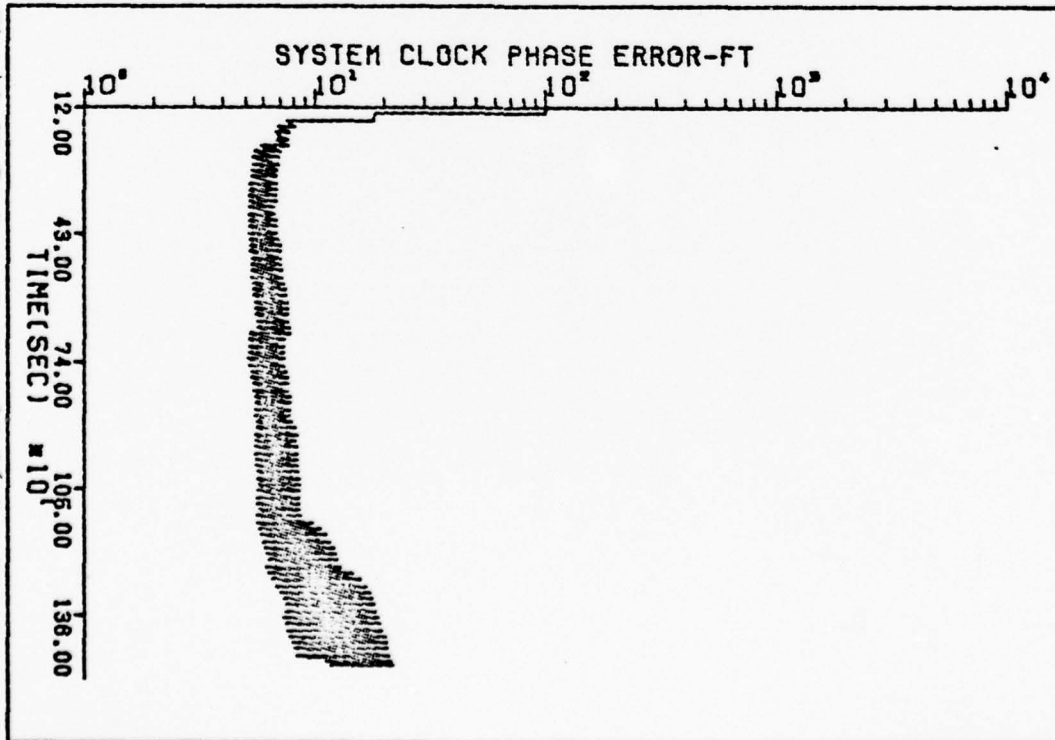


Fig 43 17-St True Error, 15.36 Sec Updt, dx₇



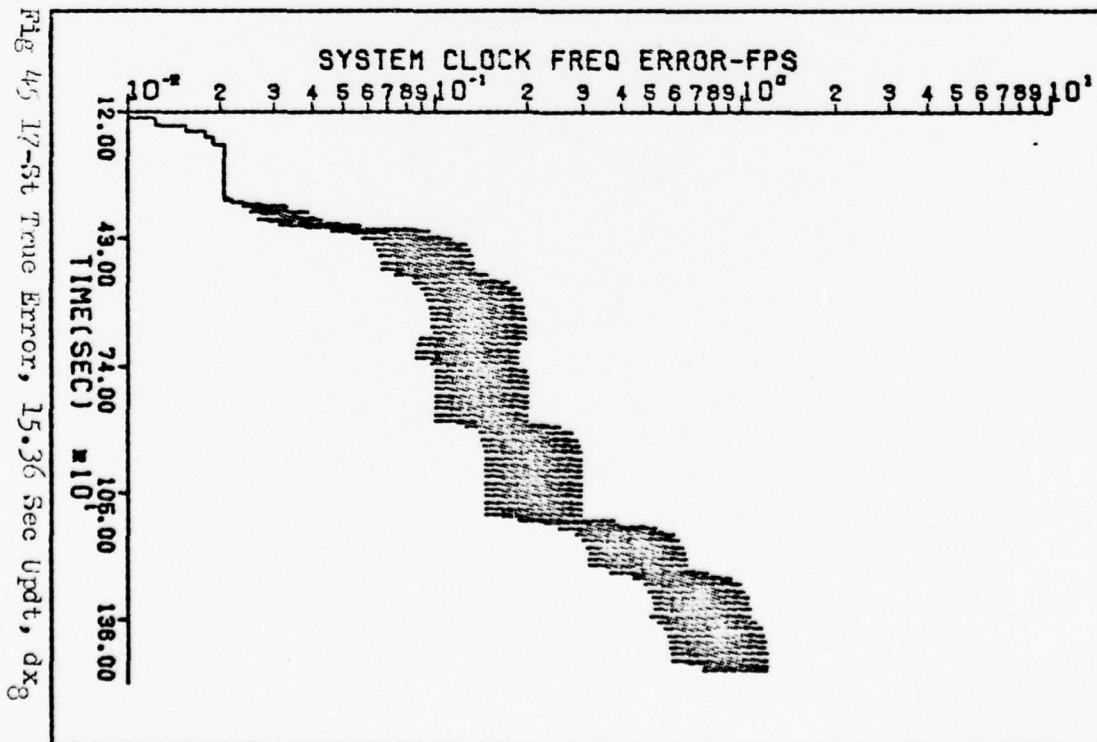
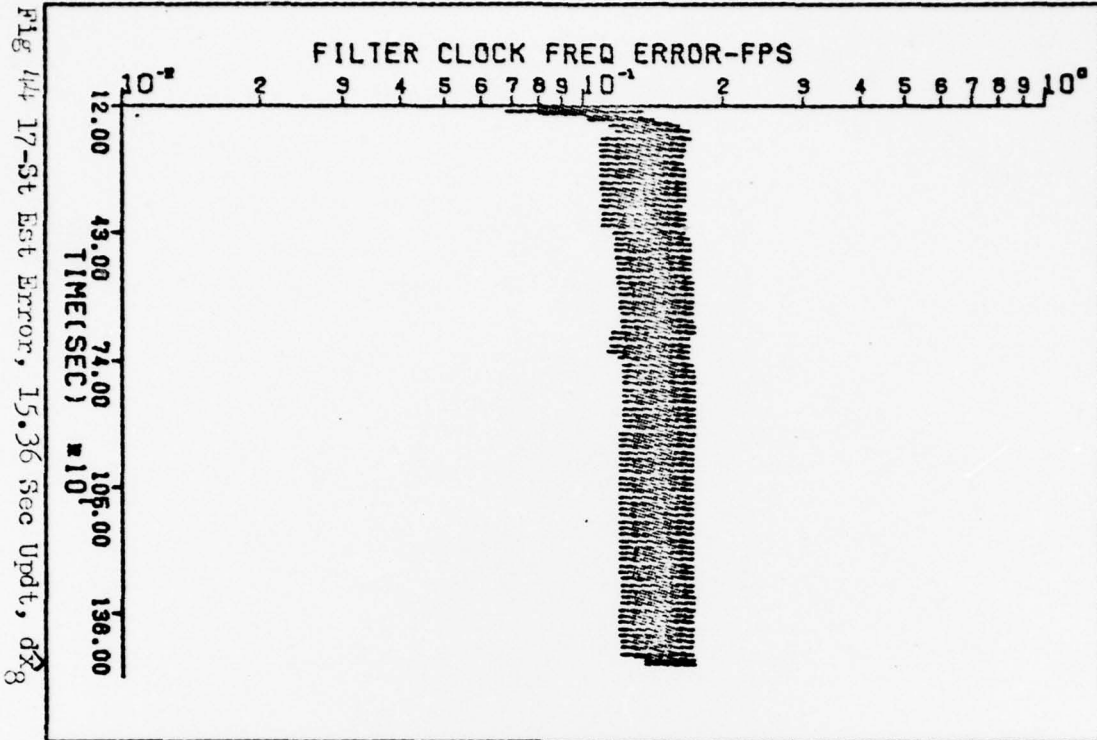


Fig 46 17-St Est Error, 15.36 Sec Updt, dx₁

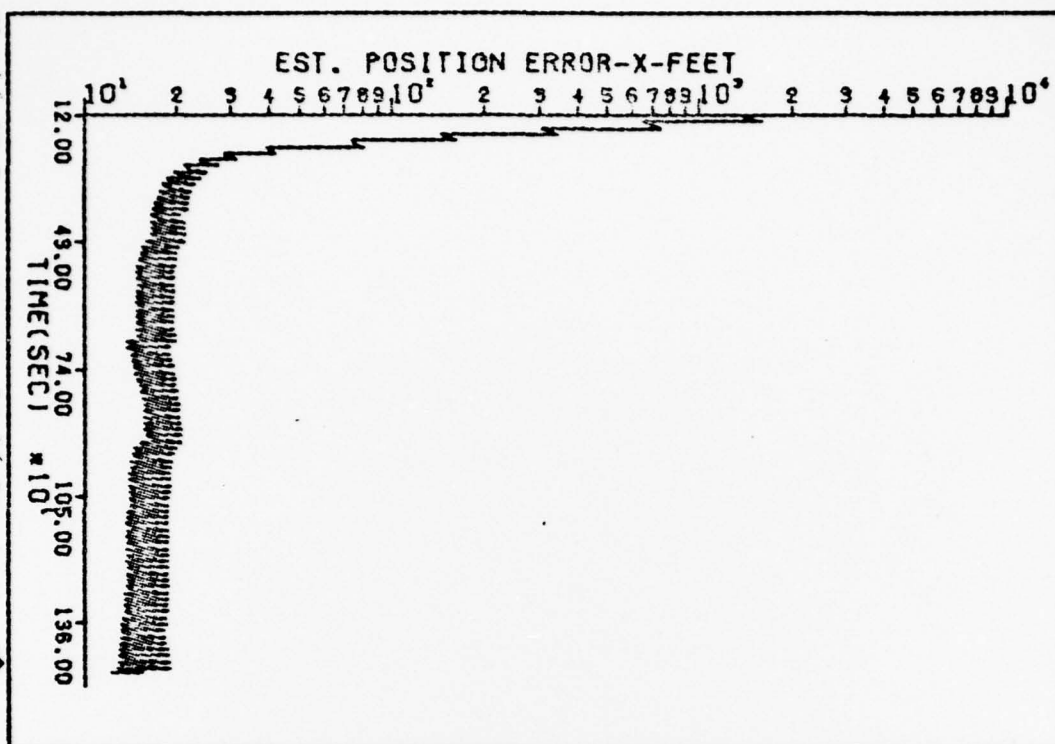
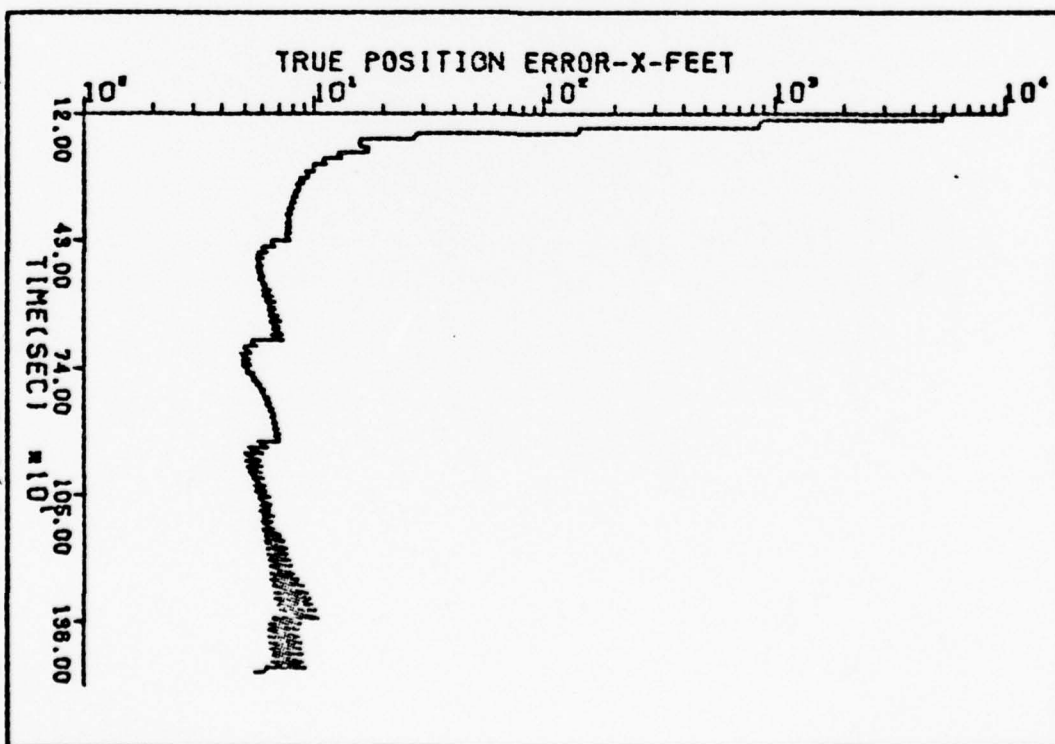


Fig 47 17-St True Error, 15.36 Sec Updt, dx₁



XX

Fig 48 17-St Est Error, 15.36 Sec Updt, δx_2

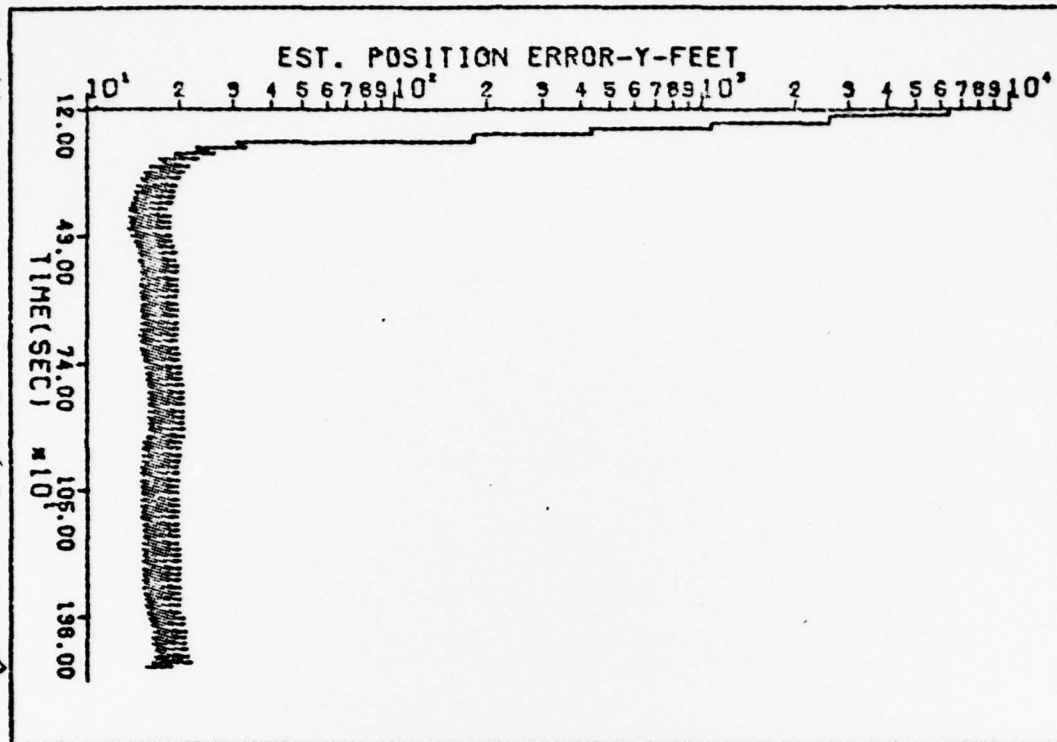
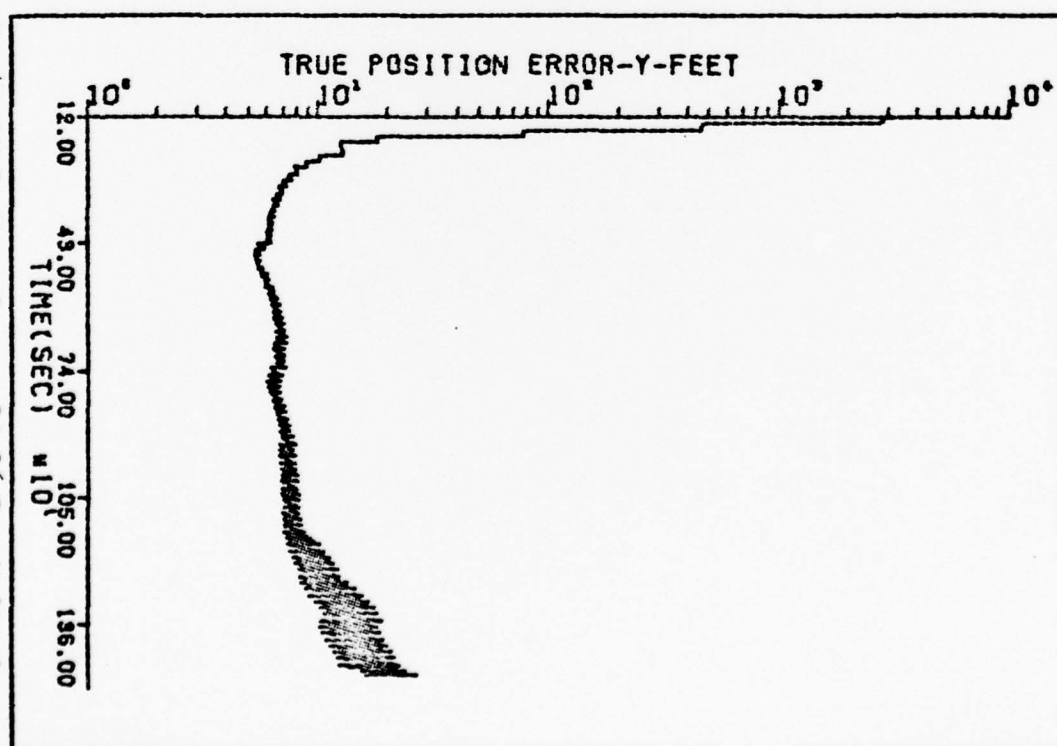


Fig 49 17-St True Error, 15.36 Sec Updt, δx_2



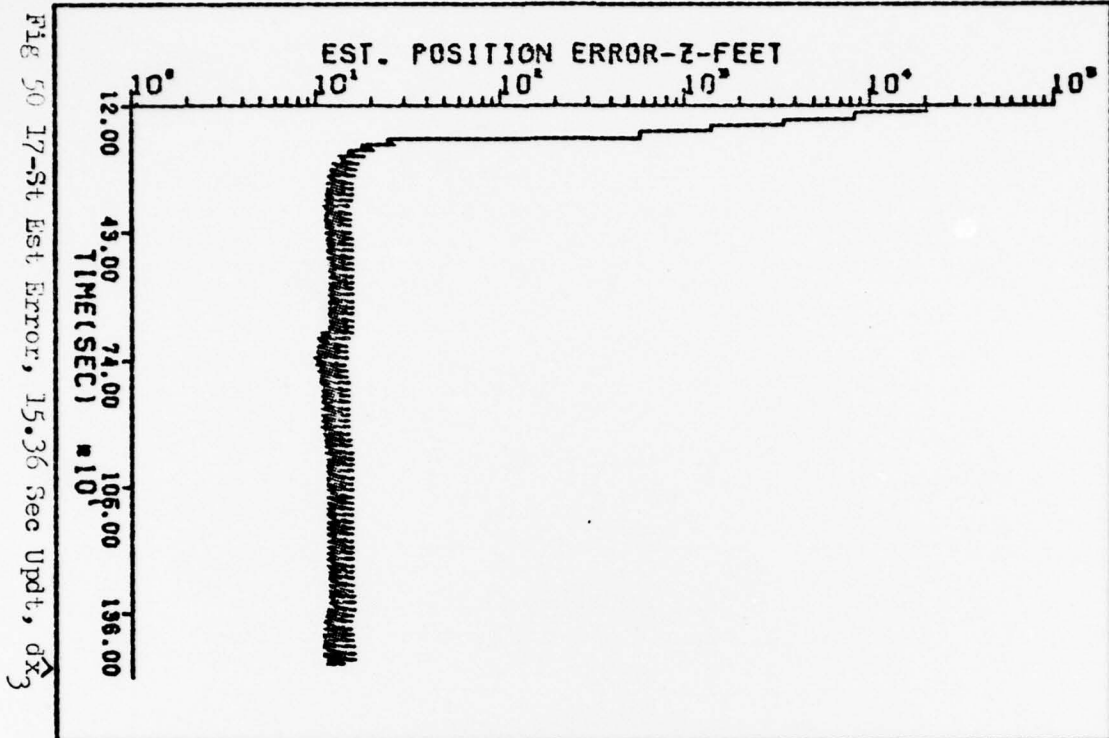


Fig 50 17-St Est Error, 15.36 Sec Updt, δx_3

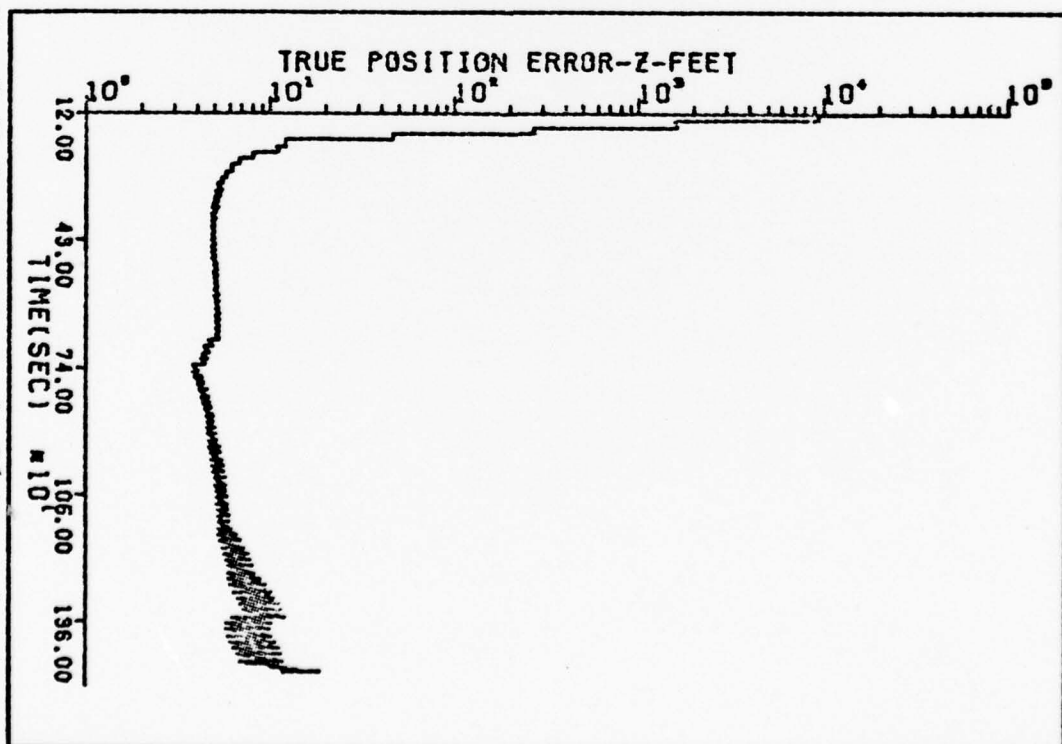


Fig 51 17-St True Error, 15.36 Sec Updt, δx_3

86

Fig 52 17-St Est Error, 15.36 Sec Updt, dx_4

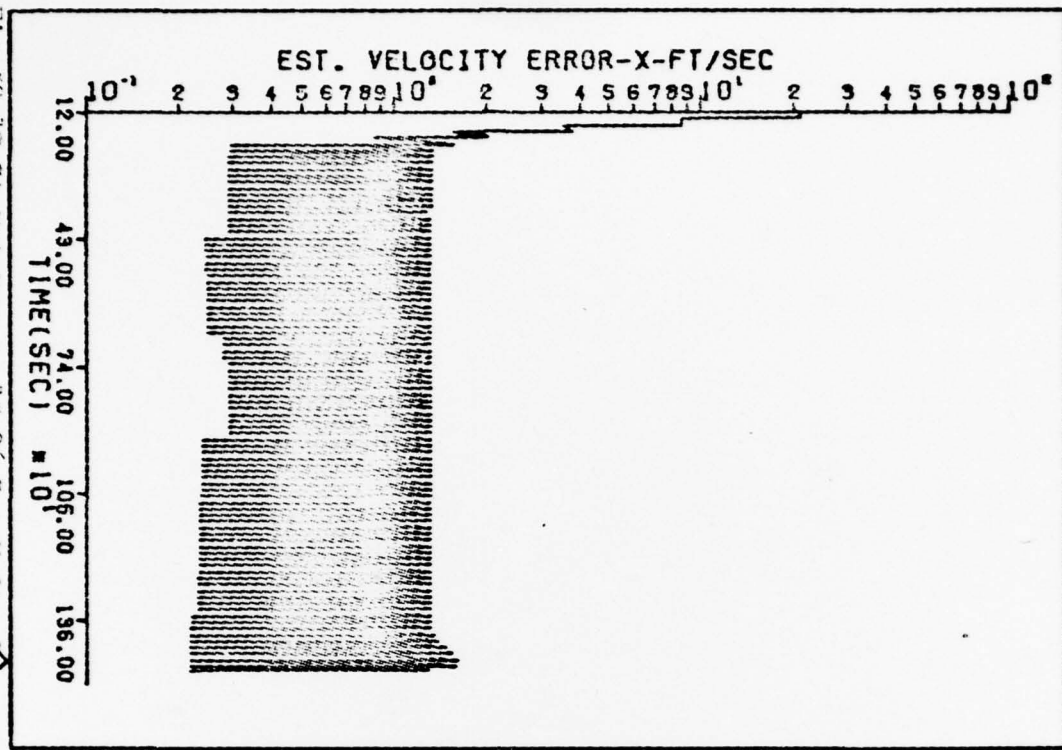
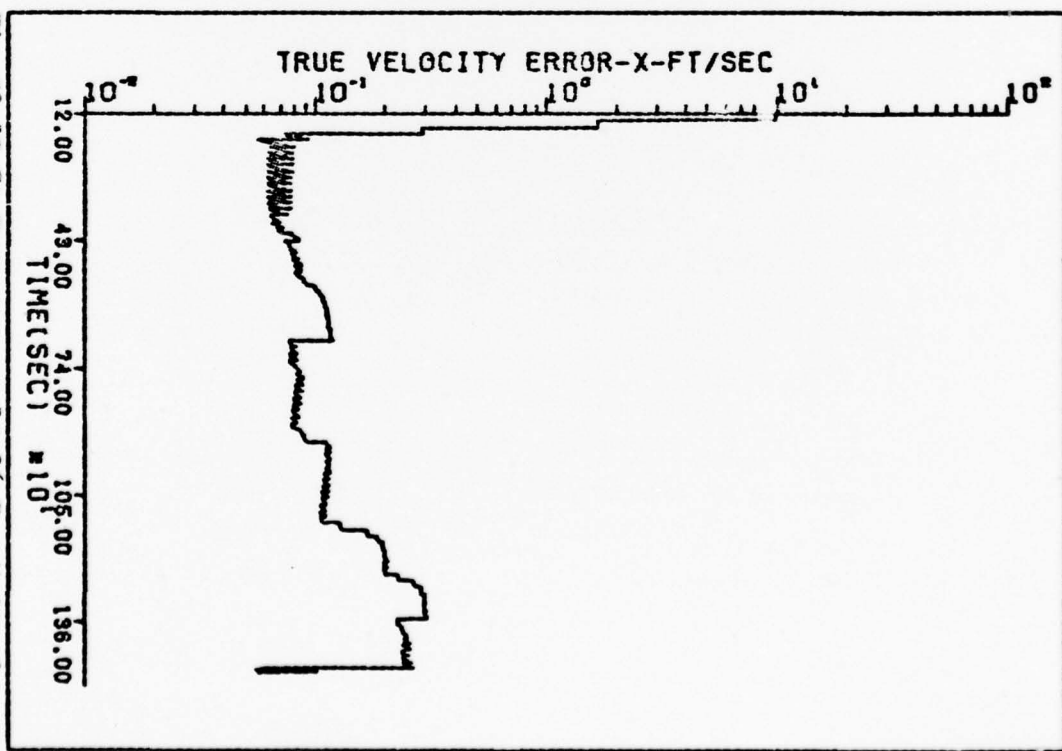


Fig 53 17-St True Error, 15.36 Sec Updt, dx_4



22

Fig 54 17-St Est Error, 15.36 Sec Updt, δx_5

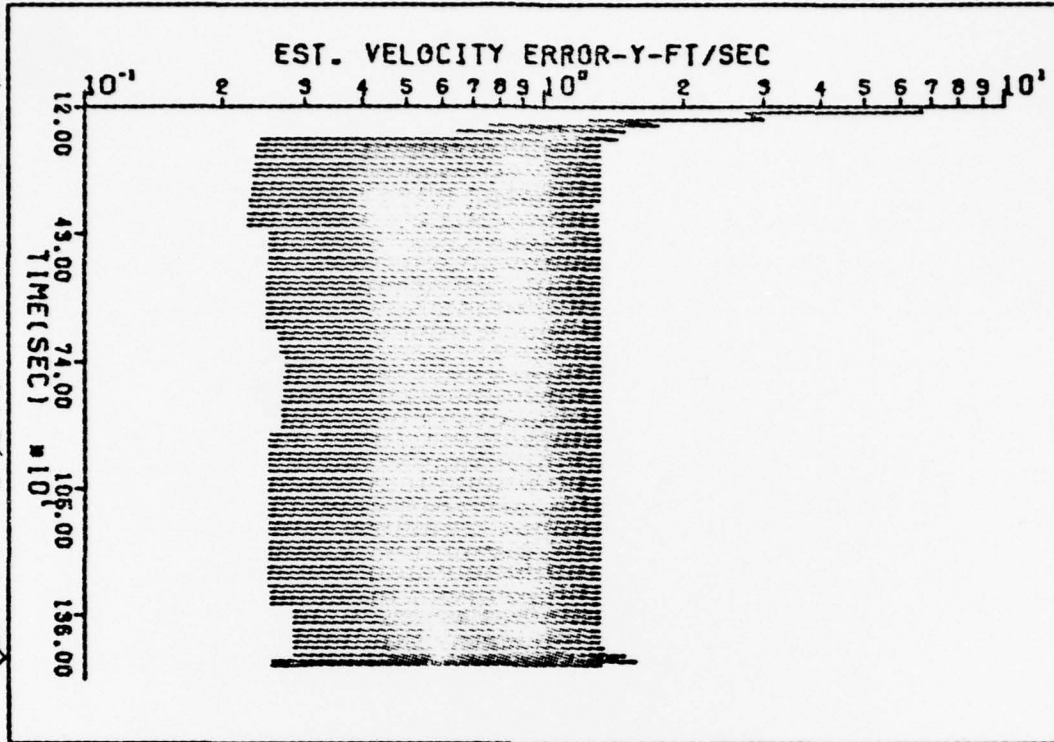


Fig 55 17-St True Error, 15.36 Sec Updt, δx_5

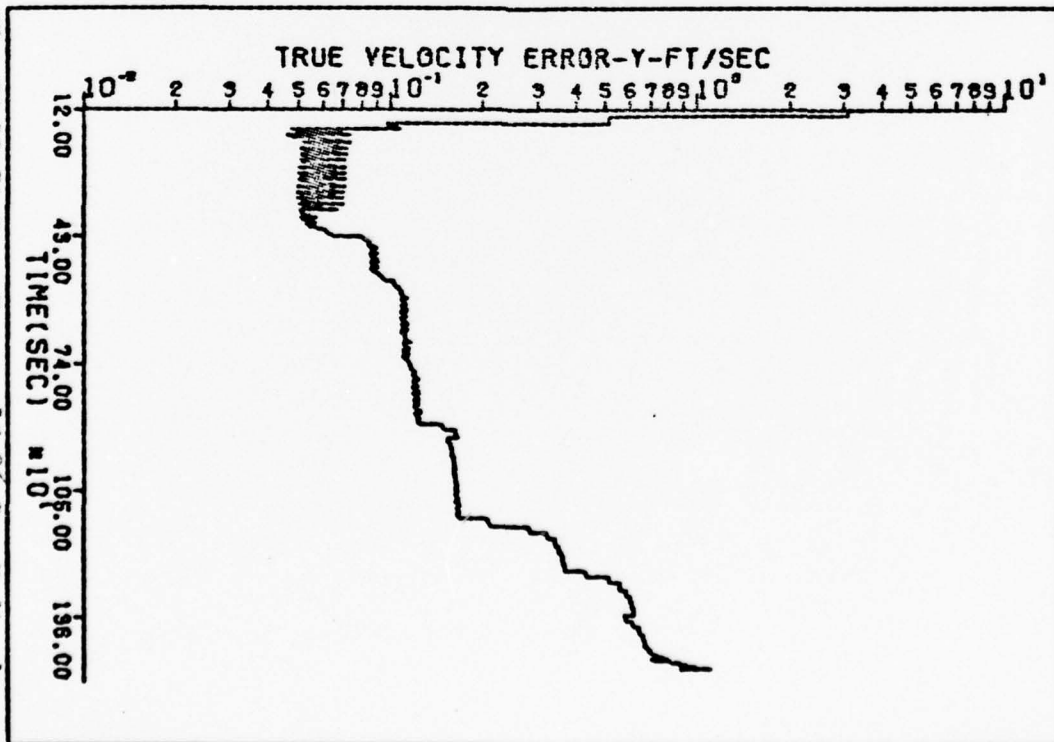


Fig 56 17-St Est Error, 15.36 Sec Updt, dx_6

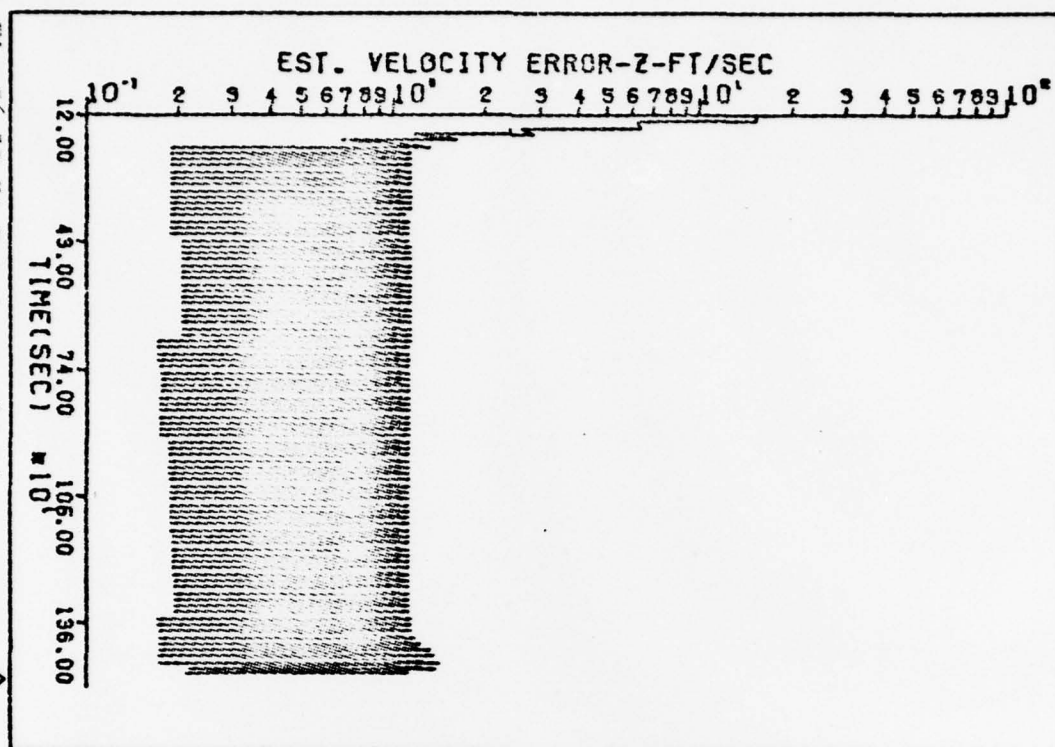


Fig 57 17-St True Error, 15.36 Sec Updt, dx_6

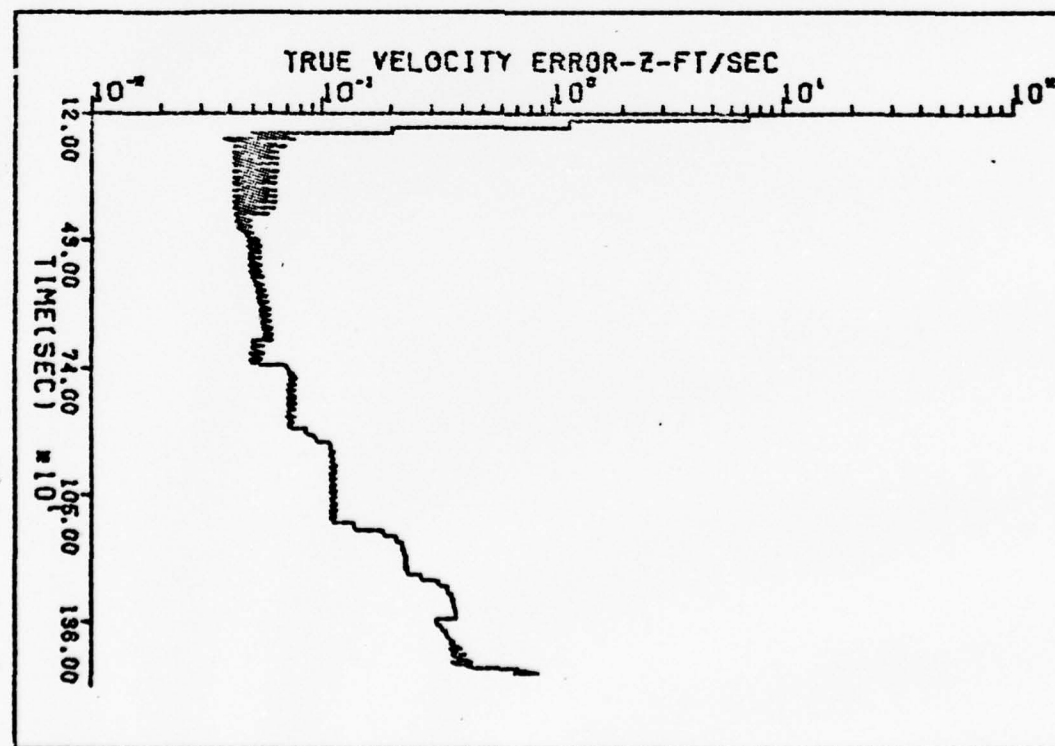


Fig 58 17-St Est Error, 15.36 Sec Updt, dx_g

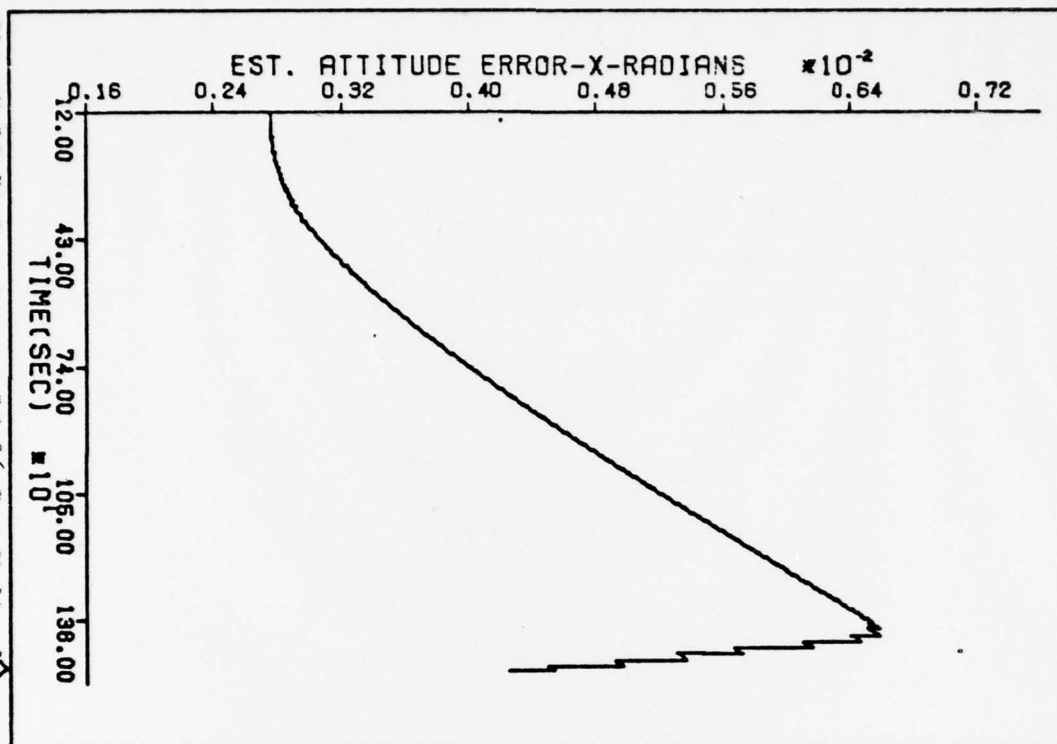
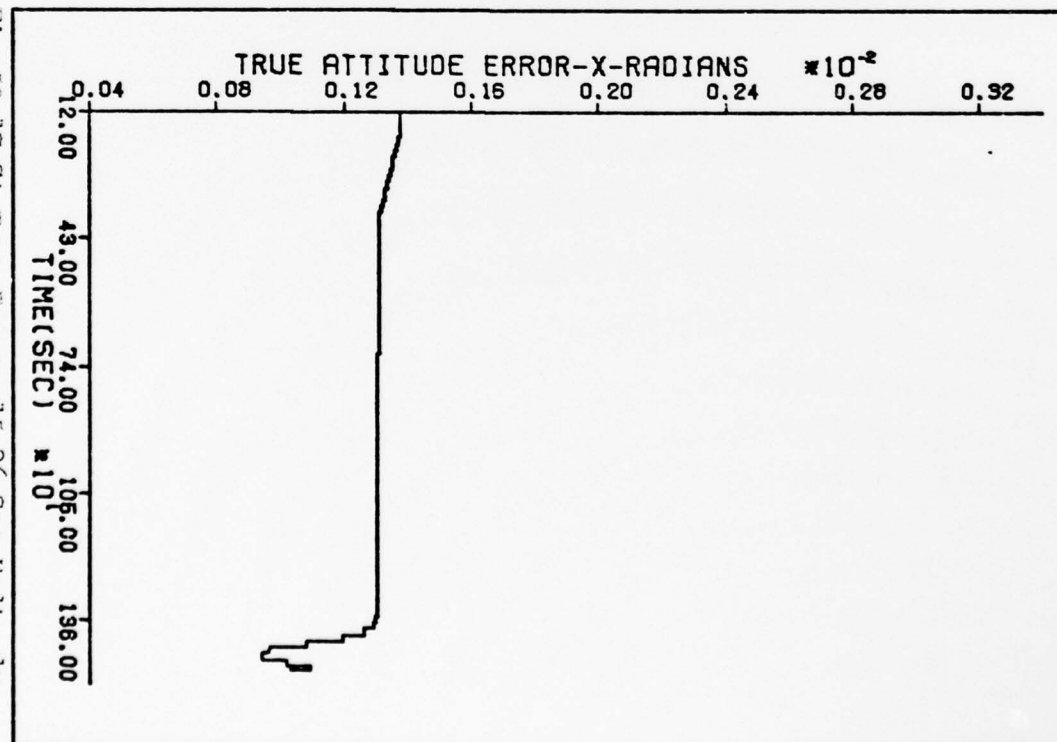
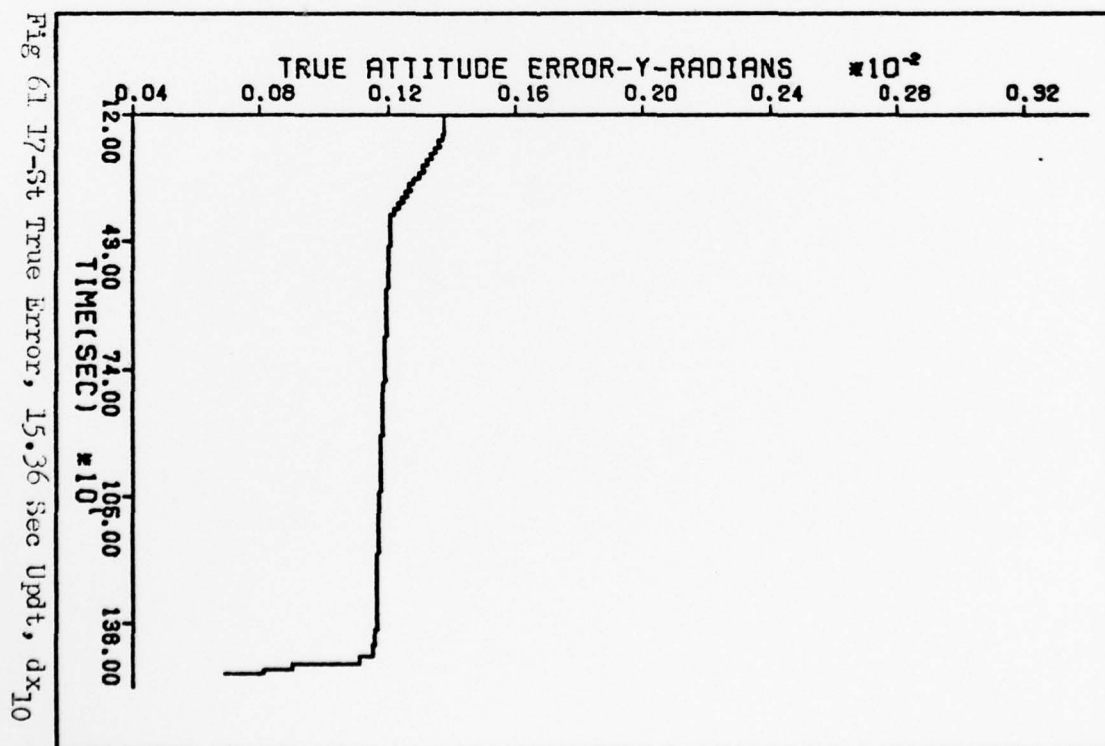
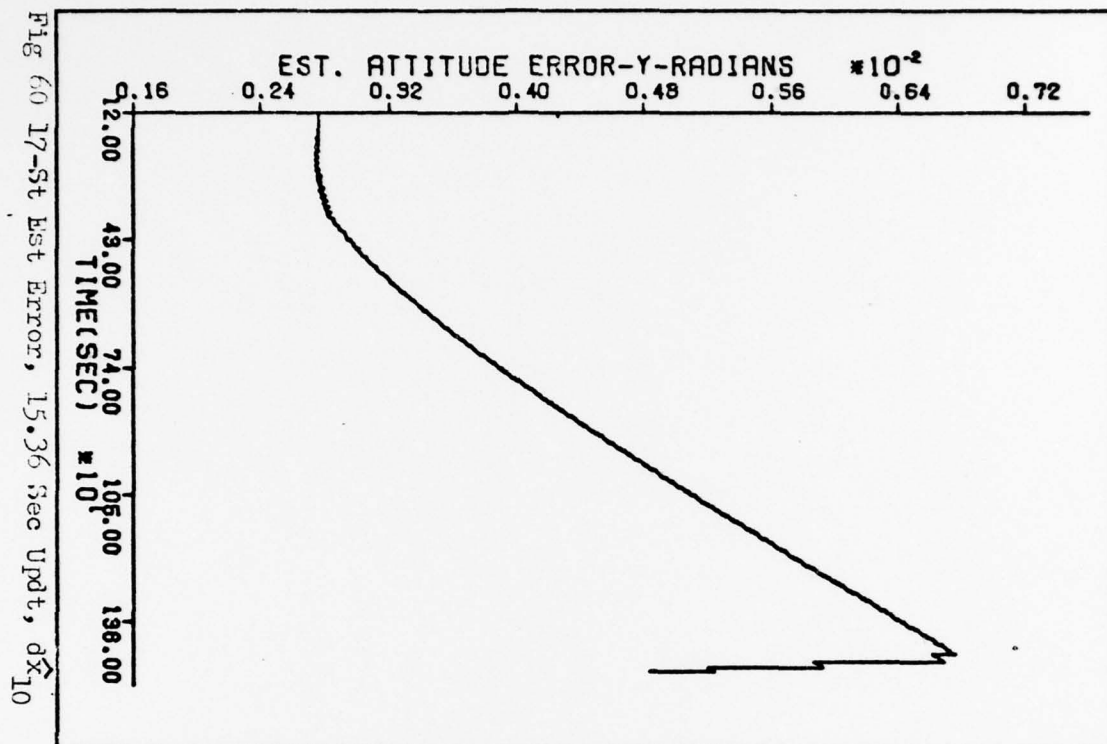
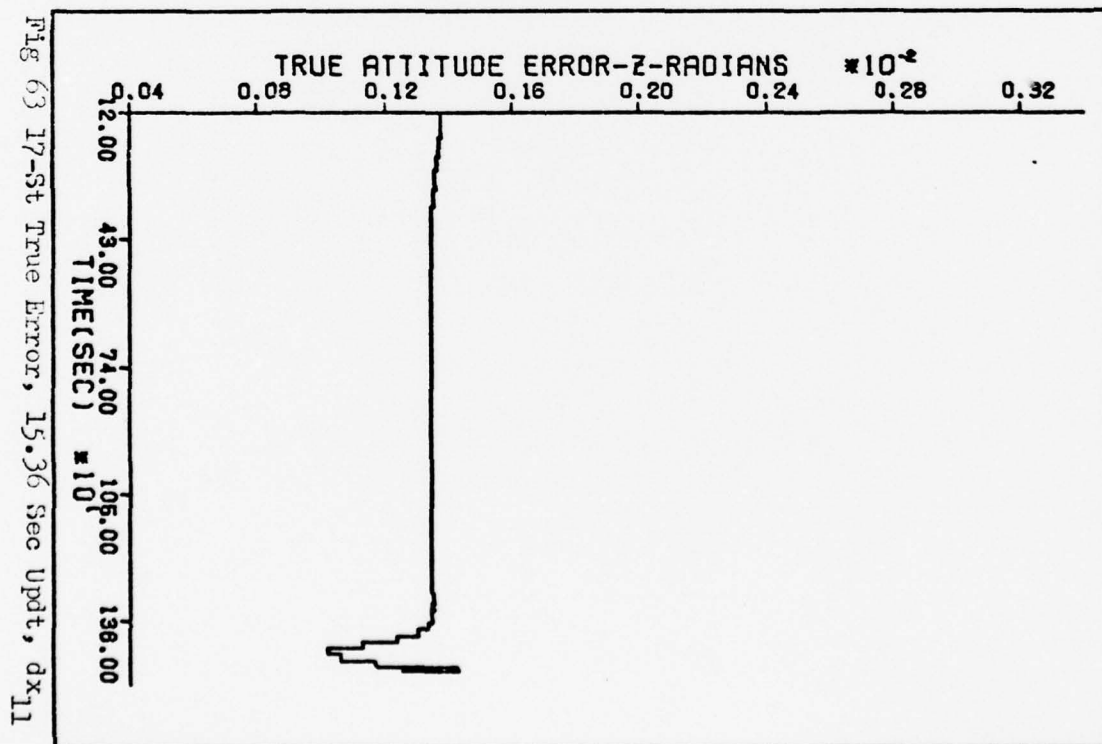
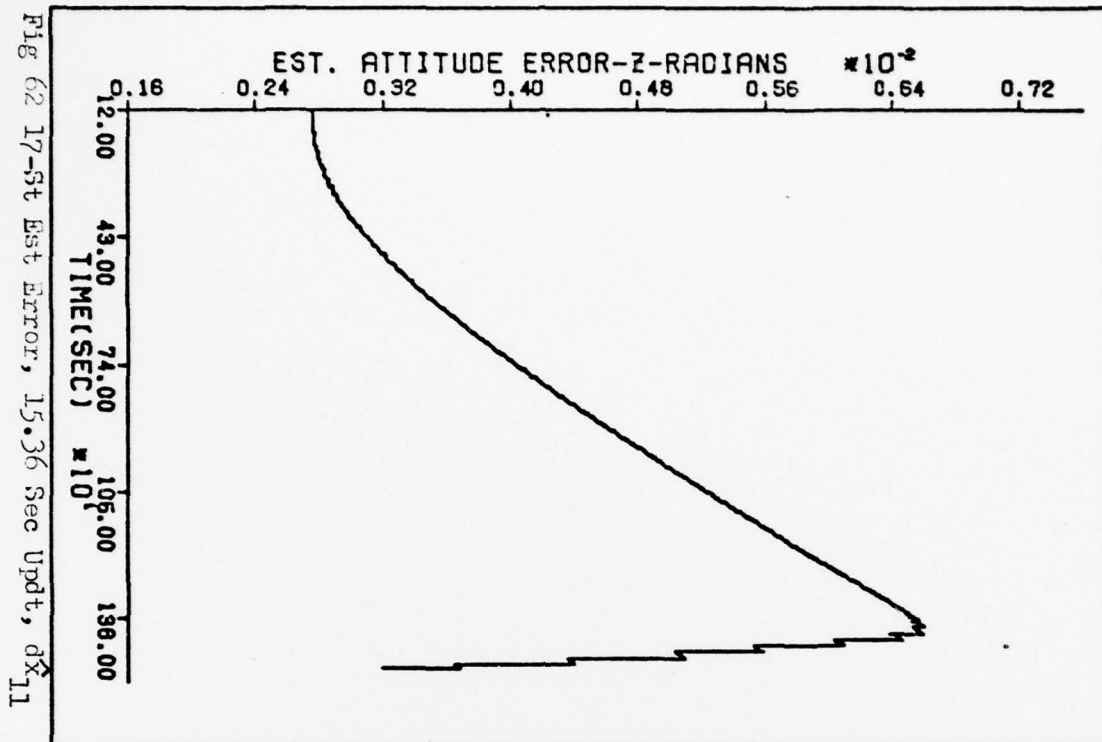


Fig 59 17-St True Error, 15.36 Sec Updt, dx_g





DATA



11-State Filter, Pre-Blackout

The following plots depict the performance of the 11-State Filter design for the pre-blackout portion of the simulation. Data points are the same as for the 17-State Filter. The measurement update period was 30.72 seconds.

XXX

Fig 64 11-St Est Error, Pre-Blackout, δx_7

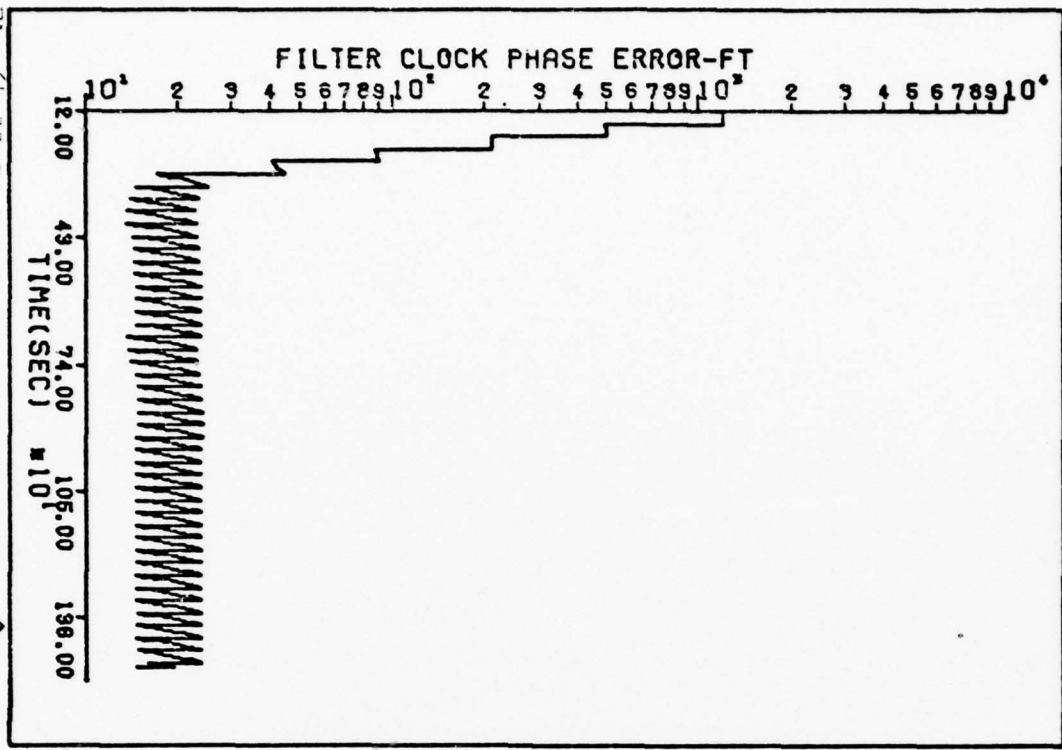
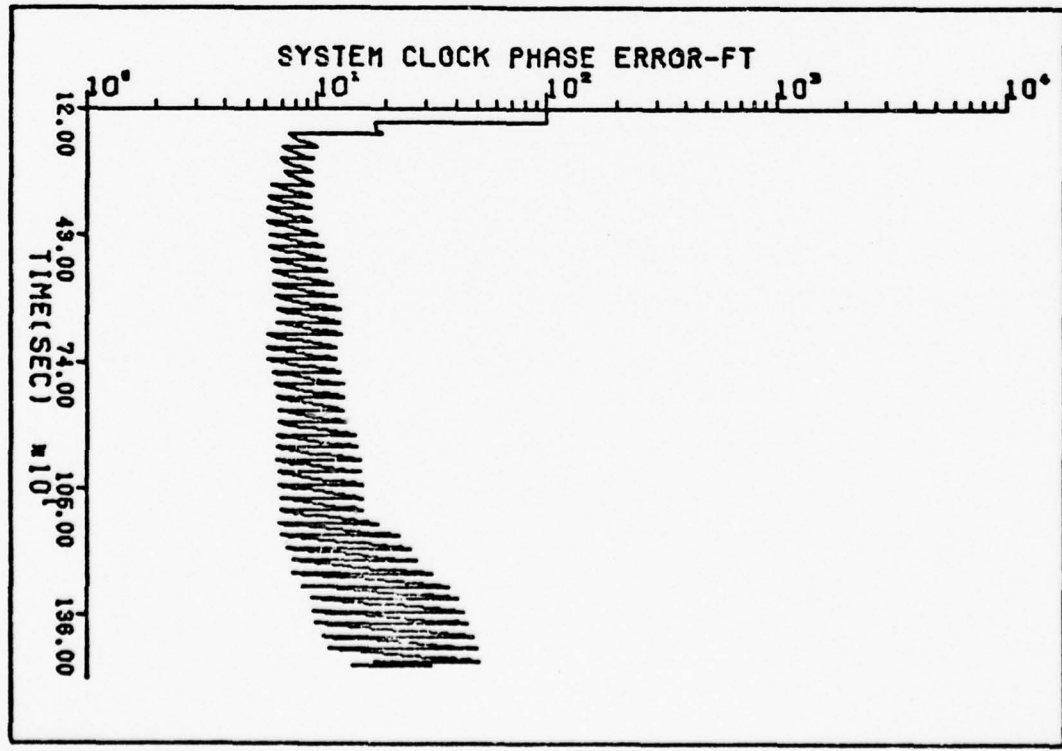


Fig 65 11-St True Error, Pre-Blackout, δx_7



XX

Fig 66 11-St Est Error, Pre-Blackout, dxg

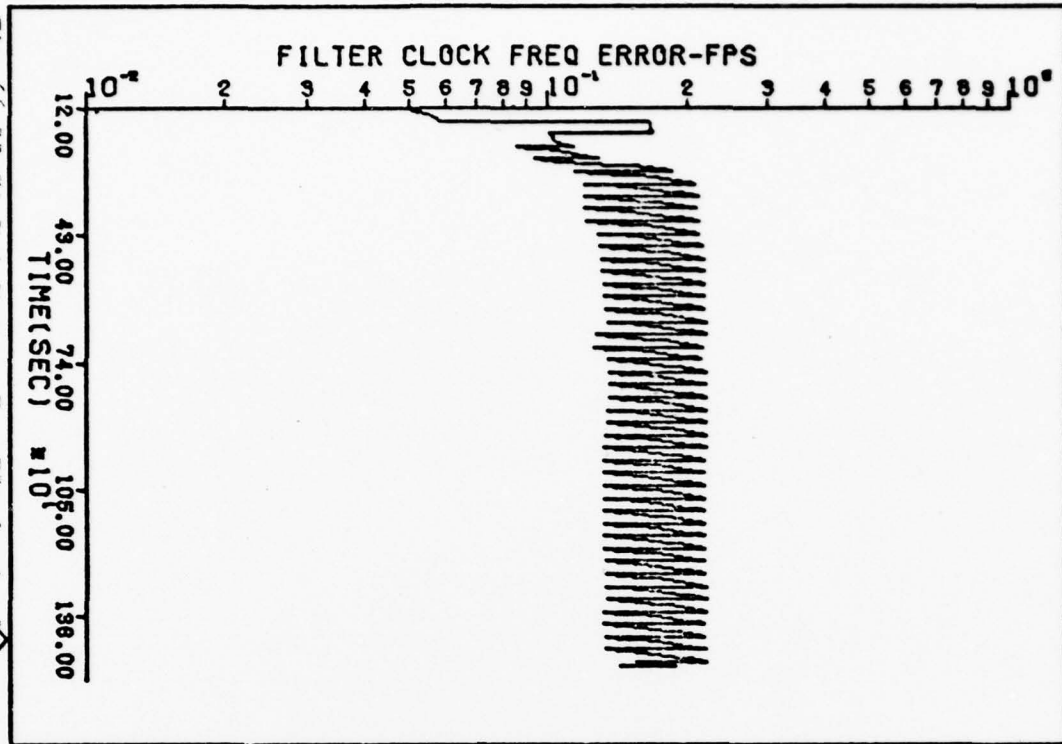
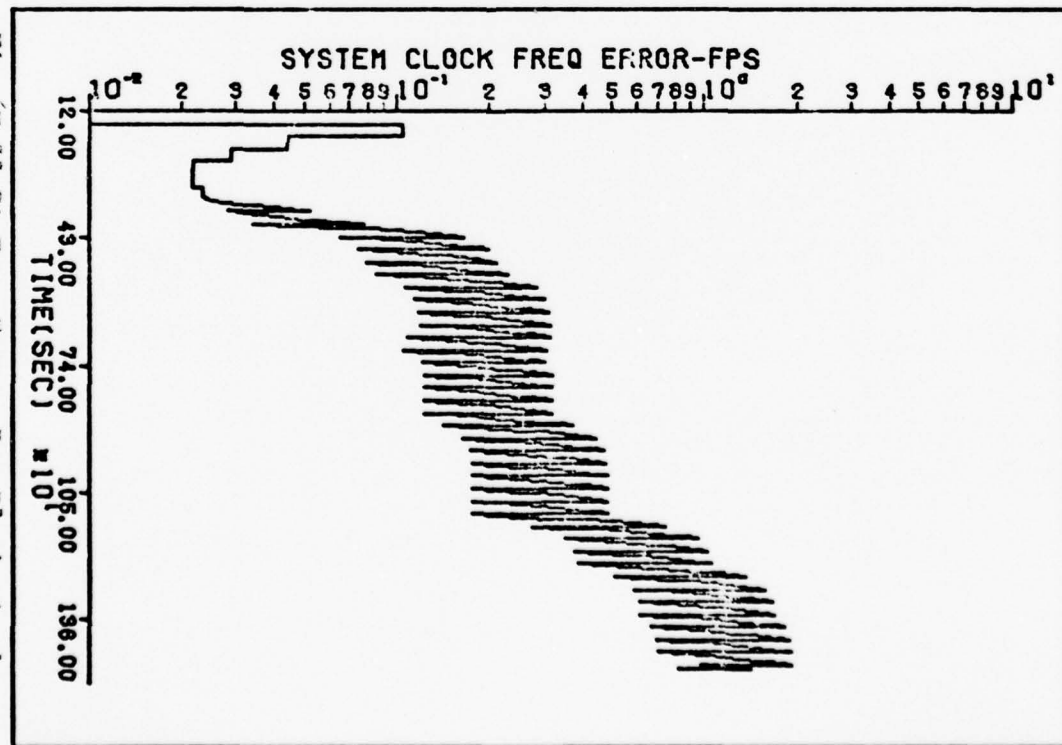
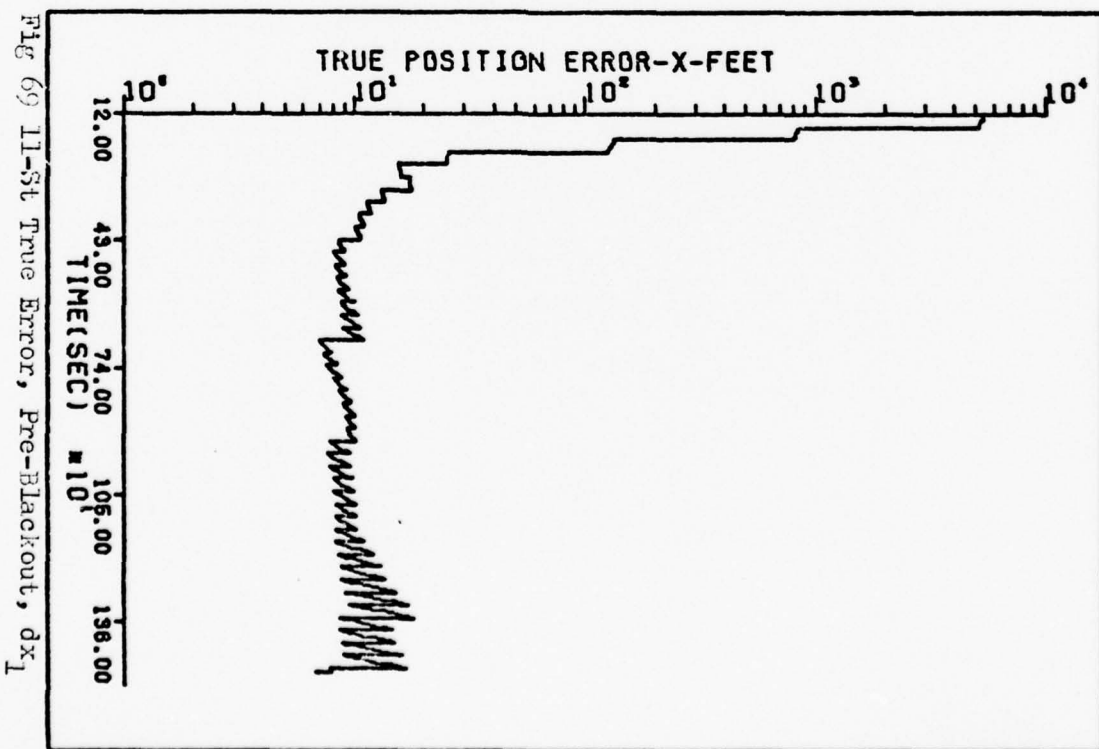
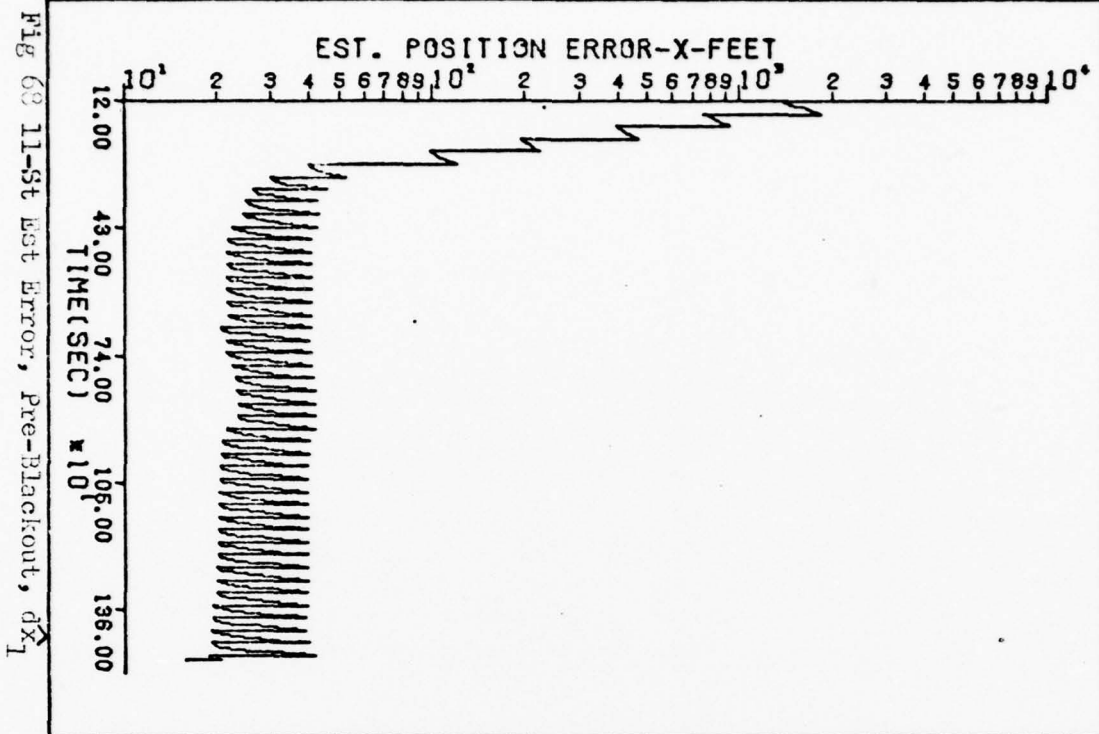


Fig 67 11-St True Error, Pre-Blackout, dxg



XX



~~105~~

Fig 70 11-St Est Error, Pre-Blackout, dx_2

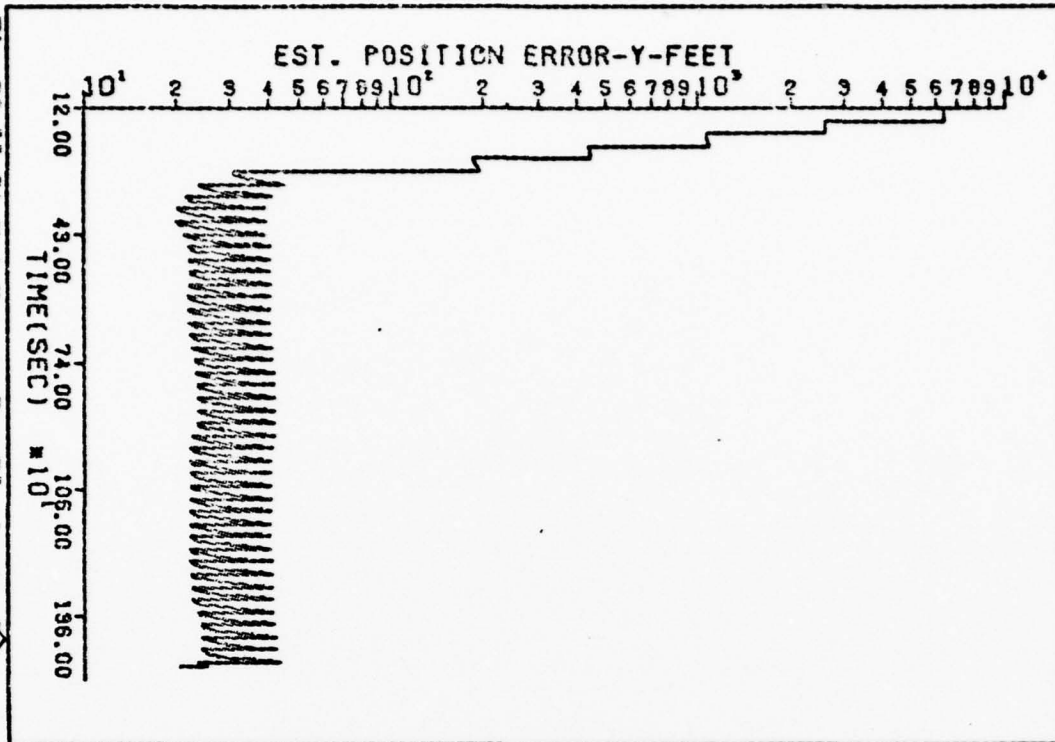
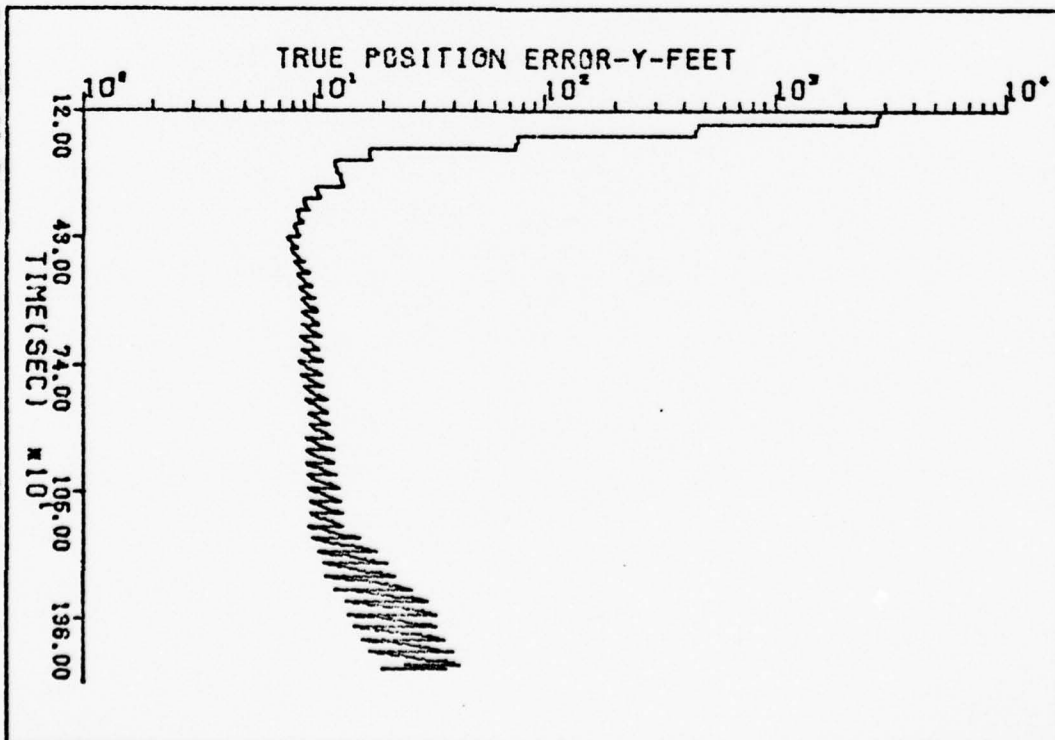
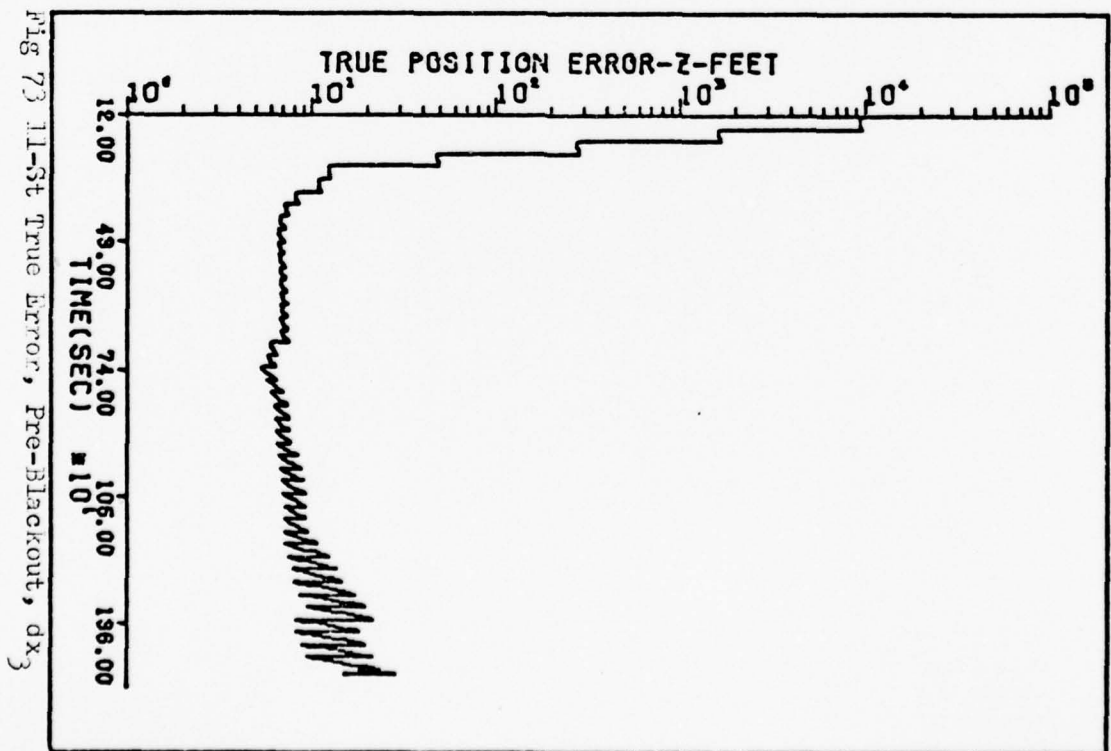
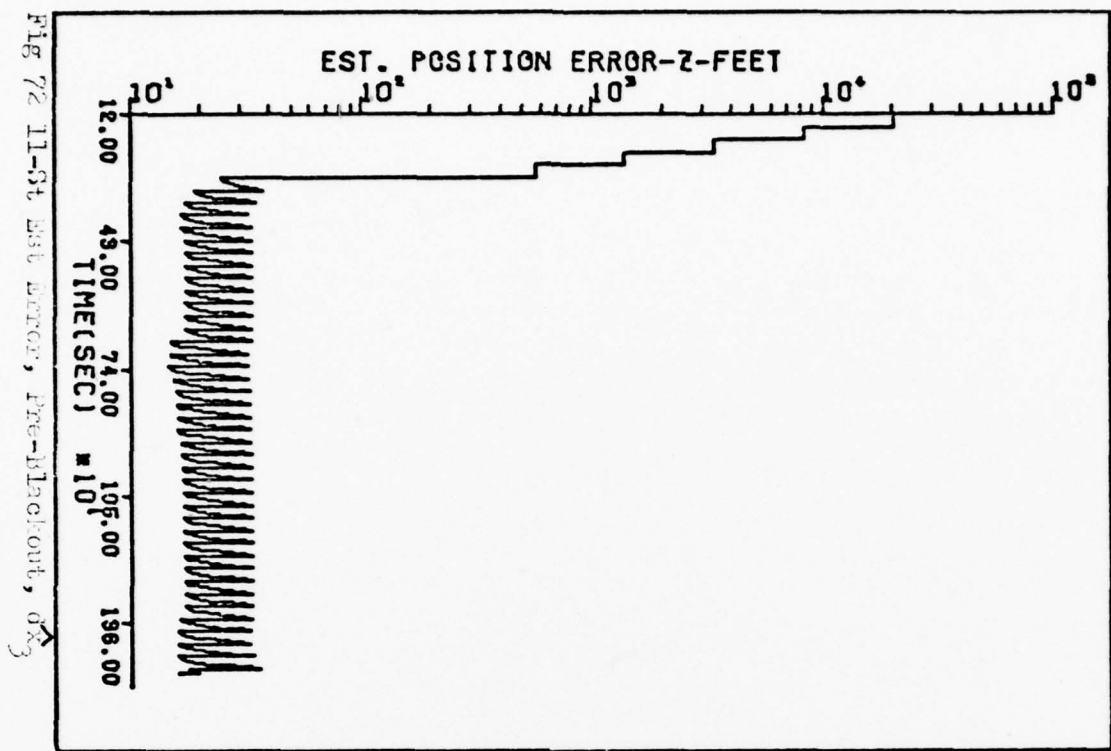


Fig 71 11-St True Error, Pre-Blackout, dx_2



dx



400

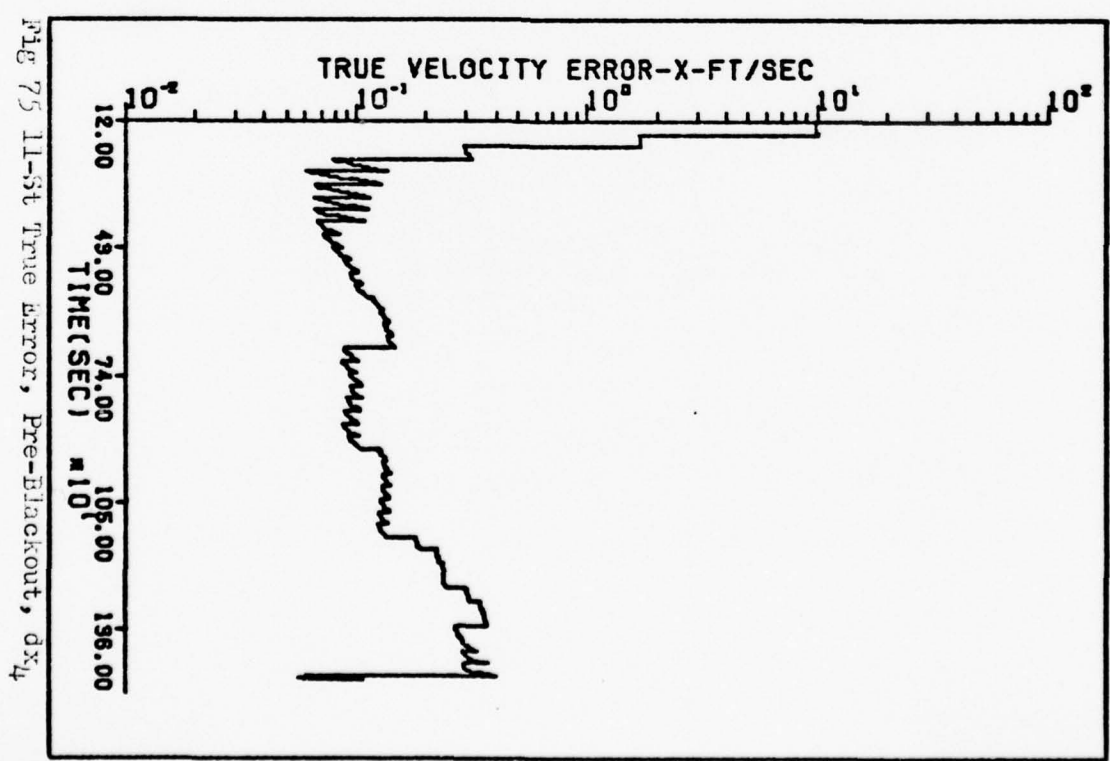
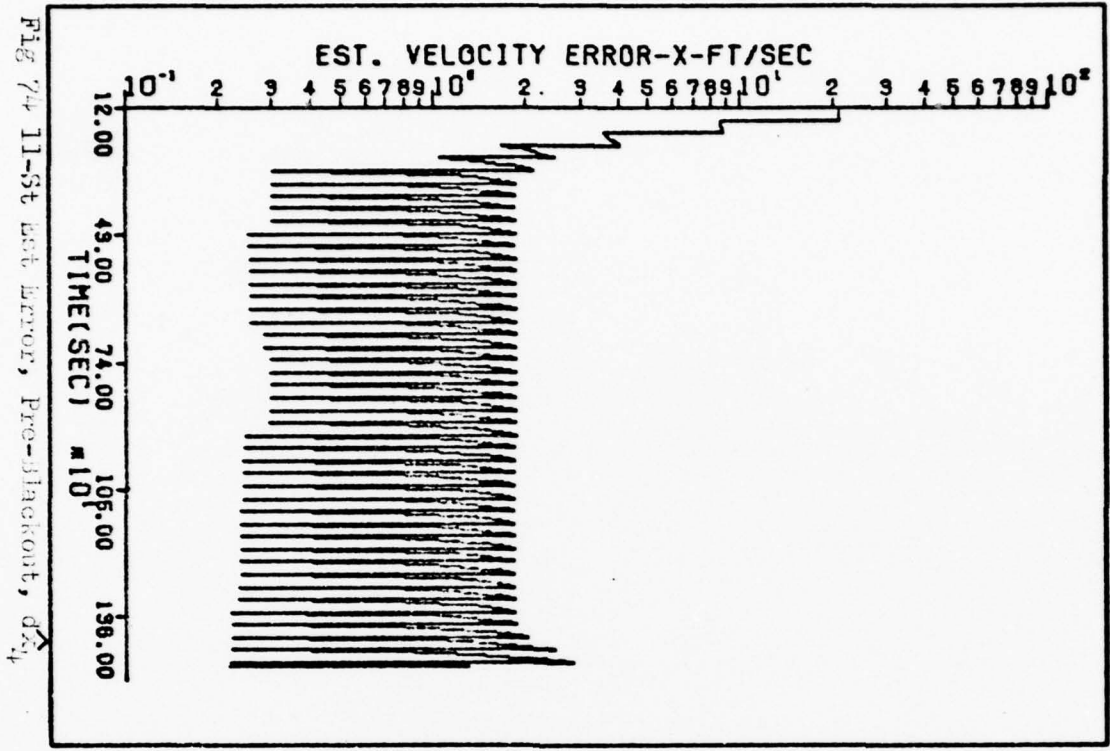


Fig 76 11-St Est Error, Pre-Blackout, dx_5

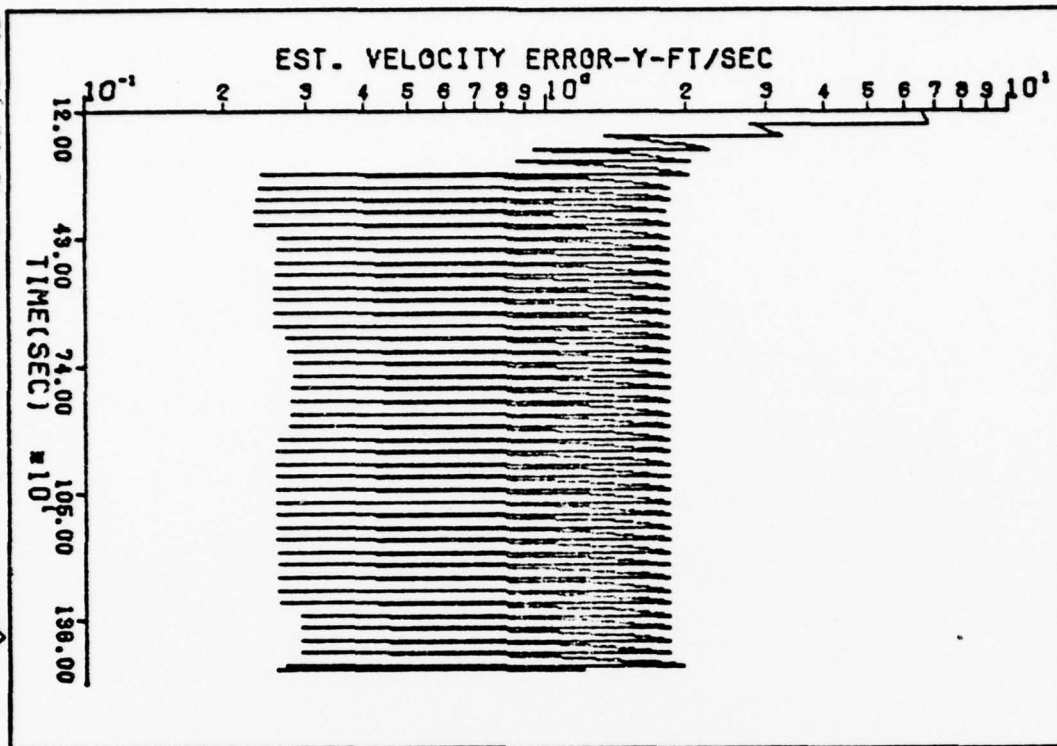
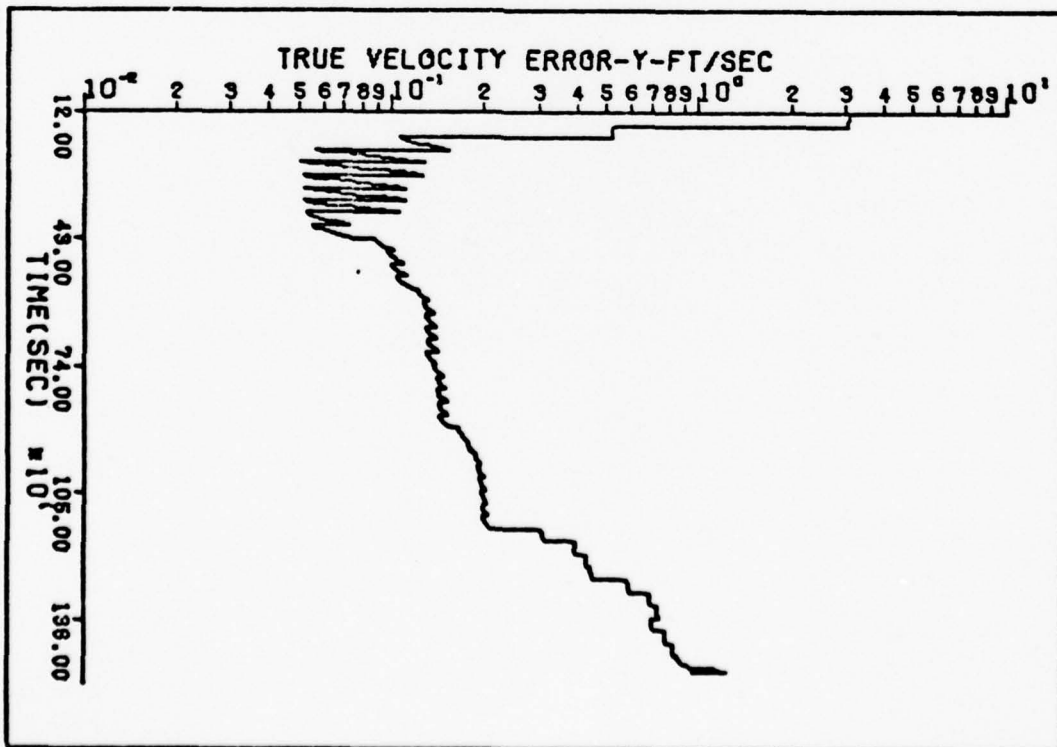
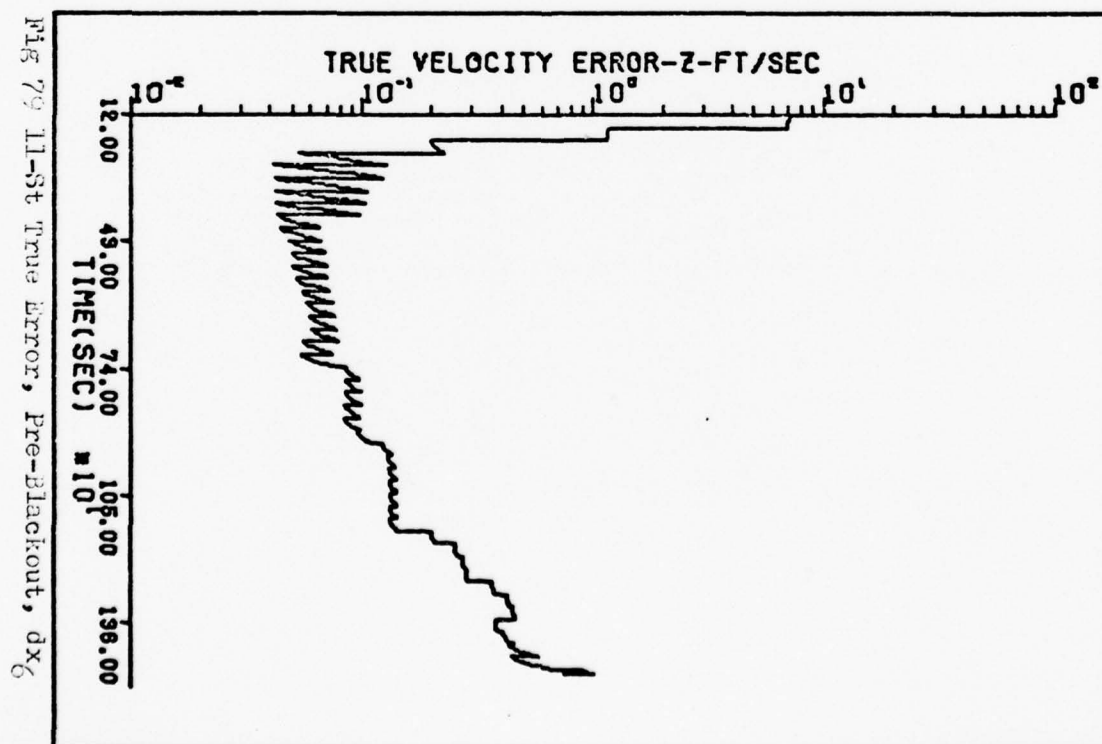
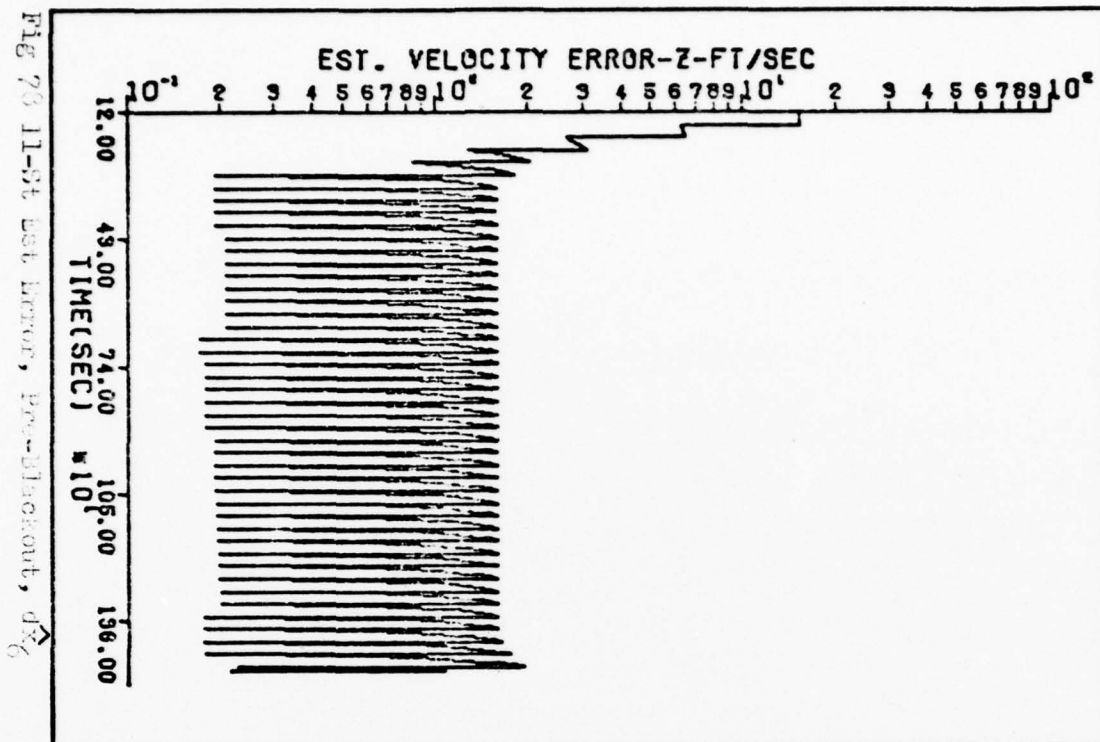


Fig 77 11-St True Error, Pre-Blackout, dx_5





XXX

Fig 80 11-St Est Error, Pre-Blackout, dx_g

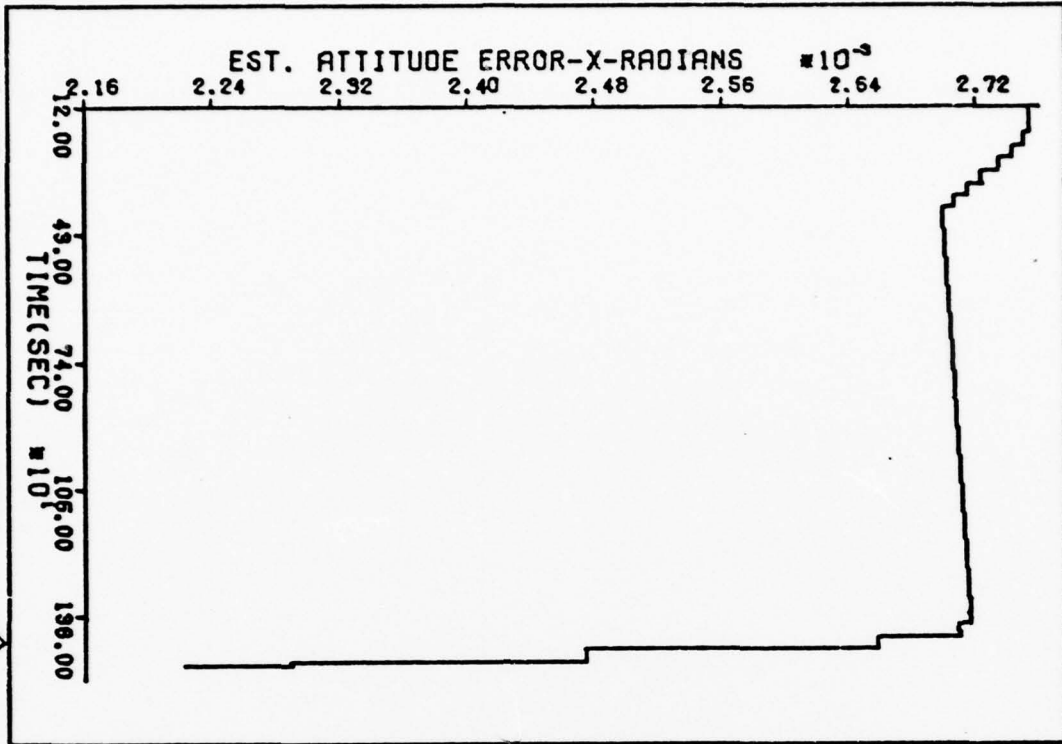


Fig 81 11-St True Error, Pre-Blackout, dx_g

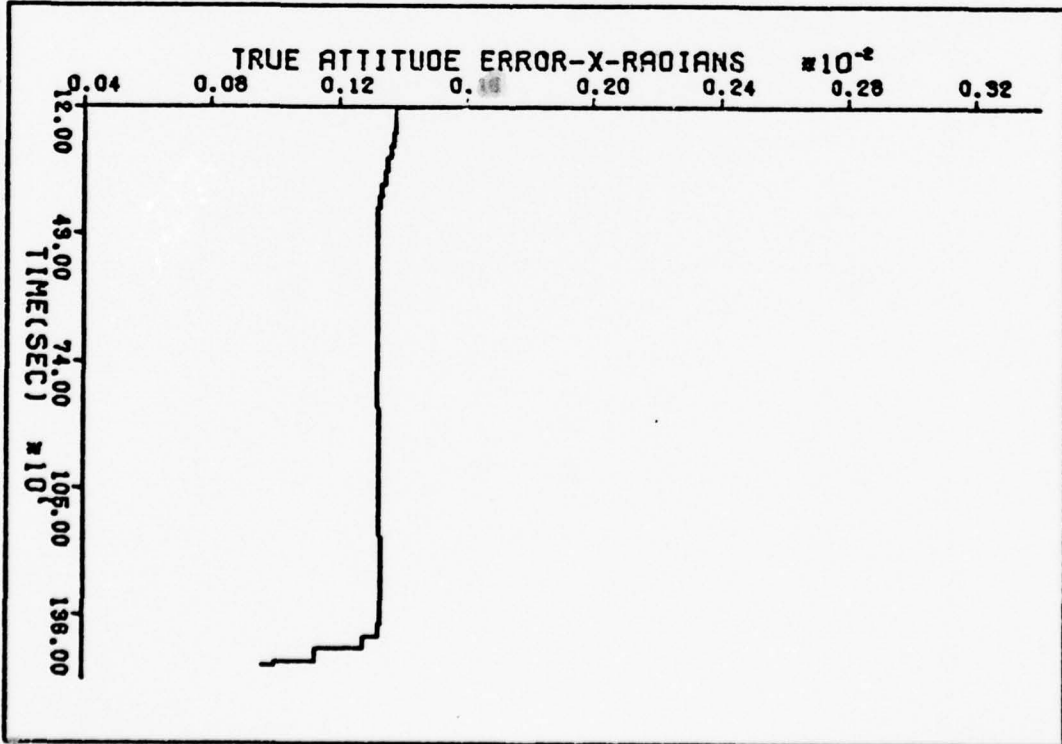


Fig 82 11-St Est Error, Pre-Blackout, δx_{10}

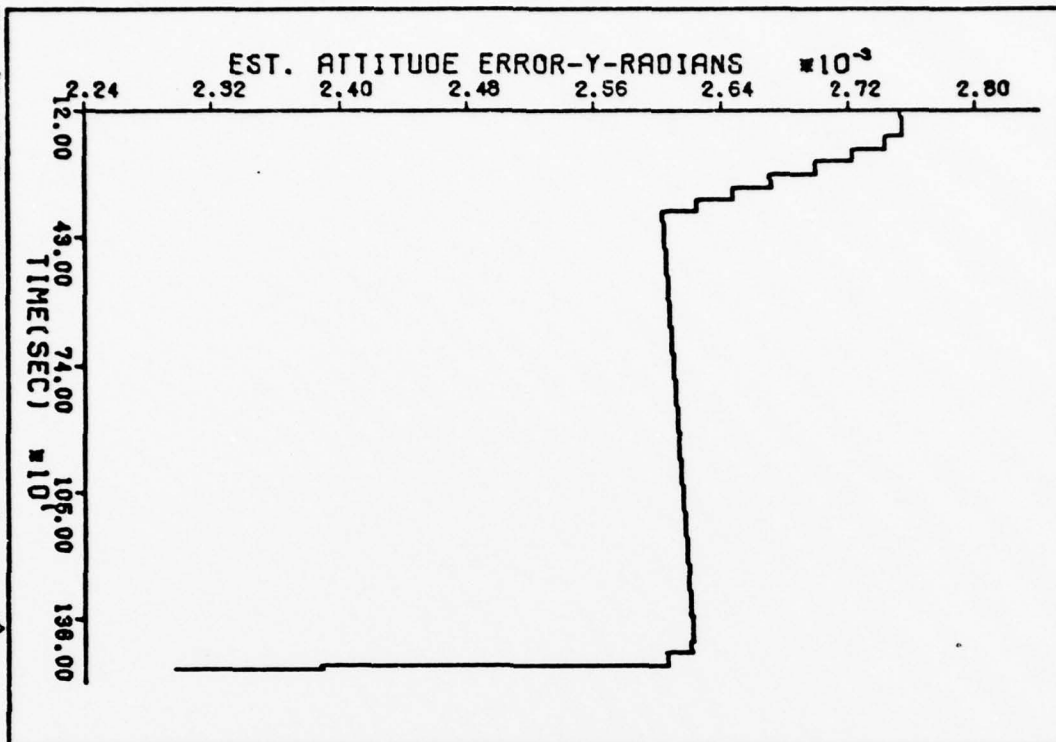
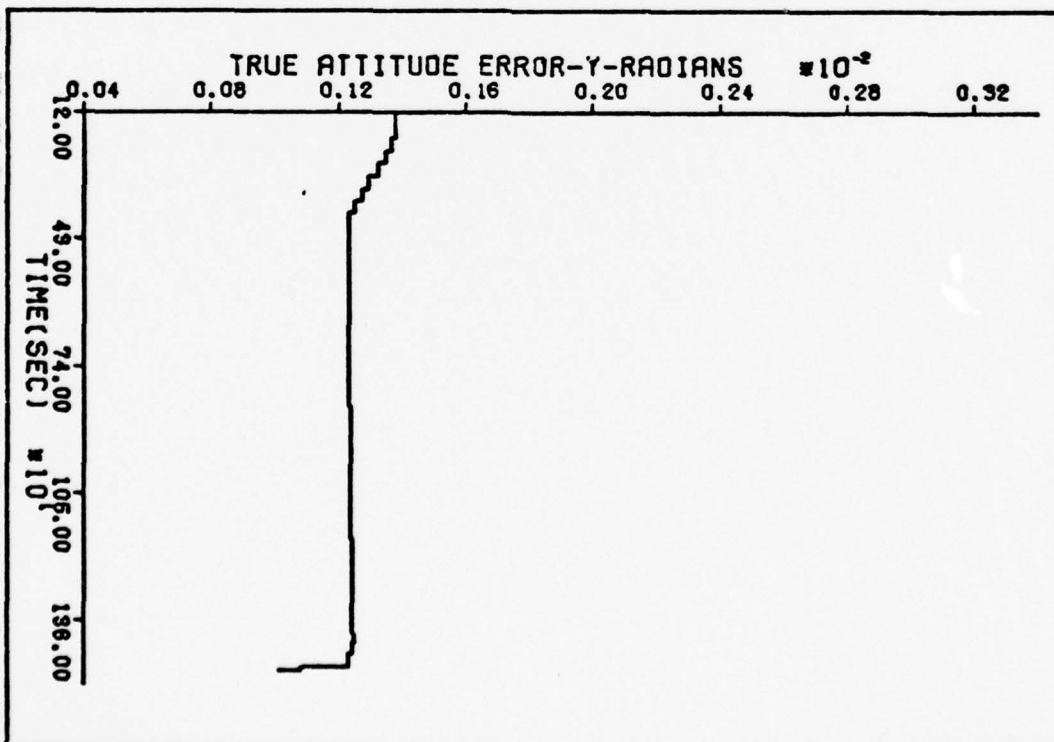


Fig 83 11-St True Error, Pre-Blackout, δx_{10}



XXX

Fig 84 II-St Est Error, Pre-Blackout, δx_{II}

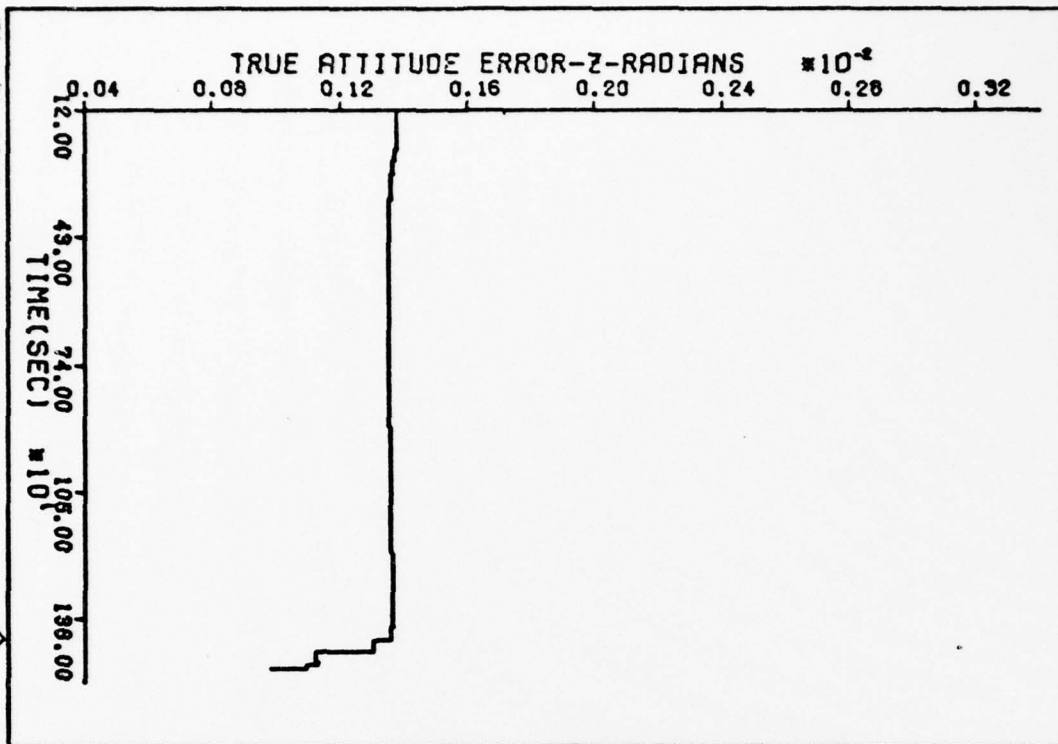
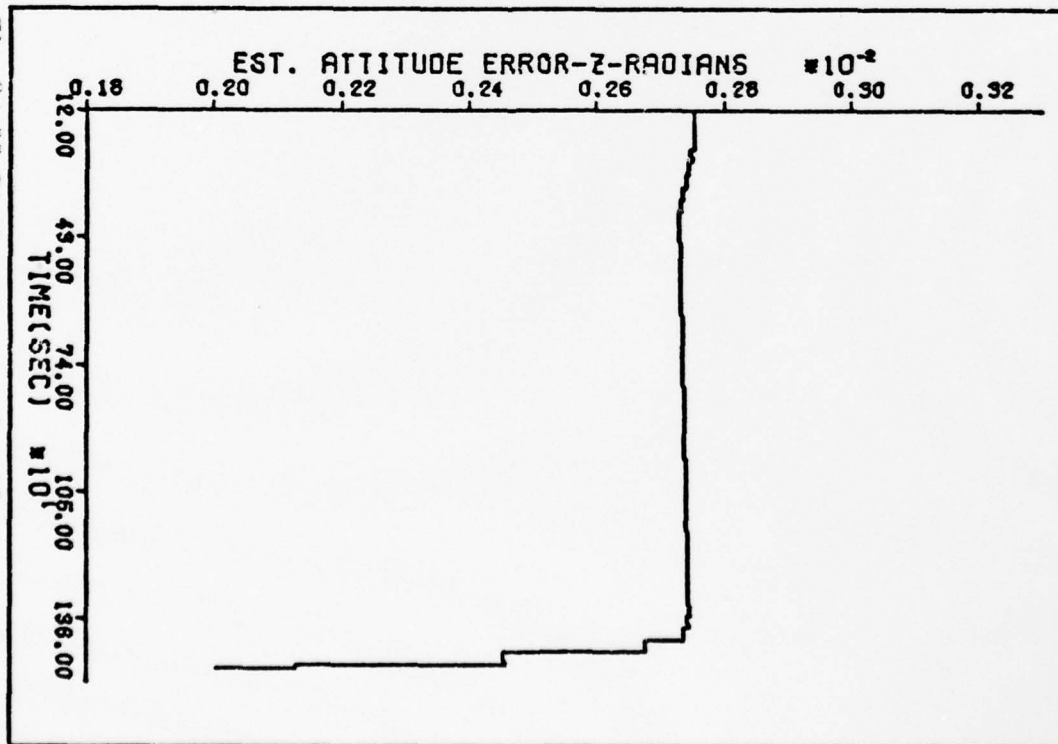


Fig 85 II-St True Error, Pre-Blackout, δx_{II}



11-State Filter, Post-Blackout

The performance of the 11-State Filter for the post-blackout portion of the simulation is plotted in this section. Initial data was taken at 21. seconds and final data was taken at 2704. seconds. The measurement update period was 30.72 seconds.

100

Fig 86 11-St Est Error, Post-Blackout, dx_7

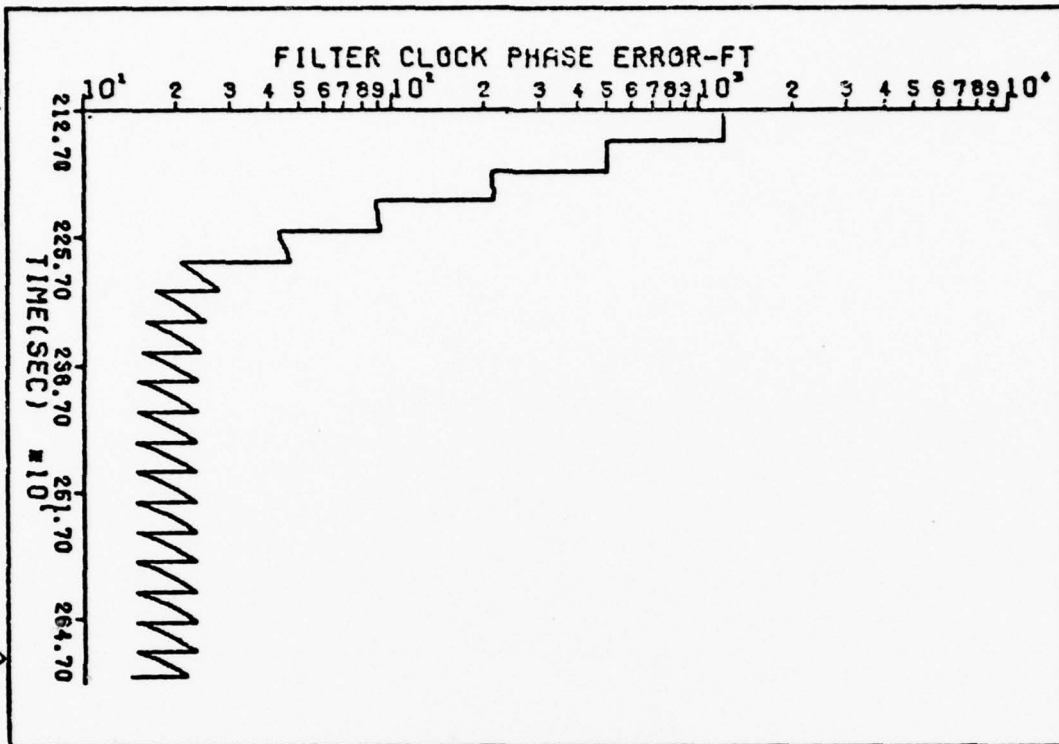
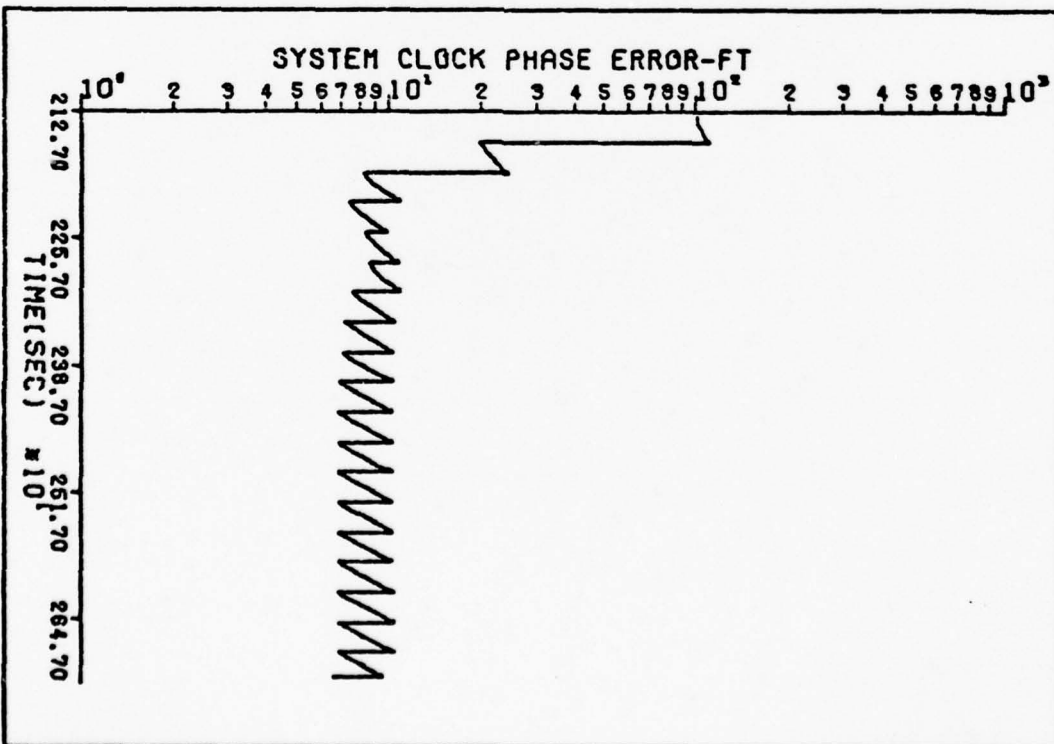
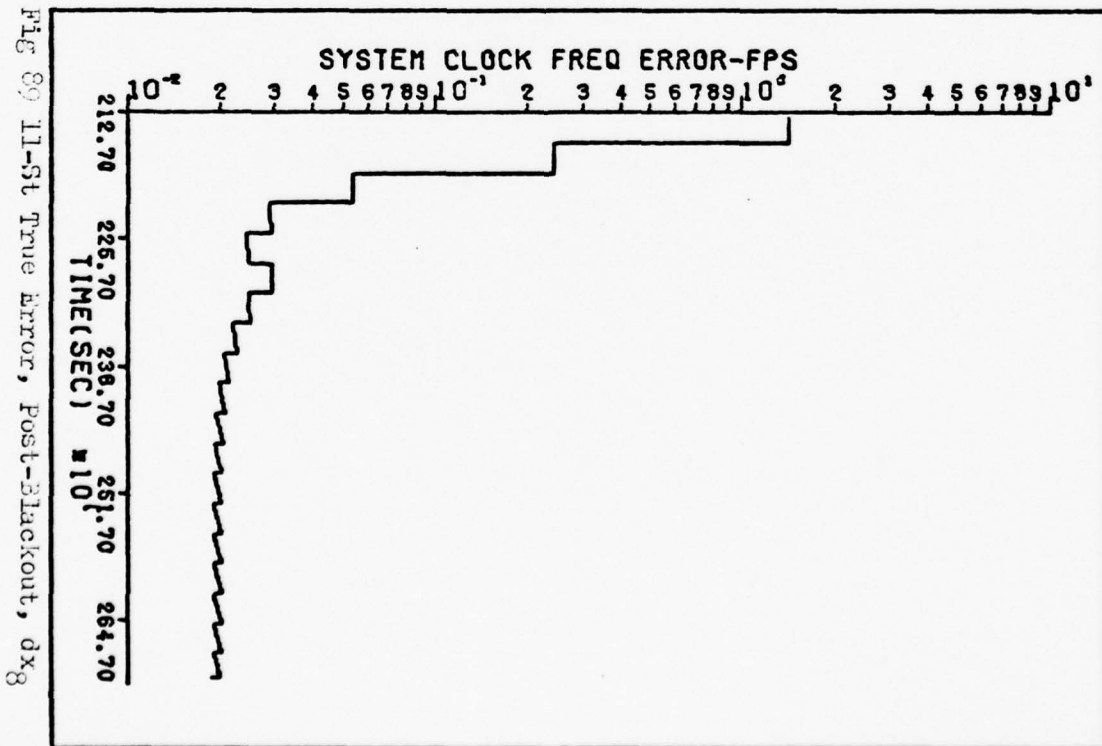
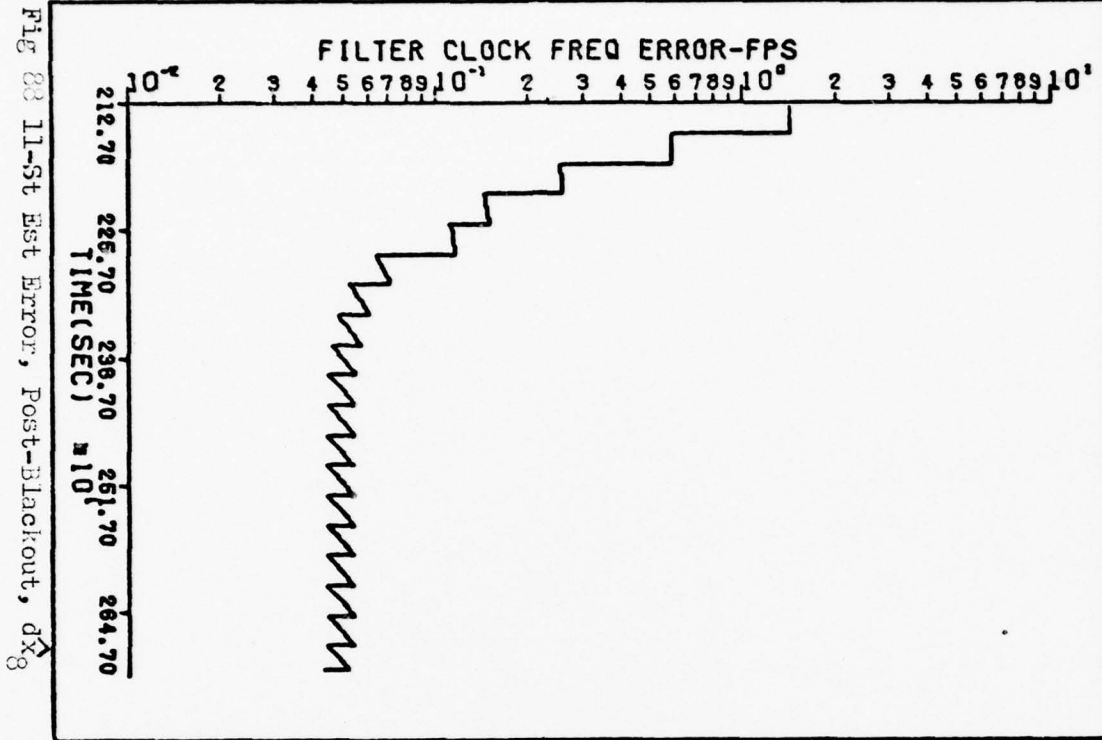


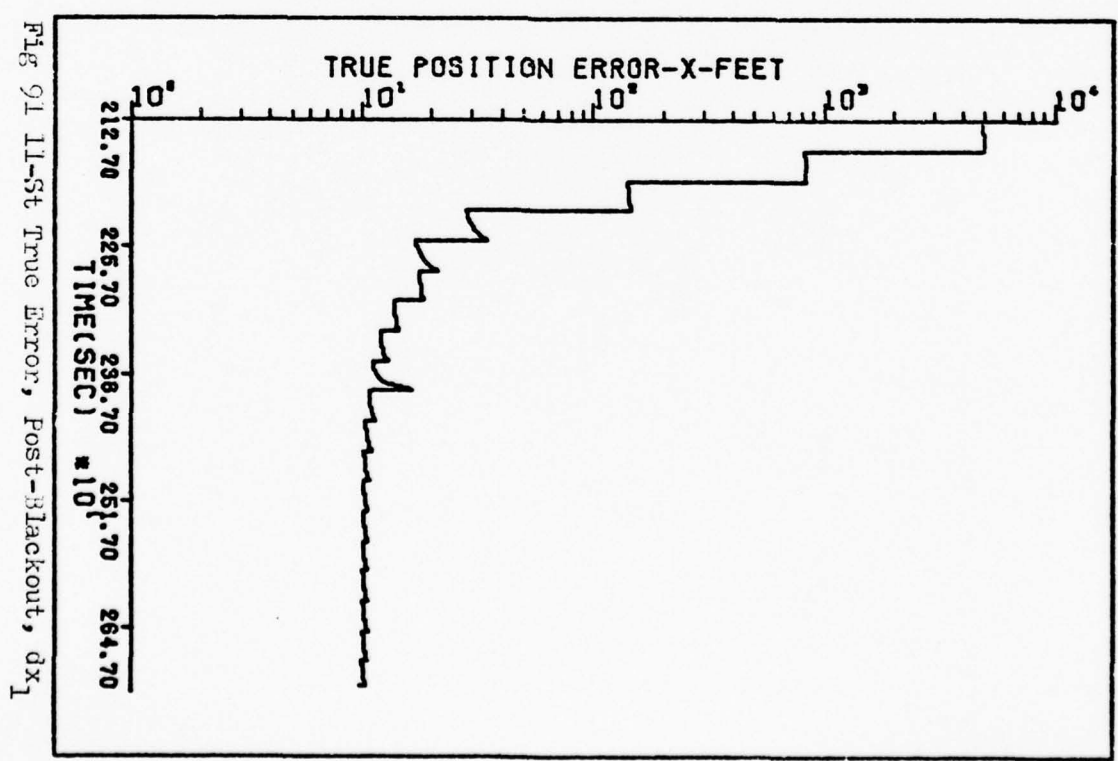
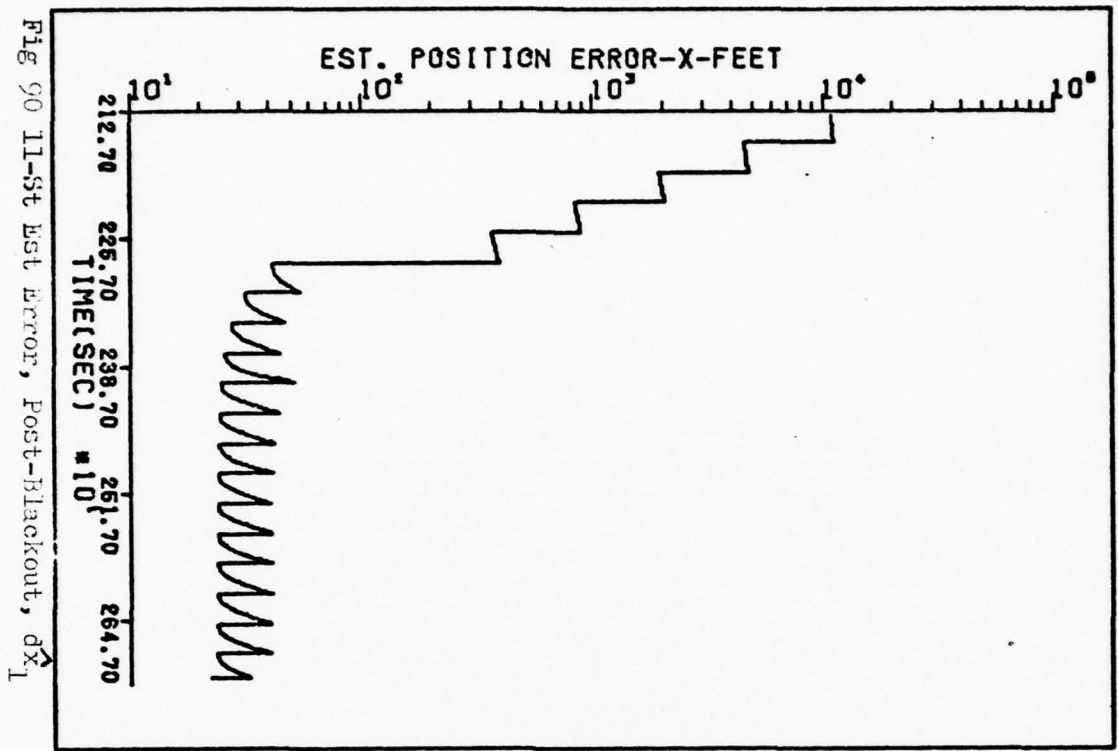
Fig 87 11-St True Error, Post-Blackout, dx_7



XXX



XXX



117

Fig 92 11-St Est Error, Post-Blackout, \hat{dx}_2

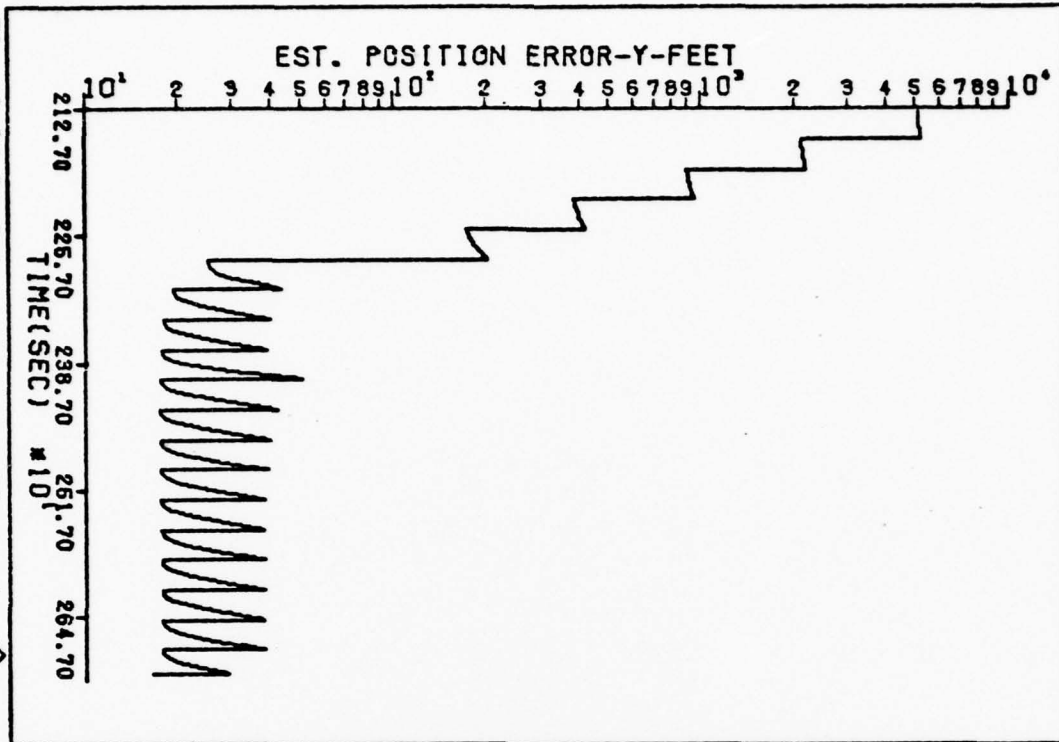
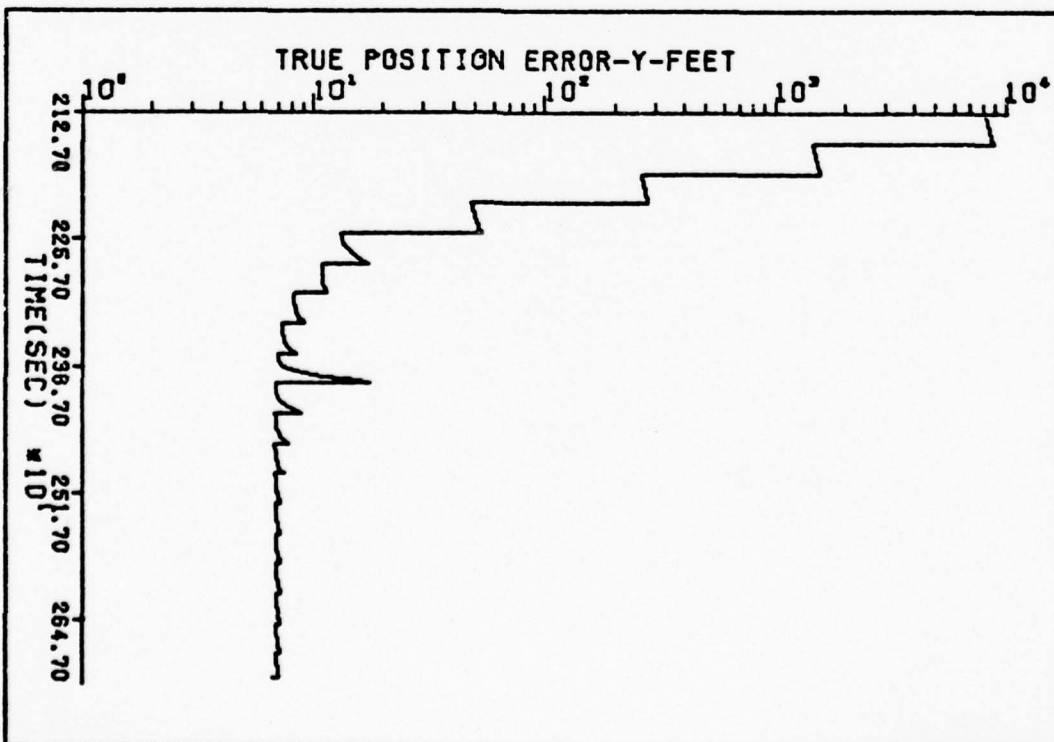


Fig 93 11-St True Error, Post-Blackout, dx_2



XXX

Fig 94 11-St Est Error, Post-Blackout, \hat{dx}_j

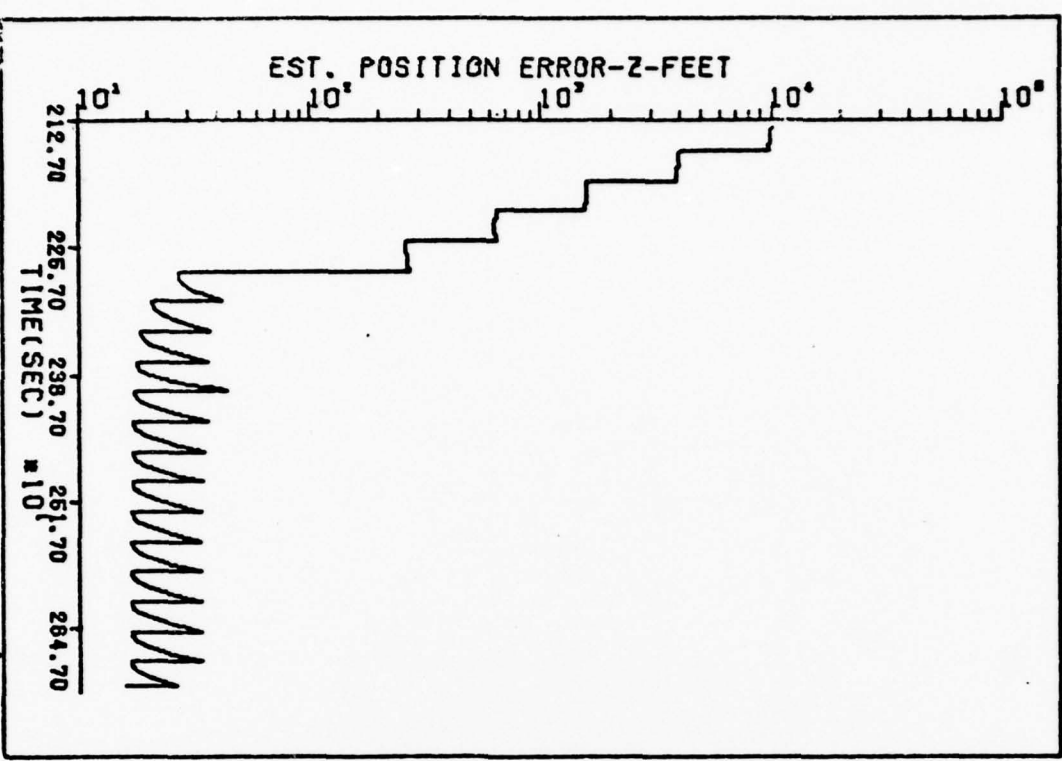
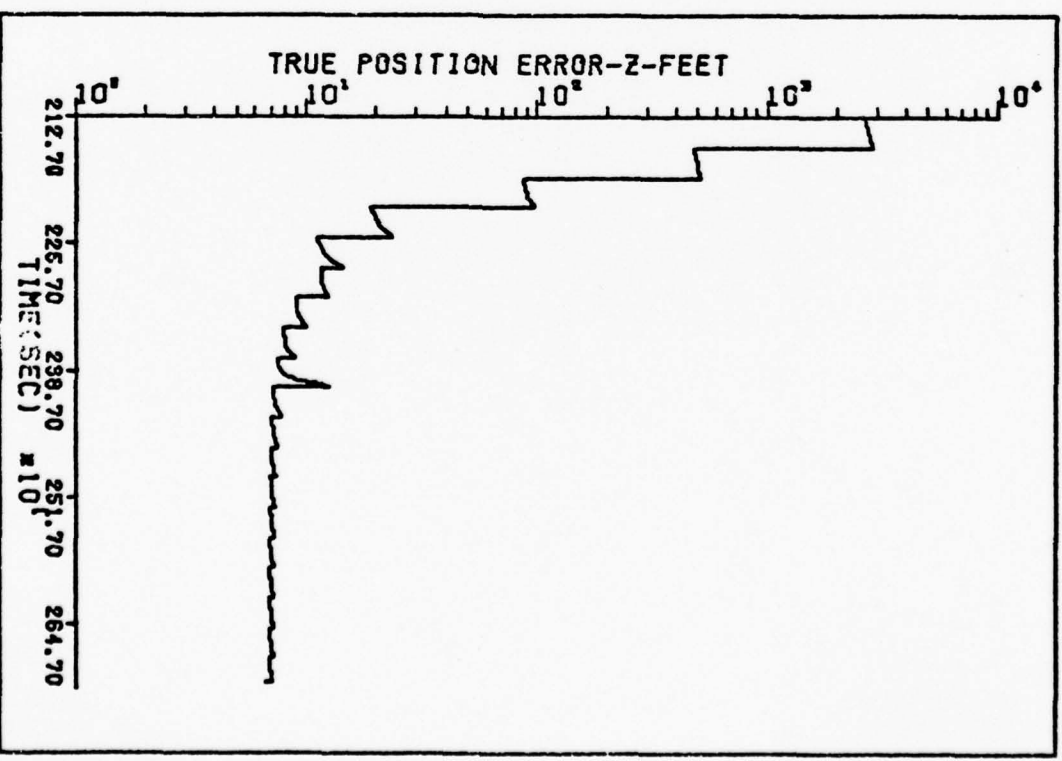


Fig 95 11-St True Error, Post-Blackout, dx_j



XXX

Fig 96 11-St Est Error, Post-Blackout, dx_y

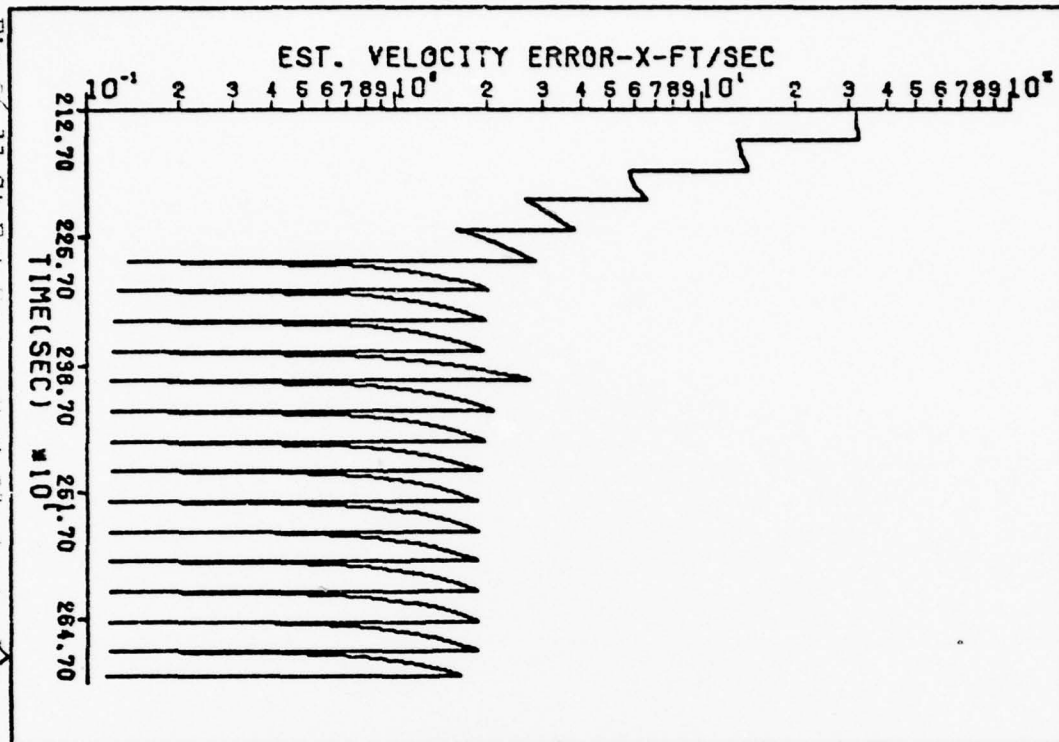
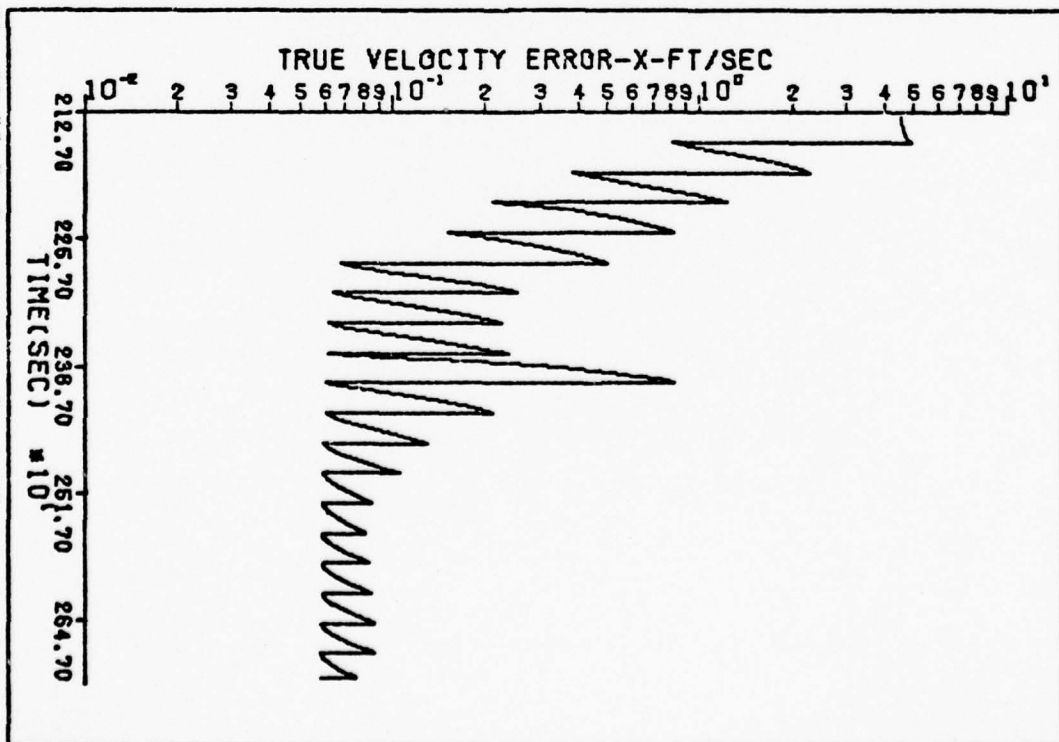


Fig 97 11-St True Error, Post-Blackout, dx_y



XXX

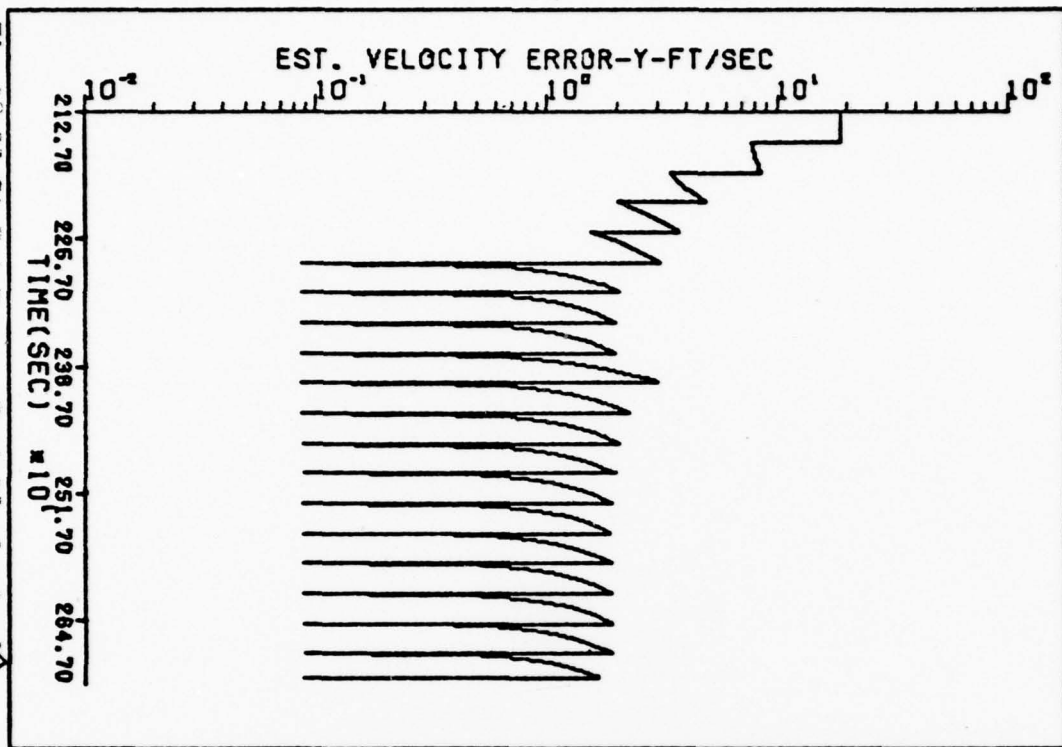


Fig 98 11-St Est Error, Post-Blackout, δx_5

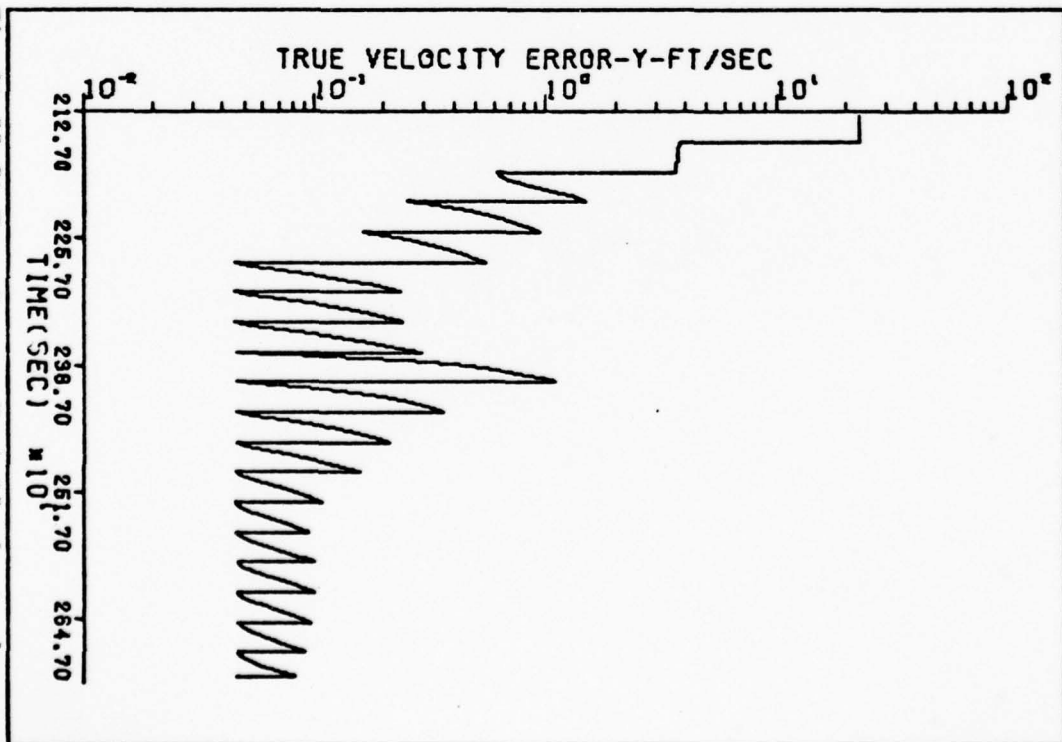


Fig 99 11-St True Error, Post-Blackout, δx_5

Fig 100 11-St Est Error, Post-Blackout, \hat{dx}_6

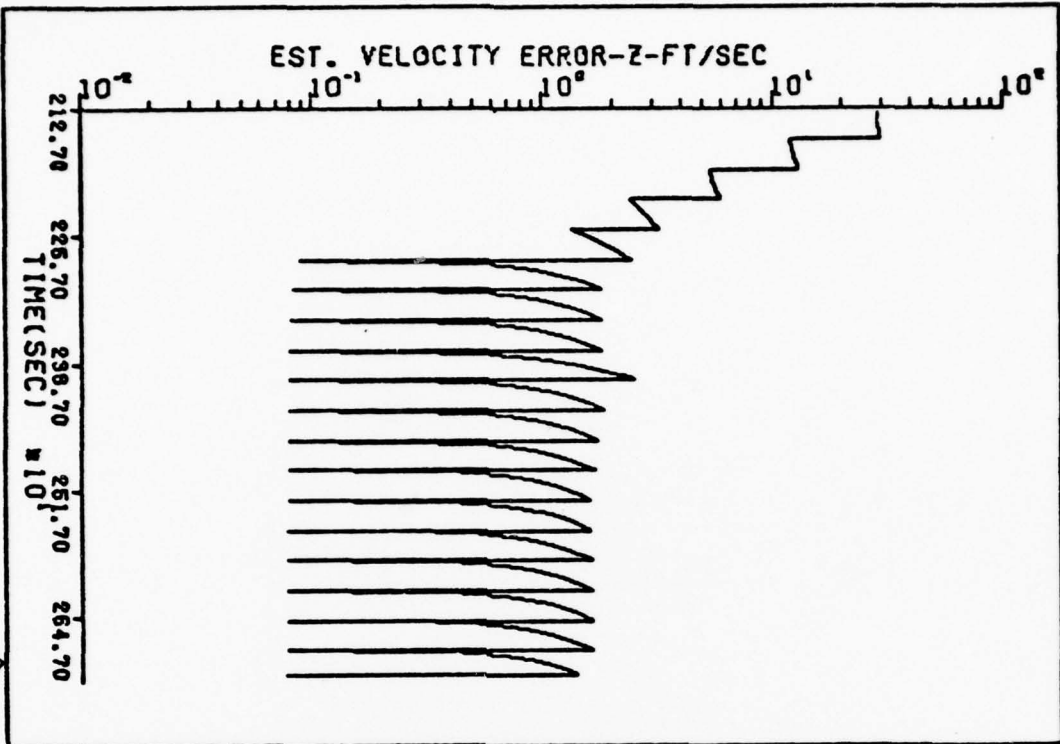
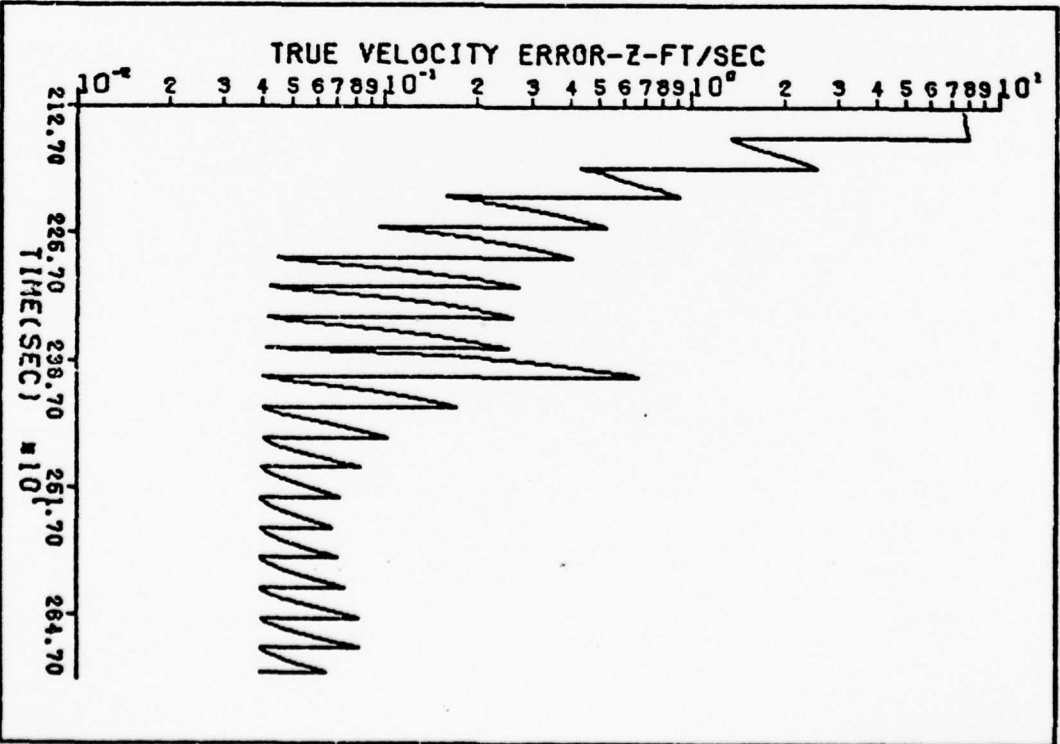


Fig 101 11-St True Error, Post-Blackout, dx_6



XX

Fig 102 11-St Est Error, Post-Blackout, dx_g

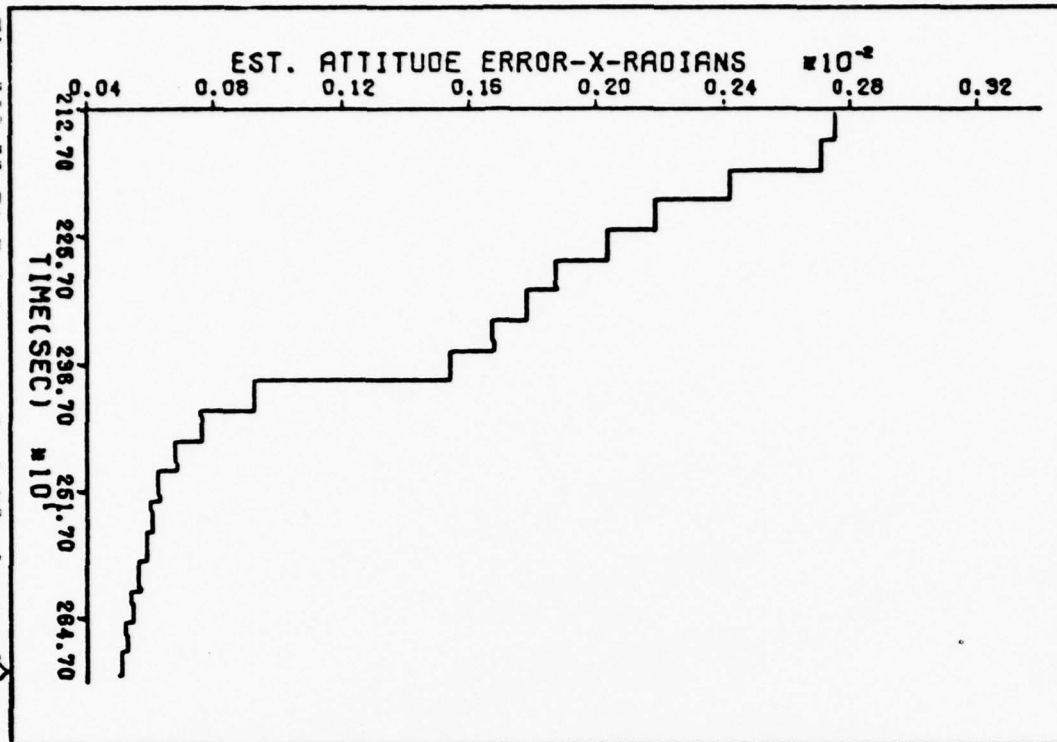


Fig 103 11-St True Error, Post-Blackout, dx_g

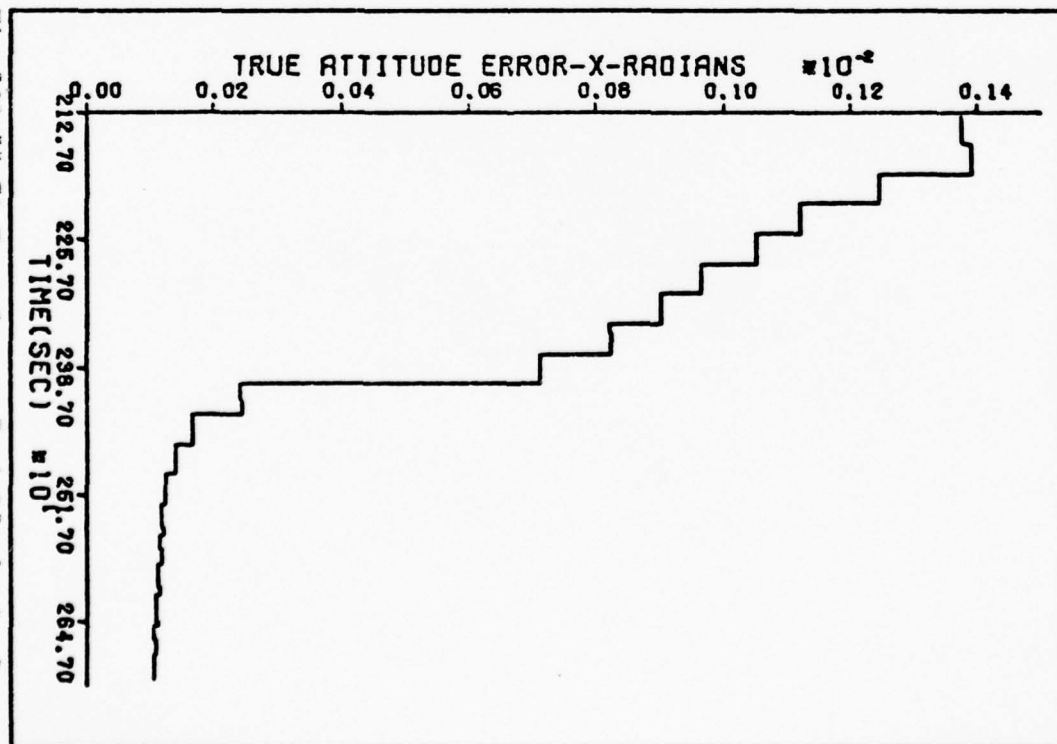


Fig 104 11-St Est Error, Post-Blackout, \hat{dx}_{10}

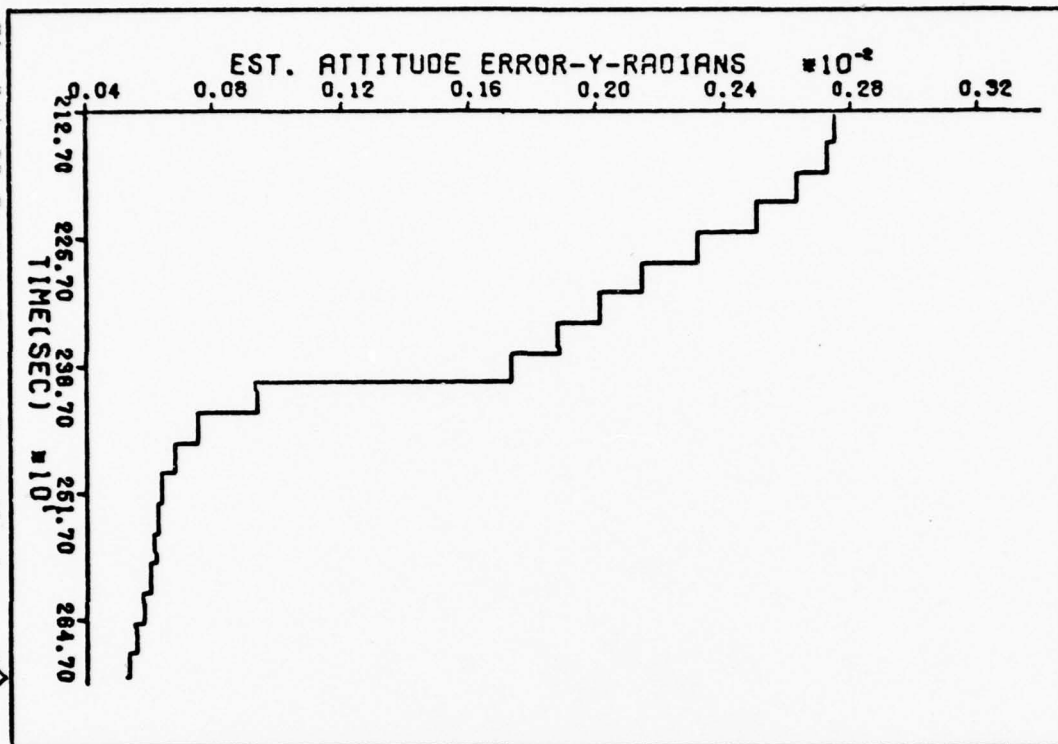


Fig 105 11-St True Error, Post-Blackout, dx_{10}

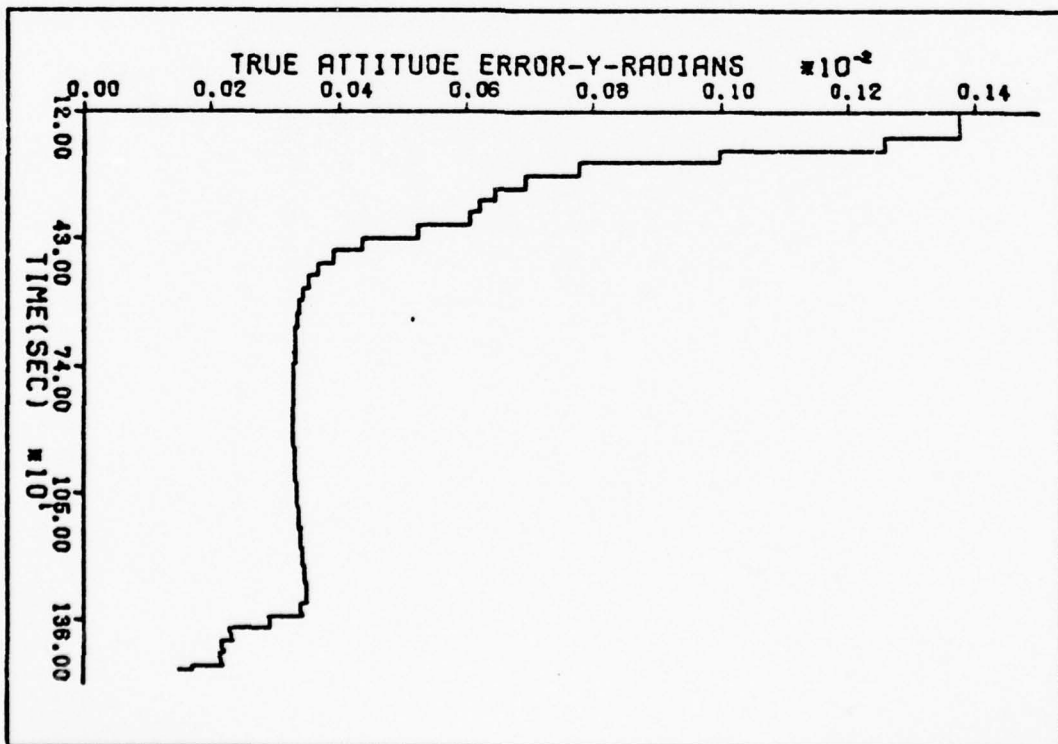


Fig 106 11-St Est Error, Post-Blackout, dx₁₁

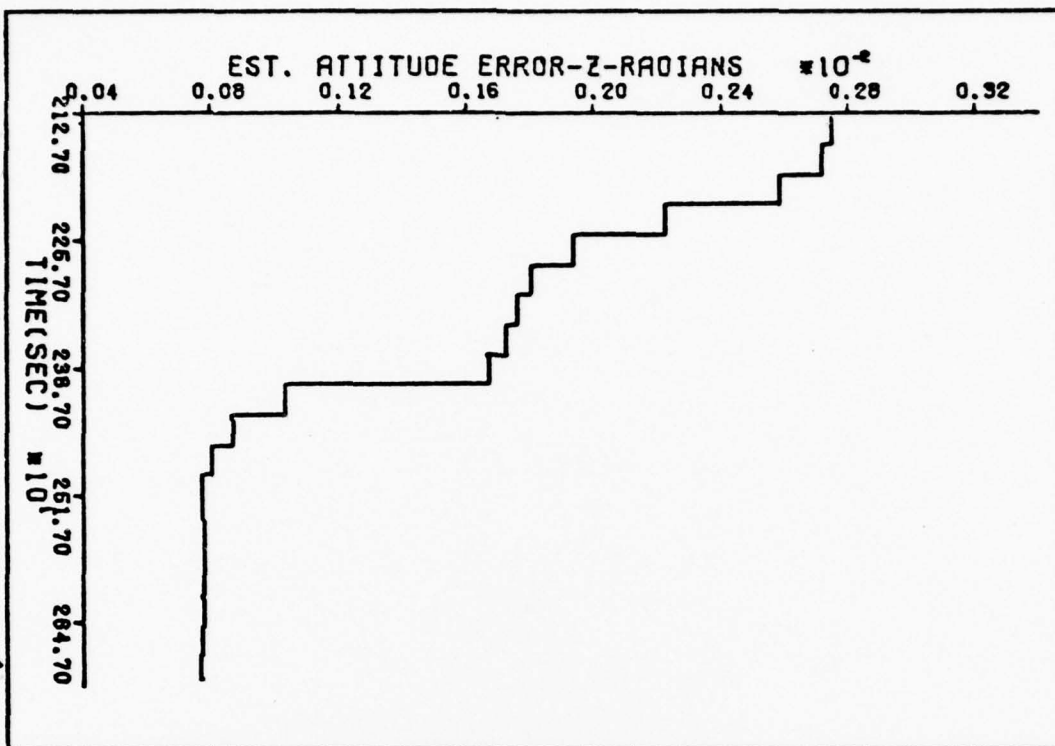
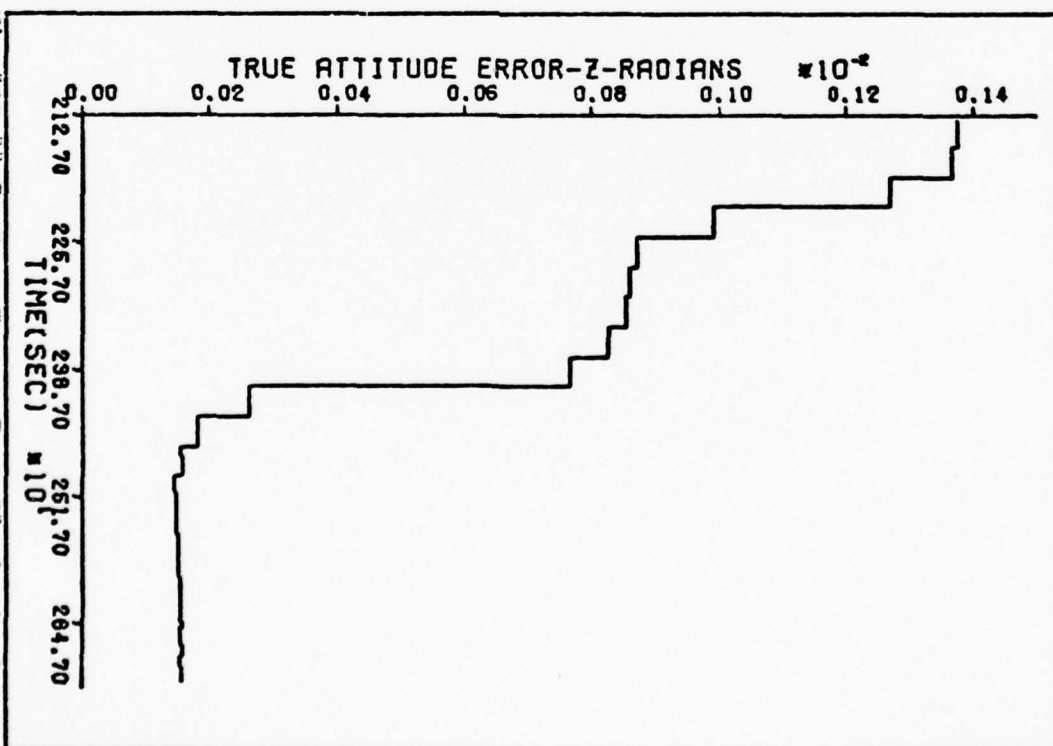


Fig 107 11-St True Error, Post-Blackout, dx₁₁



8-State Filter, Pre-Blackout

The 8-State Filter's performance during the pre-blackout portion of the simulation is presented by the following plots. Update rate and time points are identical to those of the 11-State Filter.

XXX

Fig 108 8-St Est Error, Pre-Blackout, dx_7

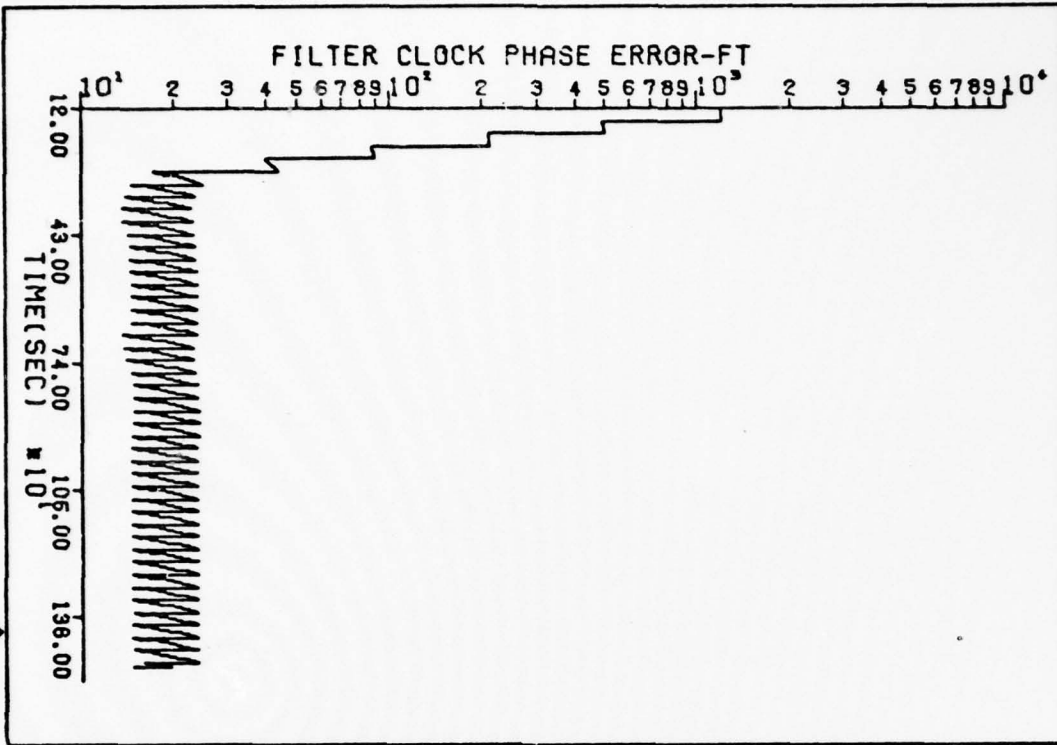
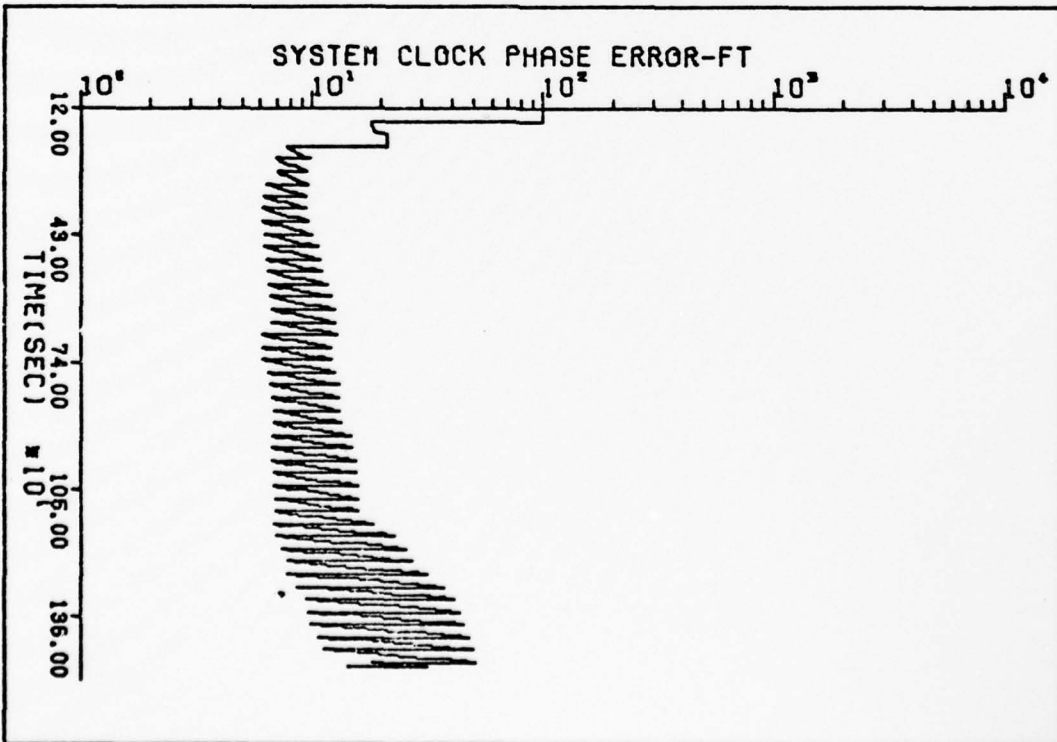


Fig 109 8-St True Error, Pre-Blackout, dx_7



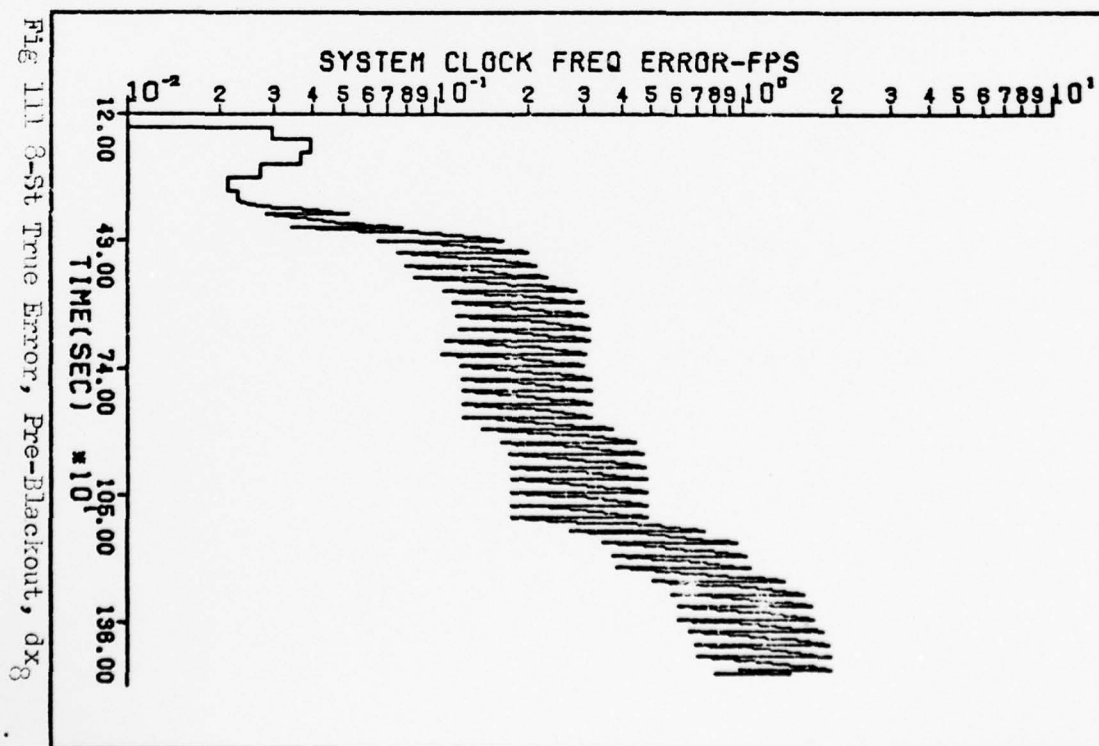
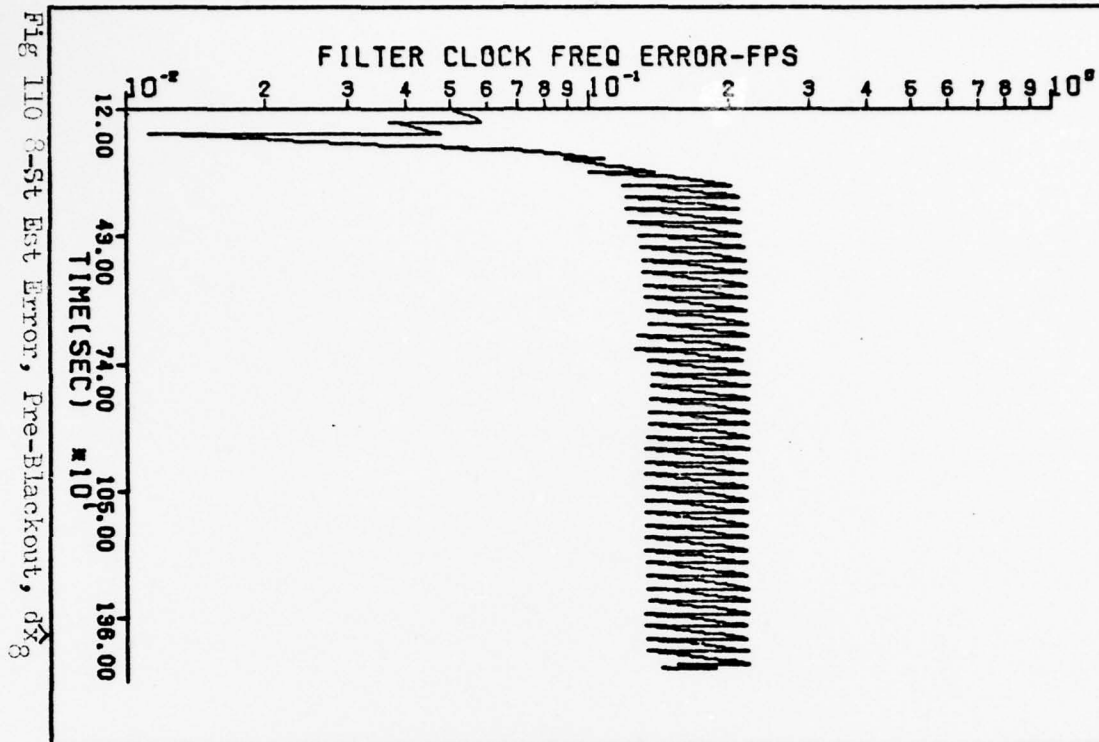


Fig 112 8-St Est Error, Pre-Blackout, δx_1

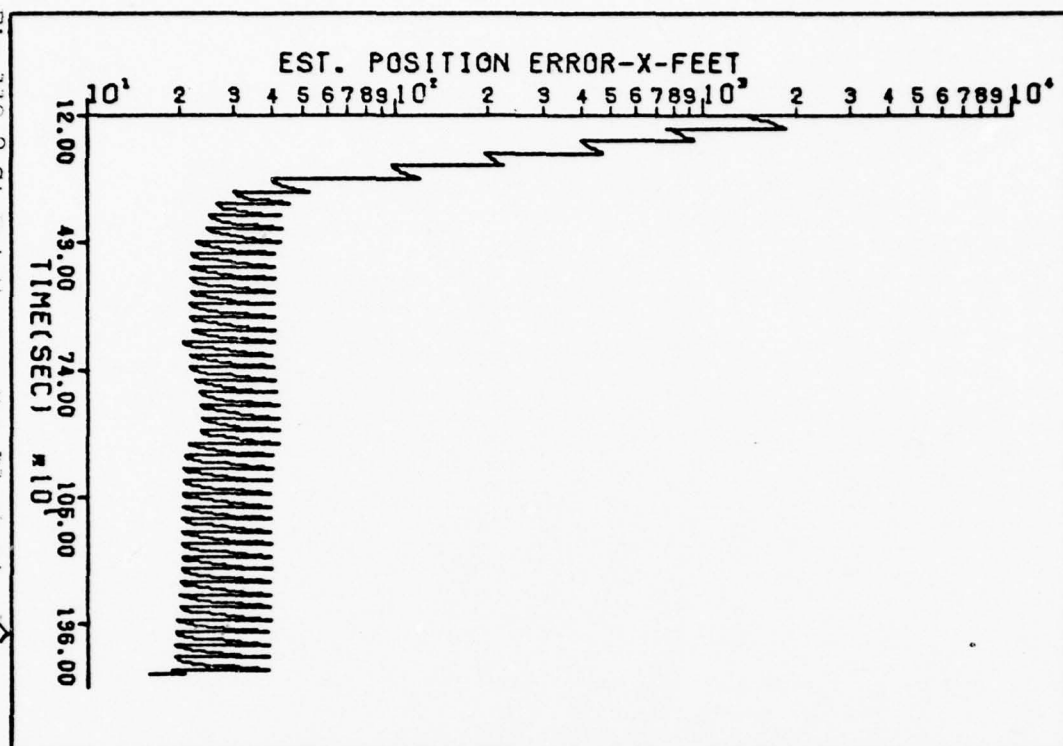
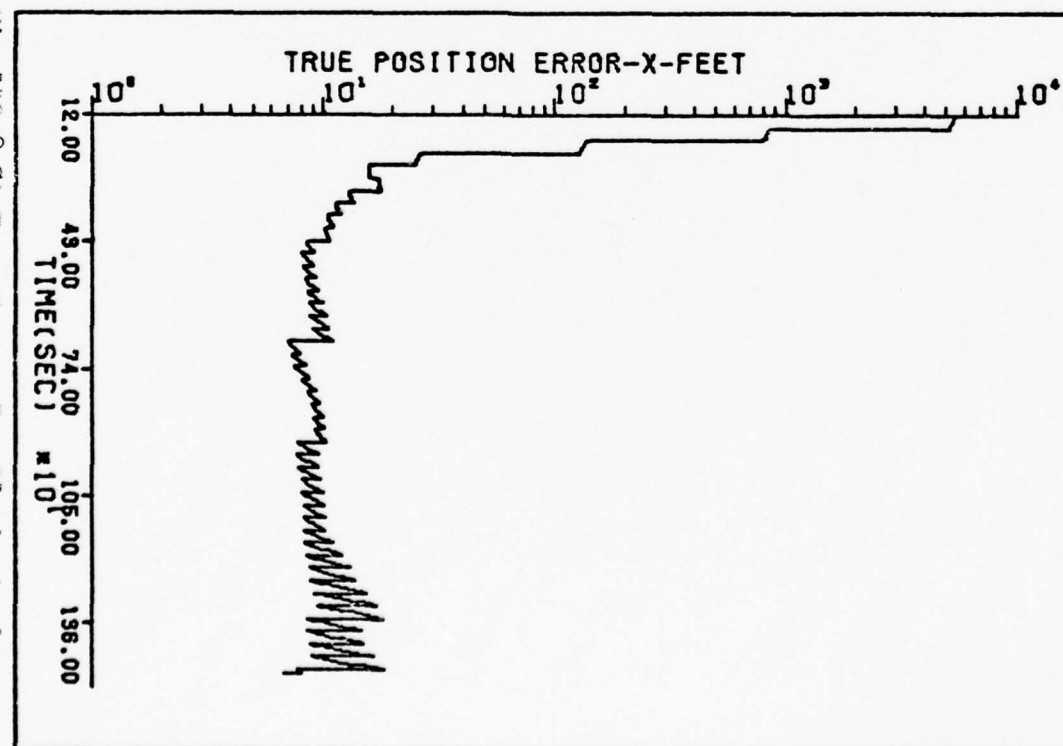


Fig 113 8-St True Error, Pre-Blackout, δx_1



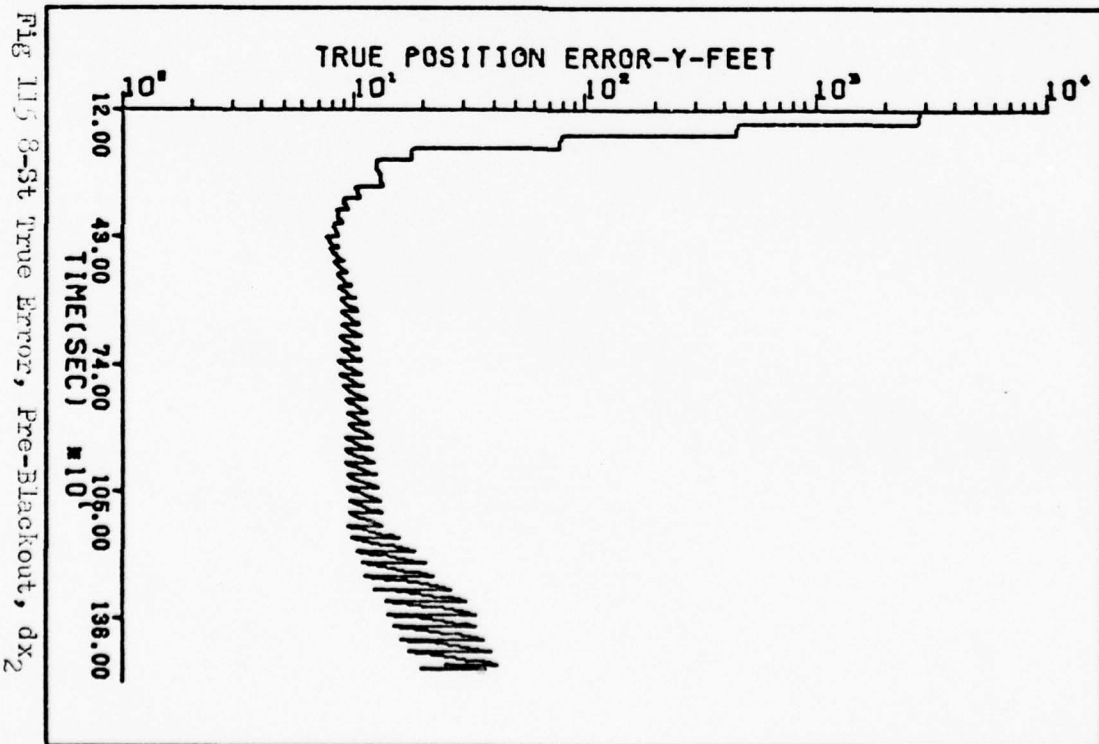
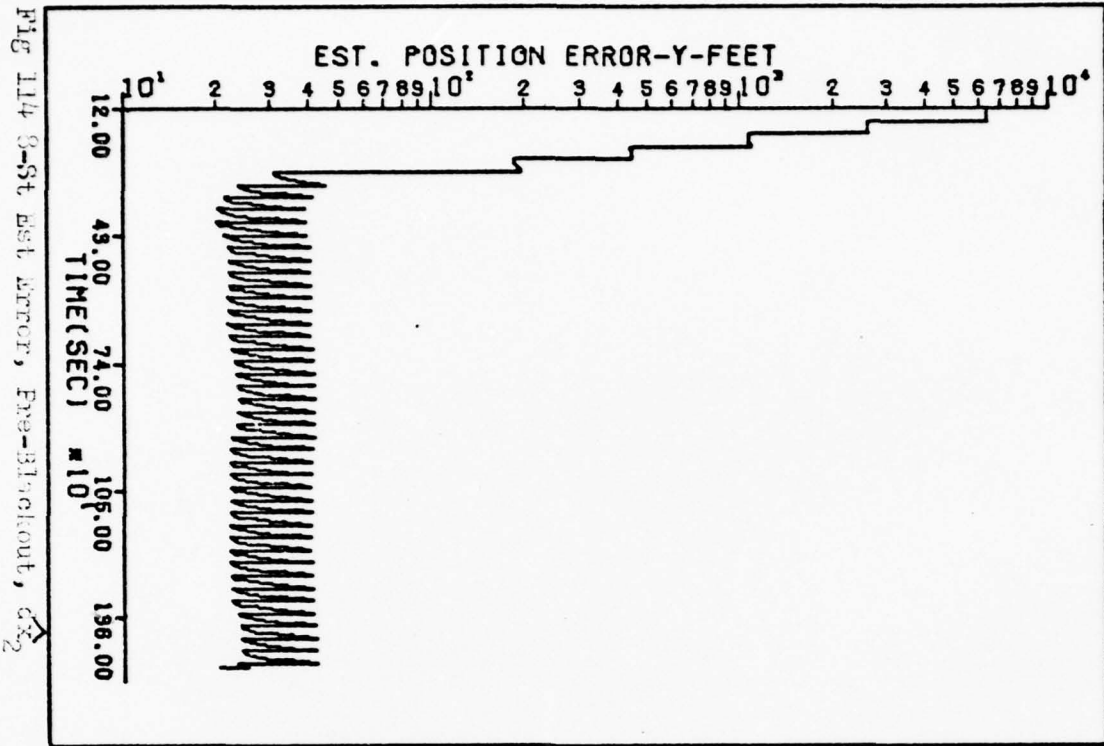


Fig 116 8-St Est Error, Pre-Blackout, dx₃

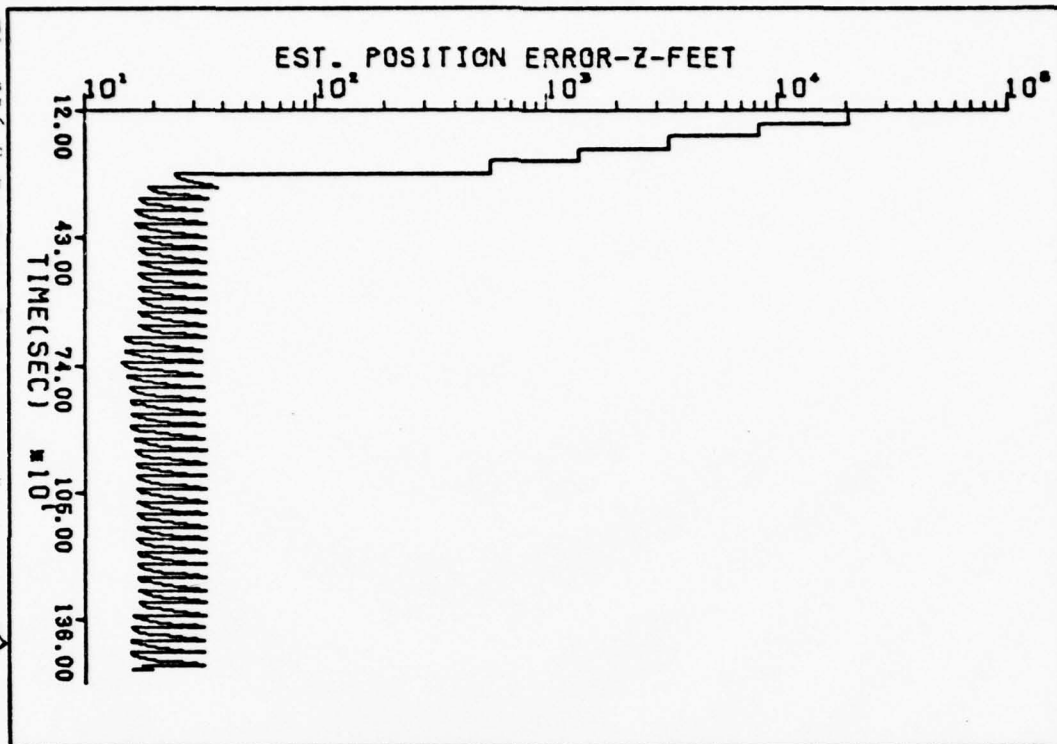
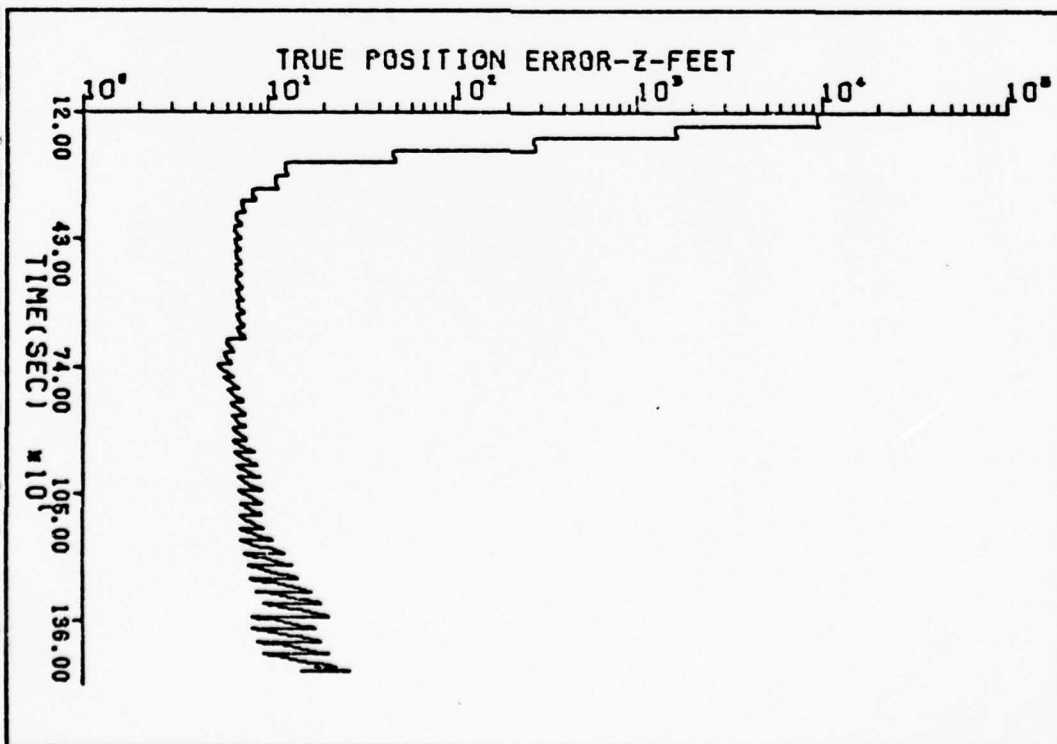


Fig 117 8-St True Error, Pre-Blackout, dx₃



XX

Fig 118 2-St Est Error, Pre-Blackout, δx_y

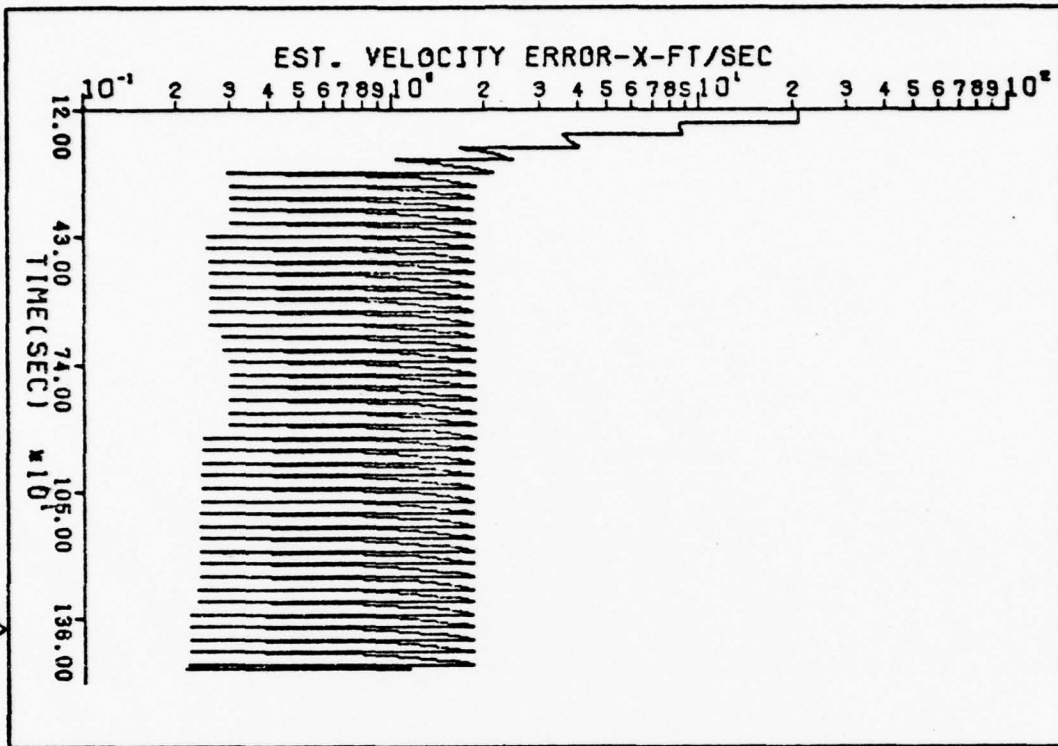


Fig 119 2-St True Error, Pre-Blackout, δx_y

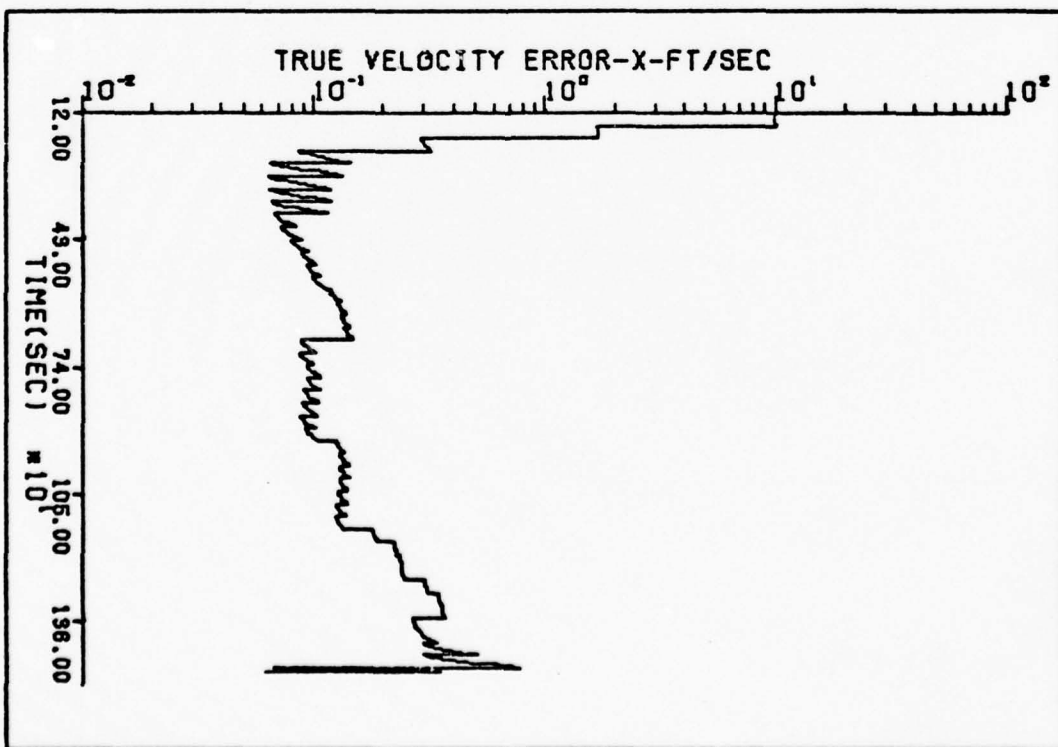


Fig 120 8-St Est Error, Pre-Blackout, dx_5

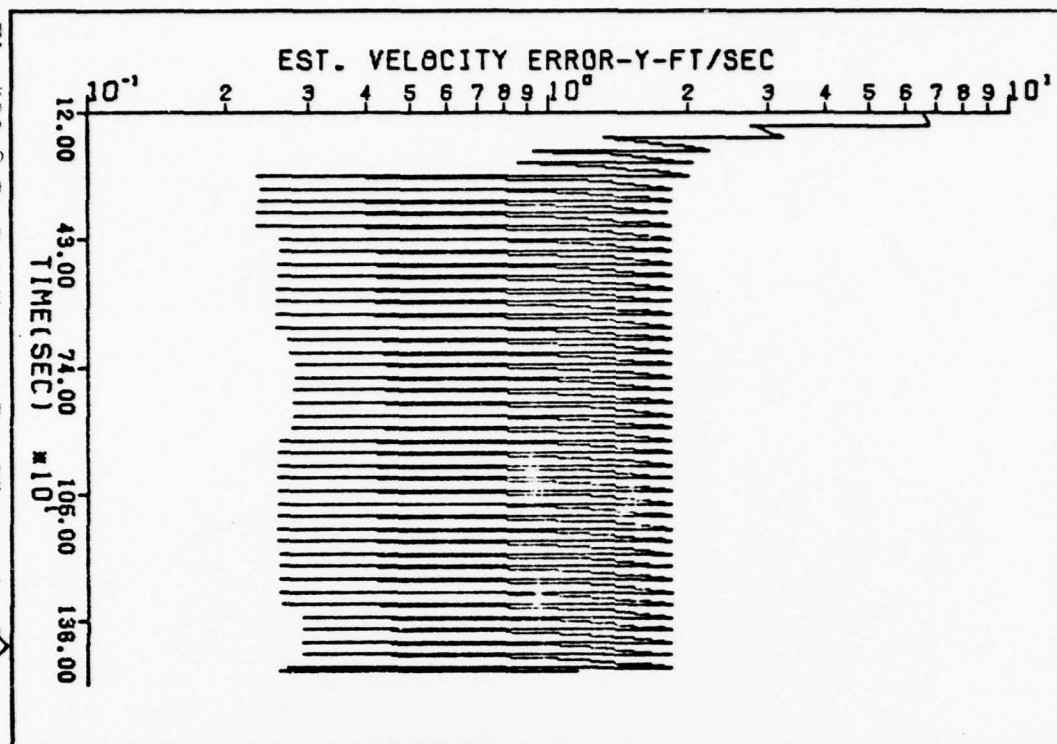
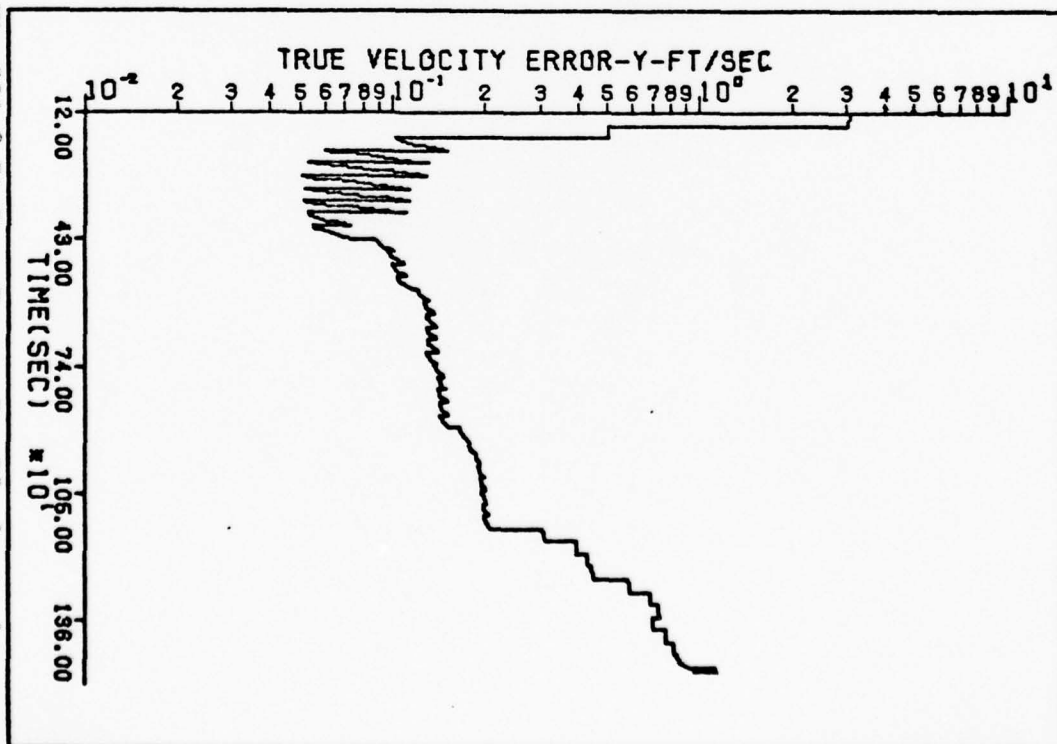


Fig 121 8-St True Error, Pre-Blackout, dx_5



XXX

Fig 122 8-St Est Error, Pre-Blackout, dx₆

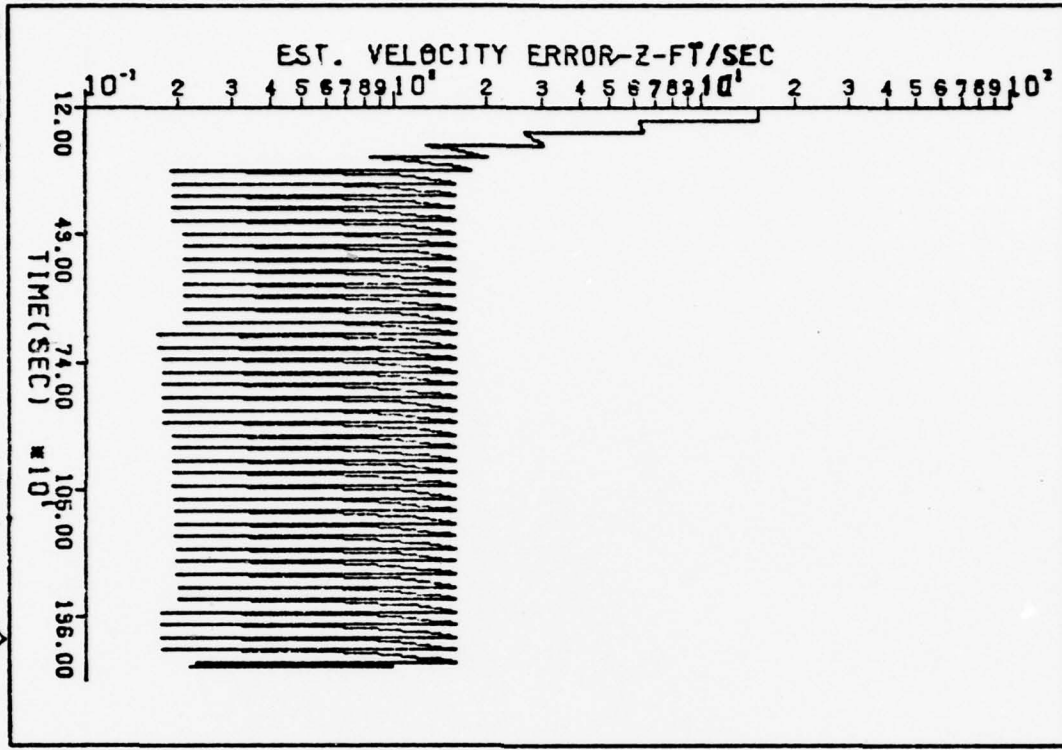
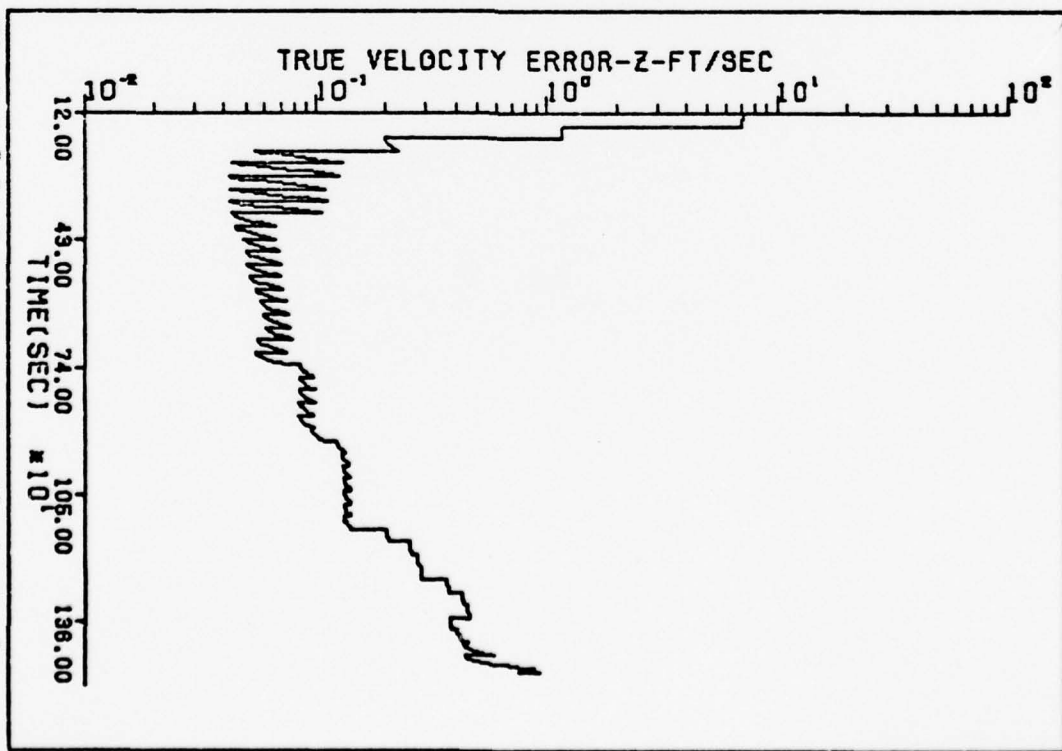


Fig 123 8-St True Error, Pre-Blackout, dx₆



8-State Filter, Post-Blackout

The following series of plots shows the performance of the 8-State Filter design for the post-blackout part of the simulation. Update rate and time points are identical to those of the 11-State Filter in the post-blackout region.

Fig 124 8-St Est Error, Post-Blackout, dx_7

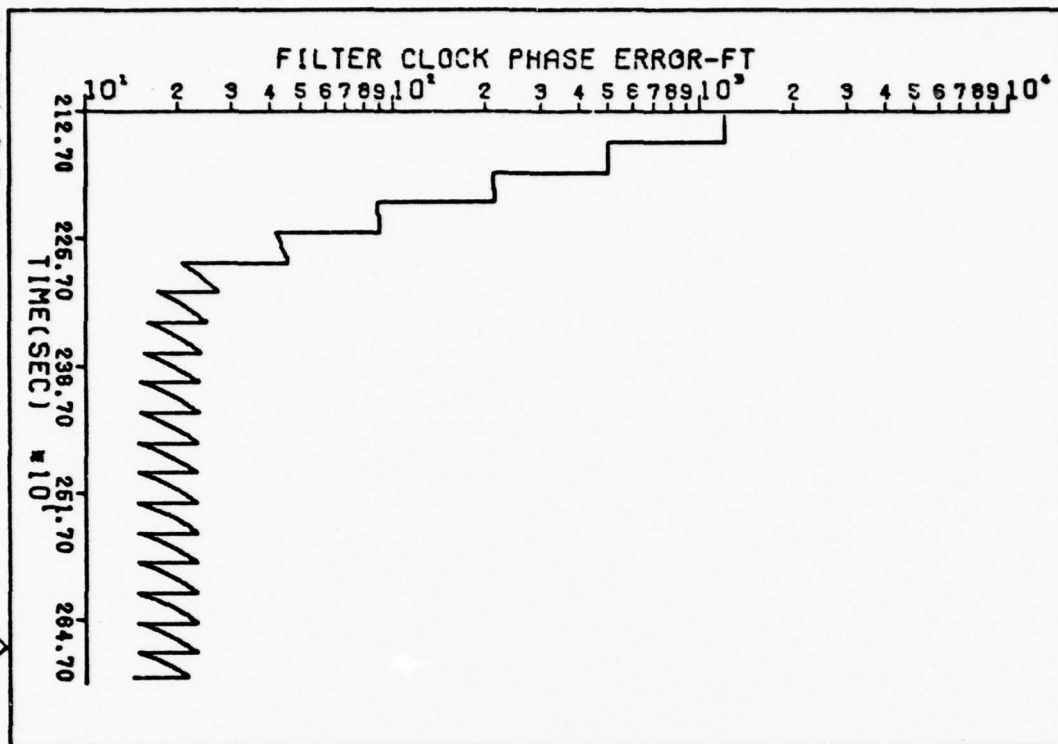


Fig 125 8-St True Error, Post-Blackout, dx_7

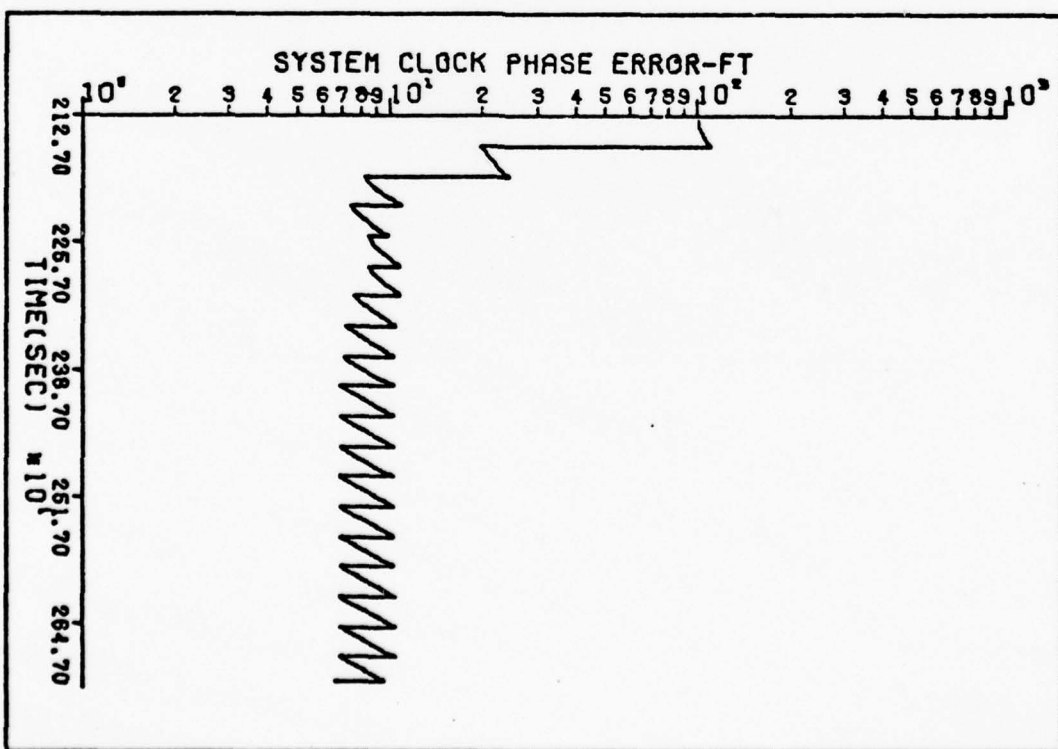


Fig 126 8-St Est Error, Post-Blackout, dxg

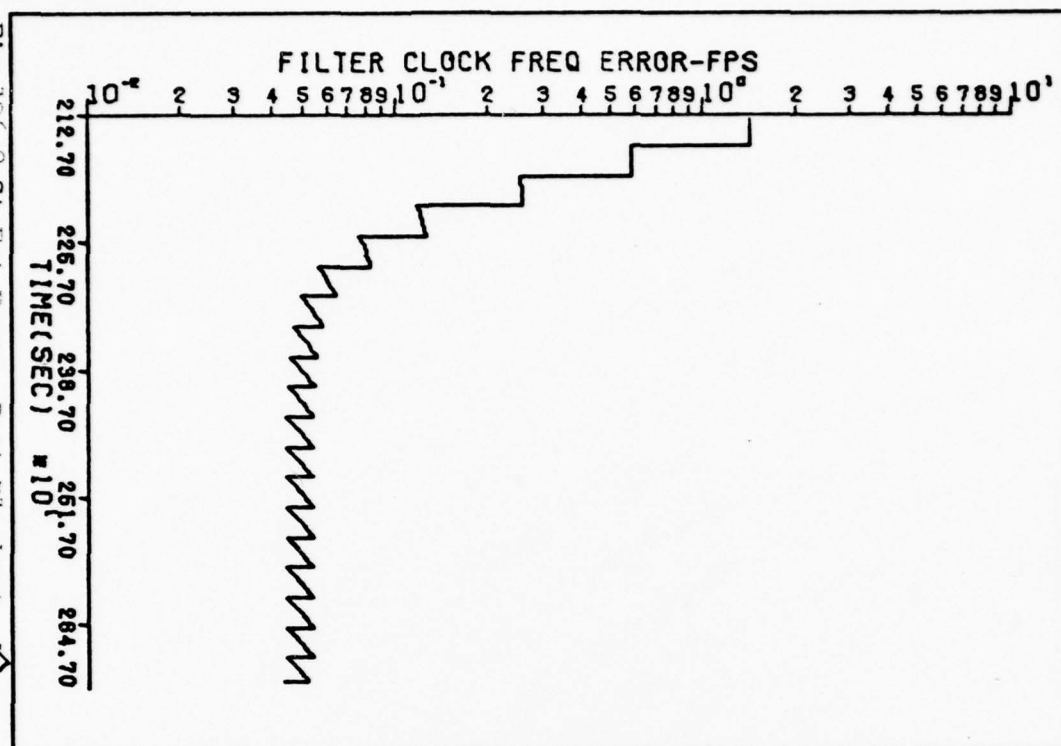
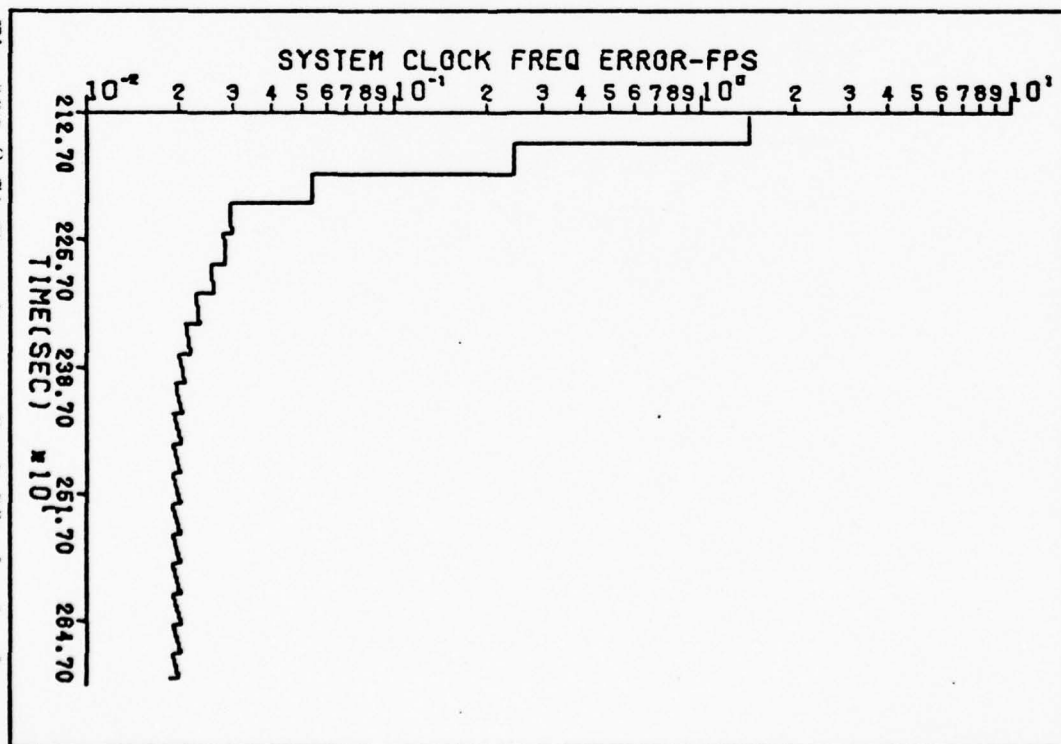


Fig 127 8-St True Error, Post-Blackout, dxg



XXX

Fig 128 8-St Est Error, Post-Blackout, \hat{dx}_1

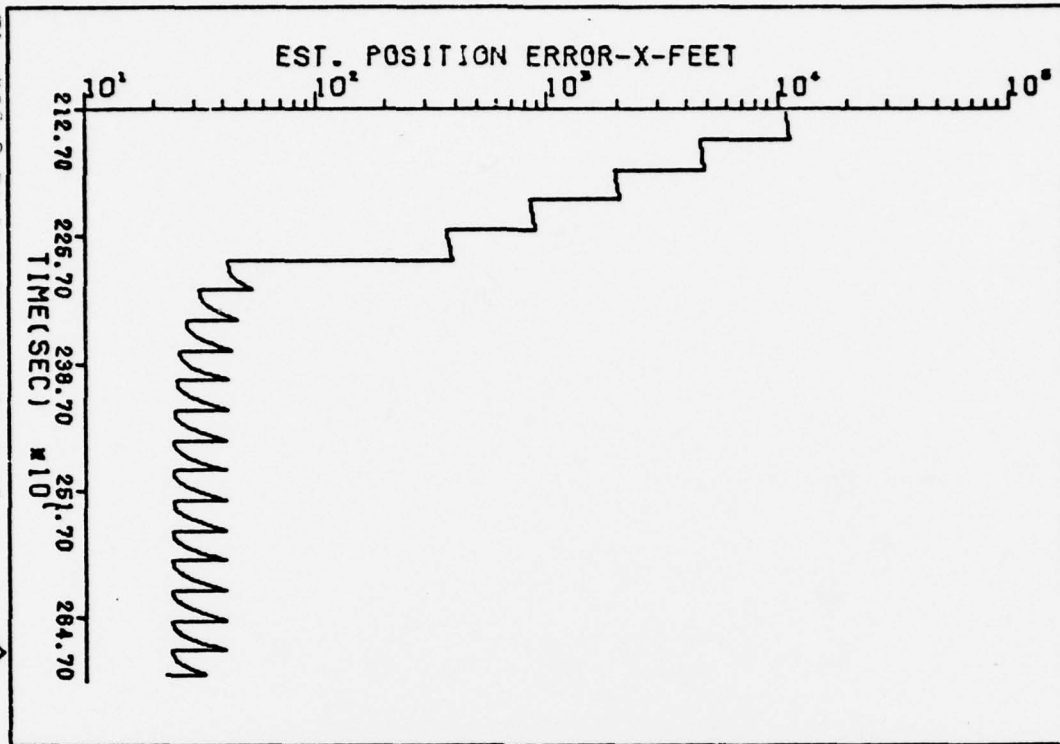


Fig 129 8-St True Error, Post-Blackout, dx_1

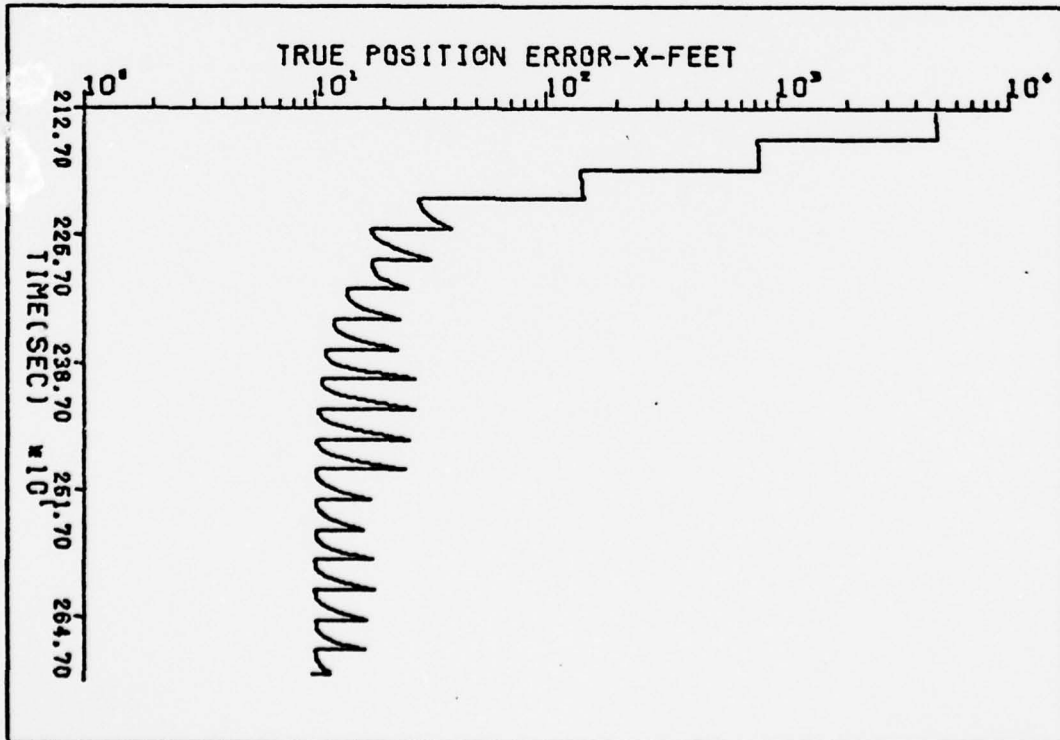


Fig 130 8-St Est Error, Post-Blackout, δx_2

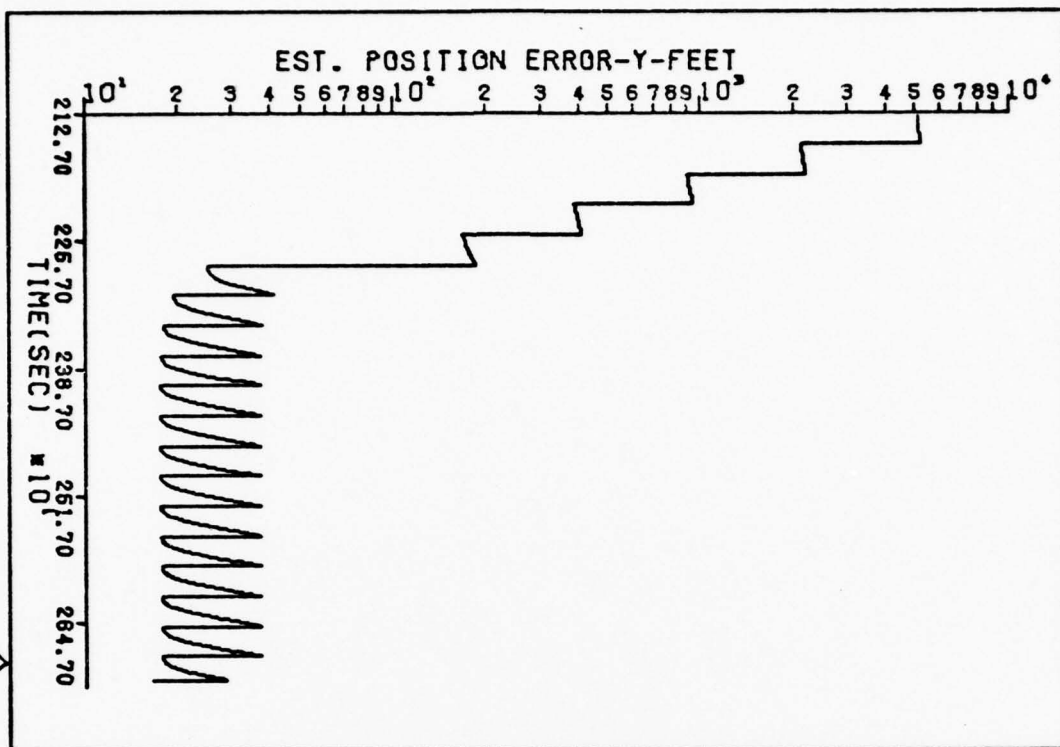
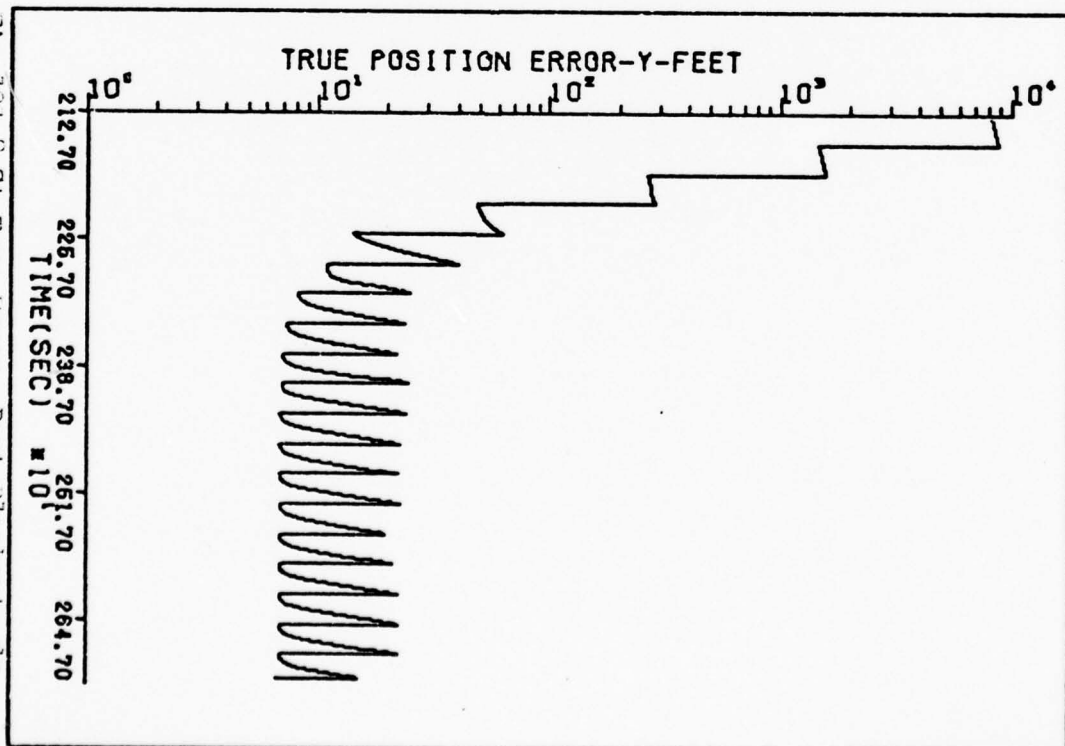


Fig 131 8-St True Error, Post-Blackout, δx_2



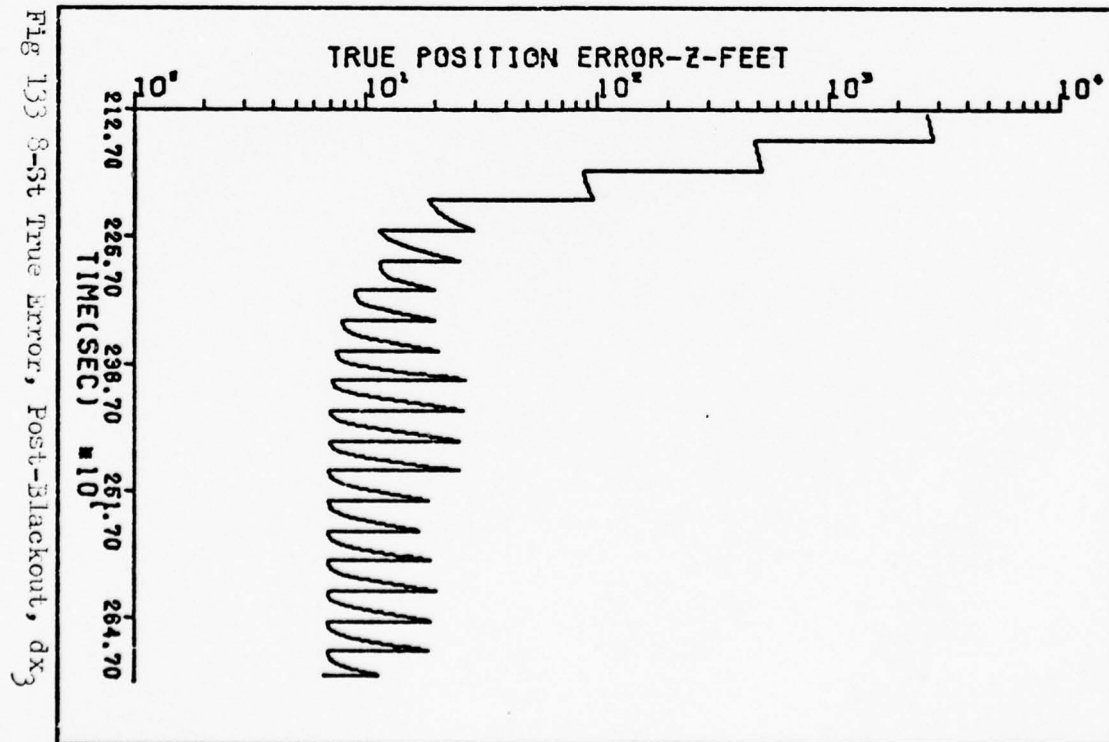
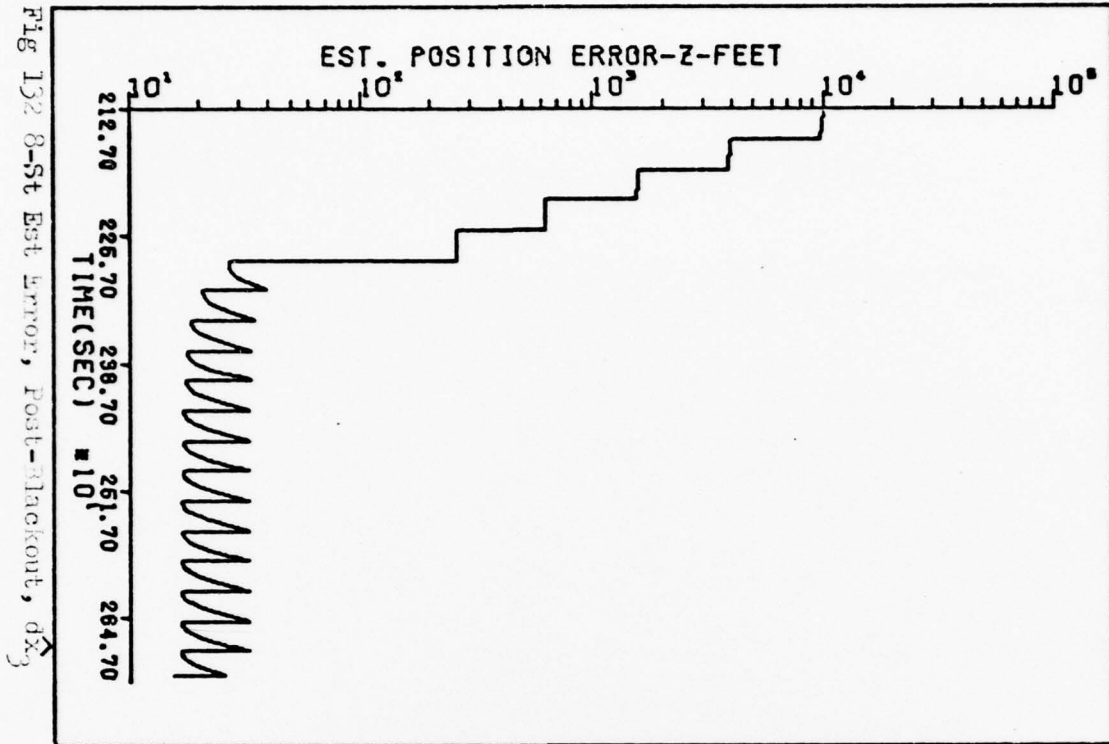


Fig 134 8-St Est Error, Post-Blackout, \hat{dx}_4

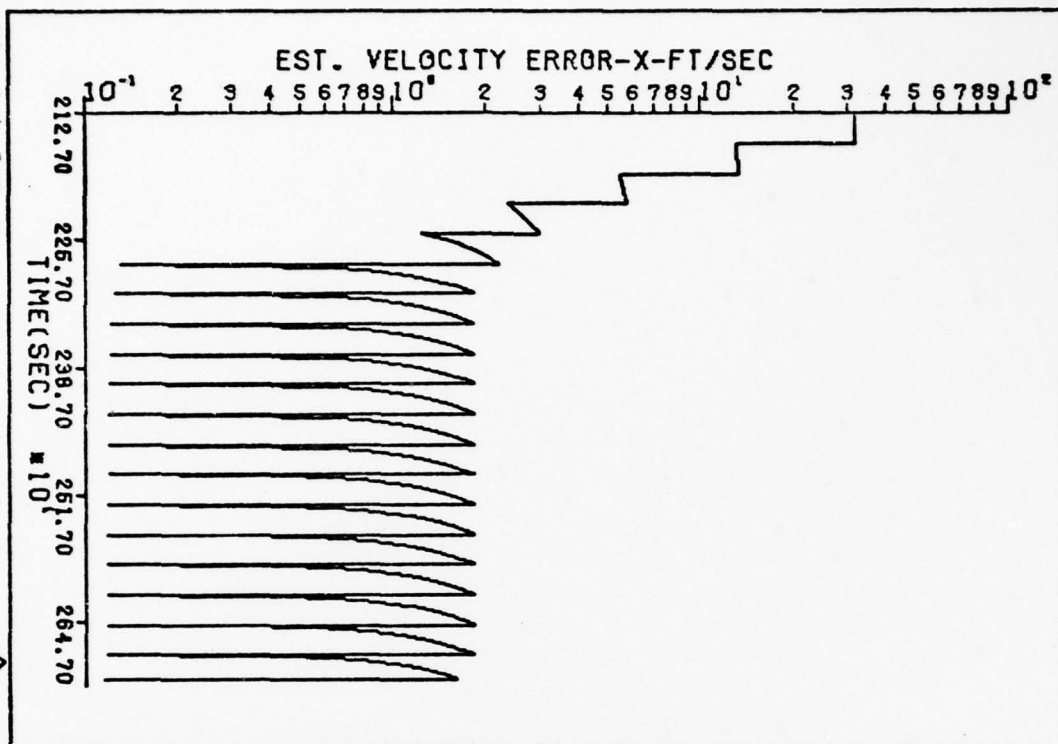
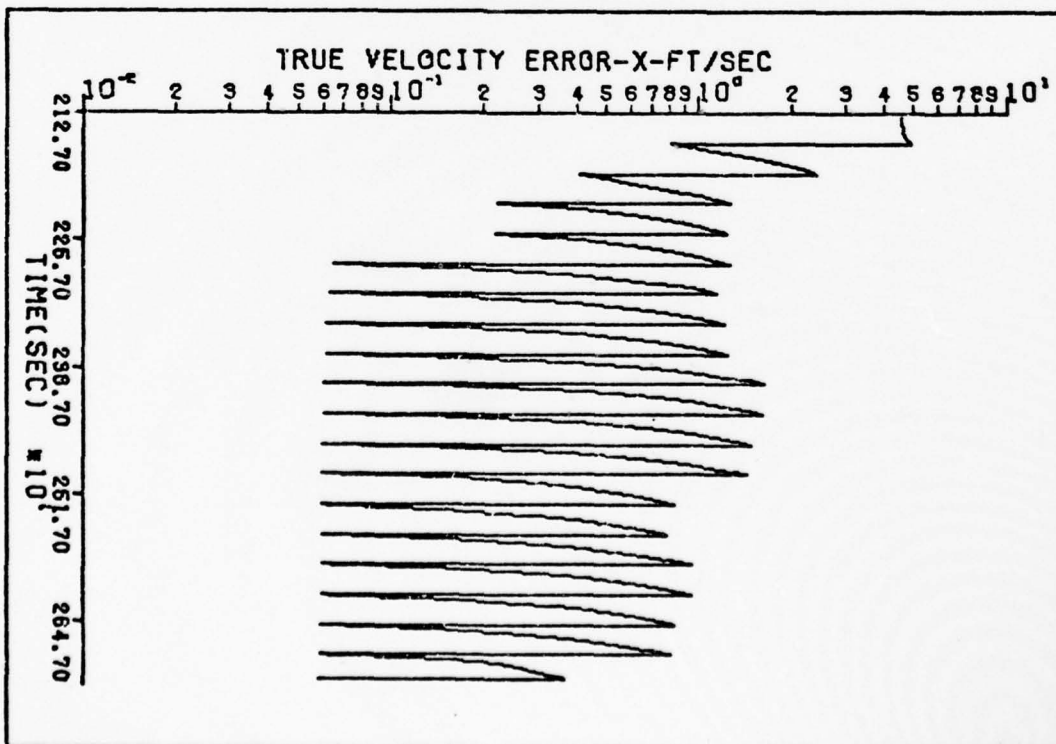
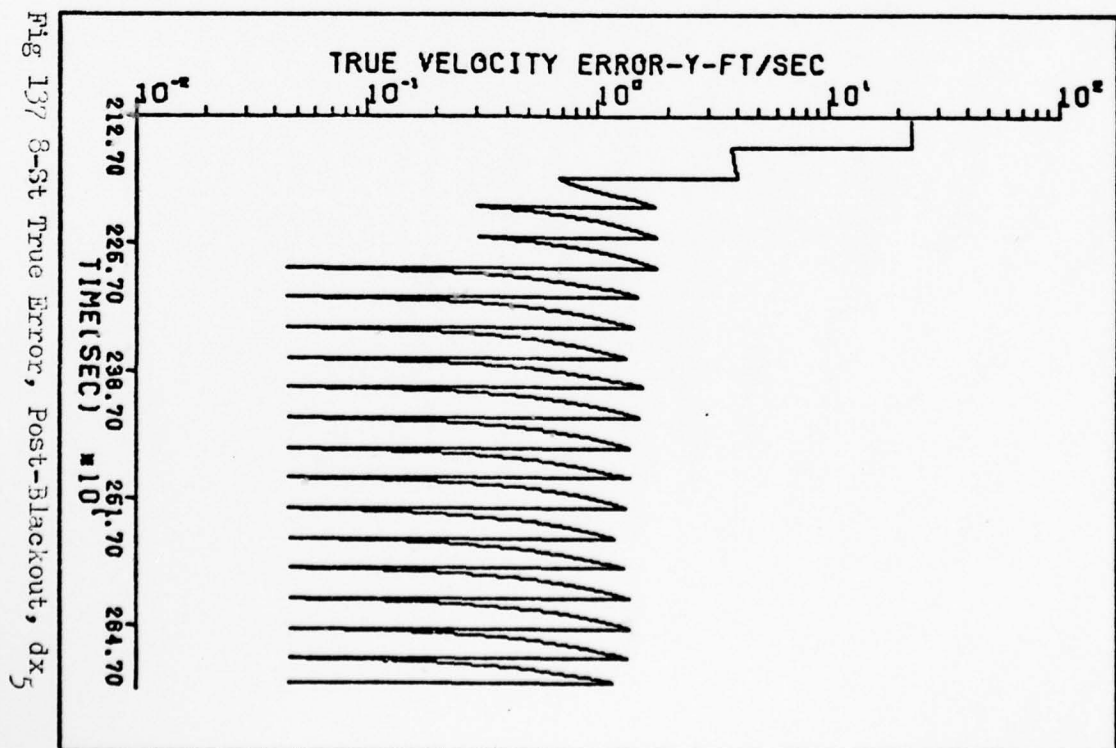
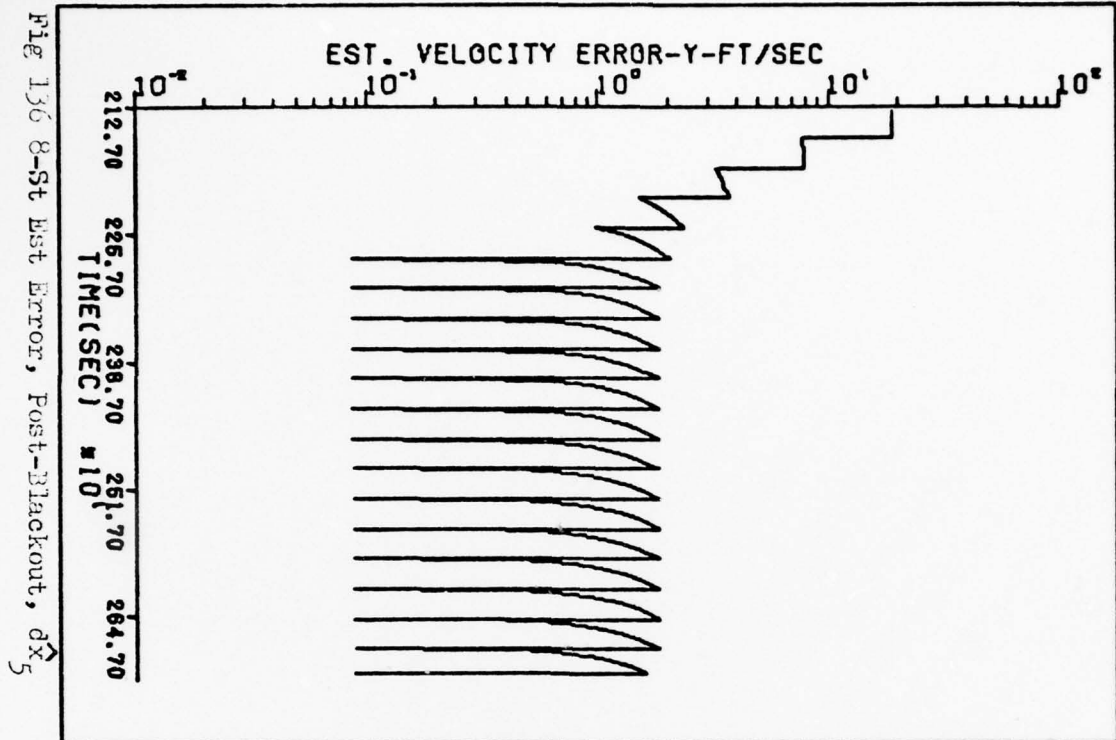


Fig 135 8-St Est Error, Post-Blackout, \hat{dx}_4





XXX

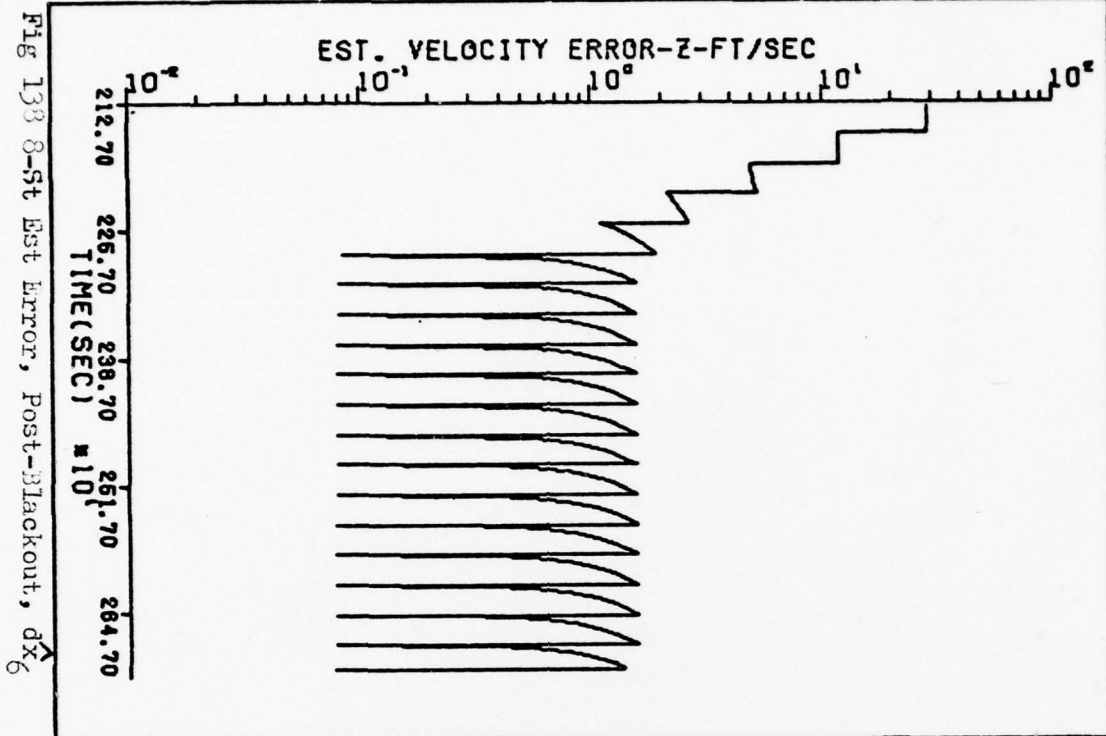


Fig 138 8-St Est Error, Post-Blackout, \dot{x}_6

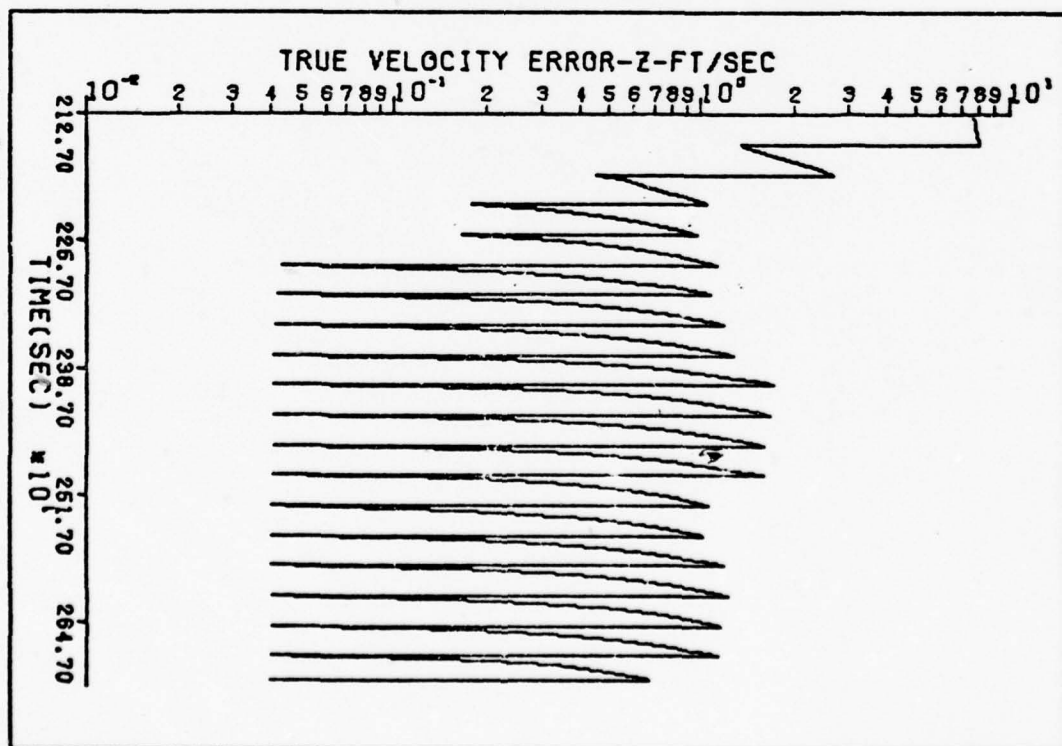


Fig 139 8-St True Error, Post-Blackout, \dot{x}_6

Appendix B

Description of Computer Programs Used

Software

This appendix discusses the important aspects of the software used in this study. The primary program was The General Covariance Analysis Program (GCAP) (Ref 6), which was developed by personnel of the Air Force Avionics Laboratory at Wright-Patterson Air Force Base, Ohio as a tool to aid in Kalman Filter design. Because of the special nature of the simulation of the GPS satellite constellations required in the modeling, the software was modified by the addition of several sub-routines. The added software was taken from another program, developed by personnel from a different branch of the Avionics Laboratory to aid in GPS receiver design, called an Integrated GPS/Inertial (IGI) simulation. These additional subroutines provided the simulation of the 24 satellite GPS constellation, the selection algorithm which examines visibility and "best" satellite configuration, and the measurement algorithm which provides Orbiter-to-satellite vectors for each of the satellites chosen.

Each of these two programs is well documented (Ref 6, 15, and 17), and thus, neither detailed description of the software or software listings will be provided. Instead, discussion will be limited to general descriptions of program organization special features, and a discussion of the satellite visibility and selection algorithm. The appendix will be closed with a short discussion of the implication of using a program that assumes complete impulsive control over estimated states.

GCAP

GCAP was designed as an efficient implementation of the covariance analysis equations. It takes maximum advantage of the sparse nature of filter and system dynamics matrices, measurement matrices and noise covariance matrices. An executive routine controls the operation of the program from initialization to final output.

Once the program is initialized, a single subroutine for integration, utilizing a fourth order Runge-Kutta integration routine, propagates the covariances of the filter and system forward in time. Elements of the dynamics matrices, noise covariance matrices, and measurement matrices are calculated by one subroutine for the filter and a separate one for the system. The filter and system each have separate subroutine groups which perform the measurement update function, called from the integration subroutine. The filter subroutine groups controlling updating compute the Kalman gain matrix, K_F , and correct the filter's estimate of the error states. The system subroutine groups, on the other hand, utilize the filter computed gain matrix to perform an update of the system error states which were being estimated by the filter. The program is completed by various input and output subroutines, and subroutines which perform the mechanical functions of matrix multiplication, inversion, transposition, etc., specialized for both sparse and full matrices. Several options are available to the user, dealing with printing and plotting functions, and the frequency with which each is performed. The program performs one complete cycle of integration, update and output for the filter, and then goes back and does the same for the system, after which the entire cycle repeats. Figure presents a generalized functional block diagram for the organization of the program.

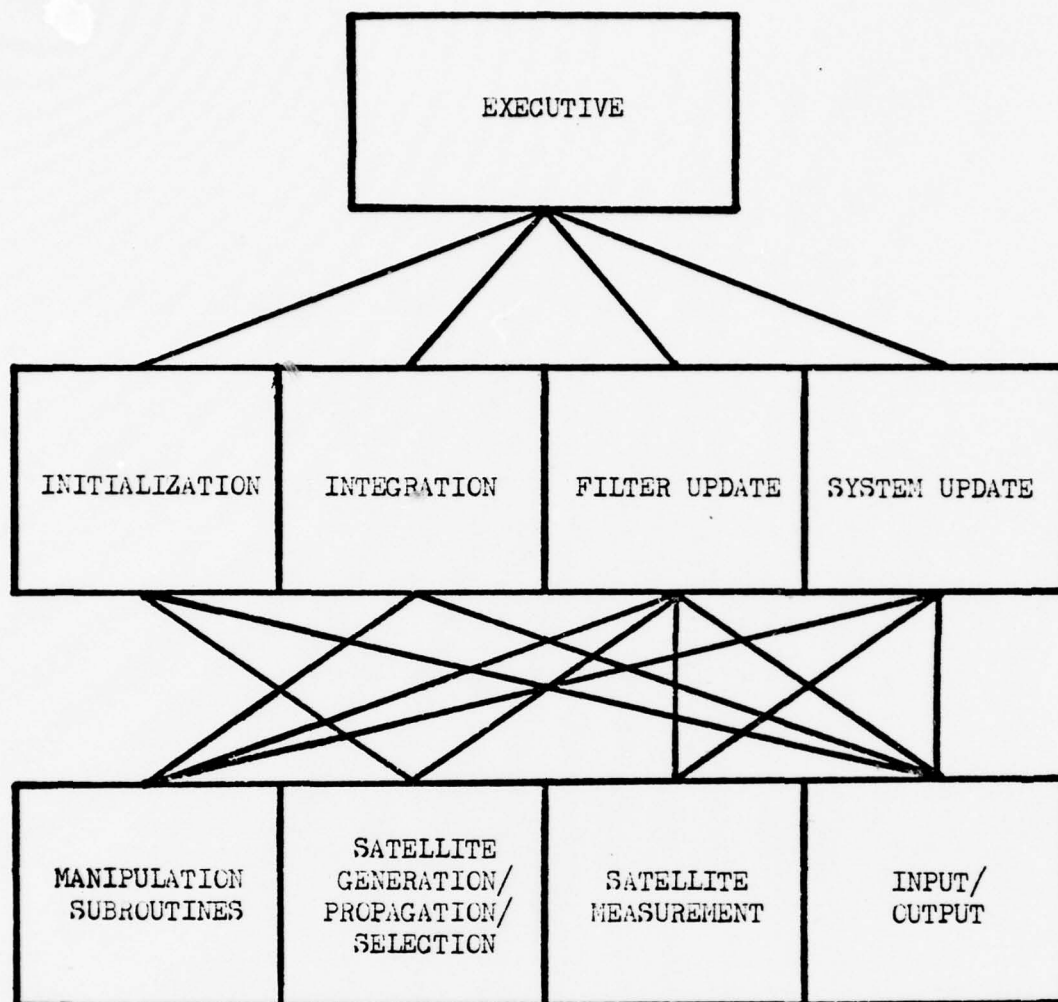


Figure 140. Generalized Functional Block Diagram for Modified GCAP

IGI

The subroutines added to GCAP from the Integrated GPS/Inertial simulation software perform the GPS satellite simulation functions. The primary subroutine of this group generates the 24 satellite constellation and propagates it forward in time. This subroutine calls another which examines the total set of satellites to decide which are in view for the Orbiter. A satellite is in-view if it is 10° or more above the Orbiter's local horizon. After the "in-view" set of satellites is selected, the set is tested iteratively to decide which four satellites

from the set will provide a geometrical configuration that will provide the navigation solution with the best accuracy.

This is done by testing for the best "GDOP" possible from the in-view set. GDOP is an acronym which stands for "geometric dilution of precision". It is defined as the ratio of the position error statistics to the range error standard deviation with the condition that all satellite range measurement errors are considered uncorrelated with equal standard deviations (Ref 1:11). GDOP depends only on the geometry of the relative positions between the satellites and a user and does not depend on the range error.

Once the optimum set of four satellites has been selected it is not necessary to perform this test again until the relative positions of the Orbiter and satellites have changed by some amount that makes another set of four better. The program provides the option of setting how often to test for in-view and GDOP conditions. The high velocity of the Orbiter during initial deorbit operations (25,000 fps) required this test to be performed fairly often. The interval was set in this study to perform this test every 61.4 seconds, or every other update period. This is approximately once every 255 nautical miles of Orbiter travel.

The measurement subroutine is called at each update interval during both filter and system update operations. In turn, it calls the satellite generation/propagation subroutine to an entry point which bypasses the in-view and selection portions and only propagates the four chosen satellites forward in time. After this, the measurement subroutine calculates the Orbiter to satellite vectors and returns them to the GCAP updating sequence. The set of subroutines is completed by a group

of inversion, multiplication, and transposition subroutines.

Impulsive Control

As mentioned earlier, the GCAP implementation assumes impulsive control over the estimated states. This means that error corrections, applied only to software in the filter case, are assumed to be applied instantaneously to a physical condition, in the case of the system. An example would be position/velocity indicators, or even more to the point, the platform misalignments. These physical corrections necessarily take a finite amount of time. Bias levels must be changed and physical movement must take place. This may take a significant portion of an estimate period if the correction is large, as during initial transients. By the time the correction is performed, the error state may have propagated forward significantly past the corrected level of the error state.

Another problem is the assumption by GCAP that the GPS receiver clock is corrected by feedback. This requires the addition of an algorithm which will send estimated errors to the GPS receiver information processing algorithms, which would accomplish this feedback function.

In this study, the changes in those states which represent physical errors are small. Thus, total impulsive control assumptions are not thought to present significant errors in the analysis, especially in the steady state, and the results are assumed valid.

Appendix C

Filter Parameter Presentation and Comparison

This appendix presents values for filter parameters and initial covariances for filter and truth model position and velocity states. No attempt is made to explain differences between TASC suggested values and values used for filter parameters in this study. The TASC suggested values are from a previous study for NASA (Ref 11:2.10-2.12).

Table XII: Comparison of TASC Suggested Filter Process Noise and Measurement Noise Strengths with Final Study Values, 11-State Filter

State Description	Units	Process Noise Spectral Density	
		TASC	Study
Position	ft ² /sec	--	--
X, Y Velocity	(ft/sec) ² /sec	0.1076	0.1076
Z Velocity	(ft/sec) ² /sec	0.1076	0.08
Clock Phase	ft ² /sec	0.1	10.0
Clock Freq	(ft/sec) ² /sec	3.0X10 ⁻⁵	3.0X10 ⁻⁵
			3.0X10 ⁻⁴
			1.0X10 ⁻³
Misalignments	(rad) ² /sec	1.037X10 ⁻¹⁰	1.56X10 ⁻¹⁰
Measurement		Noise Strength	
Pseudo-Range	(feet) ²	10,000 -- 144	10,000
			1,000
			800
Pseudo-Range-Rate	(ft/sec) ²	.0025	0.025
			0.035
			0.05

Table XIII: Full Lower Triangle of 6x6 Initial Covariance Matrix, Position and Velocity States, at Deorbit Ignition, Filter

	1	2	3	4	5	6
1	1.768×10^6					
2	-7.607×10^7	4.018×10^7				
3	-2.653×10^8	1.186×10^8	4.205×10^8			
4	2.462×10^4	-1.098×10^4	-3.838×10^4	4.381×10^2		
5	-6.706×10^3	2.991×10^3	1.045×10^4	-1.163×10^2	4.258×10^1	
6	1.772×10^4	-7.903×10^3	-2.761×10^4	3.074×10^2	-8.372×10^1	2.321×10^2

Table XIV: Full Lower Triangle of 6x6 Initial Covariance Matrix, Position and Velocity States, at Deorbit Ignition, Truth Model

	1	2	3	4	5	6
1	2.934×10^7					
2	-1.461×10^7	8.039×10^6				
3	-4.965×10^7	2.506×10^7	8.708×10^7			
4	-5.393×10^4	2.745×10^4	9.287×10^4	9.728×10^1		
5	1.649×10^4	-8.014×10^3	-2.791×10^4	-2.913×10^1	9.615×10^0	
6	-3.786×10^4	1.913×10^4	6.705×10^4	6.896×10^1	-2.079×10^1	5.062×10^1

Table XV: Full Lower Triangle of 6x6 Initial Covariance Matrix, Position and Velocity States, at Exit-Blackout, Filter

	1	2	3	4	5	6
1	1.174×10^3					
2	-3.072×10^7	2.575×10^7				
3	3.212×10^7	-3.897×10^6	1.027×10^8			
4	1.213×10^5	-5.412×10^4	-1.891×10^5	1.014×10^3		
5	-3.304×10^4	1.474×10^4	5.150×10^4	-2.136×10^2	3.543×10^2	
6	8.731×10^4	-3.894×10^4	-1.361×10^5	3.108×10^2	-5.957×10^1	8.415×10^2

Table XVI: Full Lower Triangle of 6x6 Initial Covariance Matrix, Position and Velocity States, at Exit-Blackout, Truth Model

	1	2	3	4	5	6
1	2.391×10^7					
2	1.010×10^7	6.626×10^7				
3	-2.994×10^6	-1.186×10^7	7.044×10^6			
4	5.599×10^3	3.009×10^4	-7.805×10^3	2.078×10^1		
5	2.672×10^4	1.674×10^5	-2.846×10^4	9.084×10^1	5.246×10^2	
6	-1.062×10^4	-4.301×10^4	1.657×10^4	-2.761×10^1	-1.365×10^2	5.896×10^2

Appendix D

Addendum: Results After Model Error Correction

Corrected Specific Force Schedule

As mentioned in Chapter VII, an error was made during the original study in modeling the longitudinal component of specific force on the orbiter, affecting the quartz crystal clock frequency error of the Master Timing Unit (MTU) model. This appendix presents the results of using a correct model for this specific force schedule. This is important, since the specific force model provides the primary effect on GPS clock accuracy, which in turn influences the accuracy that can be achieved at update times on both position and velocity estimates. The effects are depicted by plots of the performance of the 8-state filter designs described in Chapter VI in both pre- and post-blackout regions of operation.

The corrected specific force schedule applied to the clock model is summarized as follows. During the deorbit ignition period there is an application of thrust for approximately four minutes, followed by a period of free fall during which there is little specific force. As the Orbiter enters the atmosphere specific force slowly builds in response to atmospheric drag, commencing approximately two to three minutes prior to the beginning of assumed blackout. At exit from blackout, the longitudinal component of specific force has increased to approximately 0.008 g. It continues to build until reaching a peak of approximately 0.56g, at about four minutes prior to landing, and then rapidly decreases. At the end of the simulation, when the Shuttle is at 20,000 feet MSL, the level of specific force is 0.3 g (Ref 8:63).

The deorbit/reentry portion of the mission is one of high, almost

constant deceleration, once atmospheric entry is accomplished. This causes a constant increase in the quartz crystal clock model frequency error, and also in the clock model phase error.

Filter Modifications

Due to very limited time and resources with which to accomplish this correction, no extensive retiming was attempted. At the same time, however, it is felt that only minimal gains could be made with extensive retuning. As explained in Chapter VII, the effect of the error was mainly to interchange the characteristics of the pre- and post-blackout regions of operation. Thus, the filters were only modified basically by interchanging values of noise spectral density for the filter clock frequency error state and for the filter measurement noise on the pseudo range-rate measurements between the pre- and post-blackout regions (see Pg 51 and 53 for comparison).

This is summarized for the pre-blackout region as follows:

$$Q_{f8} = \begin{Bmatrix} 3.0 \times 10^{-5} \\ 6.0 \times 10^{-5} \\ 3.0 \times 10^{-5} \end{Bmatrix} (\text{ft/sec})^2/\text{sec} \begin{cases} t - t_0 < 85 \text{ sec} \\ t - t_0 < 150 \text{ sec} \\ t - t_0 > 150 \text{ sec} \end{cases} \quad (58)$$

$$R_{fv} = \begin{Bmatrix} 0.025 \\ 0.035 \\ 0.009 \end{Bmatrix} (\text{ft/sec})^2 \begin{cases} t - t_0 \leq 85 \text{ sec} \\ t - t_0 \leq 130 \text{ sec} \\ t - t_0 > 130 \text{ sec} \end{cases} \quad (59)$$

The values used for these quantities in the post-blackout region were:

$$Q_{f8} = \begin{Bmatrix} 3.0 \times 10^{-5} \\ 3.0 \times 10^{-4} \\ 1.0 \times 10^{-3} \\ 8.0 \times 10^{-3} \end{Bmatrix} (\text{ft/sec})^2/\text{sec} \begin{cases} t - t_0 \leq 85 \text{ sec} \\ t - t_0 \leq 130 \text{ sec} \\ t - t_0 \leq 420 \text{ sec} \\ t - t_0 > 420 \text{ sec} \end{cases} \quad (60)$$

$$R_{fv} = \begin{Bmatrix} 0.025 \\ 0.035 \\ 0.050 \end{Bmatrix} (\text{ft/sec})^2 \begin{cases} t - t_0 \leq 85 \text{ sec} \\ t - t_0 \leq 130 \text{ sec} \\ t - t_0 > 130 \text{ sec} \end{cases} \quad (61)$$

In all cases t_0 is the time at the beginning of the region of operation, either pre- or post-blackout. As explained in Chapter VI, the values are changed gradually to prevent filter corrections from driving truth model covariances negative due to numerics during the initial transient period.

It is not intended that these values be taken as final values for an implementable design. They should rather serve to indicate possible levels of achievement and starting points for final refinement.

Corrected Filter Performance

The filter performance will be discussed in reference to the performance plots for the pre-blackout region (Figures 141-156) and the post-blackout region (Figures 157-172). Much of the discussion in Chapter VII is applicable here, and thus only major differences will be pointed out.

In the pre-blackout region, the largest difference is that the system performance is much better behaved on almost all states, especially the filter clock frequency error state (see Figures 111 and 144). Only slight improvement is noted in the position error states. This suggests

a desirability to consider using a different model for the filter position error models - perhaps by adding pseudo noise to these states. In the present form the achievable accuracy in the position error is tied strictly to the accuracy achieved in the velocity error states. The velocity error states show much improvement over the earlier results (see Figures 121, 123, 154, and 156), due mainly to the improvement in the clock frequency error state, noted earlier.

In the post-blackout region, the results indicate the effect of the acceleration sensitivity in the quartz crystal clock model. The overall interpretation is still that the 8-state filter performs very adequately in bounding error growth for all states, supporting the conclusions drawn earlier. The system clock frequency error especially is adequately bounded, so that its effects are minimized (see Figure 160). A filter utilizing specific force dependent parameters, to describe the strengths of measurement noise and process noise which affect this state should provide even more benefit, however. The position and velocity error states show only slight degradation from the performances of the earlier portions of the study (see Figures 128-139 and Figures 161-172). This is probably due to the influence of actual specific force upon the filter's velocity estimates. This enables the filter to estimate the system velocity errors better, compared to the pre-blackout region in which specific force was largely absent.

Conclusion

This appendix supports the conclusions drawn in Chapter VII. These are that the 8-state filter should be a viable candidate for a GPS-aided reentry filter, and that specific force dependent filter parameters should be investigated for the GPS filter clock model.

Fig 141 8-St Est Error, Pre-Blackout, dx_7

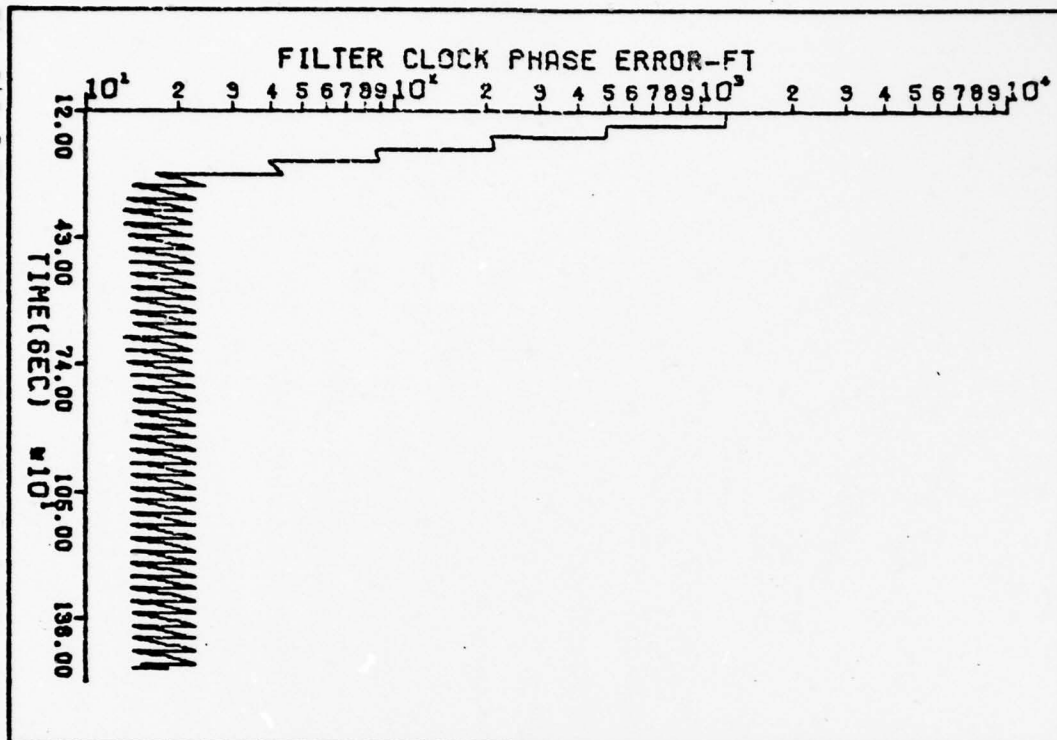
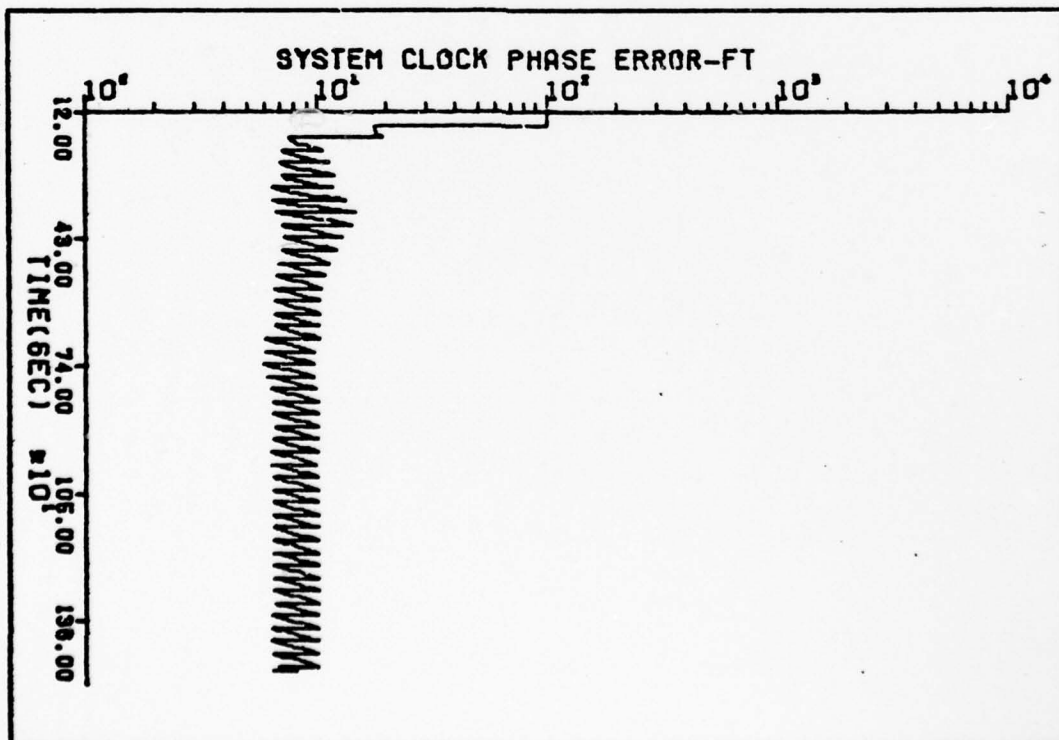
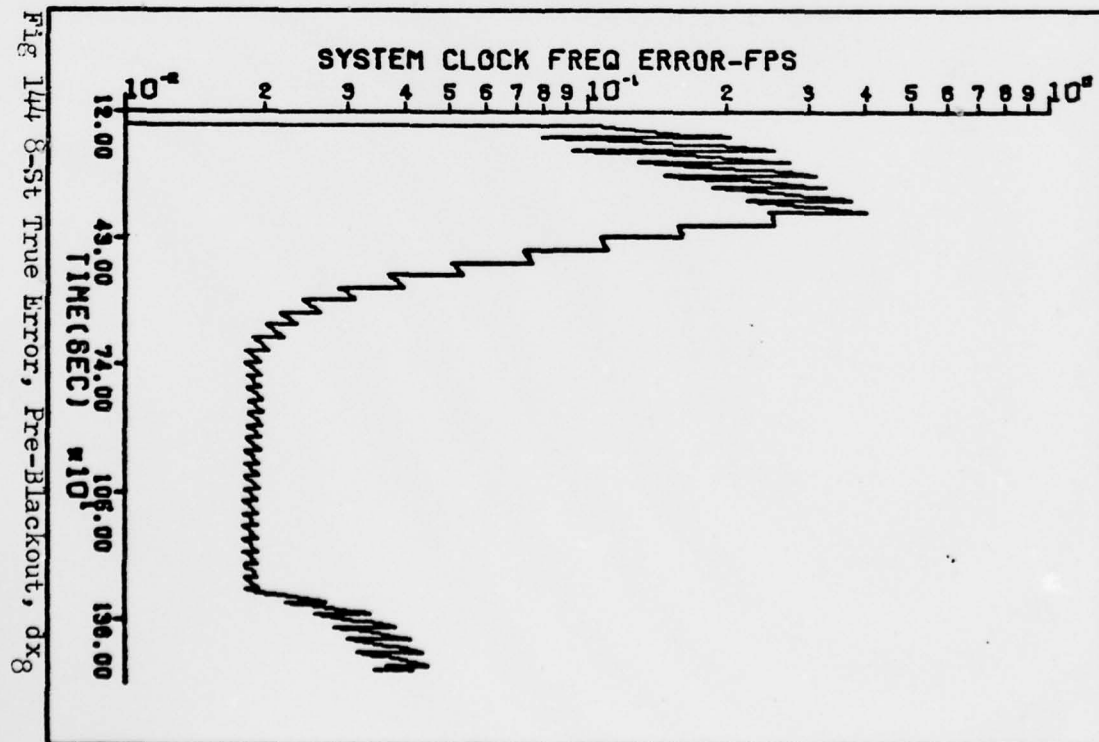
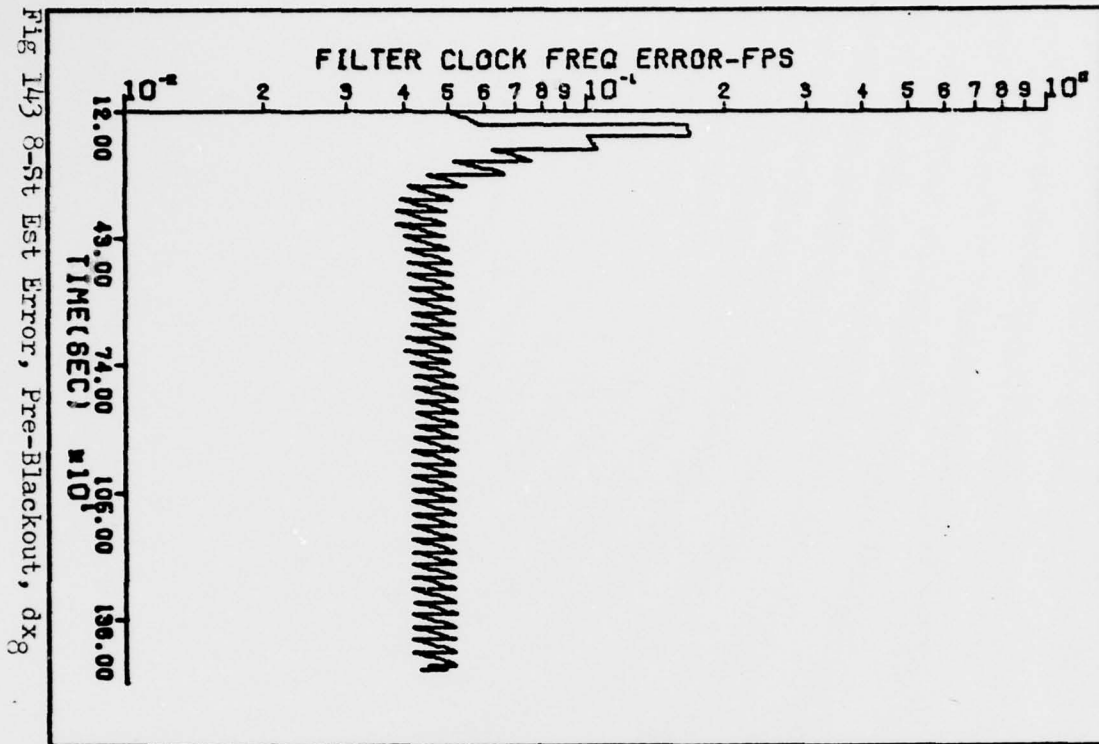


Fig 142 8-St True Error, Pre-Blackout, dx_7



XXX



AXX

Fig 145 8-St Est Error, Pre-Blackout, dx_1

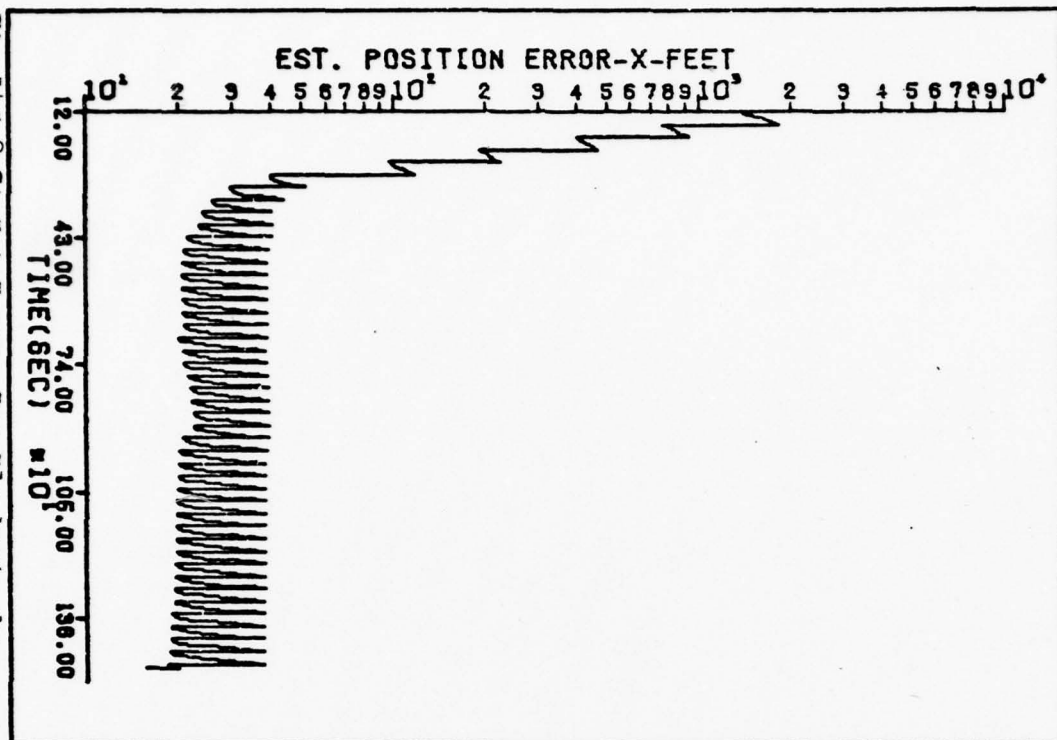
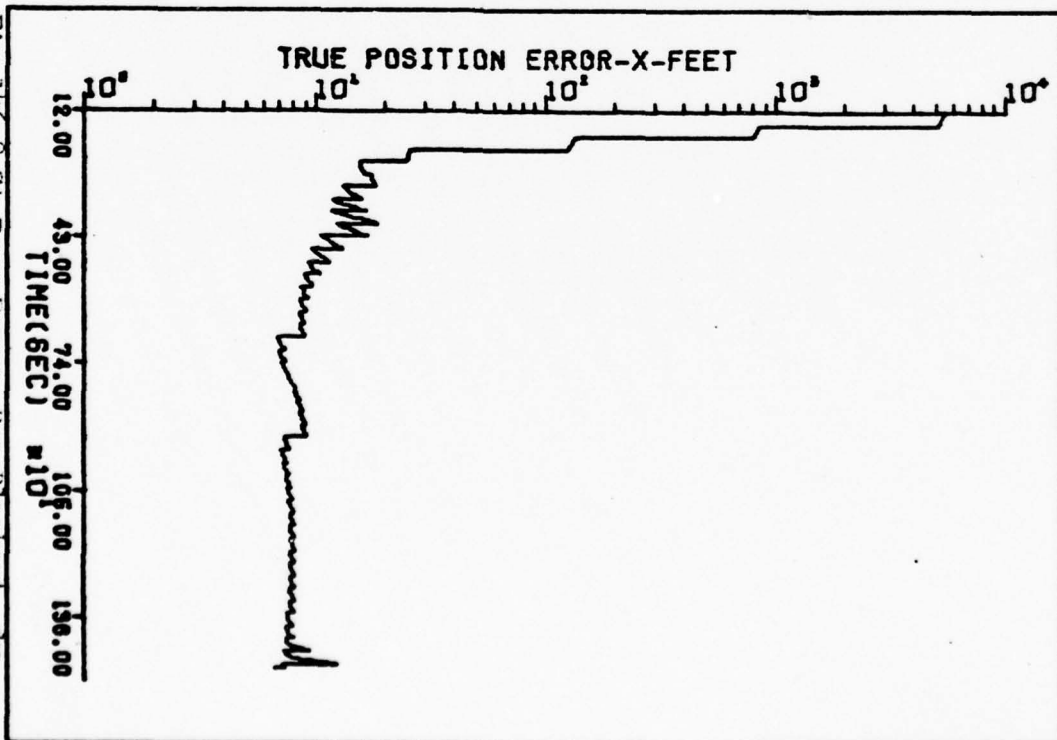


Fig 146 8-St True Error, Pre-Blackout, dx_1



XXX

Fig 147 8-St Est Error, Pre-Blackout, dx₂

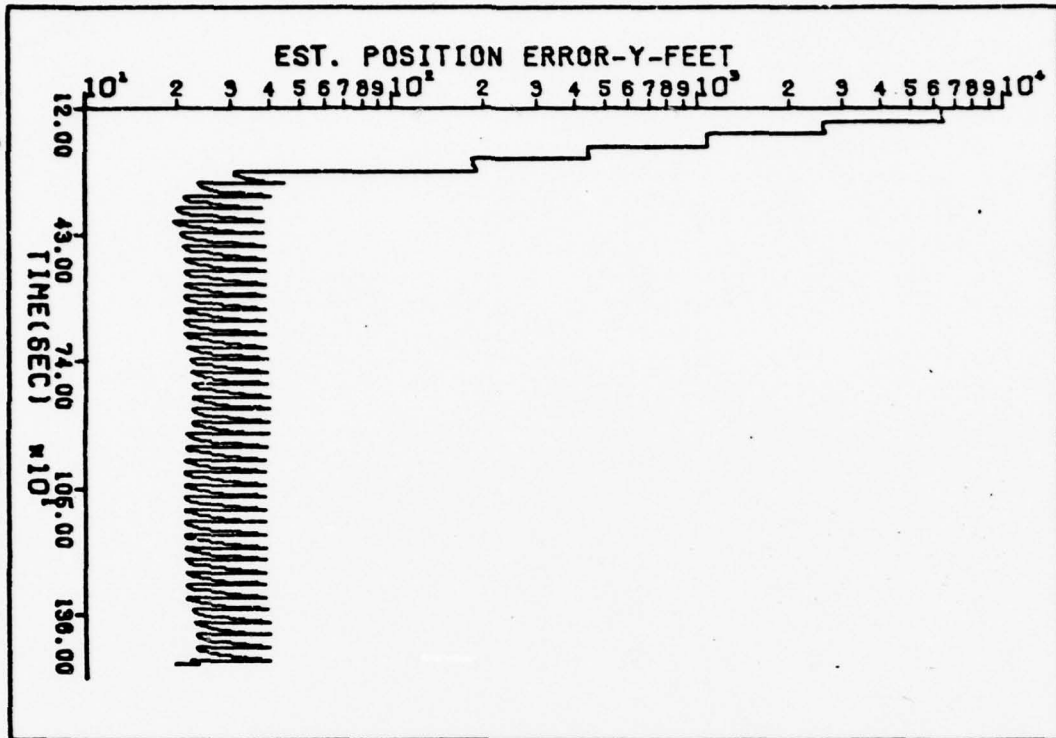
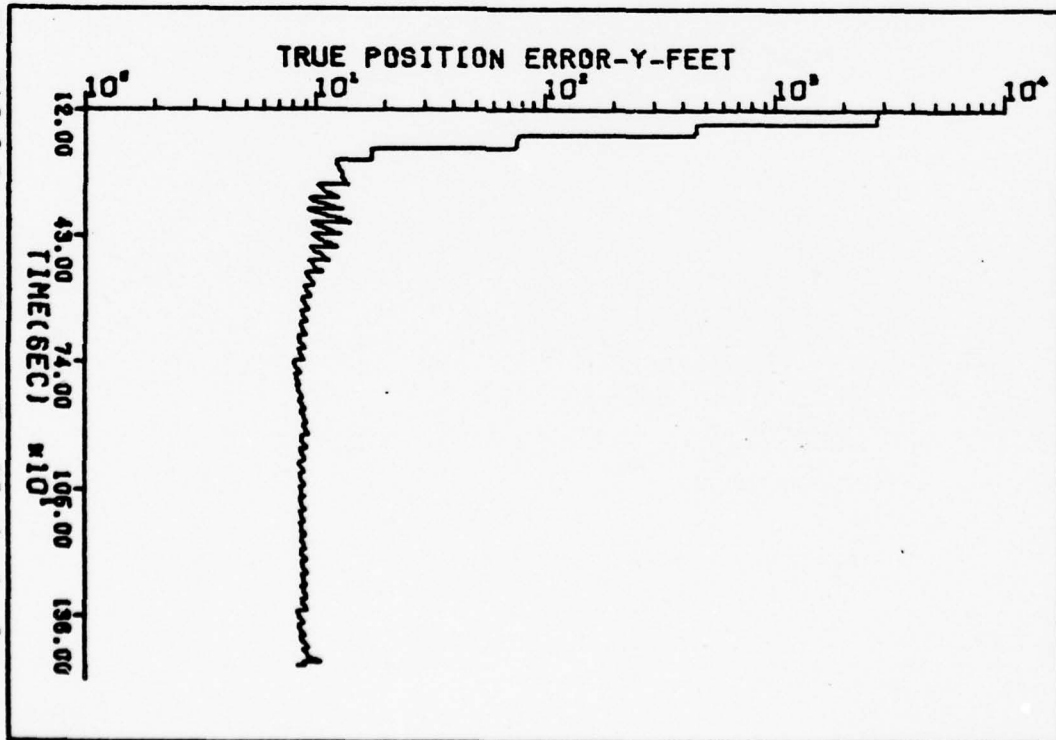


Fig 148 8-St True Error, Pre-Blackout, dx₂



207

Fig 149 8-St Est Error, Pre-Blackout, dx_3

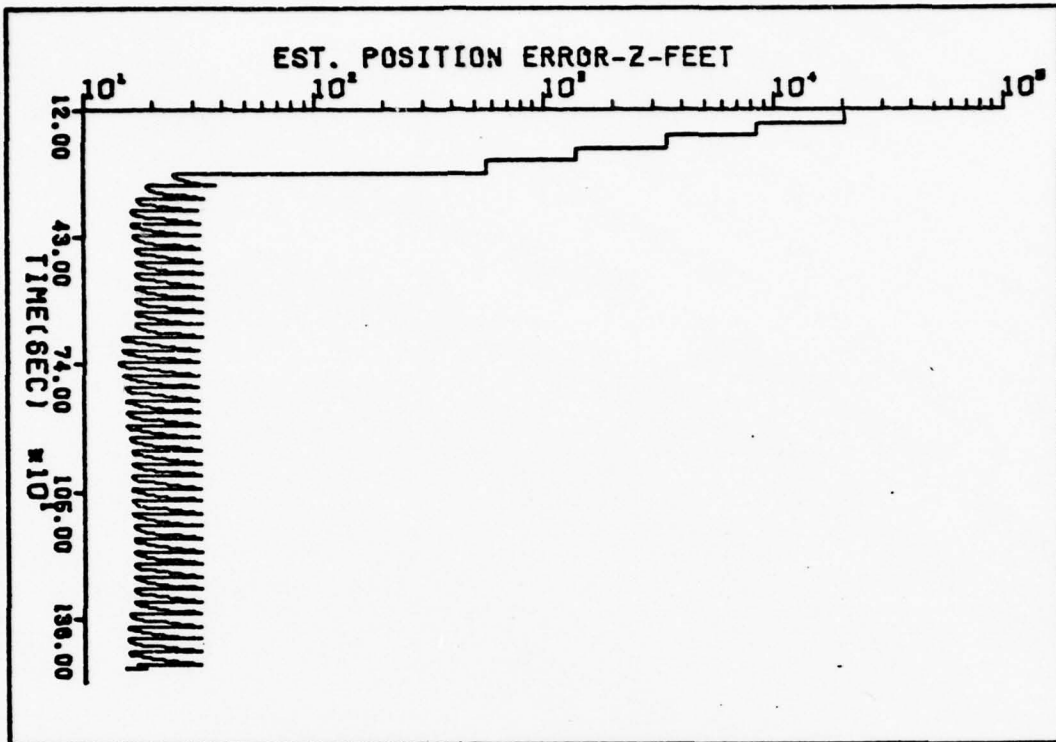
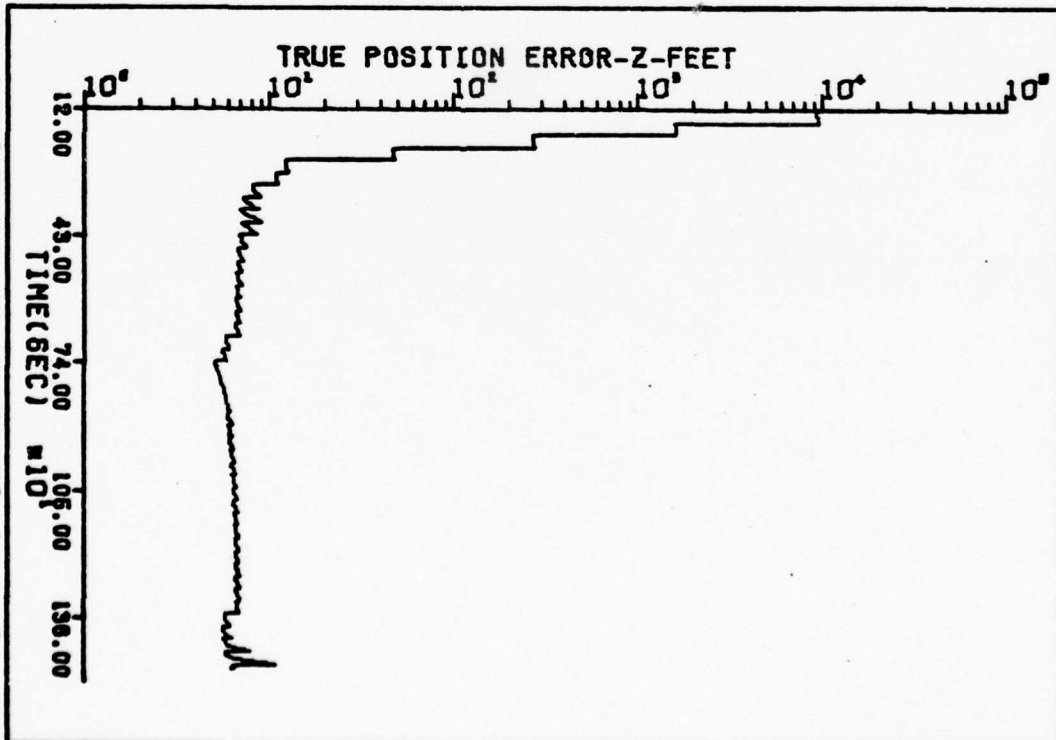


Fig 150 8-St True Error, Pre-Blackout, dx_3



XXX

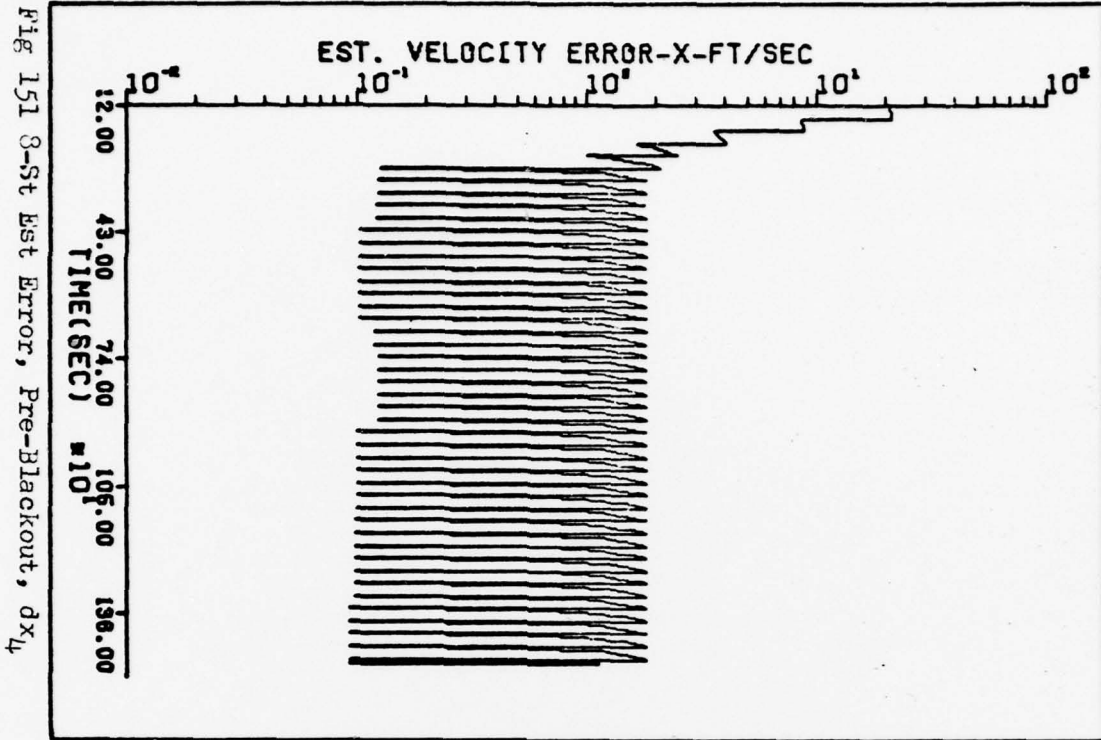


Fig 151 8-St Est Error, Pre-Blackout, dx_u

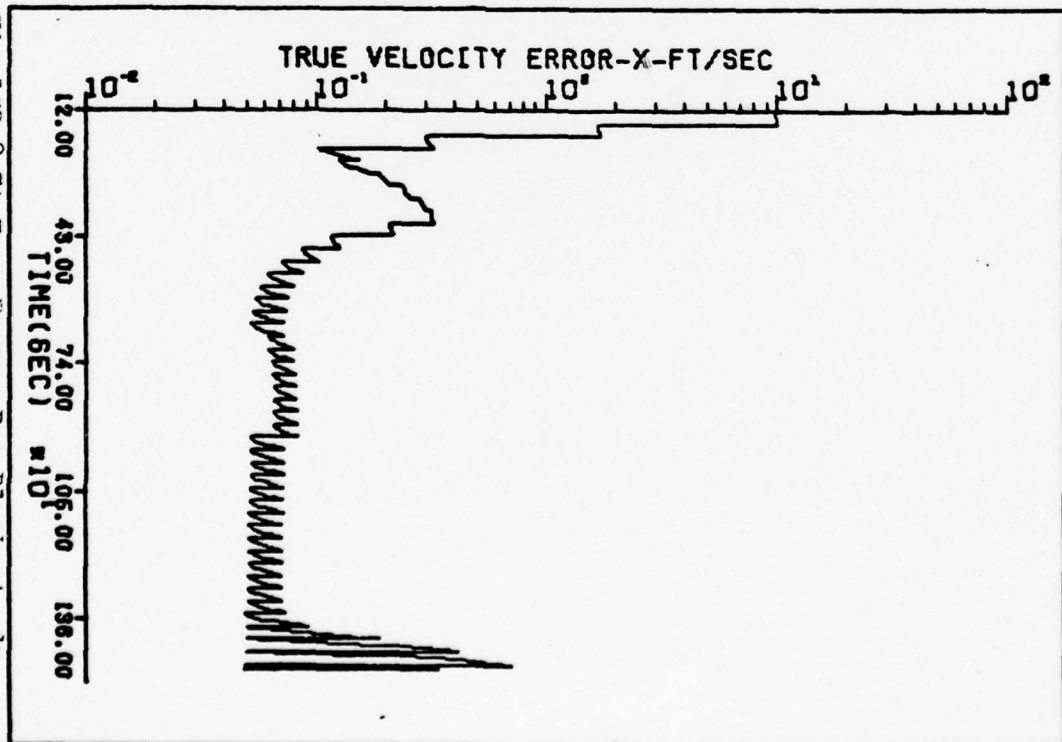


Fig 152 8-St True Error, Pre-Blackout, dx_u

XXX

Fig 153 8-St Est Error, Pre-Blackout, dx₅

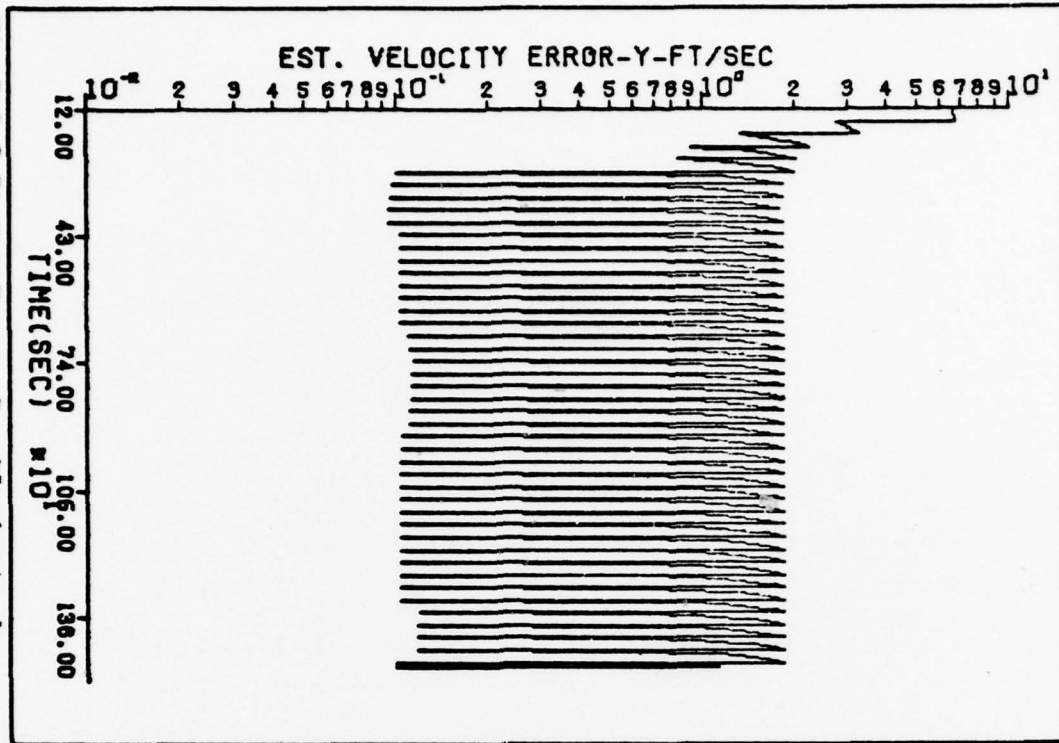
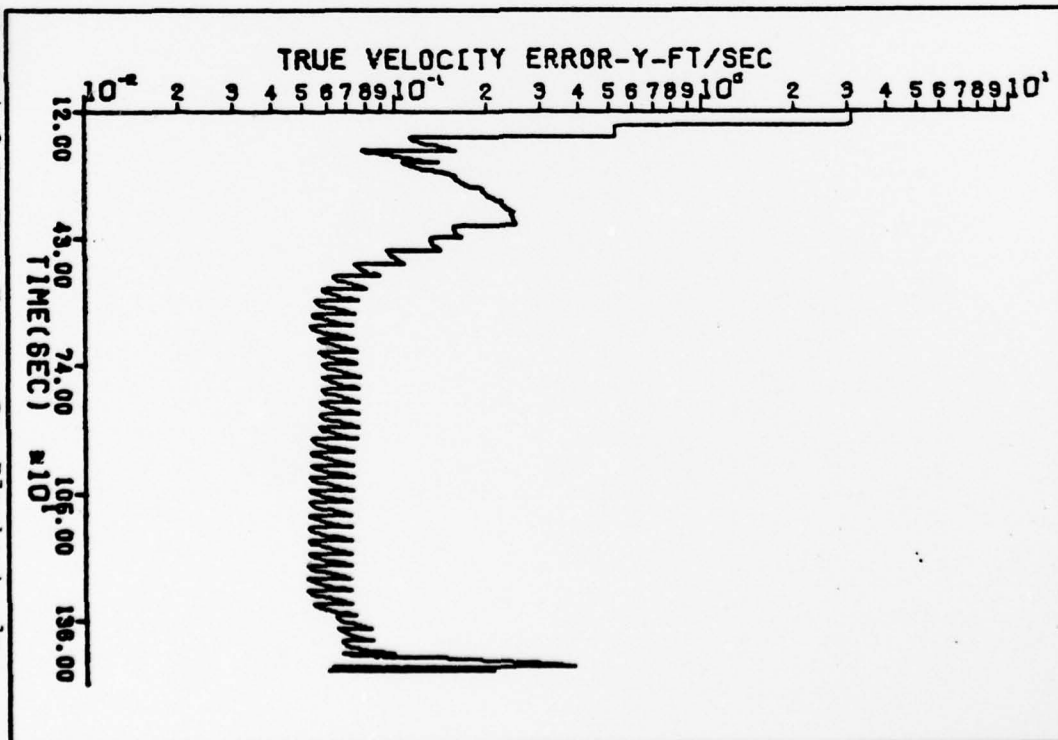
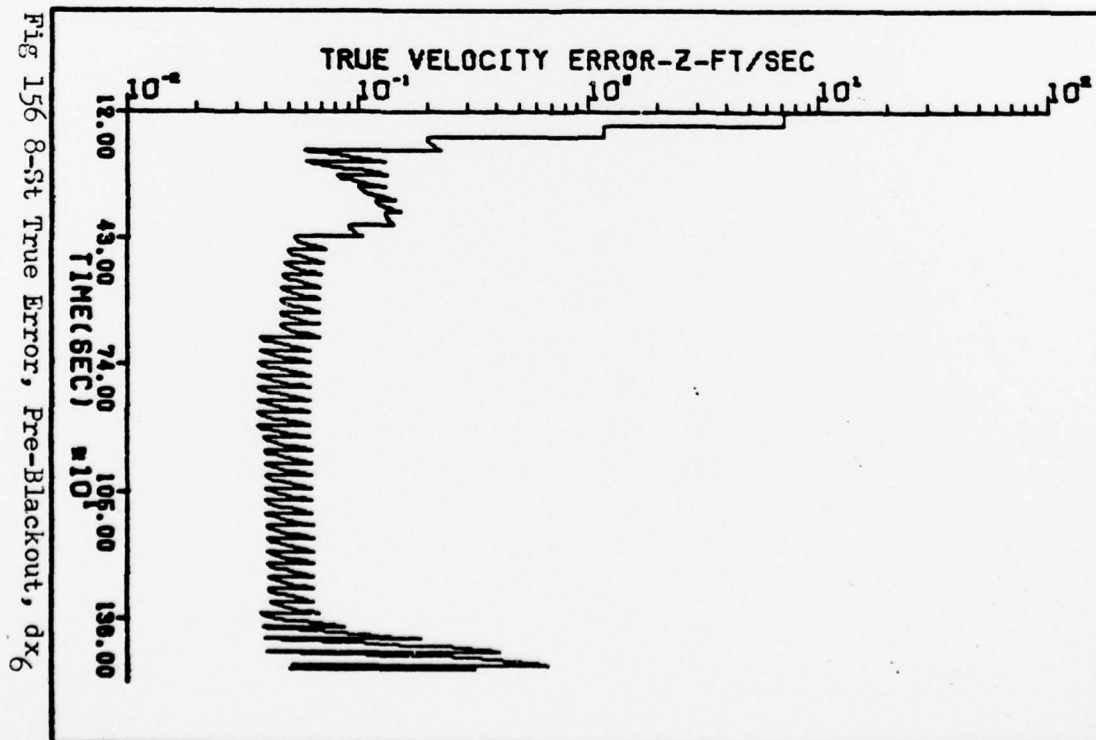
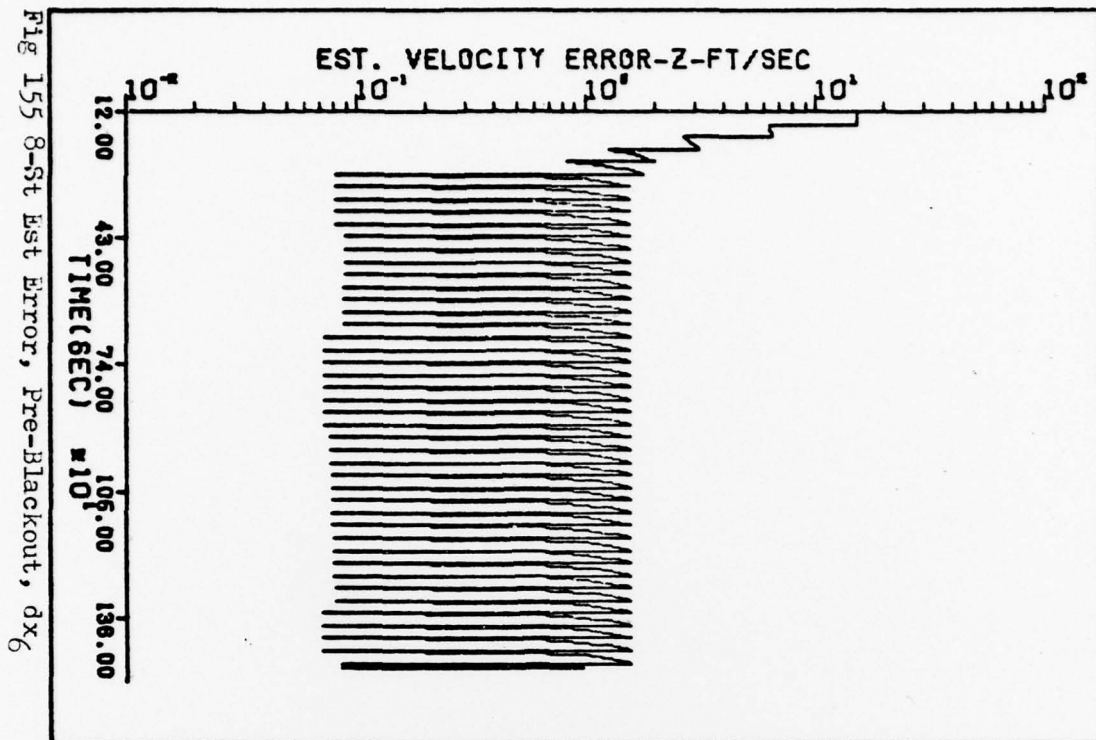


Fig 154 8-St True Error, Pre-Blackout, dx₅





The following plots (Figures 157-171) depict the post-blackout performance of the 8-state filter.

~~XXX~~

Fig 157 8-St Est Error, Post-Blackout, dx₇

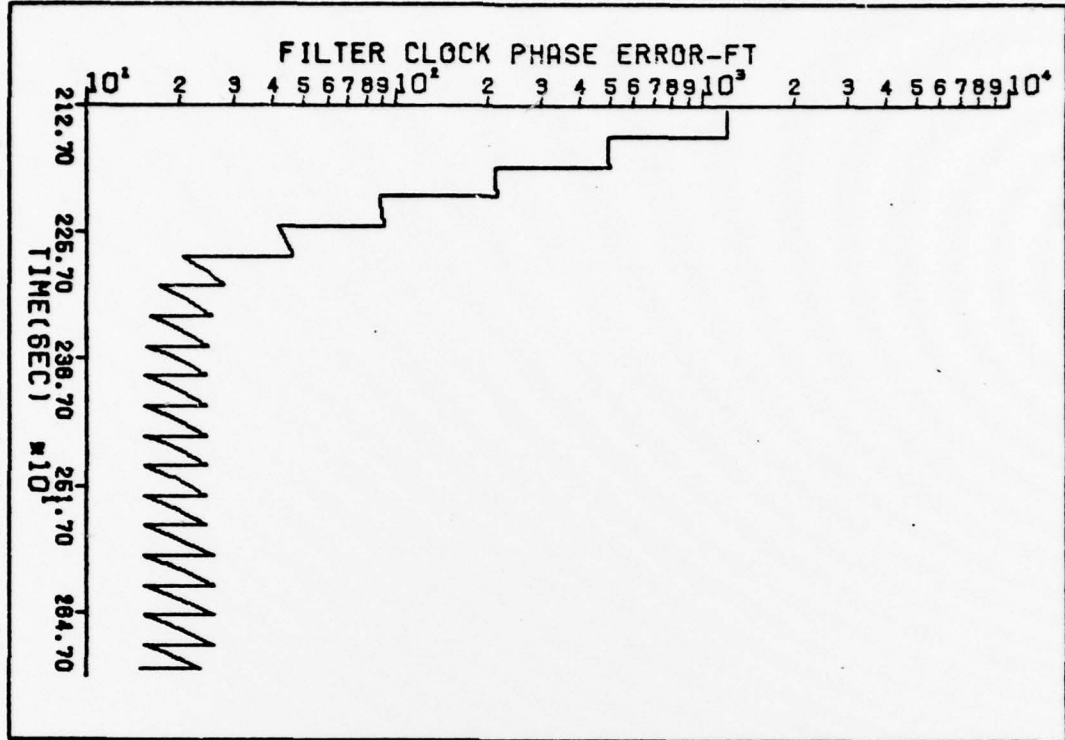
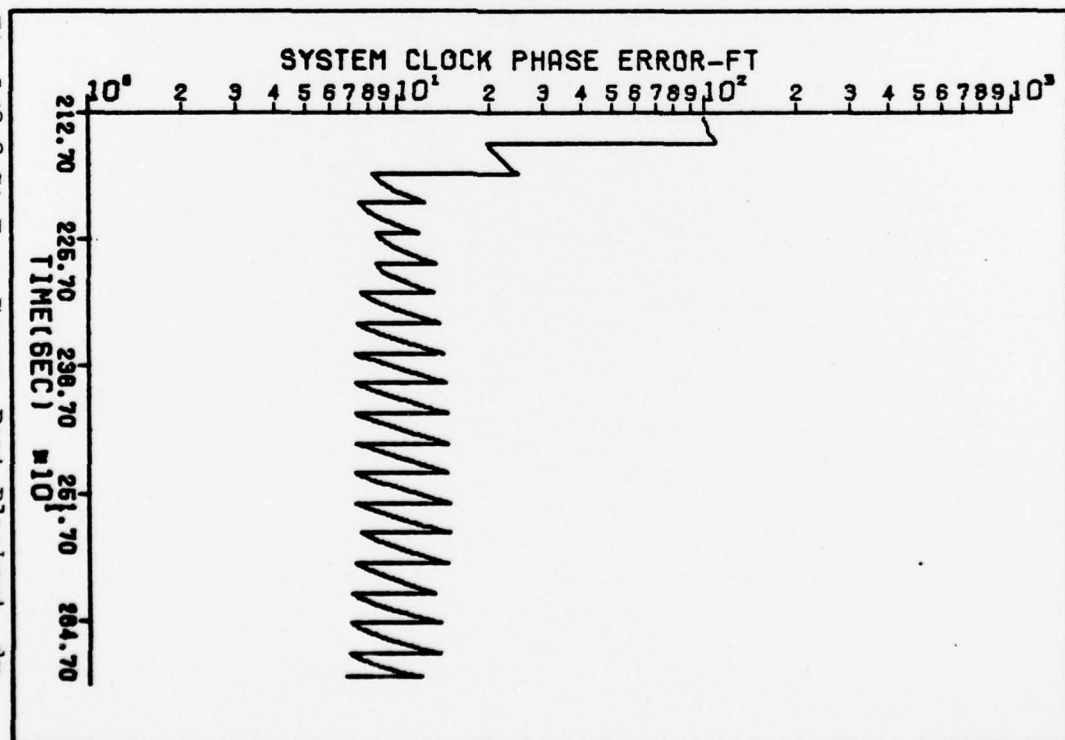
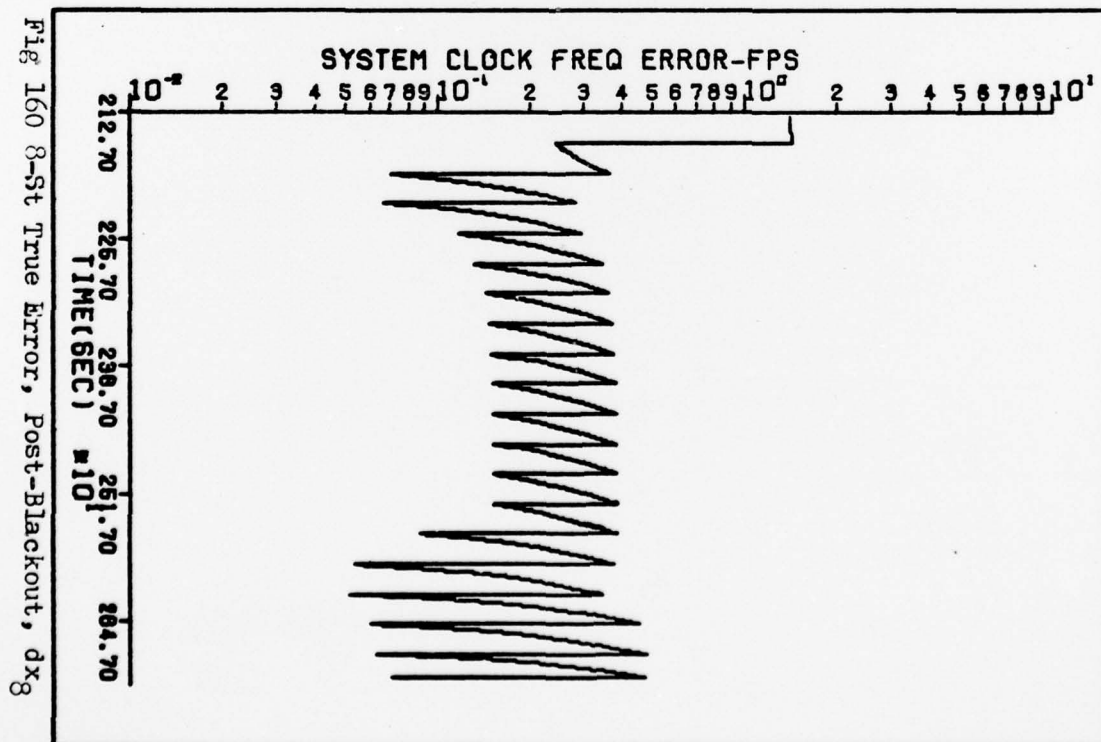
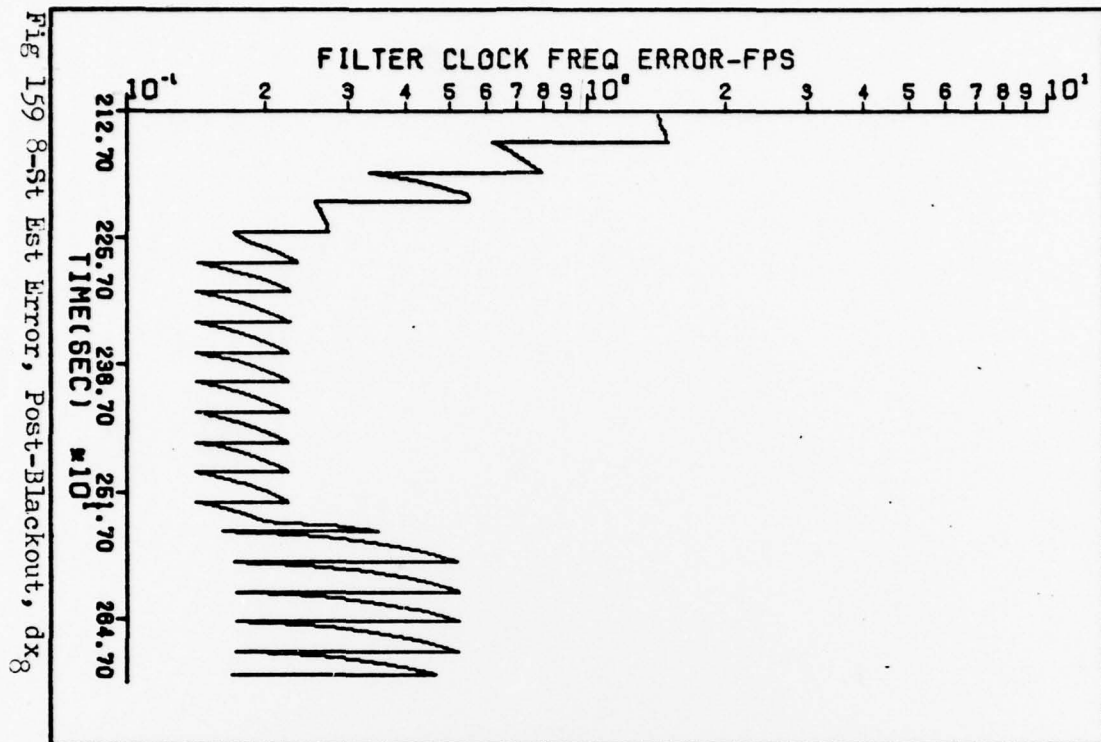


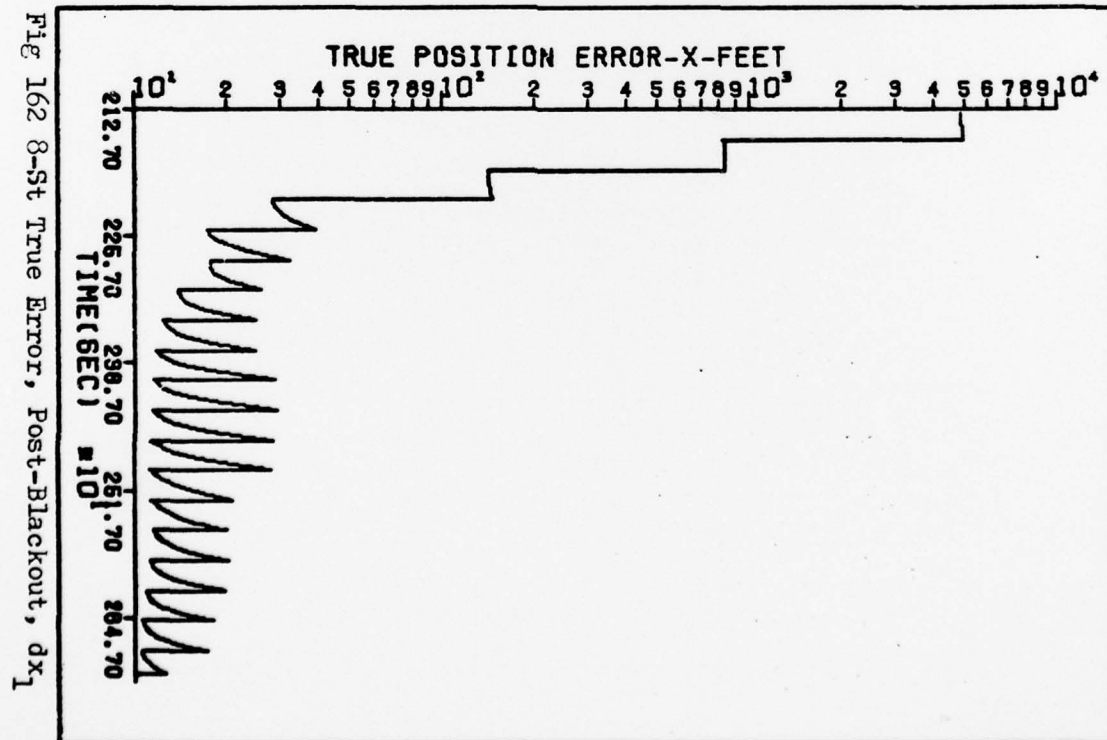
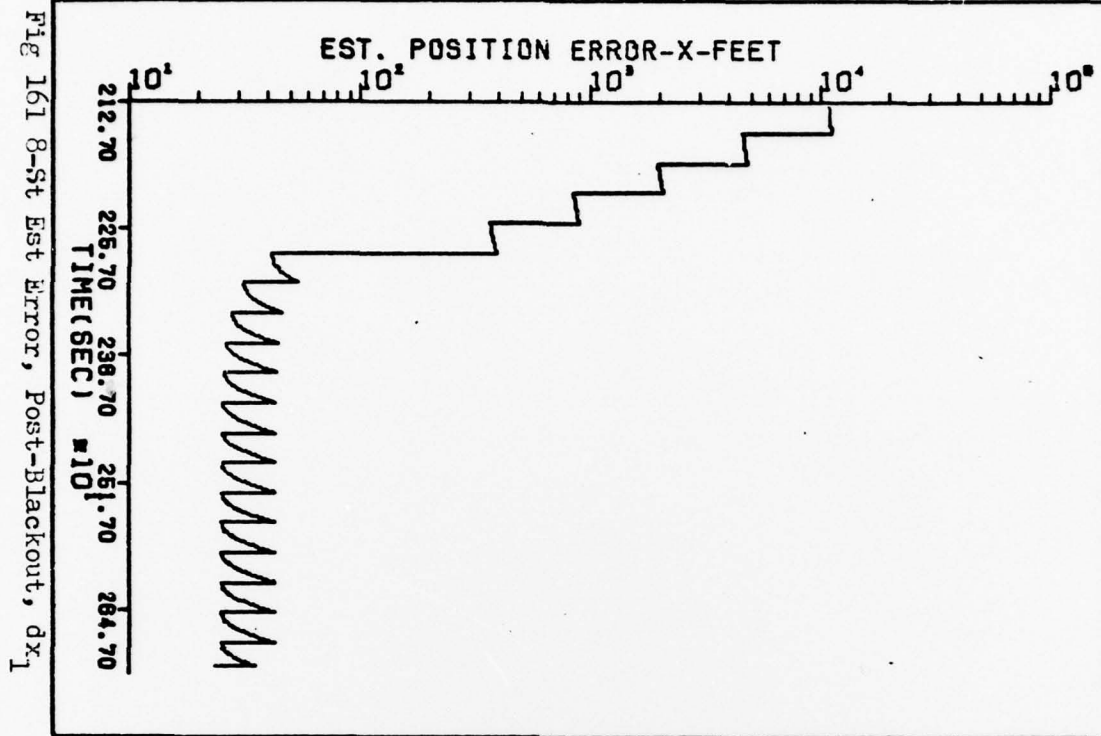
Fig 158 8-St True Error, Post-Blackout, dx₇



XX



XXX



XXX

Fig 163 8-St Est Error, Post-Blackout, dx₂

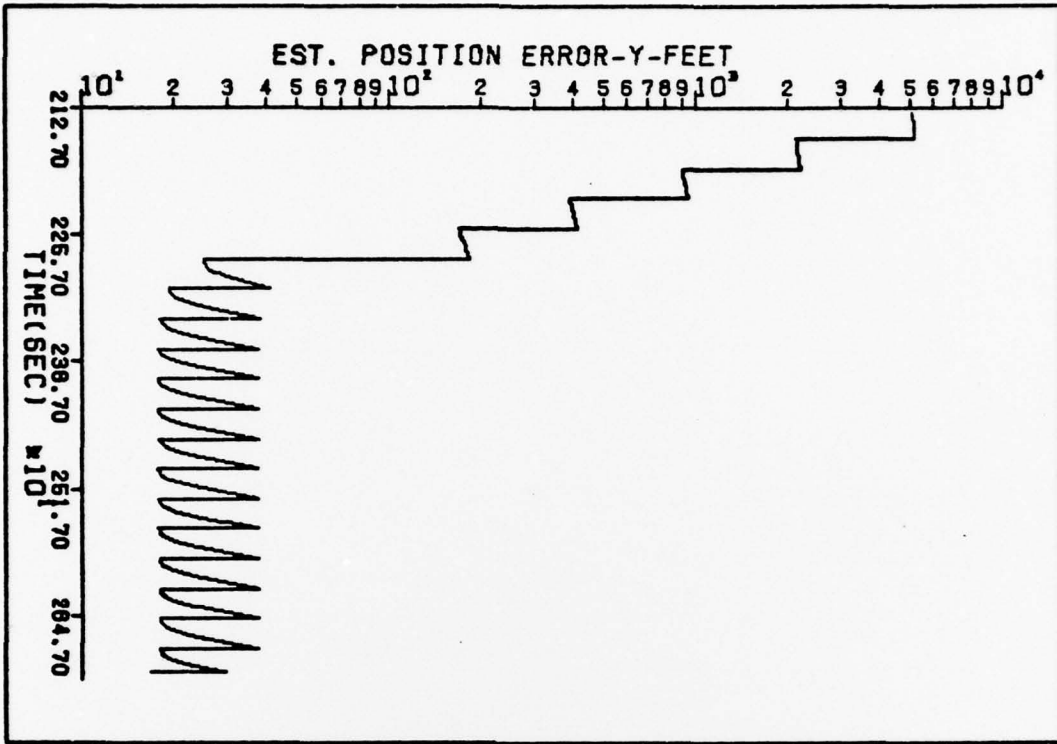
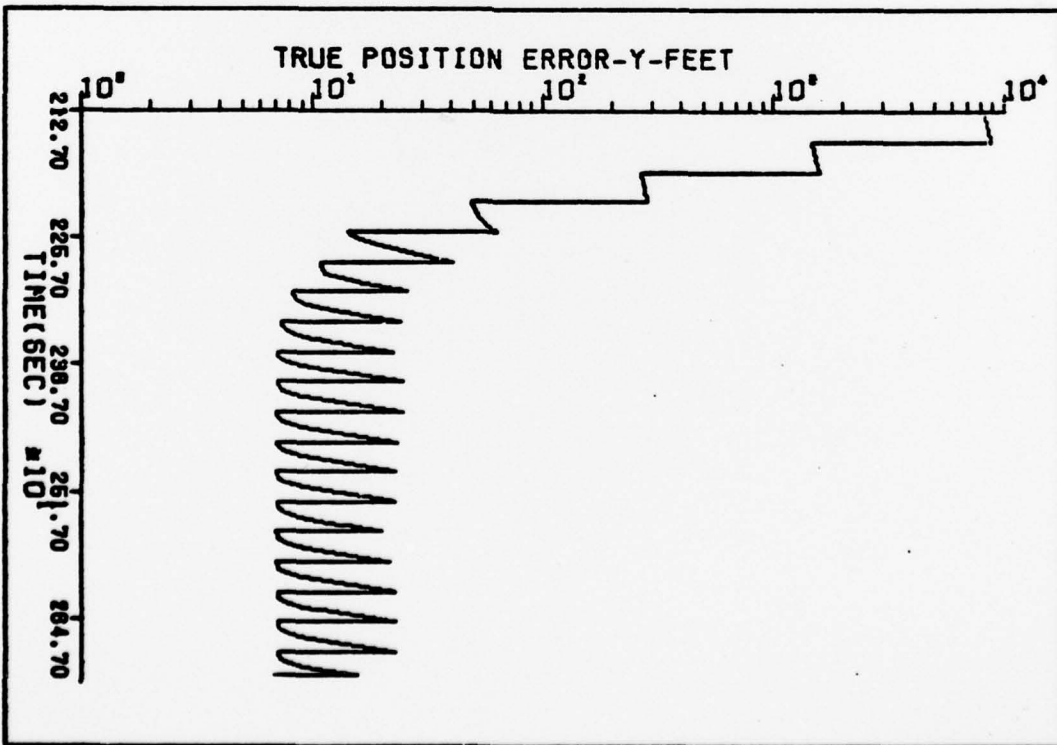


Fig 164 8-St True Error, Post-Blackout, dx₂



XXX

Fig 165 8-St Est Error, Post-Blackout, dx₃

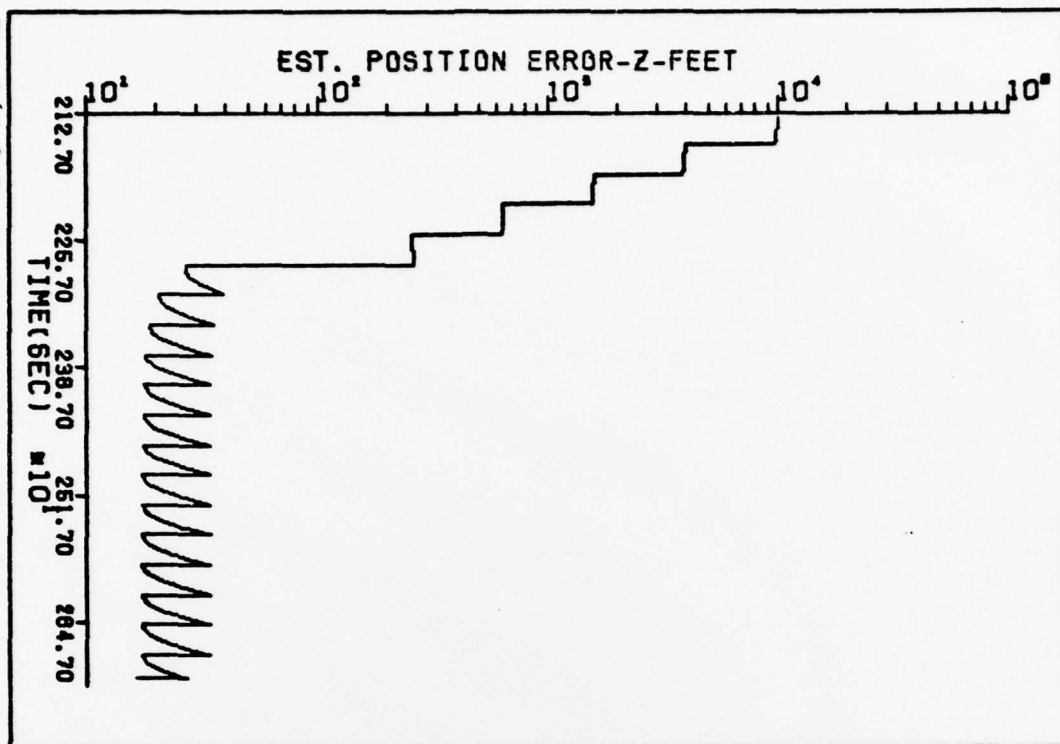
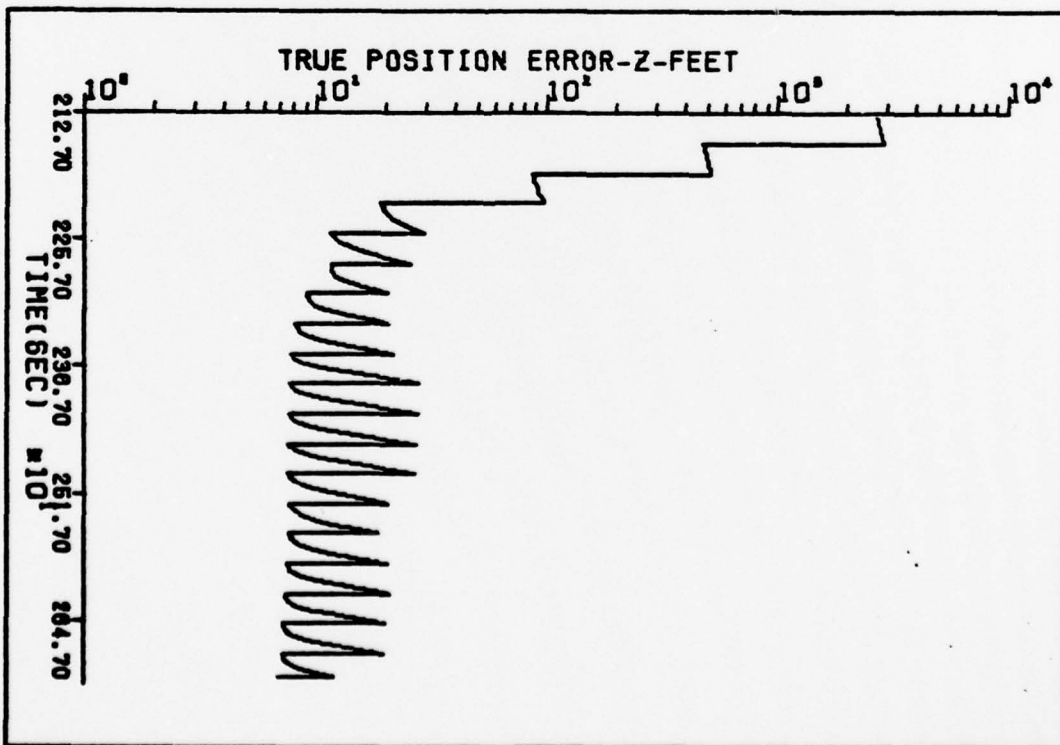
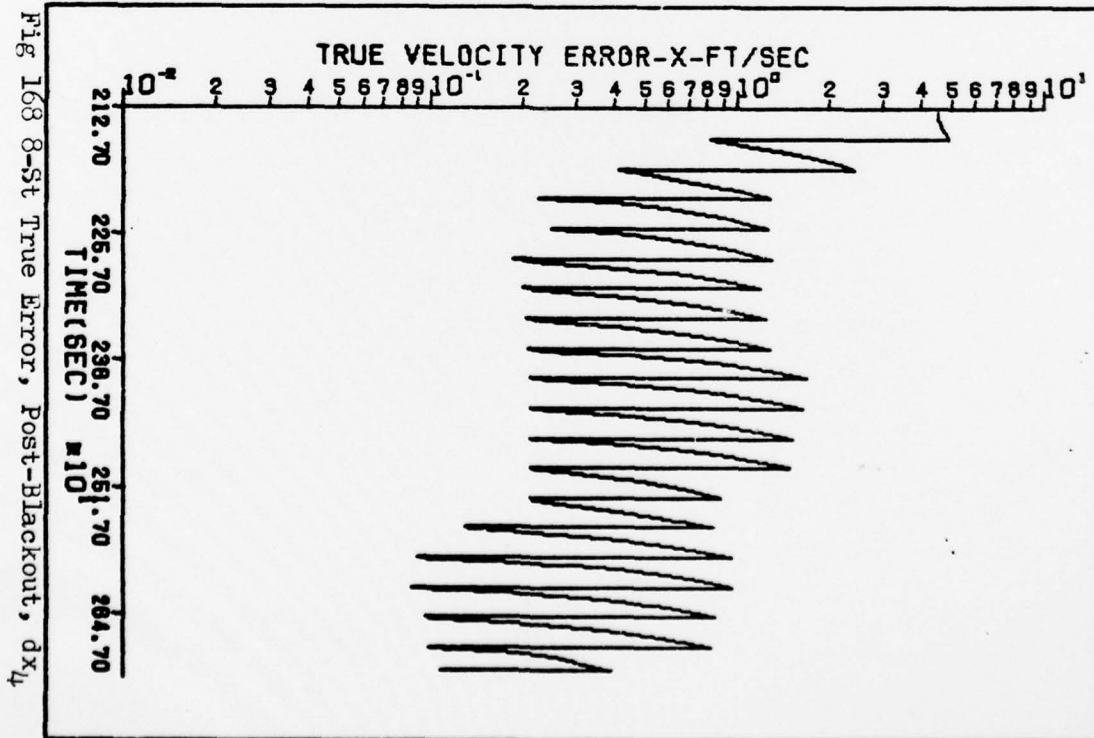
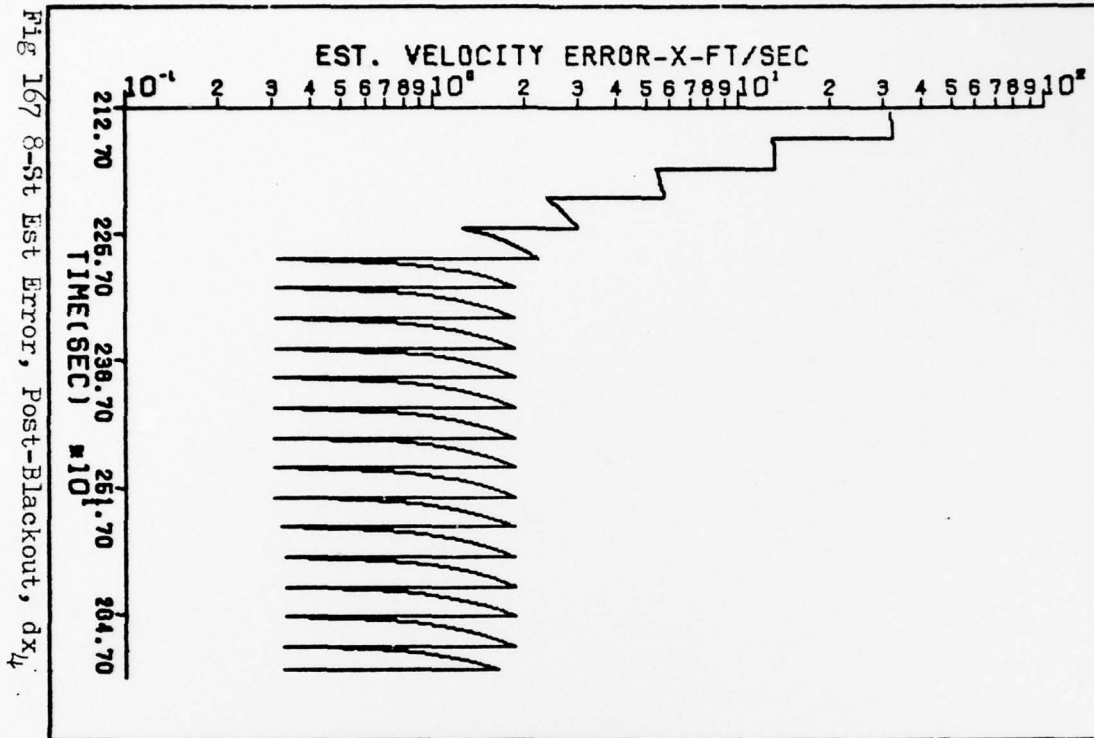


Fig 166 8-St True Error, Post-Blackout, dx₃



XXX



XXX

Fig 169 8-St Est Error, Post-Blackout, dx_5

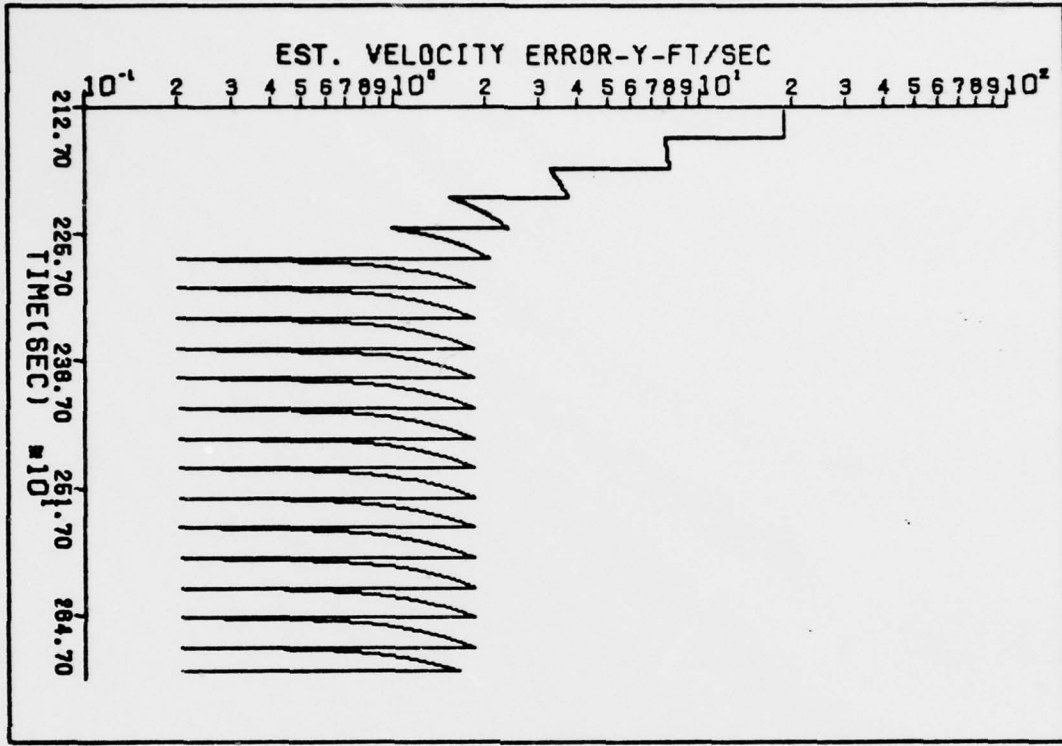
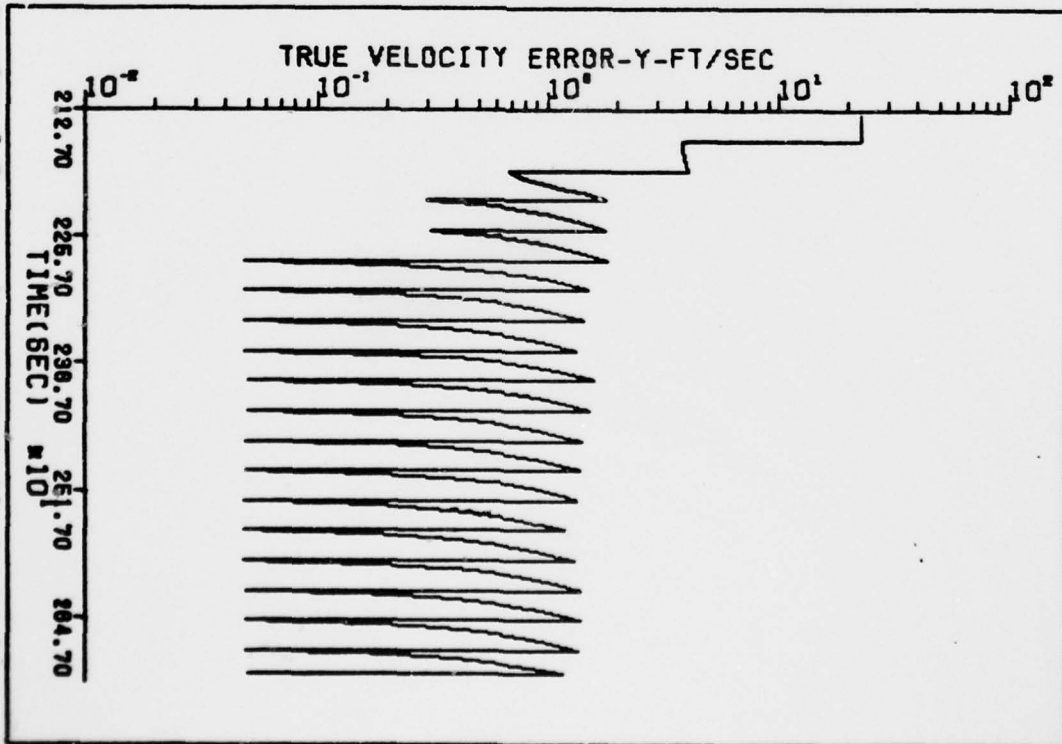


Fig 170 8-St True Error, Post-Blackout, dx_5



XXX

Fig 171 8-St Est Error, Post-Blackout, dx_6

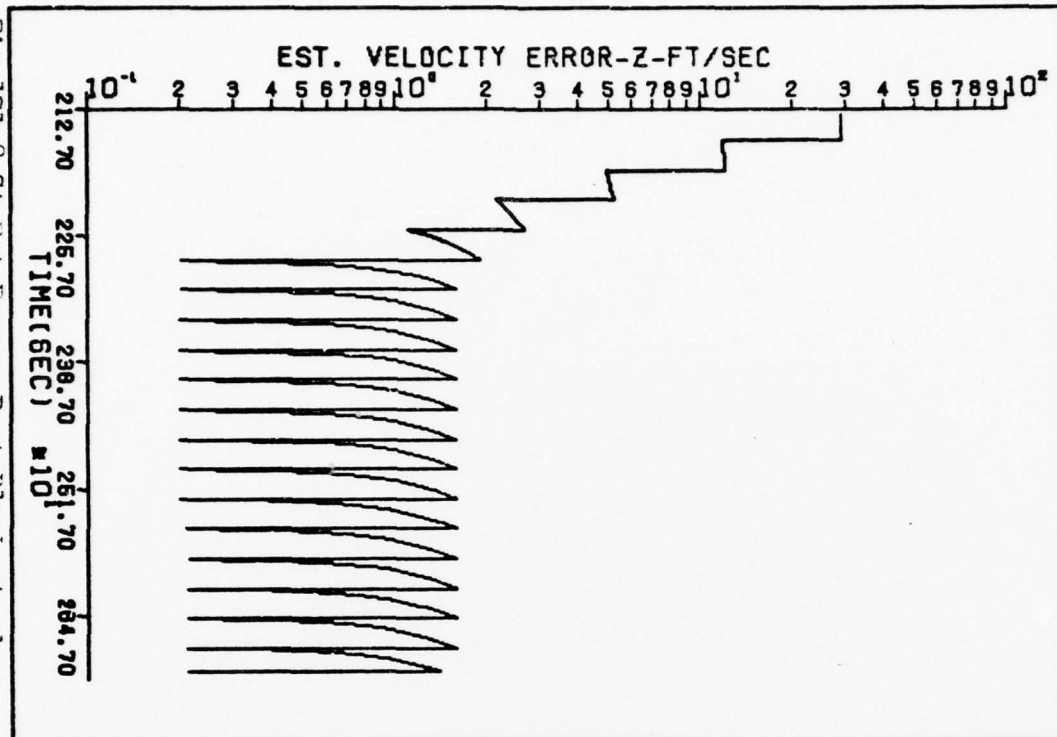
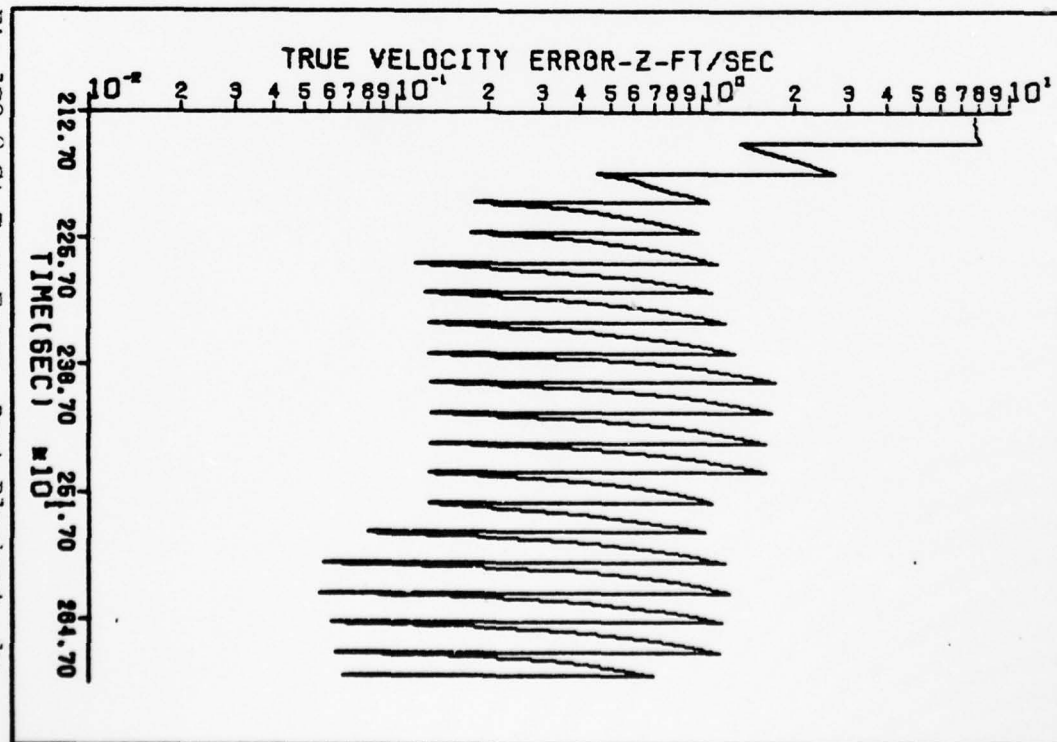


Fig 172 8-St True Error, Post-Blackout, dx_6



VITA

Dennis A. Van Liere was born on 4 December 1947 in Holland, Michigan. He graduated from high school there in 1966. He subsequently attended Michigan Technological University in Houghton, Michigan, from which he received the degree of Bachelor of Science in Electrical Engineering in June 1970. Upon graduation he received a commission in the USAF through the ROTC program, and was assigned to Navigator training at Mather AFB, California. He received his wings in April 1970, and was assigned as a Weapon System Officer in the rear cockpit of F-4 fighter aircraft. He served with operational units in Korea, The Republic of Viet Nam, and Thailand, flying 95 combat missions. He then served as instructor Weapon System Officer in the 4th TAC Fighter Wing until entering the School of Engineering, Air Force Institute of Technology, in June 1976. Permanent address: 7348 Edgewood

Jenison, Michigan 49428

This thesis was typed by Rosalie Gibler.

UNCLASSIFIED

SECURITY CLASSIFICATION OF THIS PAGE (When Data Entered)

REPORT DOCUMENTATION PAGE		READ INSTRUCTIONS BEFORE COMPLETING FORM
1. REPORT NUMBER AFIT/GGC/EE/77-10	2. GOVT ACCESSION NO.	3. RECIPIENT'S CATALOG NUMBER
4. TITLE (and Subtitle) A KALMAN FILTER DESIGN FOR THE SPACE SHUTTLE ORBITER INERTIAL MEASURING UNIT DURING DEORBIT/REENTRY USING GLOBAL POSITIONING SYSTEM SATELLITE INFORMATION		5. TYPE OF REPORT & PERIOD COVERED MS Thesis
7. AUTHOR(s) DENNIS A. VAN LIERE CAPTAIN, USAF		6. PERFORMING ORG. REPORT NUMBER
9. PERFORMING ORGANIZATION NAME AND ADDRESS Air Force Institute of Technology (AFIT-EN) Wright-Patterson AFB, Ohio 45433		8. CONTRACT OR GRANT NUMBER(s)
11. CONTROLLING OFFICE NAME AND ADDRESS Advanced Navigation Group (AFAL-RWA-1) U.S. Air Force Avionics Laboratory Wright-Patterson AFB, Ohio 45433		10. PROGRAM ELEMENT, PROJECT, TASK AREA & WORK UNIT NUMBERS Project 7071-00-12
14. MONITORING AGENCY NAME & ADDRESS (if different from Controlling Office)		12. REPORT DATE December, 1977
		13. NUMBER OF PAGES 182
		15. SECURITY CLASS. (of this report) Unclassified
		15a. DECLASSIFICATION/DOWNGRADING SCHEDULE
16. DISTRIBUTION STATEMENT (of this Report) Approved for public release; distribution unlimited		
17. DISTRIBUTION STATEMENT (of the abstract entered in Block 20, if different from Report)		
18. SUPPLEMENTARY NOTES Approved for public release; IAW AFR 190-17 JERRAL F. GUESS, Captain, USAF Director of Information		
19. KEY WORDS (Continue on reverse side if necessary and identify by block number) Kalman Filter Inertial Navigation Space Shuttles Navigation Satellites Global Positioning System		
20. ABSTRACT (Continue on reverse side if necessary and identify by block number) Three Kalman Filter implementations for the deorbit/reentry phase of a Space Shuttle Orbiter mission profile are studied. Each design uses measurements from Global Positioning System satellites to update Kalman Filter estimates of selected error states and to bound the Shuttle's INS error growth. Covariance Analysis techniques are used to compare the performances of 17-state, 11-state, and 8-state filter designs using a digital computer simulation of a NASA OFT-1 Space Shuttle mission trajectory. A 73-state truth model of the Space Shuttle IMU, the Orbiter GPS receiver Master Timing Unit, and the GPS		

DD FORM 1 JAN 73 1473

EDITION OF 1 NOV 65 IS OBSOLETE

UNCLASSIFIED

SECURITY CLASSIFICATION OF THIS PAGE (When Data Entered)

UNCLASSIFIED

SECURITY CLASSIFICATION OF THIS PAGE(When Data Entered)

satellite constellation is used as a system simulation to examine the performance of the design filters. The results are shown primarily in the form of computer-generated plots of both filter indicated errors and true system errors versus time. It is concluded that an 8-state filter design is able to perform well enough to be a primary candidate for design implementation, and also that further refinements are necessary in the user clock model of the design Kalman Filter.

UNCLASSIFIED

SECURITY CLASSIFICATION OF THIS PAGE(When Data Entered)

END

FILMED

11-84

DTIC